Mississippi River Plume Hydrography: Annual Report

Mississippi River Plume Hydrography: Annual Report

Editors

Stephen P. Murray
Jami Donley

Disclaimer

This report was prepared under contract between the Minerals Management Service (MMS) and Coastal Studies Institute, Louisiana State University. This report has been technically reviewed by the MMS and approved for publication. Approval does not signify that the contents necessarily reflect the views and policies of the Service, nor does mention of trade names or commercial products constitute endorsement or recommendation for use. It is, however, exempt from review and compliance with MMS editorial standards.

Report Availability

Extra copies of the report may be obtained from the Public Information Unit (Mail Stop 5034) at the following address:

U.S. Department of the Interior
Minerals Management Service
Public Information Unit (MS 5034)
Gulf of Mexico OCS Regional Office
1201 Elmwood Park Boulevard
New Orleans, Louisiana 70123-2394

Telephone Number: 1-800-200-GULF

Citation

About the Cover

The cover is taken from Figure 5 of this report, wind velocities observed from the R/V *Pelican* as it transits the study area during Cruise I, April 22 through May 1, 1992. See Section II, Hydrographic Survey, for a discussion.

Principal Investigators and Key Personnel

Remote Sensing and Image Processing
Nan D. Walker, Coastal Studies Institute, LSU, Baton Rouge, LA
Lawrence J. Rouse, Jr., Coastal Studies Institute, LSU, Baton Rouge, LA
Oscar K. Huh, Coastal Studies Institute, LSU, Baton Rouge, LA

Hydrographic Survey
Stephen P. Murray, Coastal Studies Institute, LSU, Baton Rouge, LA
Curtis C. Ebbesmeyer, Evans-Hamilton, Inc., Seattle, WA

Sediment Flux
Wilford D. Gardner, Department of Oceanography, Texas A&M, College Station, TX
Mary Jo Richardson. Department of Oceanography, Texas A&M, College Station, TX

Benthic Boundary Layer
L. Don Wright, School of Marine Science, VIMS, College of William & Mary,
   Gloucester Point, VA

Light and Nutrients
R. Eugene Turner, Coastal Ecology Institute, LSU, Baton Rouge, LA

Hypoxia and Pigments
Nancy Rabalais, LA Universities Marine Consortium, Cocodrie, LA

Phytoplankton
Quay Dortch, LA Universities Marine Consortium, Cocodrie, LA

Zooplankton
Richard F. Shaw, Coastal Fisheries Institute, LSU, Baton Rouge, LA

Pollutant Chemistry
Jay C. Means, School of Veterinary Medicine, LSU, Baton Rouge, LA
Debra J. McMillin, School of Veterinary Medicine, LSU, Baton Rouge, LA

Data Management
Mary L. White, Coastal Ecology Institute, LSU, Baton Rouge, LA

Program Management
Stephen P. Murray, Coastal Studies Institute, LSU, Baton Rouge, LA

Field Logistics
Rodney Fredericks, Coastal Studies Institute, LSU, Baton Rouge, LA

Table of Contents

List of Figures

xv

MISSISSIPPI RIVER PLUME HYDROGRAPHY
ANNUAL REPORT

I. Introduction

The Mississippi River Plume Hydrography study (LATEX B) is part of a larger Louisiana-Texas Physical Oceanography Program, which began in October 1991. The overall objective of our study is to determine the fundamental aspects of the velocity structure, volume and sediment flux, pollutant chemistry, and biological characteristics in the coastal plume arising from the discharge of the Mississippi and Atchafalaya Rivers. This report covers LATEX B Cruise I (April 1992) and Cruise II (October 1992). Figure 1 shows the LATEX study area.

Satellite images and observations of the hydrographic and current regimes of the coastal waters from the Mississippi Delta west and south to the Texas-Mexico border indicate the presence of a brackish water, turbid plume emanating from the discharge of the Atchafalaya-Mississippi Rivers. This plume is strongly modulated and even reversed by the annual cycle of the winds from Louisiana to south Texas. The coastal current formed by this plume is locally influenced by turbid, low salinity outflow plumes from major coastal bays (Sabine and Calcasieu Lakes and Galveston Bay). Intense northerly wind events associated with frontal passages in late fall, winter, and early spring apparently completely disrupt the Atchafalaya source of the coastal current and its dissolved and suspended sediment particulate load. The Mississippi-Atchafalaya River system typically has a peak discharge in April in excess of 30,000 m³/s and a low in September to October of about 10,000 m³/s.

These river discharges, mixing with seawater and spreading sediment over the continental shelf, create a region of altered (lowered) salinities and temperatures, a seaward sloping pressure gradient, and a resulting mosaic of water masses and fronts in the estuarine, inshore, and continental shelf areas of the LATEX region. Inner shelf distribution of waters and sediments results from the interaction of momentum, buoyancy forces, winds, waves, longshore currents, and pressure gradients (sea surface slope and density gradients). These runoff-altered shelf waters, loosely referred to as the coastal current are in fact a complex of river and estuarine discharge plumes, mudstreams from rivers, and local zones of resuspended bottom sediment—all in various stages of mixing and dispersal in the ambient gulf waters.

Fresh water distribution has heretofore been the most valuable tracer of large-scale water motion in the LATEX region. The fresh water content in the coastal plume and on the shelf is clearly an annual cycle triggered by the spring flood of the Mississippi-Atchafalya Rivers. The Mississippi-Atchafalaya discharge is advected westerly and southerly along the LATEX coastline even as far as Mexico by downcast wind components from the spring flood until early summer. The onset of strong southerly and southeasterly winds in early summer off Mexico and south Texas then exert upcoast wind stress components on the low salinity layer near the coast, reversing the flow, causing a convergence in the coastal currents, and advecting low salinity water offshore from the convergence and offshore Ekman transport in the surface layer. The brackish layer is, in a sense, peeled off and plowed offshore by the northward migrating convergence zone. The result of this activity is that nearly the entire LATEX shelf east of Galveston Bay out to the 200 m isobath is covered with low salinity water by late July. With the slackening of the strong southerly and southeasterly winds in late summer, downcast flow returns to the LATEX region and downwelling favorable winds re-establish the low salinity coastal current. Salinity in the south Texas coastal current decreases as water of northerly origin advects back into the region (Smith, 1980). Salinities gradually increase in October all along the LATEX coastal plume region as the major rivers approach low river discharges.
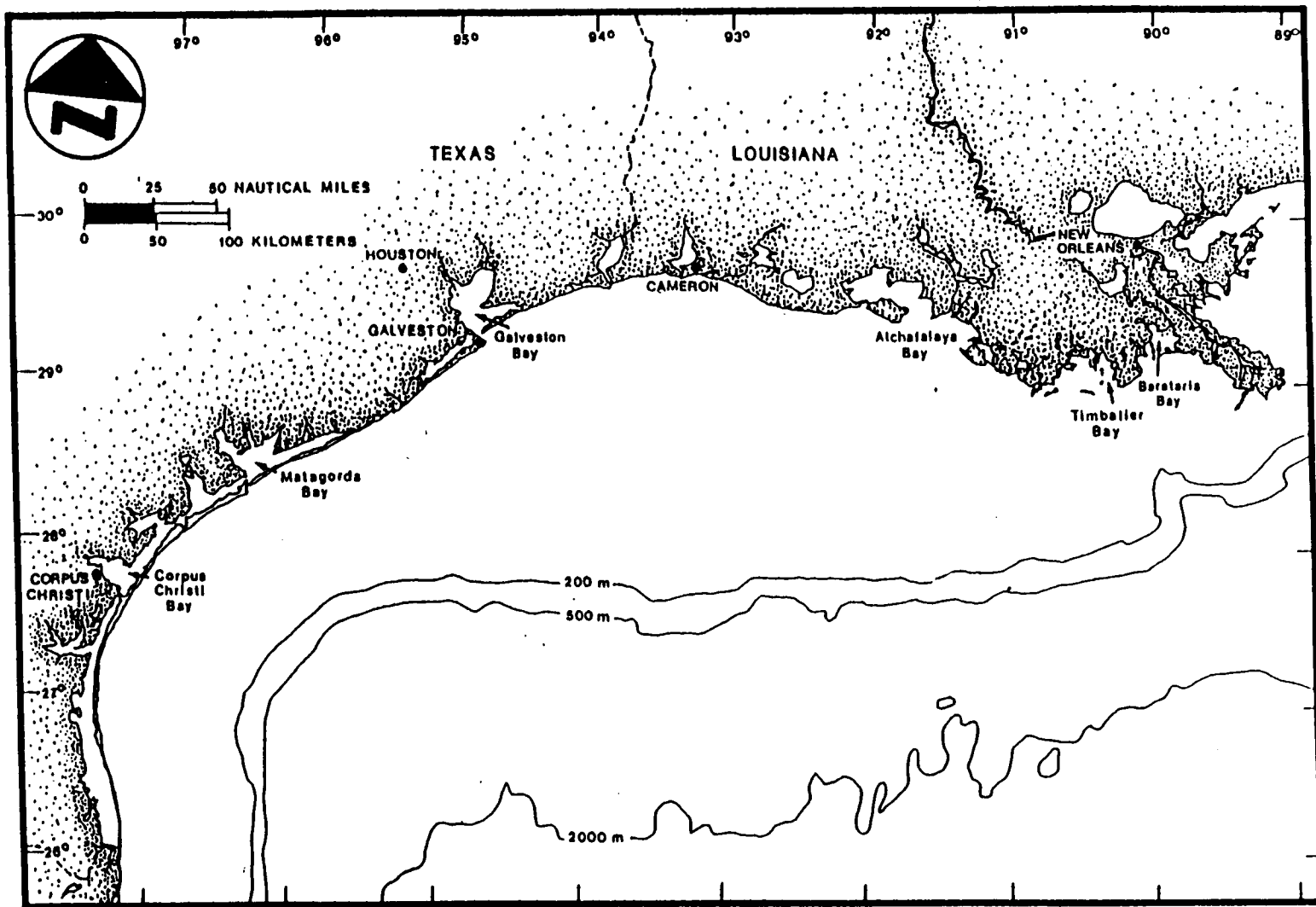
Figure 1.   Map showing the LATEX B study area.

The salient characteristics of a coastal plume current are: (a) the blocking effect of the coast on cross-shore currents; (b) shallow water depths and associated surface and bottom frictional stresses; (c) strong density stratification from heating and input of freshwater from rivers, lakes, and estuaries; and, (d) the seaward increase of water depth in association with cross-shore flow resulting in vortex stretching.

The link between coastal current dynamics, chemistry and biology is nowhere more apparent than off central Louisiana. The Mississippi and Atchafalaya Rivers (a third of the total flow of the Mississippi River system enters the Gulf of Mexico via the Atchafalaya River) are the major source of "new" nutrients to phytoplankton on the inner and mid-shelf. Since the 1950s, water quality in the Mississippi River has changed dramatically (Meade and Parker, 1985; Smith et al., 1987; Turner et al., 1987). Suspended sediments and silicate concentrations have decreased since the 1950s, whereas nitrogen and phosphorus loadings have increased. These large changes, resulting from human activities, provide a basis for concern that these loadings, combined with increased water clarity, have resulted in a "eutrophication" effect on the shelf. The area impacted by, and the duration of, hypoxia on the Louisiana shelf is of considerable concern since Louisiana fisheries lands are 28% of the U.S. total. Fish, shrimp, and benthic annual densities are severely depressed in these hypoxic zones and critical periods of the life history of several commercially important species (Renaud, 1986) may be affected. Of more recent concern is the content of chemical pollutants as they are transported via fresh water into the open Gulf waters.

This report on the first field year of LATEX B studies documents an integrated, multi-disciplinary approach that combines satellite imagery and image processing with ship surveys and scientific analyses. The shipboard activities include measurements of subsurface currents, temperature, salinity, dissolved oxygen, particulates, water clarity, inorganic and organic pollutants, primary production, plant pigments, and phytoplankton and zooplankton systematics. The objective of this report is to present the results of Year 1 field observations with minimal synthesis. Field years two and three will be detailed in future reports. The final report will present an in-depth analysis and synthesis of all data sets.

All plots, charts, tables, and other graphics produced to assist in the writing of this report but not included here will be microfiched at the close of the project.

Station Nomenclature

The CTD stations were assigned distinct numbers that correlate to specific tasks. For example, P921001 reflocts the following:
    P   = R/V Pelican
    92   = 1992, the calendar year of the cruise
    1   = the first cruise of that calendar year
    001   = the discrete station number assigned to each CTD station and used by every project task taking samples at that location.

Cruise I, April 1992, conducted the basic survey, using numbers beginning with 001. For Cruise II, October 1992, the basic survey stations were numbers 100 through 299. The plume study is a 400 series, and the front study is a 300 series. All subsequent cruises follow this system, so that each basic survey station is in as close to the same location as possible.

II. Hydrographic Survey

A. Cruise I, April 10-21, 1992 *(Stephen P. Murray)*

April 1992 was selected as the first cruise of the LATEX B program because it is the month that exhibits the long-term average high discharge in the Mississippi River and, thus, when we expect the coastal plume to be best developed. Additionally April shows frequent and strong weather variability with an average of six frontal passages (DiMego et al., 1976) . Cruise I track and stations are shown in Figure 2. Table 1 shows Cruise I statistics.

Table 1. Cruise I statistics.

ADCP	2300 km
MIDAS	2277 km
CTD Stations	127
Sediment Samples	51
Water Chemistry Samples	60
Nutrient Samples	76
Chlorophyll Samples	76
Phytoplankton Samples	76
Zooplankton Samples	114

The core survey, which will be repeated on every cruise, consists of eight cross-shore transects that make up five boxes. Each box was designed for a specific purpose: for example, Box 1 provided information on conditions upstream of the Atchafalaya; Box 2 provided information on the magnitude and direction of the major source to the plume from the Atchafalaya River; and, Box 5 provided a suite of measurements similar to Box 2 for the constricted plume in north Texas downstream of the Galveston Bay inflow.

1. Background

a. Hydrology. The total discharge down the Mississippi River at Tarbert Landing, Louisiana (upstream of the diversion into the Atchafalaya River), and the discharge down the Atchafalaya River at Simmesport, Louisiana, is shown on Figure 3. Note the unusually low peaks in the spring flood in 1992. Discharges of the Mississippi River were above 20,000 m^3/s for the first six months of 1991, for example, but exceeded this value only 20 days in 1992. The Atchafalaya River is nominally maintained at 30% of the total Mississippi River by the Old River Control Structure, but Figure 3 shows significant lows occurred in April, 1992, prior to and during Cruise I.

While the freshwater discharge into the LATEX coastal plume is dominated by the outflow of the Mississippi-Atchafalaya complex, the secondary rivers are of considerable local importance in the coastal plume. Comparison of the discharge of Texas rivers shows that peak discharges during January-March are two to three times higher in 1992 than in 1991 (1.6 x 10^6 cfs versus 0.7 x 10^6 cfs). The Brazos River outflow in early 1992 is anomalously high while the Louisiana rivers are at lows.

b. Background Meteorology. The NOAA Daily Weather Maps provide information for a synoptic scale weather analysis. On 0800 hours EST April 12 a continental scale high pressure cell occupied nearly the entire U.S. and southern Canada with a well-defined cold front
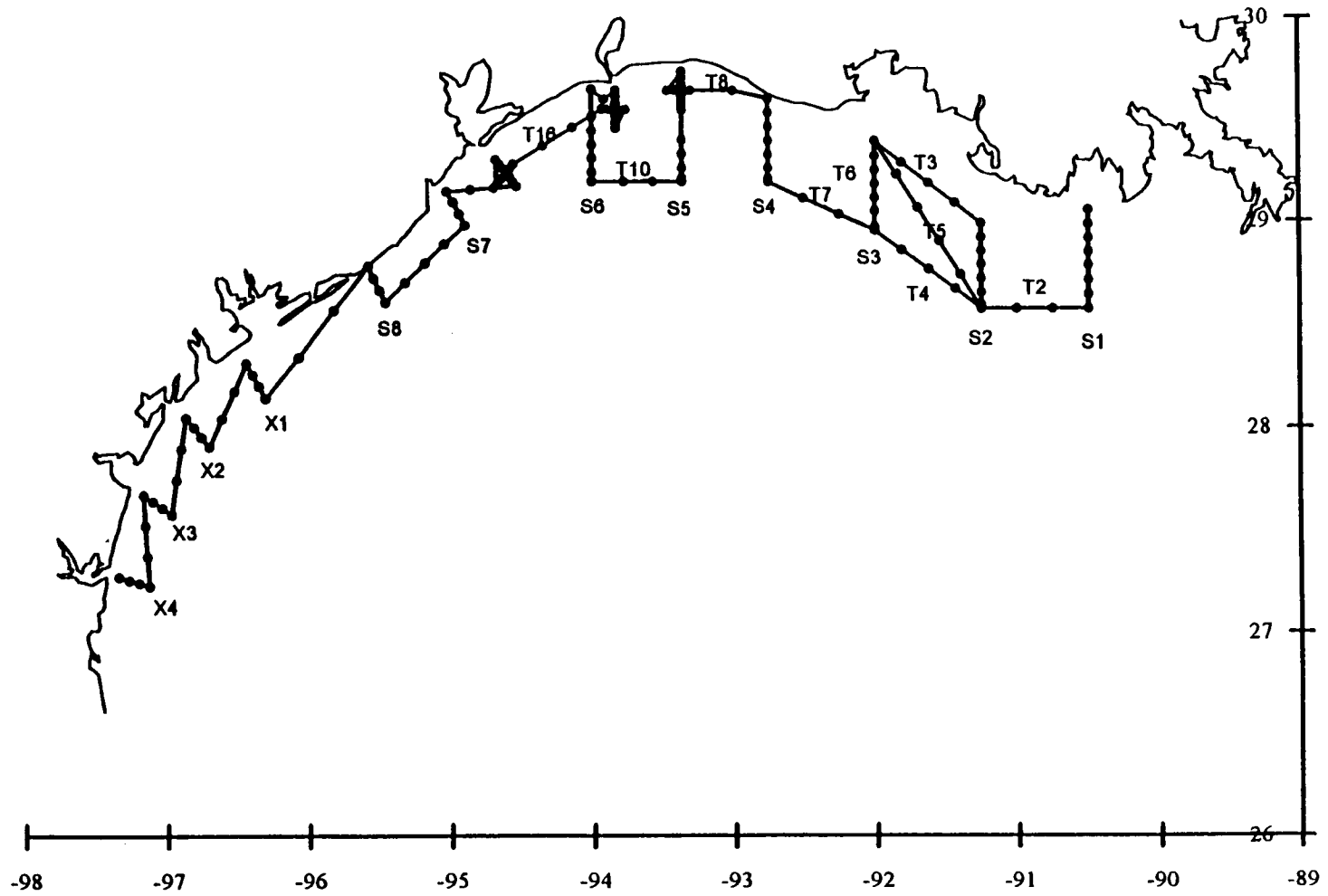
Figure 2.   Map of stations and cruise tracks.
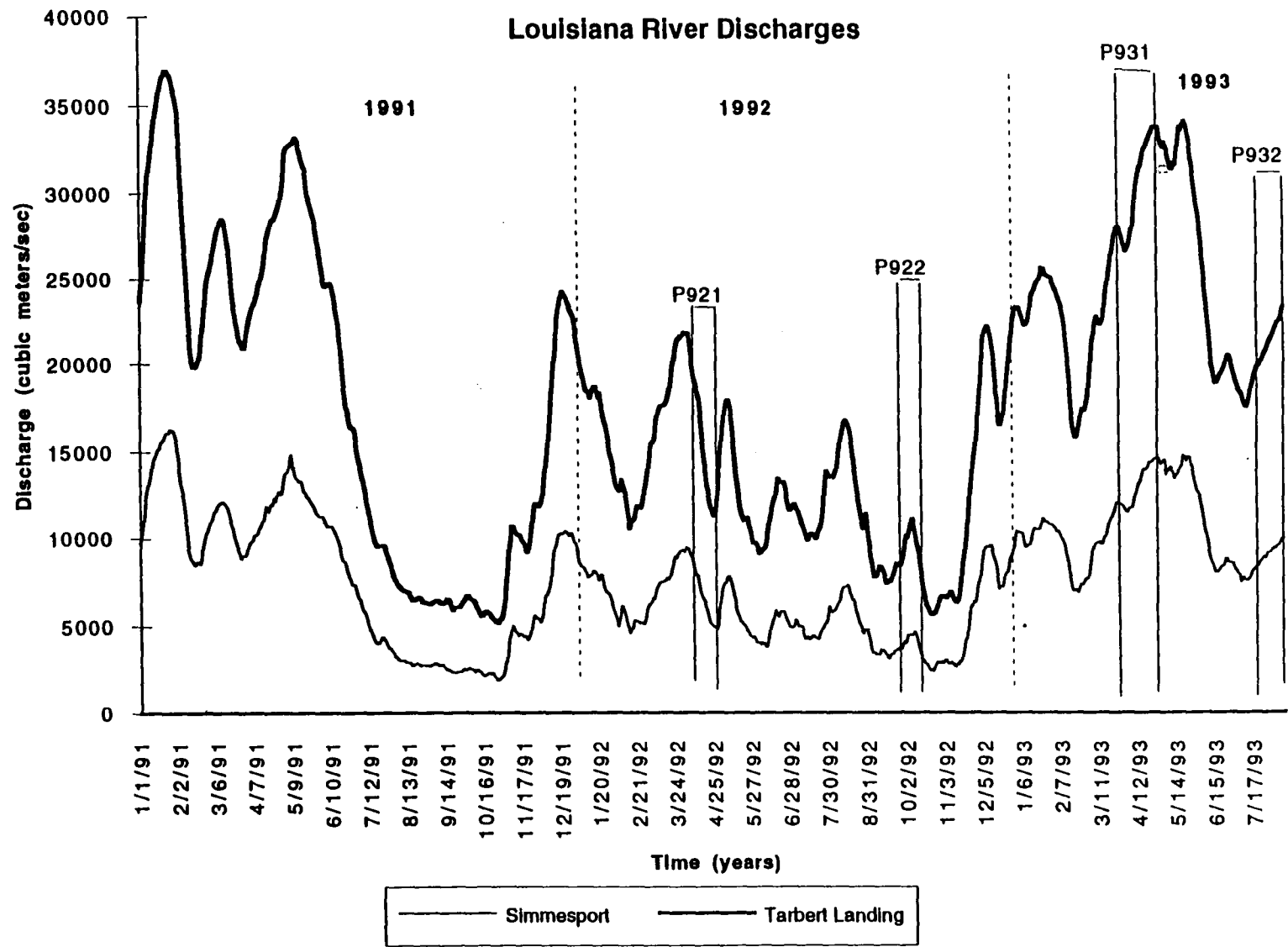
Figure 3. Freshwater discharge down the Mississippi River upstream of the Atchafalaya diversion and in the Atchafalaya River itself at Simmesport.

extending along its southern perimeter on land from northeastern Alabama to the Texas-Mexican border. There was a 6°C temperature drop across this front; winds behind the front were northeasterly at 15-20 knots. By 0800 hours EST April 13, this front crossed the Louisiana-upper Texas coast as the big high pressure cell moved east into the Atlantic Ocean bringing easterly and southeasterly winds to the coastal waters for at least seven days, until April 19. On April 20, another well-defined cold front traversed eastward across the study area. This front was oriented north-south, essentially normal to the LATEX coastline, and swept rapidly eastward at 15 miles/hour from central Texas, reaching Mobile on April 21. Winds were from the southeast before or east of the front and were from the west behind or west of the front. There was a 7°C temperature drop across this front. The LATEX B Cruise I departed Cocodrie at about 0200 local time on 22 April. A diffuse high pressure system then occupied the southeastern U.S., bringing weak, variable easterly winds to the area on April 23 and 24.

During the morning of April 25 the weather maps showed another extensive cold front, which extended all the way from northern Mexico to the North Carolina capes, impacting the LATEX area. This front, in contrast to the previous one, transited the coast in a quasi-parallel fashion between Corpus Christi and Mobile. Northerly winds from the high pressure cell behind this front dominated the study area until the afternoon of April 27 in south Texas, while in central Louisiana its influence persisted until the morning of April 29. Around mid-day of April 27, a mesoscale (sub-synoptic) low pressure system formed in south Texas forcing strong southerly winds over south Texas coastal waters until the end of April 29. A diffuse high pressure cell centered in the Gulf just east of Louisiana brought southerly and southeasterly winds to the Louisiana shelf April 29-May 1.

The time series behavior of the wind velocities along the coast is best illustrated from the three available Coastal Marine Automated Network (CMAN) stations at Grand Isle, Sabine Pass, and Port Aransas. Figure 4 shows this data from April 19-30. The velocity sticks on April 19 and 20 show the end of the long period of southeasterly winds set up by the big high pressure cell off the eastern seaboard. For analysis purposes this is referred to as Wind Episode I. The effect of the eastward movement of the ensuing north-south oriented front brought northeasterly winds first to Port Aransas and, in turn, Sabine Pass and Grand Isle. These winds lasted for only about 24 hours and are referred to as wind Episode II. The succeeding weak high pressure system brought moderate southeasterly winds to the northern LATEX shelf on April 22-25, as seen in Figure 3 (Wind Episode III). The orientation of this front early on April 26 was quasi-parallel to the Louisiana coast as it passed and showed an almost simultaneous onset of northerly winds at all three stations (Figure 3), which lasted for 1.5 to 3 days, depending on location (Wind Episode IV). It is important to note the large phase lag from north to south in the re-establishment of southerly winds after Wind Episode IV. Southeasterly winds on the back side of the high pressure cell began mid-day on April 27 at Port Aransas, late on April 27 at Sabine Pass, and not until early on April 29 at Grand Isle. South-southeasterly winds over the south Texas shelf off Port Aransas/Corpus Christi, and southeasterly winds off the central Louisiana shelf continued through the end of Cruise I on May 1 (Wind Episode V), except for the effect of a strong mesoscale low pressure system, which briefly brought northerly winds to the Sabine Pass and Port Aransas stations on April 30.

Another instructive view of the wind forcing is that measured from the ship as it transited through the time and space varying wind field. Figure 5 shows the absolute wind velocities measured from the ship from line S1 at the beginning of the cruise to its western most limit just beyond line X3.

Synoptic pictures of the wind field illustrate the long-shore coherence of these wind episodes. Maps were constructed from offshore weather buoys, CMAN stations and MMS LATEX A meteorological buoys. The synoptic wind field on the morning of April 21 shows the north-south oriented front sweeping eastward through the study area. Episode II was well-

8
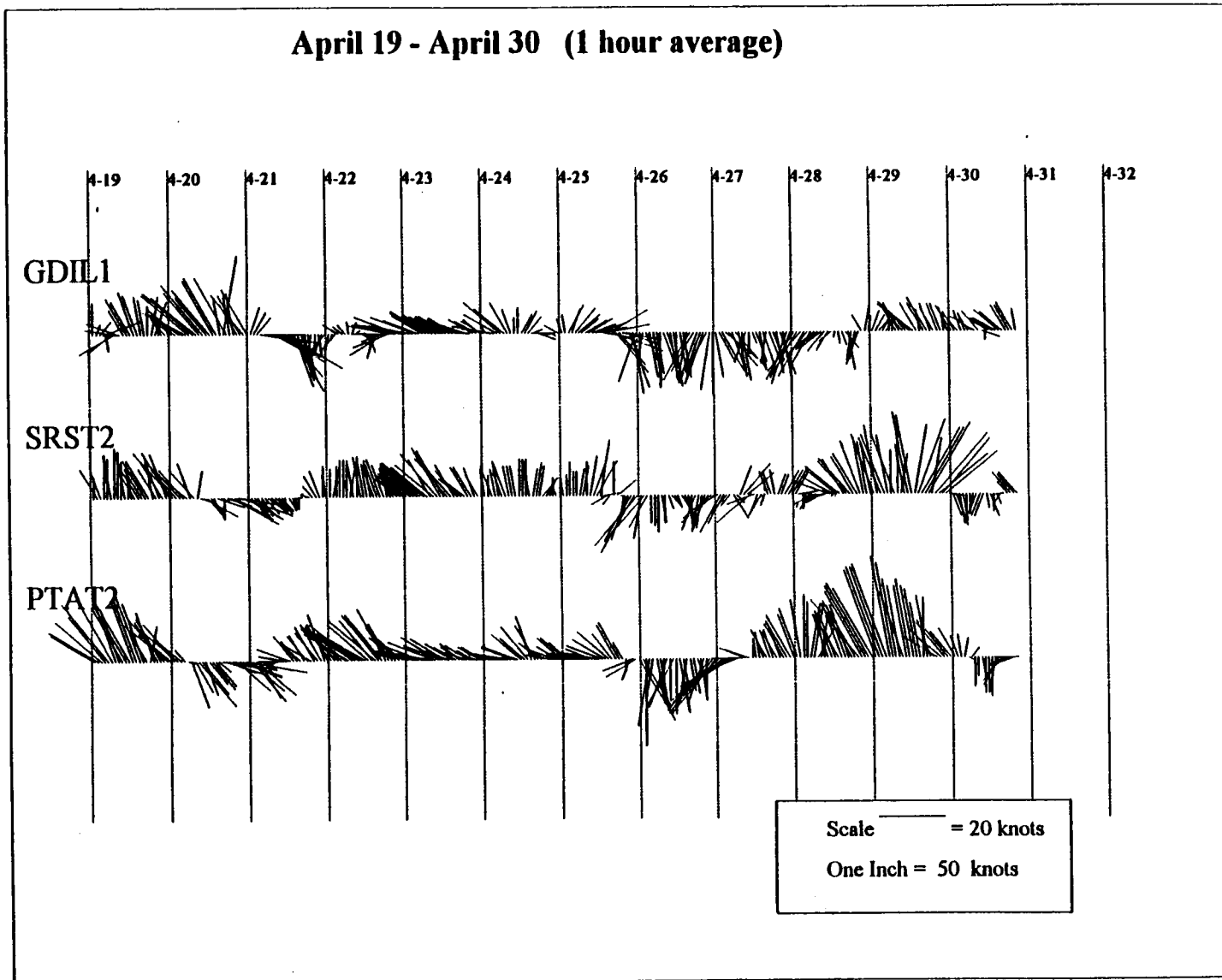
Figure 4.   Time series of three coastal wind stations (C-MAN).
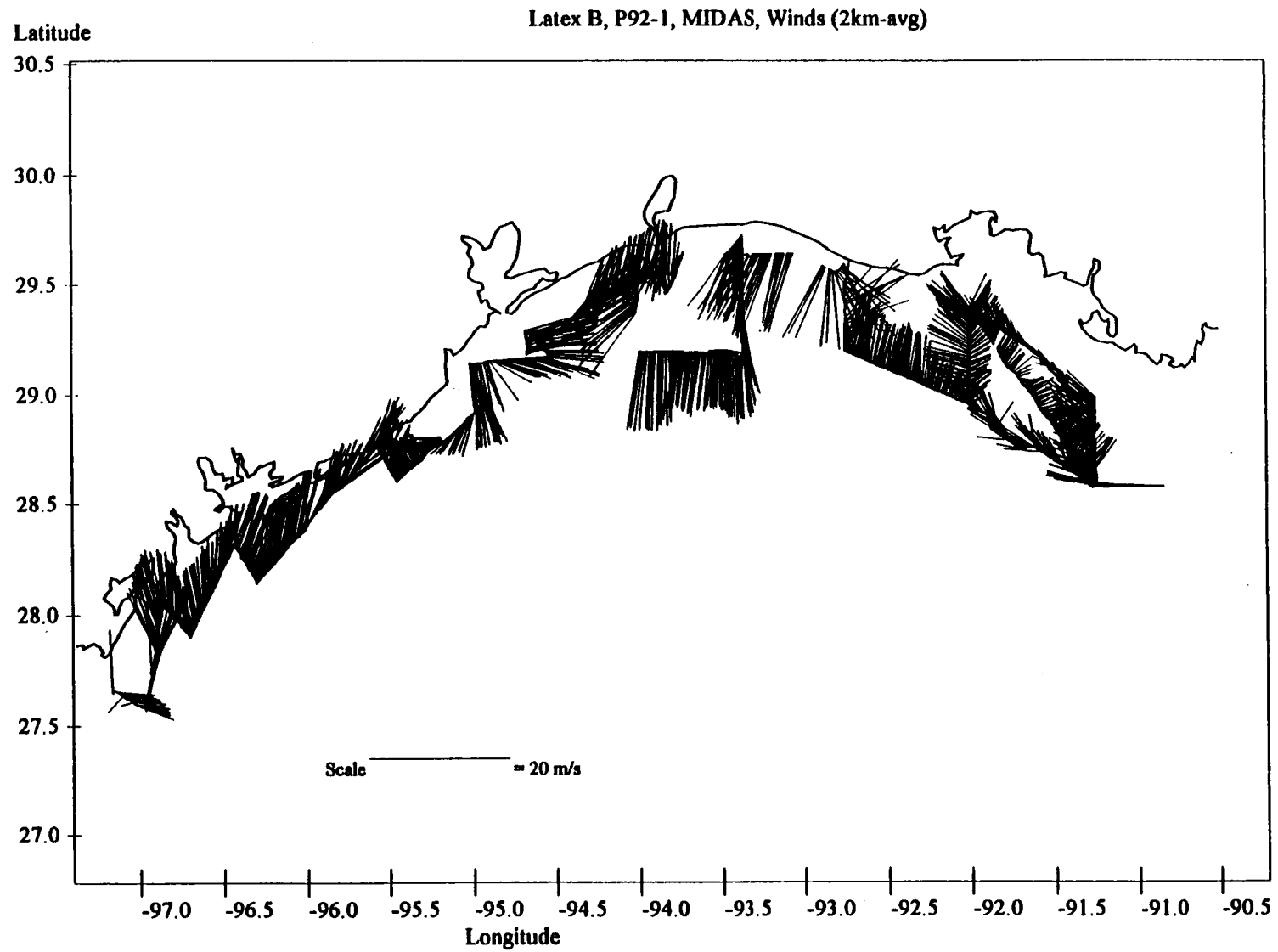
Figure 5. Wind velocities observed from the R/V *Pelican* as it transits the study area during Cruise I.

established in all but the eastern-most part of the study area, which shows north winds at the front near 91°W, and Episode I southeast winds at the Grand Isle CMAN station. The coherence of the Episode III wind field late on April 22 extends over seven degrees of longitude. It is clear from this data that five different wind regimes of alternating reciprocal wind directions affect Cruise I and that these wind regimes on the shelf have longshore coherence of ~600 km and offshore coherence of 200 km or more.

c. Sea Level Response. These wind episodes are clearly reflected in the response of the sea level along the LATEX coast shown in Figure 6. The trends are evident at all the Louisiana sites illustrated, but the signals are suppressed and magnified at Cocodrie and Eugene Island, respectively, as these stations are inside the bays (see Figure 1). Cameron and Fresh Water Bayou experience a 40-50 cm setup during the long period of onshore winds of Episode I (see Figure 2). The north winds of Episode II lasted only 36 to 48 hours but drove the water level down 30 and 40 cm at Cameron and Fresh Water Bayou, respectively. Episode III begins with strong onshore winds that initially raise the sea level 20 cm, but as the wind strength decreases, sea level resumes its decreasing trend for the remainder of this episode. The north winds of Episode IV keep the sea level depressed for the duration of this episode. With the ensuing onshore southeasterly winds of Episode V, the sea level rebounds 40 cm at Cameron and Fresh Water Bayou. Thus, even a cursory comparison of coastal winds and coastal sea level indicates a strong coherent response of the LATEX coastal waters to local wind forcing in the 3 to 6 day (weather) band.

d. Satellite Data Acquisitions (Oscar K. Huh, Nan D. Walker, and Lawrence J. Rouse, Jr.). Useful NOAA AVHRR satellite imagery were acquired following both cold front passages, particularly the last, most energetic one as discussed above. A series of sea surface temperature and turbidity front analyses were faxed to the ship, including four types of analyses: SST overview, SST area enlargements, turbidity overview, and turbidity enlargements, for April 21, 22, 27 and 28, 1992. Antenna system difficulties in the Earth Scan Laboratory restricted data acquisition from other days. The northwesterly winds of the cold front passages resulted in the relatively small turbid and thermal estuarine/riverine discharge plumes of the LATEX area to streams to the southeast.

A series of five AVHRR images were acquired during this cruise between April 21-29, as follows:

N11.920421.2033Z	21 April, 1992	2033Z
N11.920422..2018Z	22 April ,1992	2018Z
N11.920426.2111Z	26 April, 1992	2111Z
N11.920427.2049Z	27 April, 1992	2049Z
N11.920428.2046Z	28 April, 1992	2046Z

The quality of the April 26 imagery was poor, so only the remainder were analyzed.

The oceanography products of sea surface temperature and ocean albedo/turbidity charts were created from the digital five channel data of the NOAA-11 AVHRR. The numerical values of ocean albedo in Channel 1 (orange-red, 0.58-0.68 μm) minus the values of ocean albedo in Channel 2 (near IR 7-1.1μm) plus atmospheric corrections as calculated using the method of Stumpf (1992) provide ocean reflective brightness, which is a function of turbidity, i.e., the suspended sediment load. These images will be referred to as turbidity images. In these daytime passes, numerical values of temperature in Channels 4 (10.5-11.5 μm) and 5 (11.5-12.5 μm) are used to calculate atmospherically corrected sea surface temperature imagery using the standard MCSST algorithm. We thus examine synoptically and sequentially two parameters: oceanic temperature and turbidity of the LATEX area.

April 21, 2033Z. In Figure 7, the major SST and turbidity fronts are displayed in relation to the LATEX B cruise track. It is apprent that the ship traversed both the major SST and
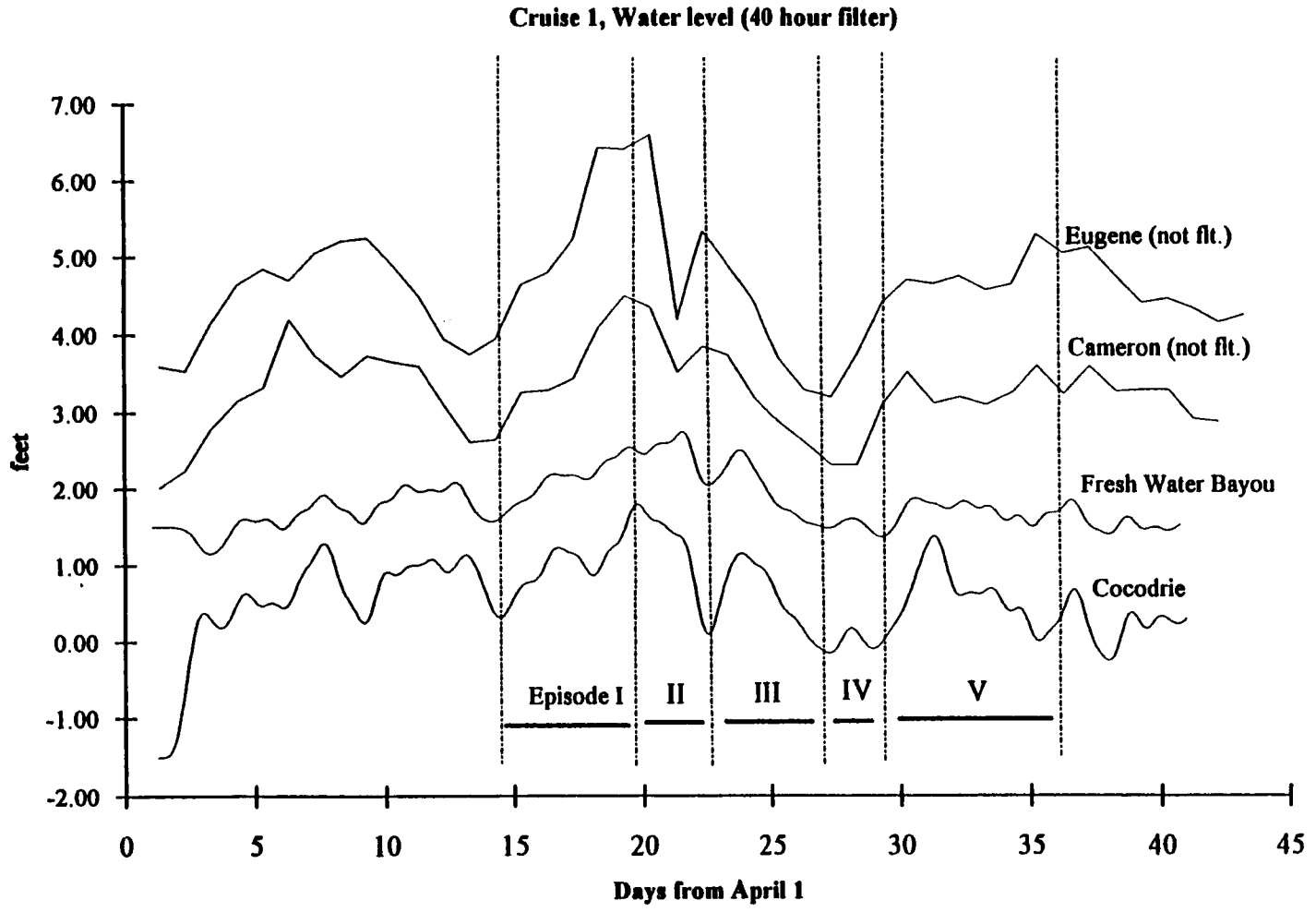
Figure 6.   Water level data for Louisiana coastal stations.
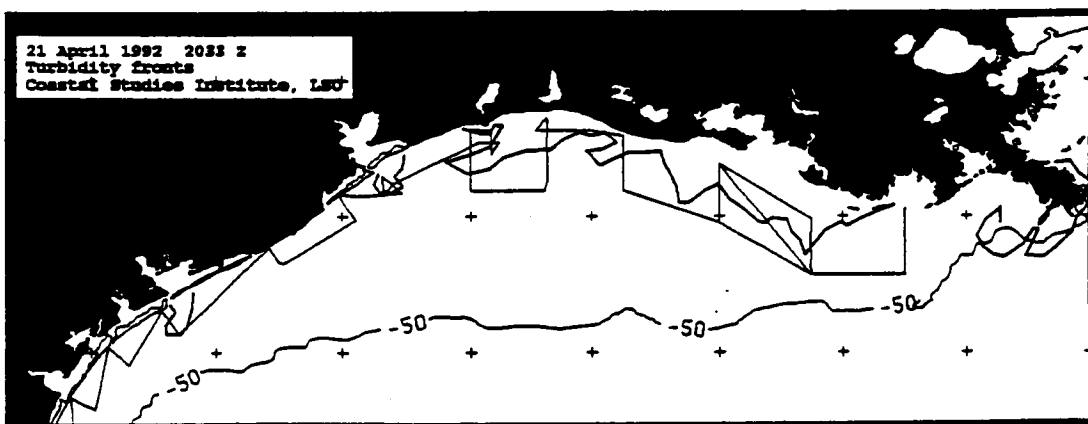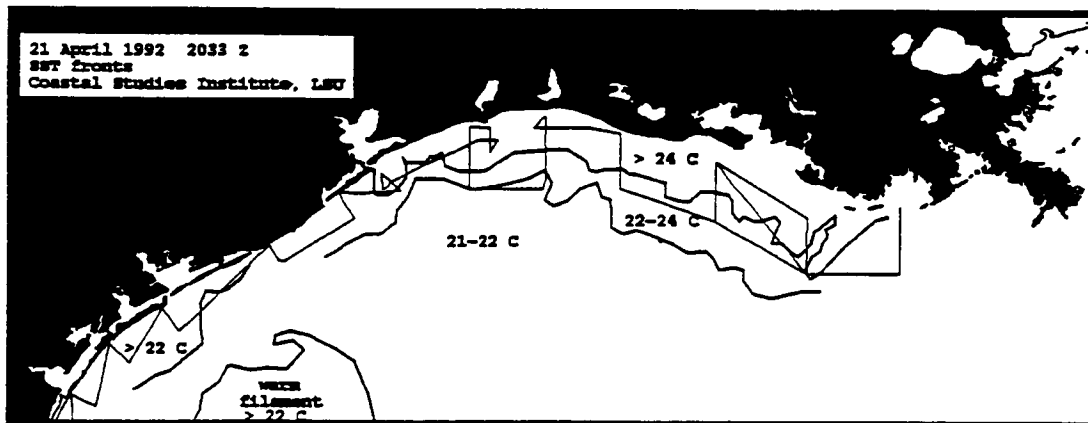
Figure 7. Satellite image information of April 21, 1992: (a) major SST fronts in relation to the cruise track; (b) major turbidity fronts in relation to the cruise track.

turbidity fronts in the nearshore region. An additional temperature front was observed seaward of the cruise track. Both temperature fronts were relatively weak. The inshore fronts separated the relatively warm coastal waters from the cooler waters mid-shelf. The surface temperature structure was typical of spring in that the costal waters had warmed because of a net positive heat balance resulting from increased insolation and less frequent cold-air outbreaks. The mid-shelf region was slower to warm as a result of its depth. Although the Atchafalaya and Mississippi River waters were relatively cool, they warmed more quickly than ambient shelf waters, probably caused by a shallow pynocline, which confined the solar heating to the surface waters. SST gradients offshore of the Atchfalaya were on the order of 0.5 C/10 km.

A relatively wide turbid zone was observed in the satellite data seaward of Atchafalaya Bay (A) and seaward of most estuaries further west. Suspened sediment data collected on the ship revealed a high turbidity spike at the inshore station near Marsh Island. This high value of 227 mg/l was mainly inorganic sediment. Although on April 21 a wide turbid zone was observed seaward of Sabine Lake (Figure 7b), the cruise data revealed sediment concentrations less than 4 mg/l in this area several days later. This sediment plume may have originated as wave-suspended sediments seaward of Atchaflaya Bay, which were subsequently transported westward.

On the large scale, an anticyclonic Loop eddy (probably a shallow feature) was situated about 35 km south of the Mississippi delta. The warm water zone associated with this eddy extended from 86 to 91W. In addition, Eddy Triton was situated in the northwestern Gulf of Mexico near 26 N, 95 W. Warm water on the northern margin of this eddy is apparent in Figure 7a.

The following additional observations can be made from SST and turbidity information of April 21, 1992 (Figure 7) and April 22 (not shown):
(1) Highest reflectances are found, as expected, in the vicinity of Atchafalaya Bay, the Mississippi Delta region, Lake Pontchartrain and Galveston Bay, due to the effects of runoff and cold front stirring of bottom sediment in shallow waters (Figure 7b).
(2) Turbid waters of the Atchafalaya flowed SSE, presumably in response to the NW cold front winds.
(3) Mississippi delta turbid plumes flow SW, outlining an anticyclonic gyre in the Louisiana bight/Mississippi canyon area. The thermal data of Figure 8a show a similar circulation pattern.
(4) A turbid zone of waters along the Chenier Plain (just south of White Lake shows the Atchafalaya mudstream (Wells and Kemp, 1981).
(5) An anticyclonically curved plume of turbid-cool waters is seen immediately offshore from Sabine Pass (Figure 8).
(6) Both turbidity and temperature outline the discharge plume of Galveston Bay.
(7) There is little discharge of turbid water from the Terrebonne-Timbalier Bay areas, with only a hint of discharge from Barataria Bay.

April 27. The turbidity image shows discharge plumes oriented due south from outlet channels (Figure 8). The cruise track did encounter most of the turbid estuarine plumes, as revealed in the satellite data. The thermal imagery from this satellite pass are redundant with the turbidity data (and thus not shown), with more subtle differences between plumes and offshore waters.

April 28. All the turbid plumes in the LATEX area have been reoriented from the south to the east (Figure 9) from April 27 to 28. An enlargement of the Texas shelf with the main turbid plumes is hown in Figure 9, since the LATEX B cruise was in this region at this time. Along the Texas coast, the orientation of the sediment plumes changed dramatically over 24 hours as a result of an abrupt wind shift. As a result of high water vapor levels the thermal

14
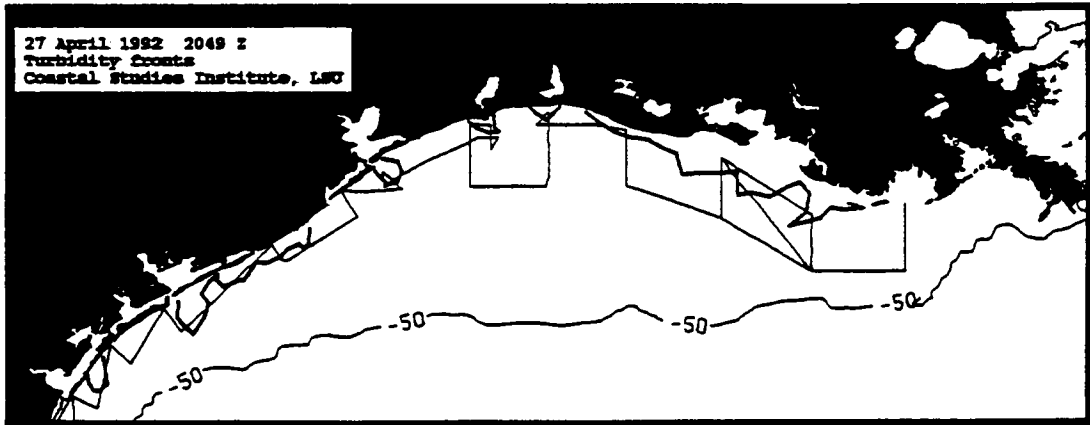
Figure 8. Turbidity fronts on April 27, 1992, in relation to the cruise track.
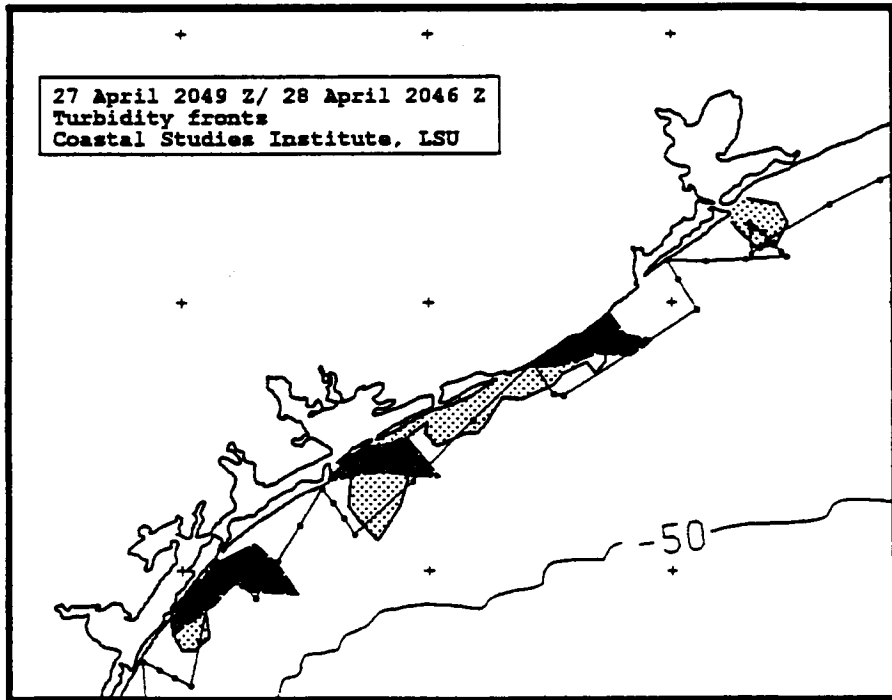
Figure 9. Comparison of turbid plumes on April 27 and 28, 1992, along the Texas coast.

imagery was not found as useful in tracking the plumes during the latter part of the cruise. The following additional features were evident:

(1) the Atchafalaya coastal mudstream that flows past Freshwater Bayou appears to have blown seaward;

(2) a warm water plume from the mouth of the Atchafalaya Bay extended seaward to the SSE on April 28 (not shown);

(3) a relict warm water plume from the mouth of Atchafalaya extended WSW;

(4) the lack of evidence for a "relict plume" to the west shown in the turbidity image suggests that temperature is more conservative than turbidity.

In summary, three atmospheric frontal passages occurred during this cruise: a weak cold front oriented normal to the coast; a strong cold front oriented parallel to the coast; and, a weak warm front from the south. Satellite data revealed plume extensions from Atchafalaya Bay to the SSE and from the mouth of the Mississippi to the SSW. Turbid plumes were observed emanating from Calcasieu, Sabine and Galveston Bays. An inner shelf eddy off Sabine Pass was detected on April 21 and 22, in both temperature and suspended sediment signatures. The discharge plumes offshore from the estuaries were observed to change orientation between April 27 and 28, from southerly to easterly and northeasterly orientations. On April 28, a plume of warm water was seen flowing from the Atchafalaya to the southeast. SST data suggest both an active plume (to the southeast) and a relict plume (to the west) emanating from the Atchafalaya Bay mouth.

2. Surface Property Fields at Constant Depths

An underway recording device referred to as the MIDAS (Multiple Interface Data Acquisition System) logs salinity, temperature, transmissivity and chlorophyll from water taken from 1 m below the sea surface. Numerous other parameters, including relative and absolute winds and navigation parameters, are also logged on the MIDAS. MIDAS samples all parameters at a 10- (or 12-) second interval. A nominal ship speed of 3-4 m/s is equivalent to a spatial sampling interval of 30-40 m; for clarity and data reliability we plot 500 m averages of MIDAS data. Figure 10 shows considerable alongshore structure in the MIDAS surface salinity field, keeping in mind the variability in the wind field discussed above. The long period of SE winds during Episode I would no doubt drive the low salinity Atchafalaya discharge well to the west during the seven day duration prior to Cruise I, thus building a sizable coherent coastal plume in that direction. Satellite images have consistently shown that the northerly winds, such as in Episode II, drive the Atchafalaya outflow plume offshore to the southeast. At the beginning of Cruise I, a pool of higher salinity water with an alongshore length scale of ~100 km and with a maximum salinity at 32 psu dominated the eastern offshore edge of the study area, being centered around 90°30'W. The Atchafalaya discharge plume at 92°W is skewed slightly to the southeast (cf. the 25 psu isohaline), perhaps a residual of the Episode II winds. The lowest salinity measured in the Atchafalaya outflow is 16 psu, high for the flood season but consistent with the low river discharge.

Isohalines in the 26-27 psu range run quasi-parallel to the coast from the easternmost section at 90°30' over 400 km to near Galveston Bay where they abruptly bend seaward. This significant change in the salinity field west of Galveston suggests the possible presence of a major circulation feature in this area. Note also the zone of high salinity water with a cross-shore scale of ~100 km, again at the outer edge of the survey lines and centered at 93°45'W. Subsequent cruises suggest this to be a permanent feature, sometimes associated with strong onshore currents as observed with the ADCP.

Figure 10 also shows that surface salinities below 25 psu are common in the inner shelf waters east of Galveston but are rare southwest of that location. The influence of the Brazos River outflow, historically high in Spring 1992, and the Galveston Bay outflow can be seen in

16

Latitude

30.0

29.5

29.0

28.5

28.0

27.5

27.0

-97.0 -96.5 -96.0 -95.5 -95.0 -94.5 -94.0 -93.5 -93.0 -92.5 -92.0 -91.5 -91.0 -90.5

Longitude
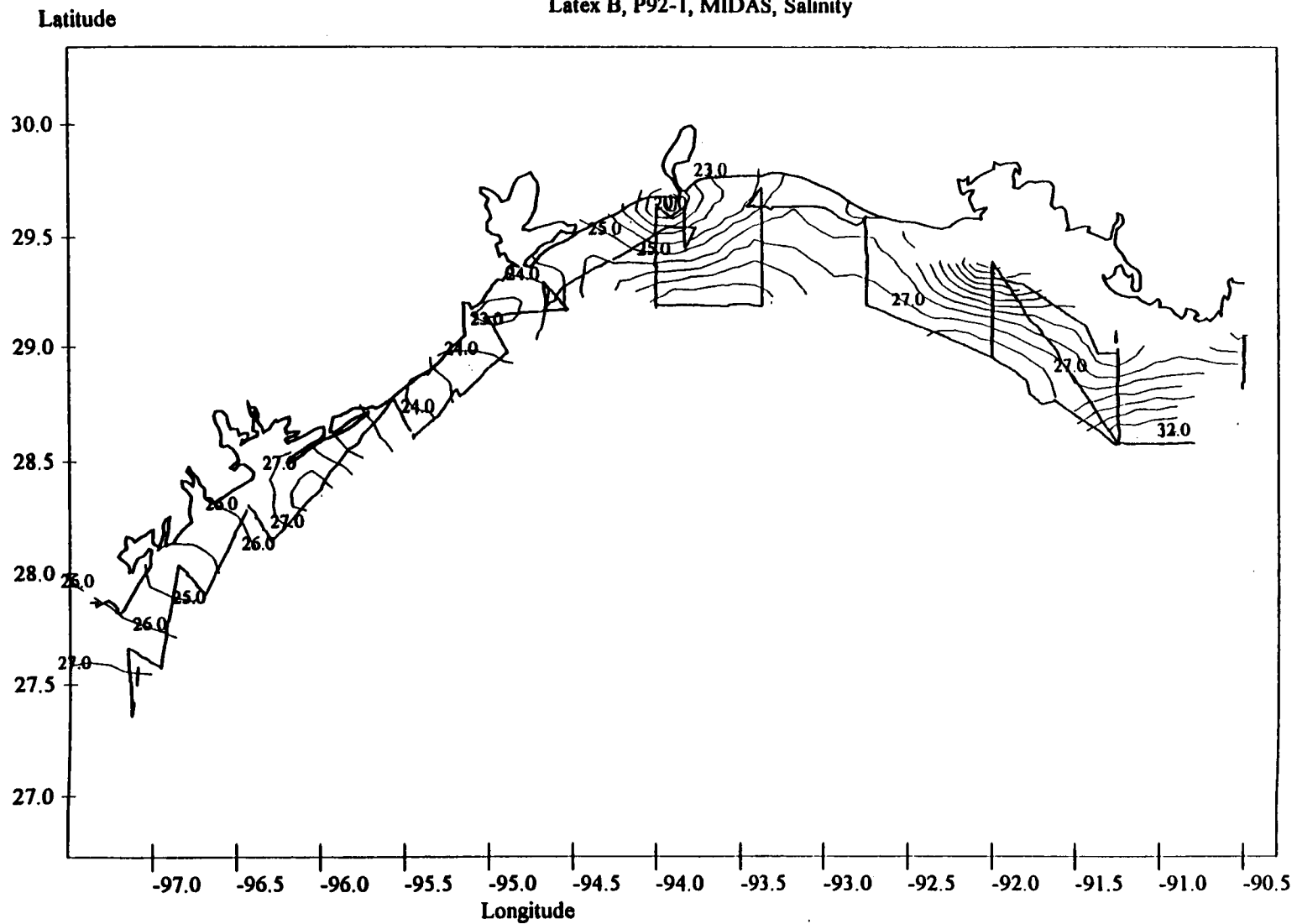
Figure 10. MIDAS surface salinity (psu).

17

the small plume of waters with salinity less than 24.5 psu southwest of the Galveston entrance. The bull's eye of high salinity at 96°W is likely an outflow from Matagorda Bay, whose waters are often hypersaline because of the intense evaporation in the south Texas bays.

The surface temperature field from the MIDAS (Figure 11) is extremely uniform, varying only 1°C over the entire study area. It is interesting to note, in terms of thermal satellite imagery interpretation, the weak correlation between the high salinity domes at 91°W and 93°30'W and their own temperature field. Similarly, the low salinity plumes at Galveston and Sabine are not reflected in the MIDAS temperature field. The Atchafalaya plume has only a weak temperature signal in Figure 11. The salinity at the 7 m level from the CTD station data is shown in Figure 12. Note the isohalines again tend to be oriented parallel to the coast as far west as Galveston reflecting the continuity of the coastal plume over that distance. Immediately west of Galveston Bay entrance, a large area of low salinity water was encountered which derived from the anomalously high spring outflow of the Brazos River. West of 95.75° salinities have returned to the background levels of .28-30 psu expected for this depth level. Note, however, the lack of longshore continuity in the isohalines in this western region reflecting the increased importance of local processes (e.g., effluents from the Texas bays).

At the 15 m level (Figure 13) the salinities are markedly higher in the eastern region south of Atchafalaya Bay where they reach 35 psu. There is a sharp decrease of salinity at this level to the west down to 32 psu at about 93.3.°W. Higher salinities (34 psu) appear again south of Galveston. West of Galveston, salinities remain in the 31-32 psu range. The salinity distribution at this level raises the possibility of upward entrain-ment of deeper salinity water underneath the Atchafalaya and Brazos outflow plumes.

3. Vertical Sections

a. Salinity and ADCP Velocities. Here we discuss the hydrographic sections largely in the chrono-logical order they were occupied. This has the distinct advantage of discussing sections in quasi-synoptic clusters, suitable for comparison and contrasting to the Wind Episodes discussed above. In all but a few sections (with low data quality) the MIDAS near-surface salinity, averaged over 500 m increments, has been combined with the CTD data to produce the vertical sections. This greatly enhances the resolution of the near-surface structure of the plume. The vertical section of salinity along our easternmost line S1 (Figure 14) shows almost a textbook picture of a coastal plume. A prism of low salinity (buoyant) water hugs the coast with lowest salinities of ~24-25 psu nearest the shoreline. The low salinity plume extends seaward about 50 km. The isohalines at the base of this plume are horizontal over most of this distance before rising abruptly to the sea surface at a fairly uniform spacing as distance increases offshore. The halocline is strongest and thickest inshore, decreasing from 1.3 psu/m at station P921001 in 10 m of water to 0.5 psu/m at station P921006 in 19 m of water. The thickness of the surface mixed layer, as evidenced by the vertical isohalines, increases offshore from 4 to 7 m, and the center of the halocline deepens from 6 to 9 m. For discussion purposes we can take the zone of the 33-34 psu isohaline and its intersection with the sea surface as the outer boundary of the coastal plume. The steeply inclined isohalines at the outer edge of the section indicate an onshore-directed stress, no doubt from the wind. Note the presence of full salinity Gulf water below 20 m at the outer edge of this section. Near the bottom the 34, 35 and 36 psu isohalines slope down to the coast, suggesting a wedge-like intrusion of this denser high salinity water. It appears likely that the fresh water in this section is not of Atchafalaya River origin, as the section is 100-150 km east of the Atchafalaya River mouth. Winds blew from the northwest during Episode II for about 36 hours, which even for a 1 knot current would displace Atchafalaya water only ~50 km to the east. Prior to Episode II, winds were unfavorable for eastward flow. The Mississippi River itself, augmented by outflow from the bays and channels of the Mississippi bight, is apparently the freshwater source for this section.

18
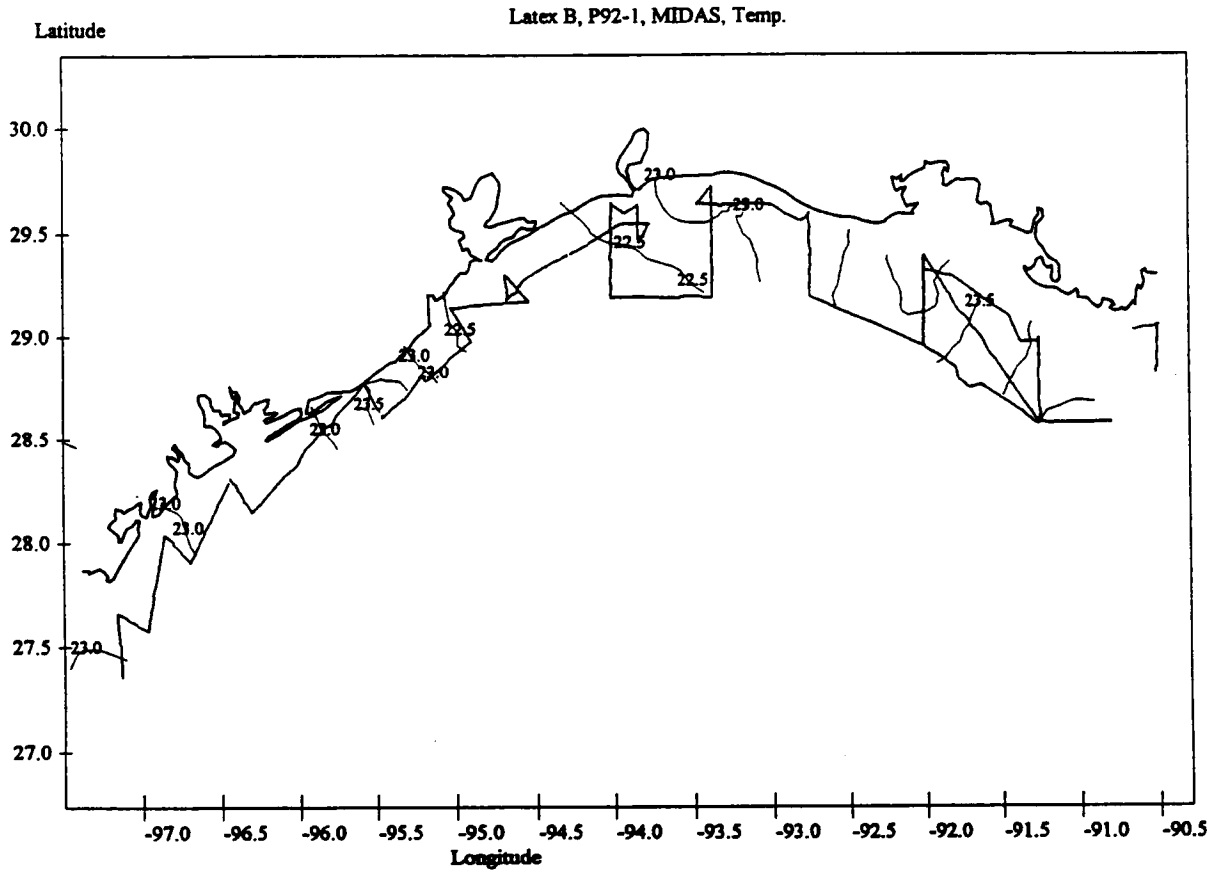
Figure 11. MIDAS surface temperature.
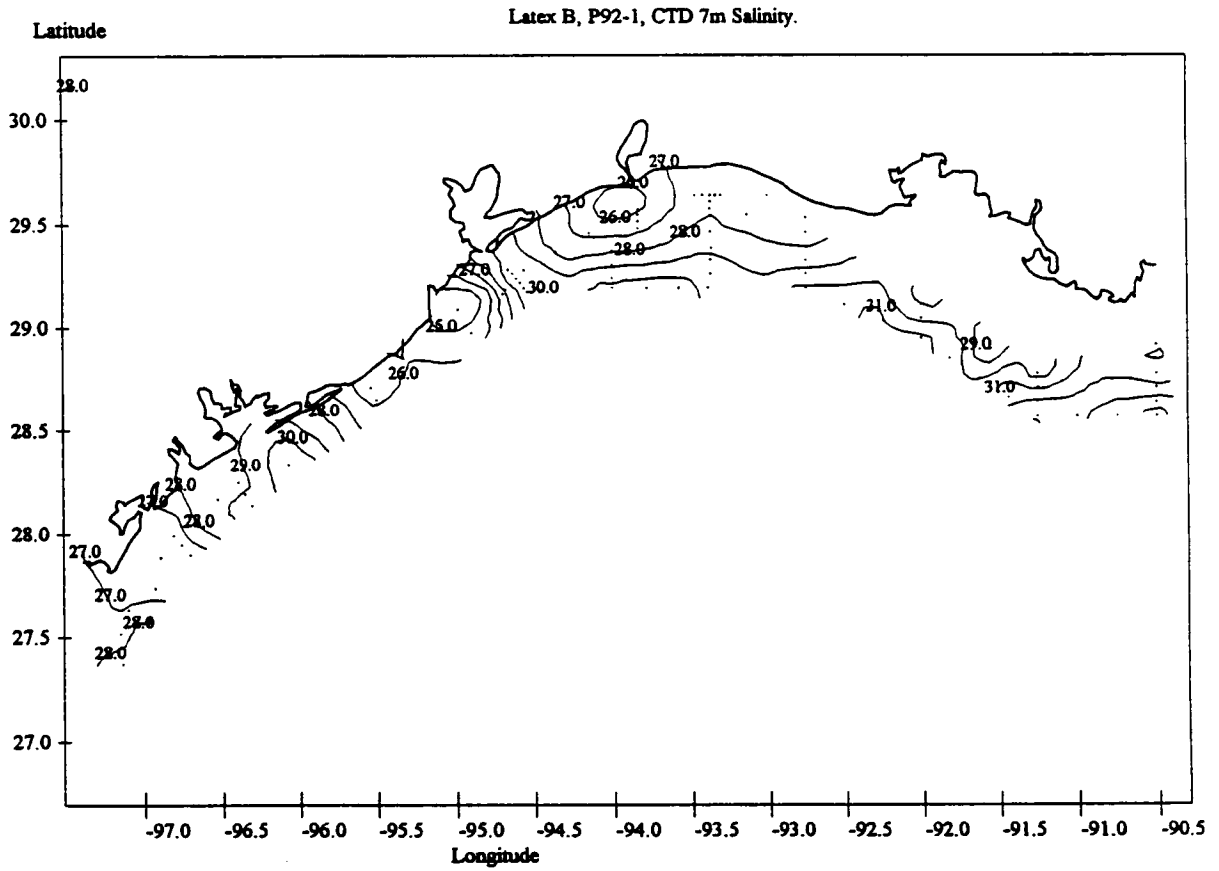
Figure 12. Salinity at the 7 m level.
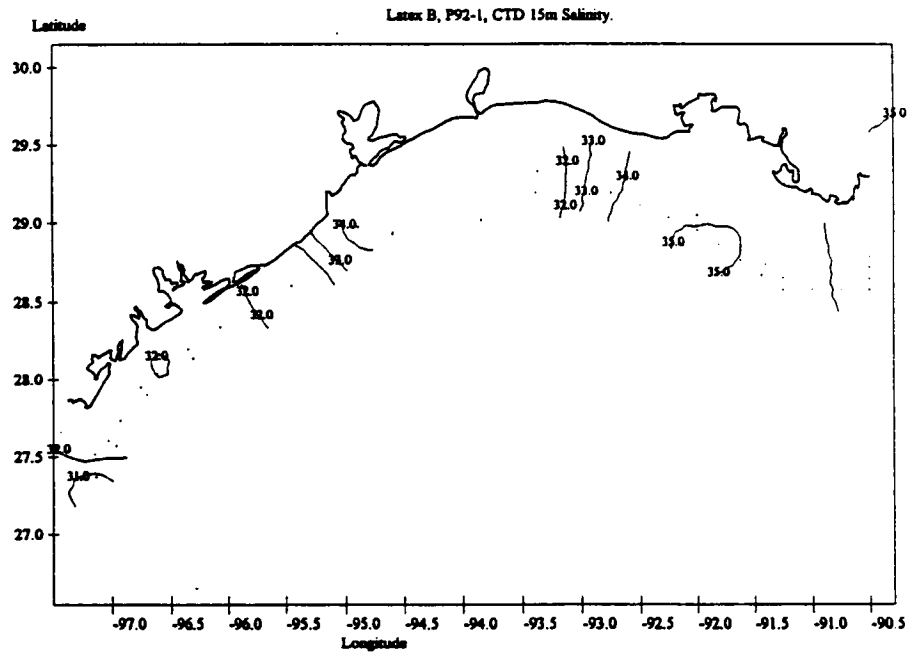
Figure 13. Salinity at the 15 m level.
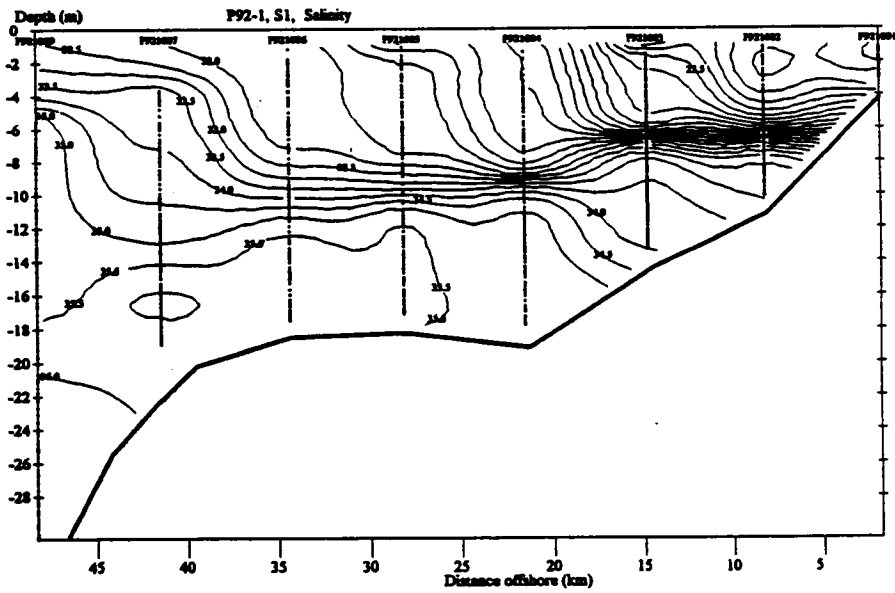
Figure 14. Salinity, section S1.

Only Cruise I was conducted with the ADCP transducer mounted on a towed sled. During the frequent heavy weather encountered on this cruise, the data quality was less than anticipated because of the severe sled motion, and considerable data had to be removed in the quality control phase. Subsequent cruises were conducted with the ADCP transducer mounted on a frame rigidly attached to the side of the ship, which resulted in a marked increase in data quality. Section S1, located 80 km east of the Atchafalaya River outflow, had almost no usable ADCP data because of equipment problems, which were, however, cleared up in time to obtain good data on the following Section T2. It is clear, nonetheless, from the structure of the salinity and density contours that the currents in S1 are strongly coherent in the westward direction.

Transect T2 is a 75 km east-west tieline between S1 and S2. The hydrographic structure of the coastal plume from S1 appears to be deflected seaward as it nears the very shallow ramp of the Atchafalaya Delta. Thus, T2 presents an oblique view of the outer edge of the coastal plume resembling an offshore-to-onshore section as the ship transits from east to west. Above 12 m depth the flow was northeastward, and below this level the flow was northwestward. Note that T2 is in relatively high salinity seaward of and along the outer edge of the coastal plume, and this water is moving northward into the coastal front mixing zone.

Section S2, shown in Figure 15, presents a generally similar picture of the coastal plume to that seen in S1, but one that differs significantly in detail. S2 is located on the eastern flank of the subaqueous depositional ramp of the Atchafalaya Delta. Vertical mixing is more intense on this shallow ramp as evidenced by the weak halocline 2 m off the bottom. Near-shore salinities are ~1 psu lower here than at S1, reflecting the proximity of the Atchafalaya River mouth. The 34-35 psu zone of isohalines intercepts the bottom only 15 km offshore from the inner station in S1, but in S2 the 34-35 psu zone intercepts the bottom more than 35 km offshore from the inner station. It is clear that the pressure of the Atchafalaya outflow is much more strongly felt at S2, both in driving the high salinity Gulf water seaward and in increasing the freshwater content of S2 through mixing. S2, the eastern edge of the Atchafalaya box, displays a coherent, well-defined coastal current with a prominent jet, well correlated to the density structure. Currents in the jet (Figure 16) are moving northwestward along the isobaths. Seaward of the 33 psu isohaline the data suggest a countercurrent to the northeast consistent with the western edge of T2.

Section S3, shown in Figure 17, is located off the western end of the Atchafalaya Bay mouth and, given the southeasterly winds of Episode III, we expected to see larger amounts of fresh water in this section. Indeed, note the 30 psu isohaline at the surface has moved from 28 km offshore in S2 to about 50 km offshore in S3. Correspondingly, in the deep salty water, the zone where water in the 33-34 psu range strikes the bottom, the isohaline moves offshore between S2 and S3, i.e., 30 km offshore in S2 and 42 km offshore in S3. The U and V velocity components for S3 are shown in Figure 18.

Sections S2 and S3 are the east and west ends of a rhombus-shaped box designed to determine the hydrographic structure of the Atchafalaya River outflow. T3, T4, and T5 are the inner, outer, and diagonal sections outlining this "Atchafalaya box." T3 in Figure 19 shows the low outflow salinities of 20-24 psu across the section, resulting from significant tidal and wind induced mixing inside Atchafalaya Bay. The core of the low salinity outflow (19.5-20.0 psu) appears near the western end, in agreement with satellite images. The corresponding velocity components are shown in Figure 20. Figure 21 shows the salinity on the 120-km long diagonal (T5) along what we expected (from satellite images) to be the longitudinal axis of the outflow. It is an excellent section showing the piston-like push of the shallow plane jet out onto the shallow shelf. Moving seaward (SE) along the jet we see a zone of intense mixing extending 40 km out from the mouth, with the salinity increasing from 13.5 psu up to 25 psu . From 45 km to 70 km out along the section, the horizontal salinity gradient weakens dramatically increasing from 26 psu to only 27 psu. A very strong halocline exists seaward (SE) of and beneath the 28 psu

Figure 15. Salinity section S2.

23

(a)

(b)

Figure 16. ADCP S2: (a) U component; (b) V component.

Figure 17. Salinity section S3.

25

(a)
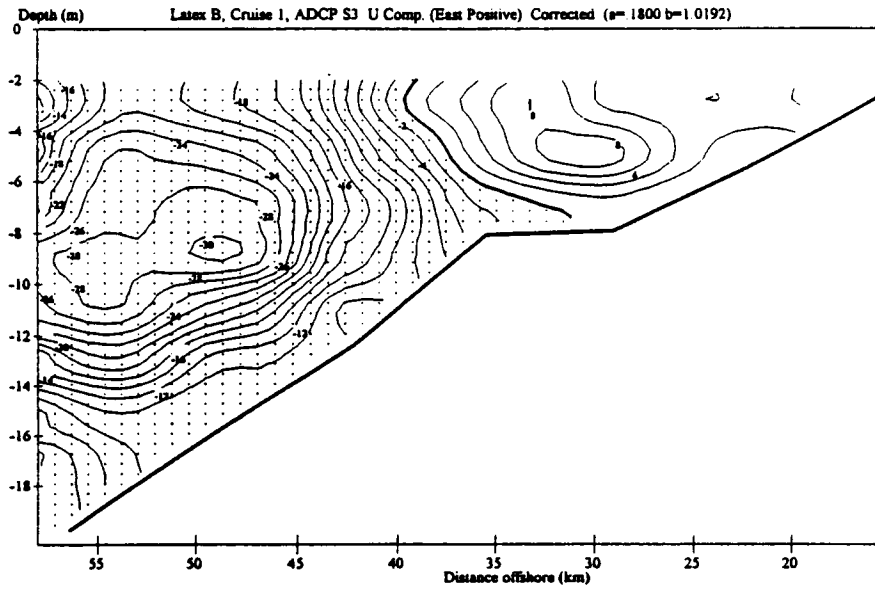
(b)
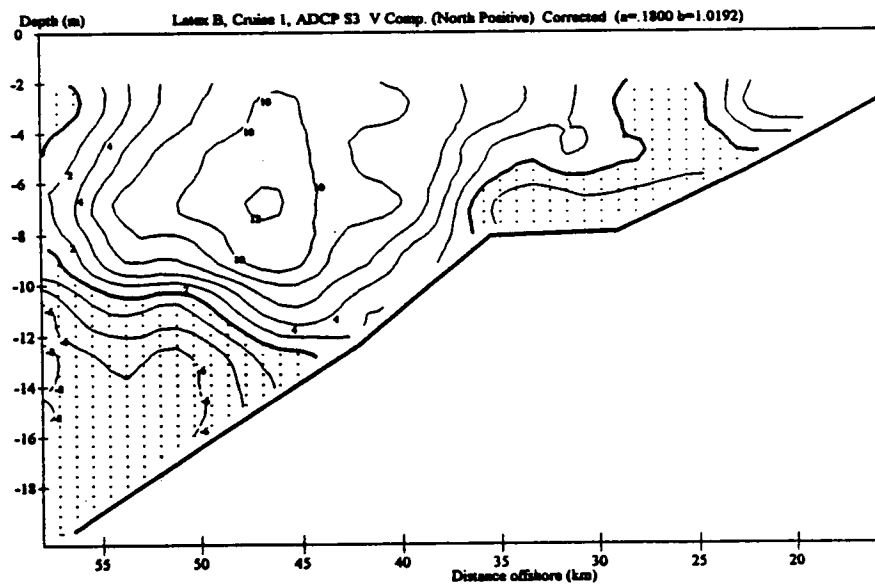
Figure 18. ADCP S3: (a) U component; (b) V component.

26

Figure 19. Salinity transit T3.

(a)

(b)
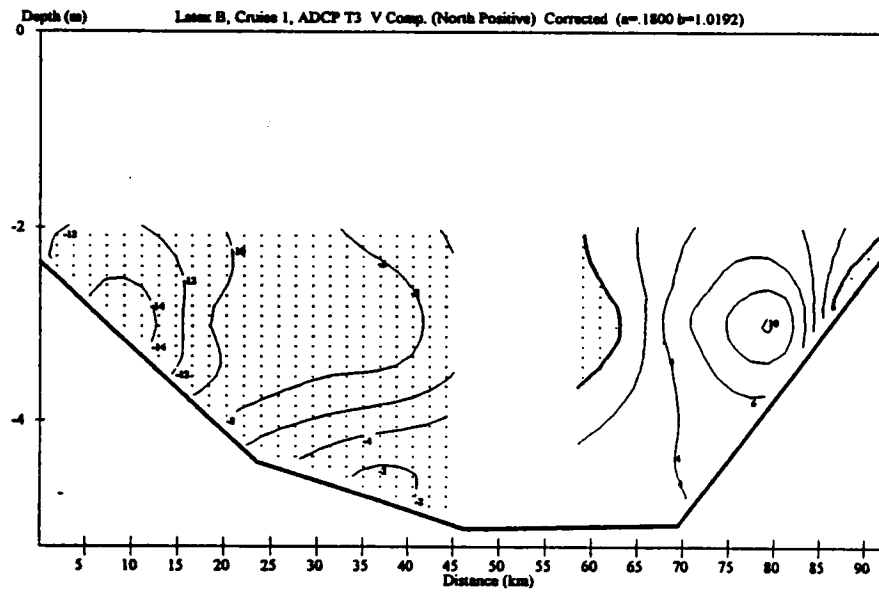
Figure 20. ADCP T3: (a) U component; (b) V component.

28
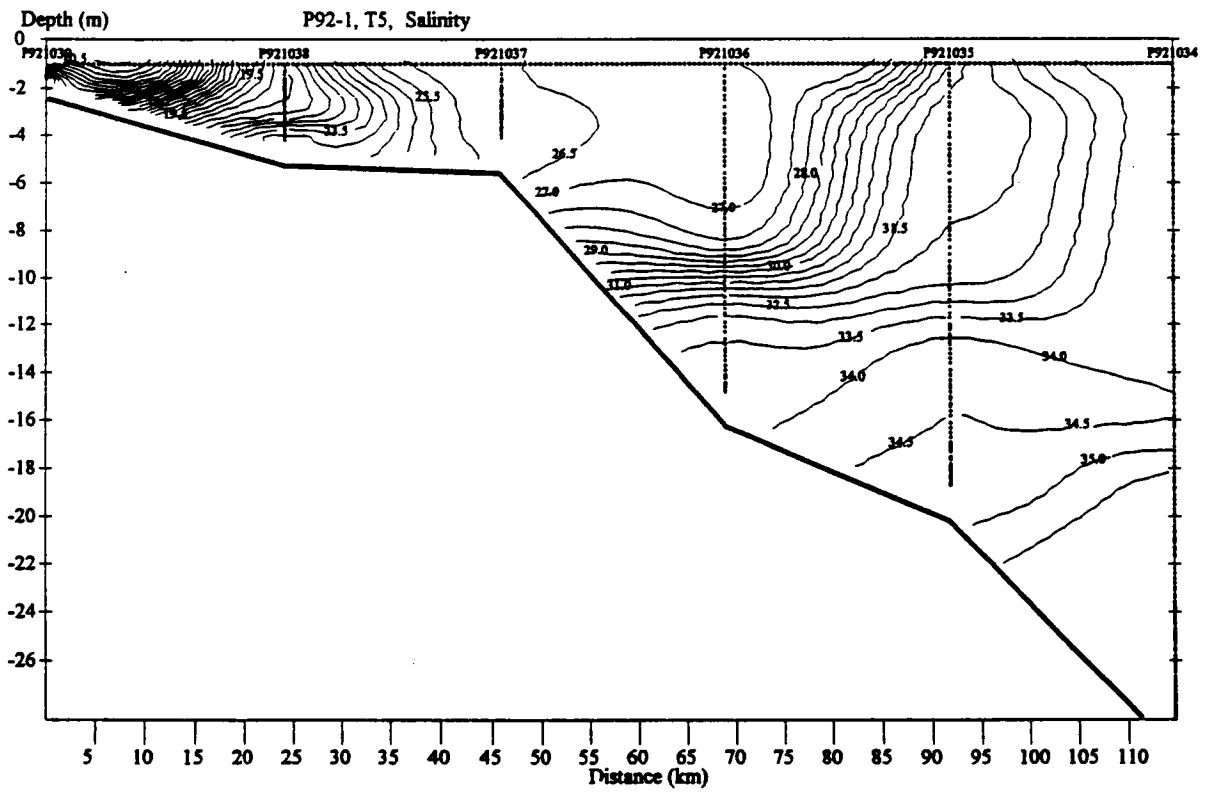
Figure 21. Salinity transit T5.

isohaline marking the inner edge of the frontal zone where the outflow jet impacts the Gulf waters. This frontal zone is ~30 km in width. Note the higher salinity Gulf water intruding up the slope under the outflow jet. The east-west and north-south velocity sections on the diagonal section T5, shown in Figure 22, are in clear agreement with the above interpretation from the salinity distribution.

T4 is the outer edge of the "Atchafalaya box." The salinity distribution in T4 (Figure 23) shows the coastal plume from the east occupying the eastern edge of this section in agreement with the flow field seen in Figure 22. The salinity field in T4 also reflects the seaward extension of the outflow jet in the center of this section, in agreement with the flow field indicated in Figure 22. Note that the salinity in the core of the outflow jet, by the time it has reached T4, has increased up to 28 psu. The water in the upper 7 m west of the jet core appears strongly mixed with the outflow plume water and perhaps is laterally entrained by it. The upper layer outflow appears to be riding over the high salinity Gulf water with considerable mixing between them. In this regard note the high salinity isohaline layer occupying the bottom 4 m.

The velocity components for T4 are shown in Figure 24. The complex flow field in the Atchafalaya box warrants further comments. The inflow from Atchafalaya Bay through the shallow T3 section into the coastal plume was shown in Figure 20. It is reassuring to note the flow in the western two-thirds of this section (containing the lowest salinity core) is southeastward, consistent with historic observations of the outflow plume. The eastern one-third flows northeasterly reflecting the impact of the momentum from the inshore end of Section S2. Remember T5 (Figure 22) runs along the expected location of the axis of the Atchafalaya outflow plume. Note the distinct zone of southeastward flow marking the plume itself (compare Figure 21). Further seaward along this line, the flow reverses direction, becoming northwestward and forming an impact-like convergence zone between the outflow plume and the northwestward flowing offshore waters. The momentum of the plume can also be seen to penetrate through and past the outer border of the Atchafalaya box, i.e., line T4 (Figure 24). Because of the intense mixing, the core salinity of the plume in T4 has increased to 28 psu (Figure 23). In Figure 24, 45-65 km, the low salinity core is seen to be moving southwestward but there is strong vertical shear such that the near surface waters have speeds 14-16 cm/s below the speeds at the 10 m depth. This is clearly a wind shear effect as the winds during line T4 were in direct opposition to the southwest set of the plume current as it cuts through line T4. The west end of T4 (Figure 24) has strong northward currents that extend from the surface to 8-10 m below the surface. In order to complete the "Atchafalaya box," the S3 line was transited again without CTD stations. While northward flow is dominant in the outer half of both sections, considerable difference between the sections is evident. Note the almost 180° wind shift between S3 and T6 in Figure 5.

Note the isohalines slope down to the west indicating the coastal plume is oriented obliquely offshore across this line. Indeed the lowest salinities are at the western end of this section.. This section cuts through a strong jet exceeding 35 cm/s about 30 km from the western end of this line. The salinities in the jet of 28-30 psu are quite similar to the salinities of the jets seen in S2 and T4 suggesting continuity between these sections.

Section S4, 75 km west of the Atchafalaya River outflow, was occupied during the northerly and easterly winds of Episode IV. The salinity structure of the coastal plume here (Figure 25) appears markedly different than at S2 and S3. The upper 4 m have a uniform salinity across the entire section. Additionally, the zone between 5 and 10 km from the coast is essentially vertically isohaline. This distribution is consistent with a surface layer driven offshore by the northerly winds of Episode IV. The local concentration of low salinity waters within 5 km of the coast, a persistent feature in many of these sections, is likely the result of freshwater drainage forced from bays, bayous and canals along the coast. The velocity sections for both U and V components (Figure 26) are also markedly different than previous sections.

(a)
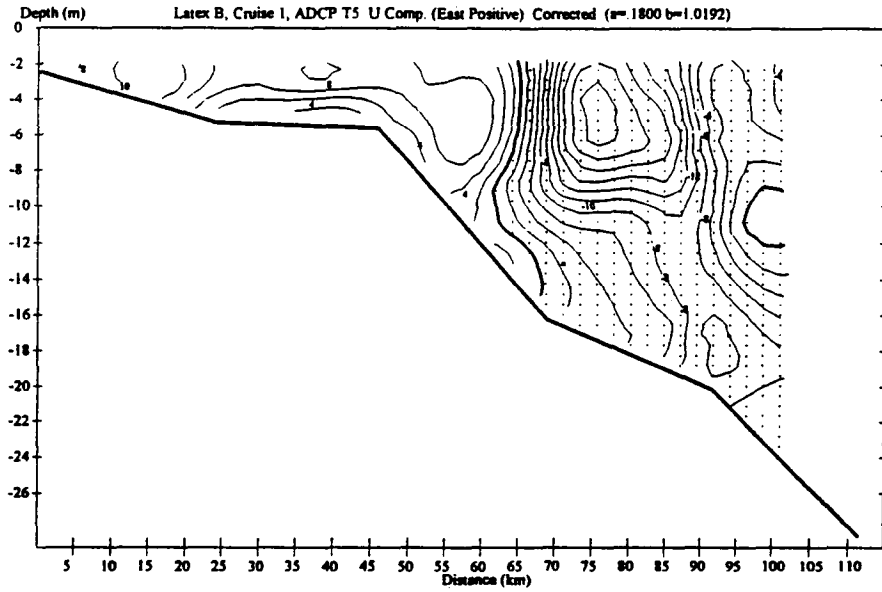
(b)
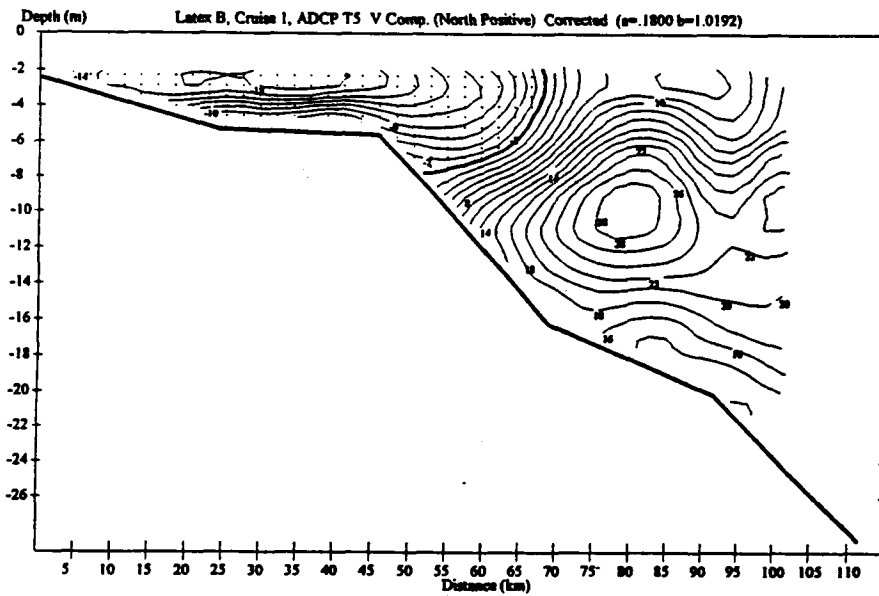
Figure 27 (b) cont'd.

Figure 22. ADCP T5: (a) U component; (b) V component.

31
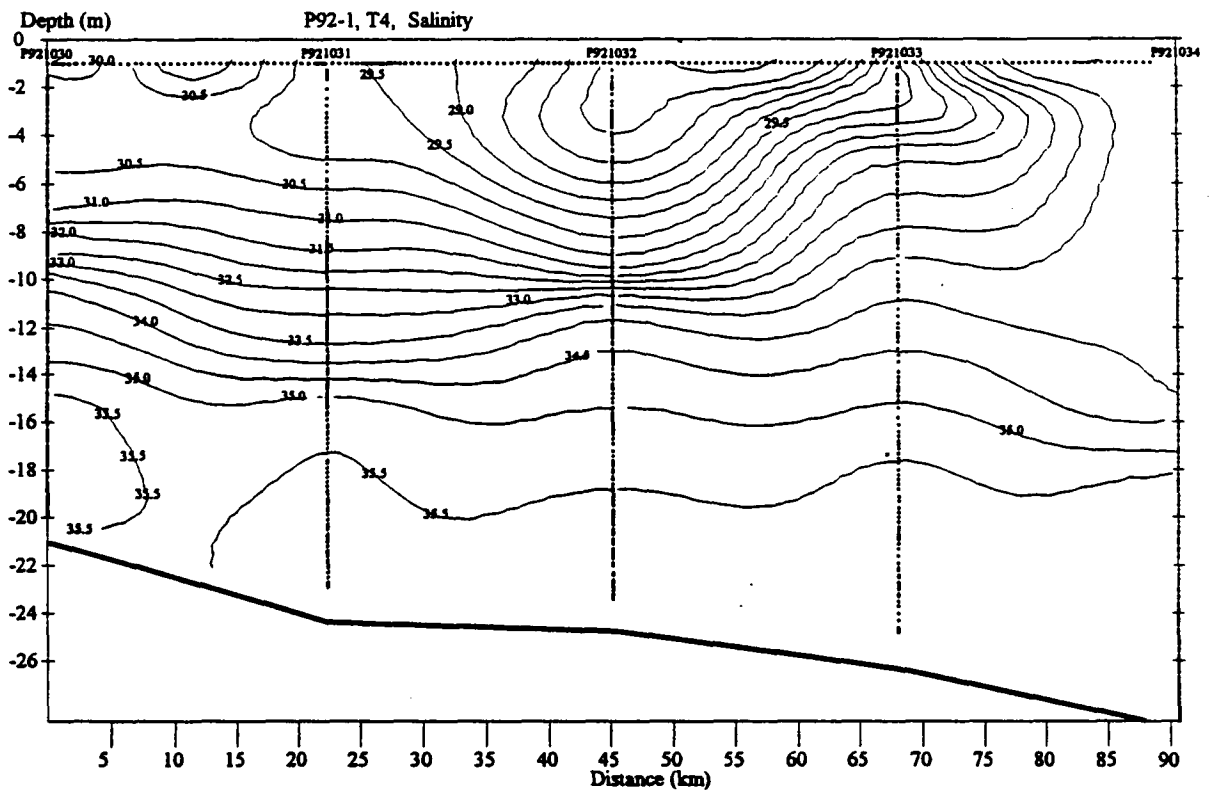
Figure 23. Salinity transit T4.

(a)
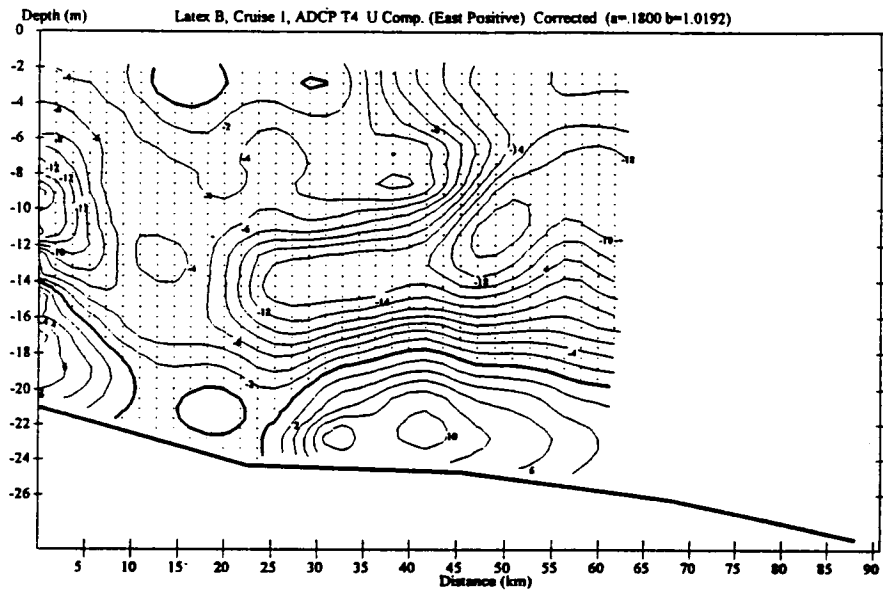
(b)
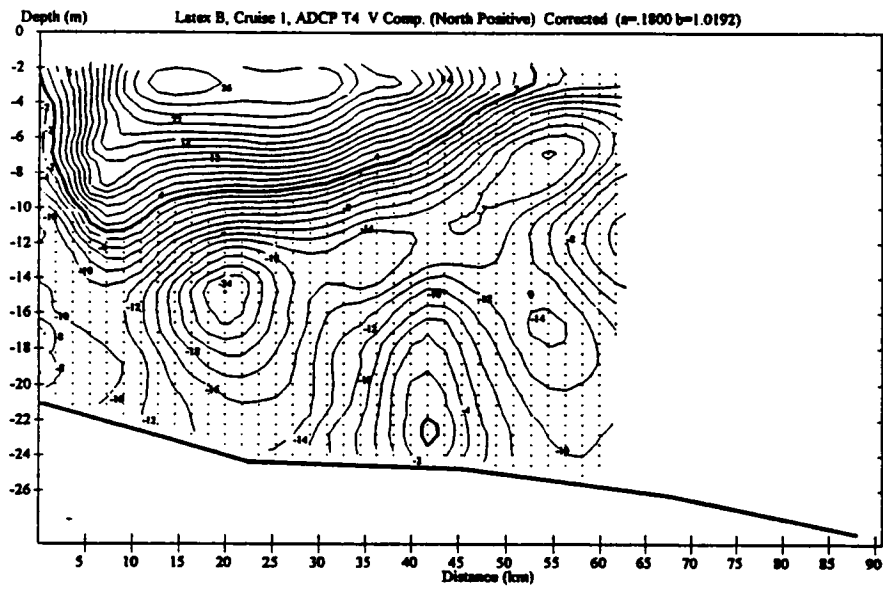
Figure 24. ADCP T4: (a) U component; (b) V component.

33
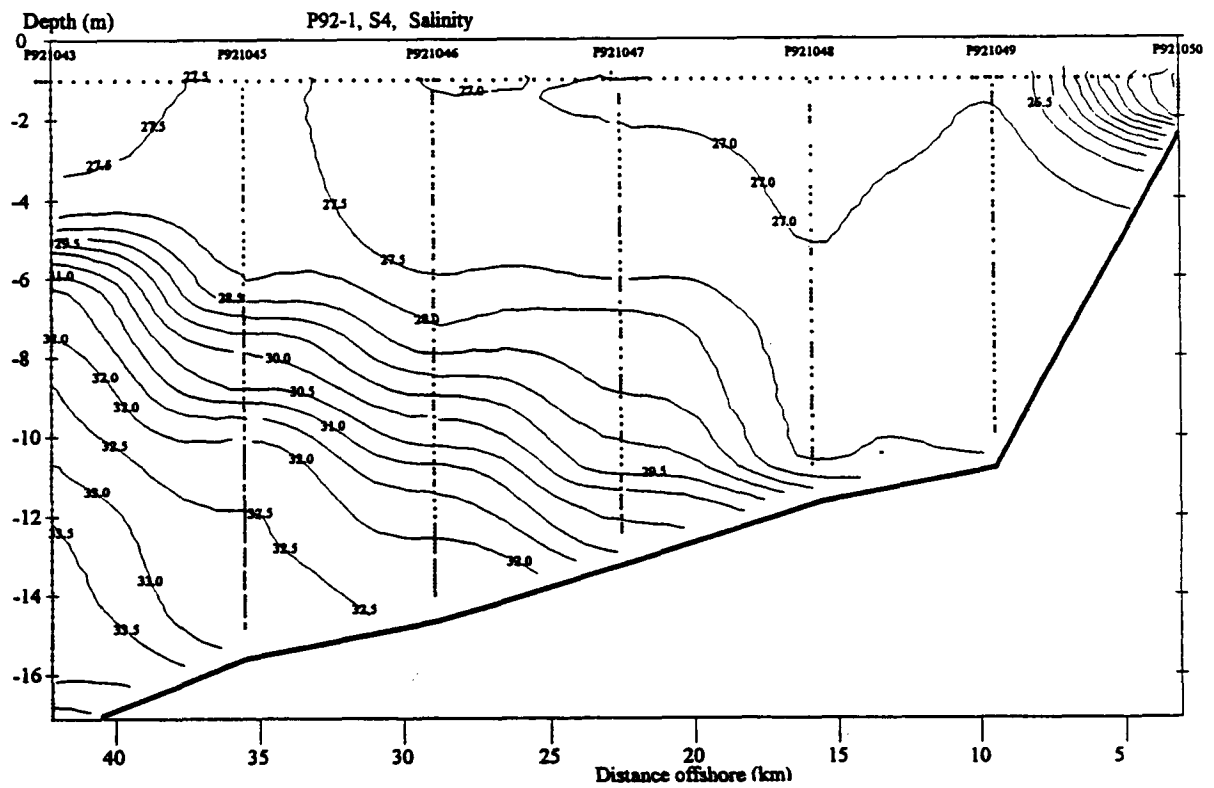
Figure 25. Salinity section S4.

(a)
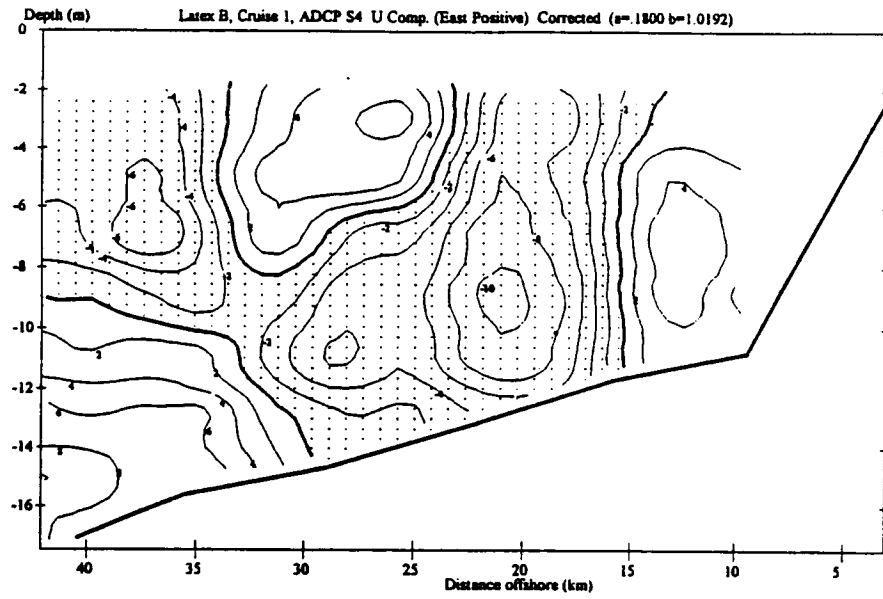
(b)
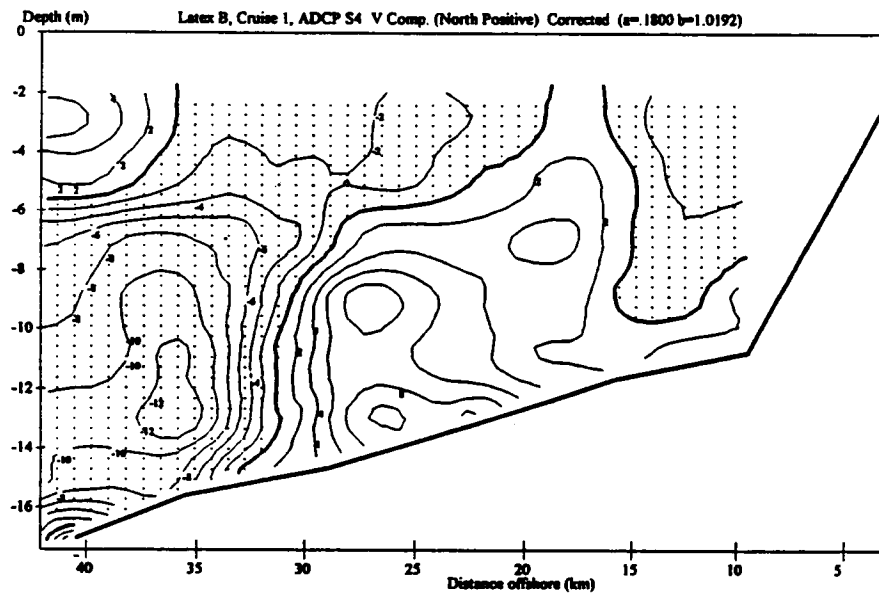
Figure 26. ADCP S4: (a) U component; (b) V component.

35

The flow is relatively disorganized and broken into 3-4 cells of ~10 km scale (see especially Figure 26). Note the absence of the well-defined jet seen in the earlier sections. The deep high salinity water (>32 psu) at the outer edge of the section flows to the southeast in a manner coherent with the salinity distribution. The section T8 occupied on the transit west to S5 was in very shallow water and yielded only MIDAS data (included in Figure 7).

Low salinities of the coastal plume in S5 (Figure 27) extend well offshore; our outer station over 60 km from the coast recorded only 29.5 at the surface. The coastal plume at this section is a large, well-developed coherent structure, probably extending over 80 km from the coast. However, despite the strong northerly winds prior to and during the measurement of S5 (see Figure 4), the isohalines slope sharply up to the surface. This implies an onshore-directed pressure gradient, perhaps associated with forcing from the outer shelf. Such a force would be necessary to overcome the seaward directed wind stress, which would produce an isopycnal upper layer with flattened isohalines as seen in S4. The velocity components along S5 are shown in Figure 28. Although current velocities are predominately to the NW above the 10 m level, speeds are considerably reduced, e.g., there is no well-defined jet. This long period of offshore northerly winds appears to considerably decelerate the current, drive surface water offshore, and initiate vigorous vertical mixing beyond 30 km offshore.

The tieline T10 lacks any significant thermohaline structure, but note that bottom salinities become abruptly higher at the western end of the section, perhaps indicating an onshore intrusion focused in this area. Strong northerly winds persisted during T10 and the velocity components along T10 remain weak (≤ 10 cm/s) but predominately westward-directed. The V component has a marked cellular structure, a spatial non-uniformity that appears representative of strong offshore wind conditions.

The vertical salinity structure of S6 (Figure 29) is remarkable. In the outer 25 km of this section, the upper 8 m is nearly homogeneous, the isohalines being almost vertical. A strong halocline between 6 and 9 m does extend over the inner half of this section. Considering the persistent northerly winds prior to and during S6, it is surprising to see that the isohalines in the 28-31 psu range are not flattened out in the offshore direction, indicating offshore transport in the surface Ekman layer as seen at S4 (Figure 25). The slopes of the outer isohaline suggest to the contrary that an onshore-directed pressure gradient is pushing the water in this section toward the coast. The velocity data in Figure 30a shows a strong (36 cm/s) jet in the westward direction, and Figure 30b does indicate a fairly uniform 10 cm/s current component northward toward the coast.

After S6 was completed the winds again shifted abruptly, marking the start of the period of south and southeasterly winds, referred to as Episode V. The significant observation from this figure and the MIDAS surface salinity in this area is that the western end of the line represents a significantly different hydrographic regime than the east end off Sabine. Note the 3 psu increase in salinity between P921092 and P921093. These show a general onshore-northwestward flow through the section. A zone of low salinity offshore flow, however, is evident at the eastern end of this section near Sabine Pass. A second zone of stronger southward (offshore) flow also coincides with a lens of lower salinity water between stations P921091 and P921092.

Section T15 begins off the Galveston Bay Pass in 14 m water depth and continues farther westward, cutting an ~45° oblique section through the central Texas coastal plume. The velocity components show a strong southward flow in a narrow zone off Galveston and a general onshore flow over the rest of the section, consistent with the structures observed in S5 and S6.

The salinity structure in the Sections S7 and S8 (Figures 31 and 32) are markedly similar. The offshore drift in the surface Ekman layer and the northerly winds during S7 will drive the surface water offshore, flattening the isohalines, and breaking down the strong horizontal salinity gradient at the seaward edge of the coastal plume. This leaves a quasi-homogeneous surface

36
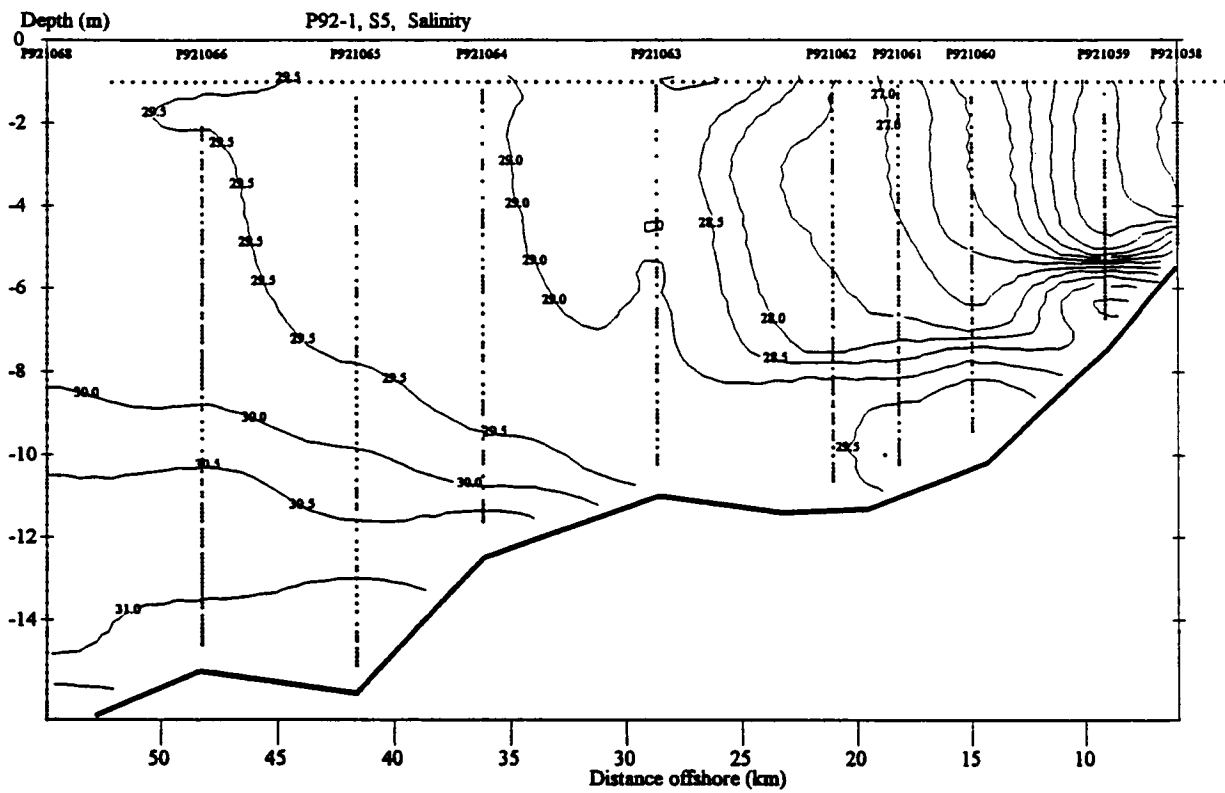
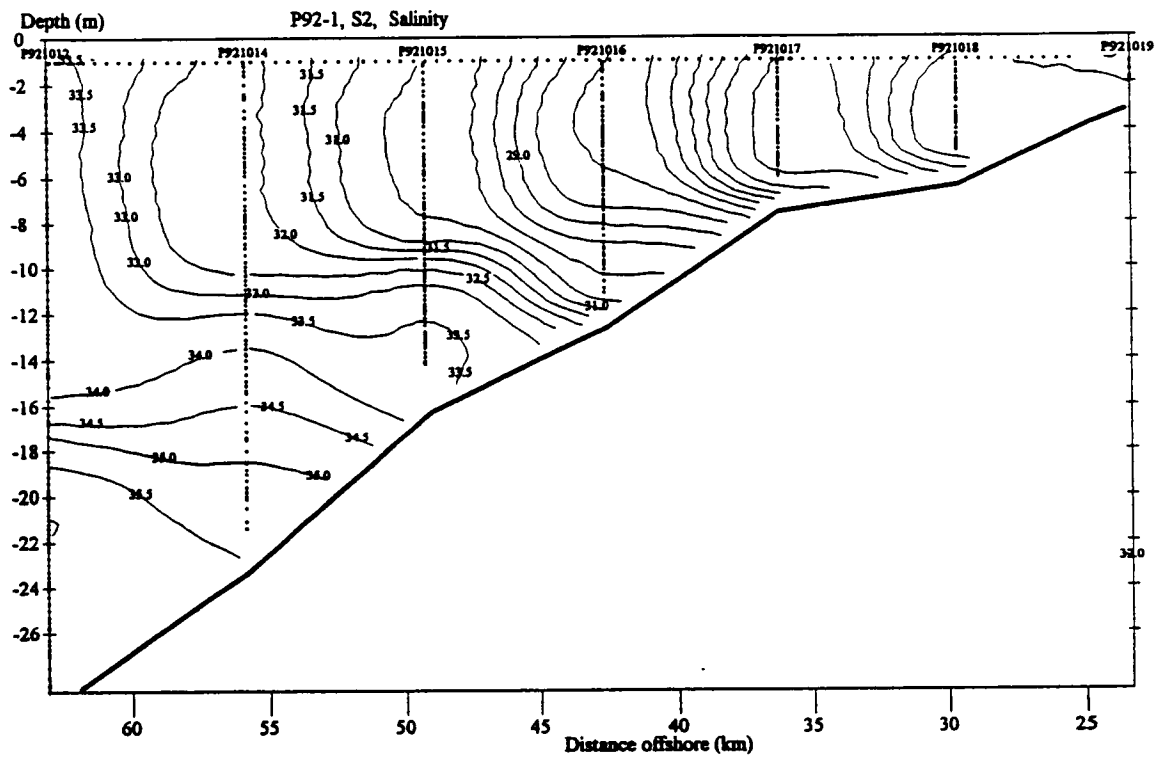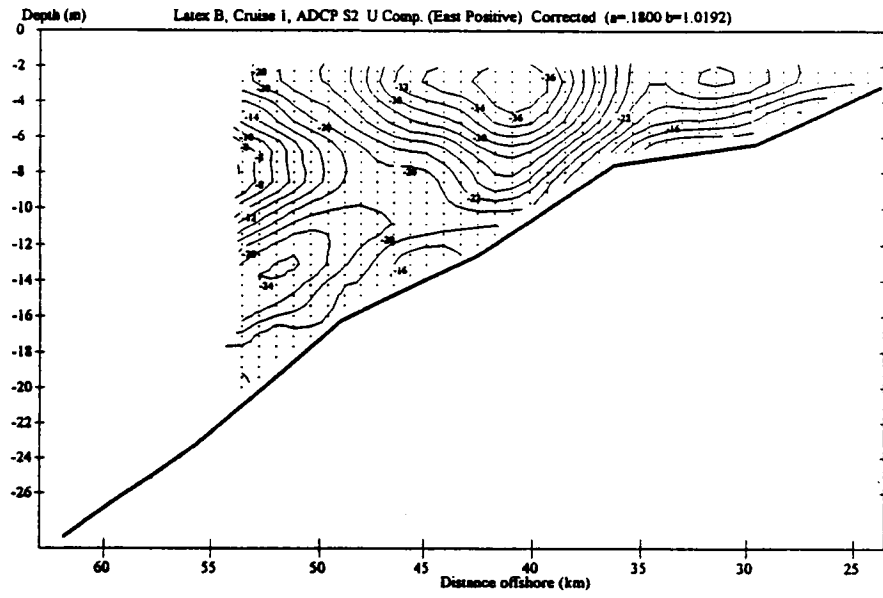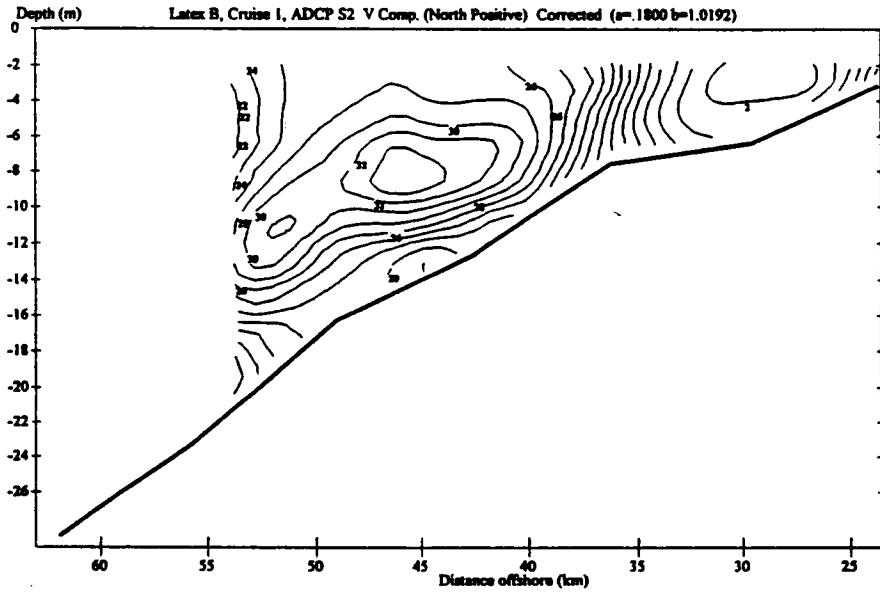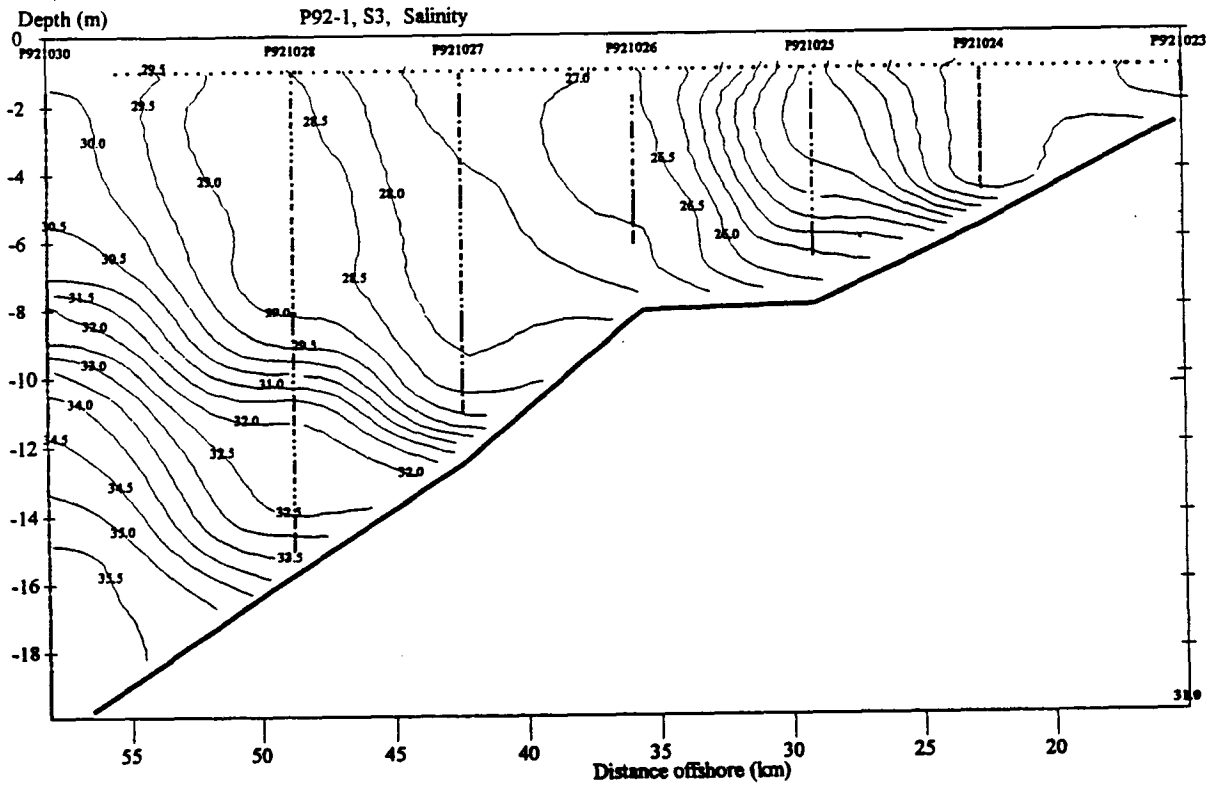Figure 27. Salinity section S5.

(a)
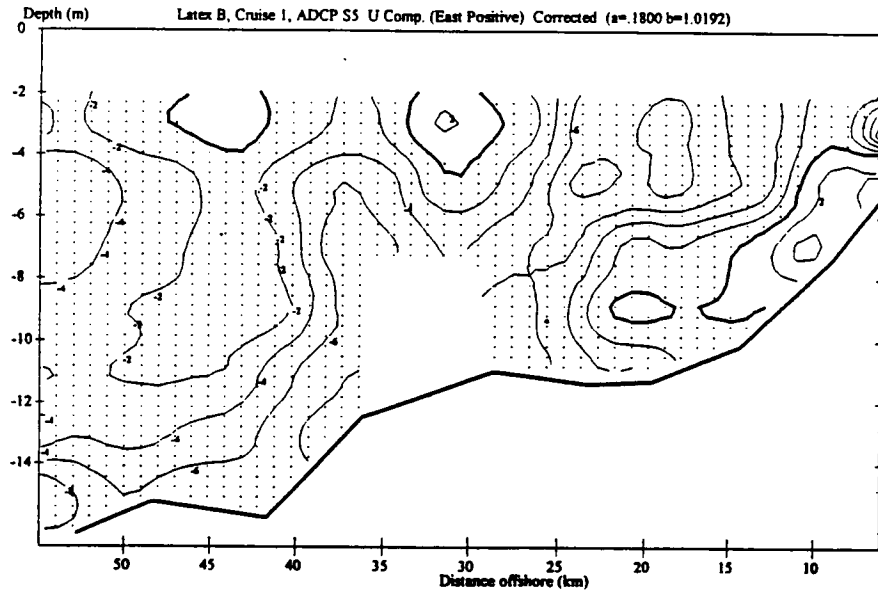
(b)
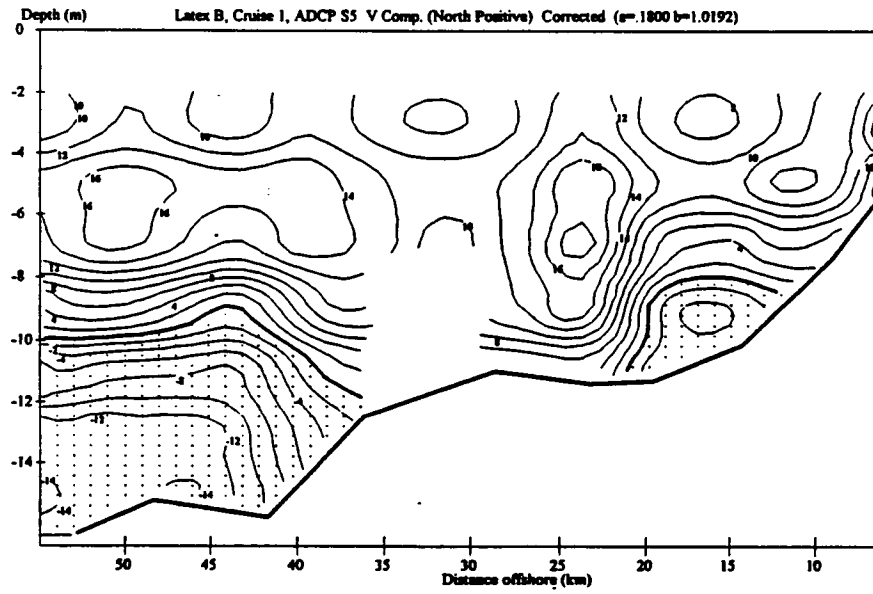
Figure 28. ADCP S5: (a) U component; (b) V component.

38
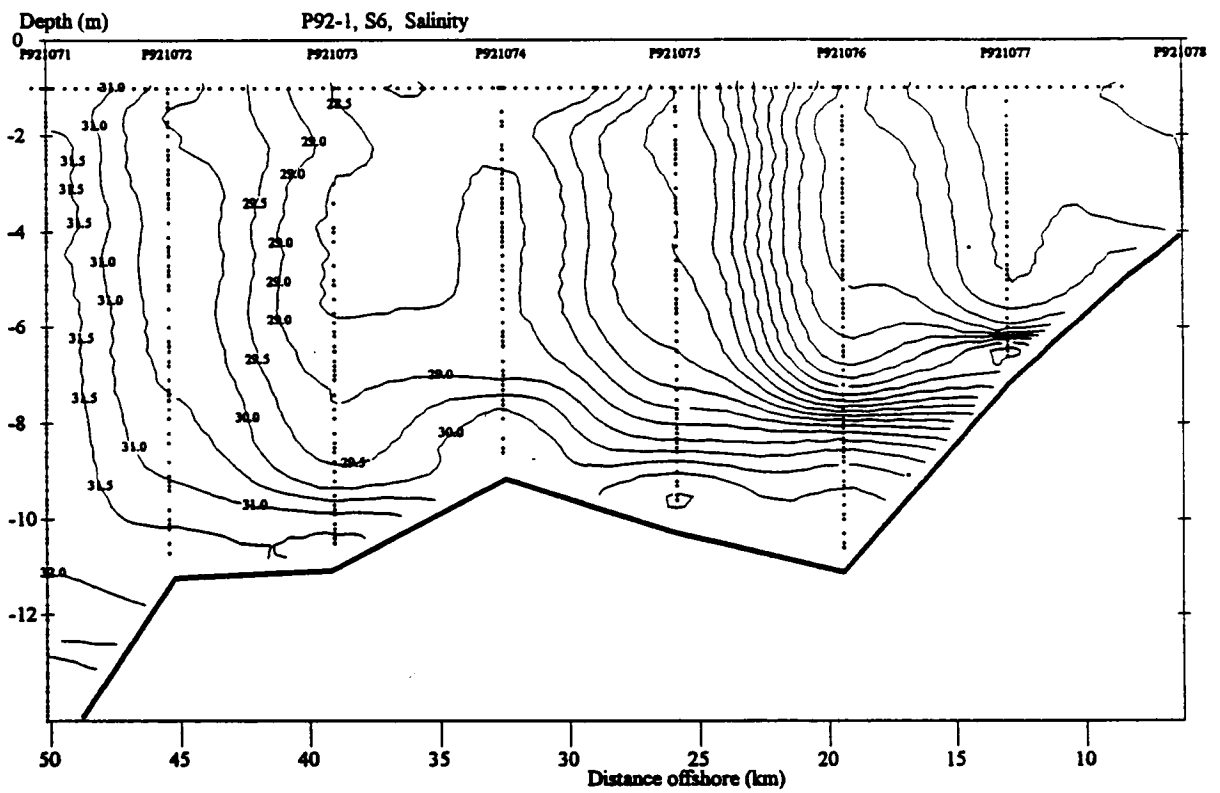
Figure 29. Salinity section S6.

(a)
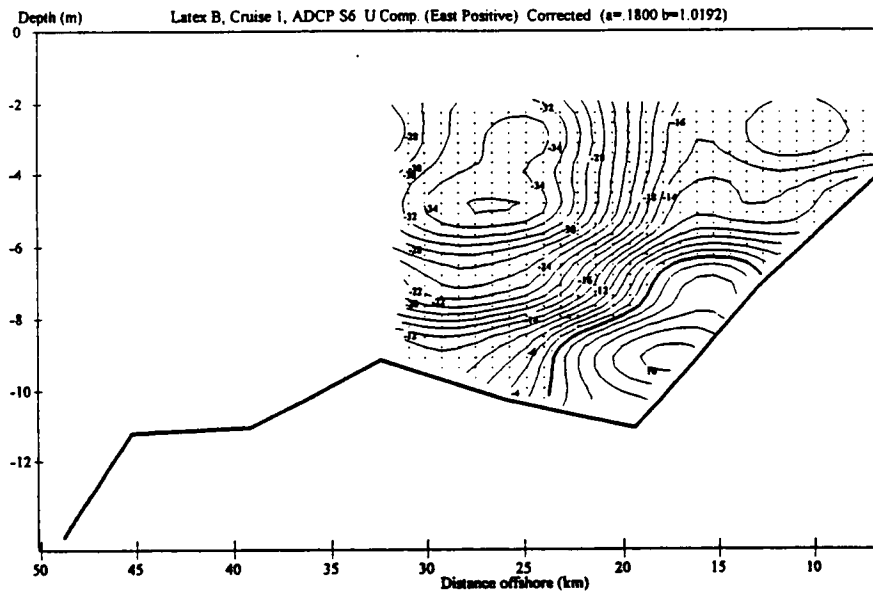
(b)
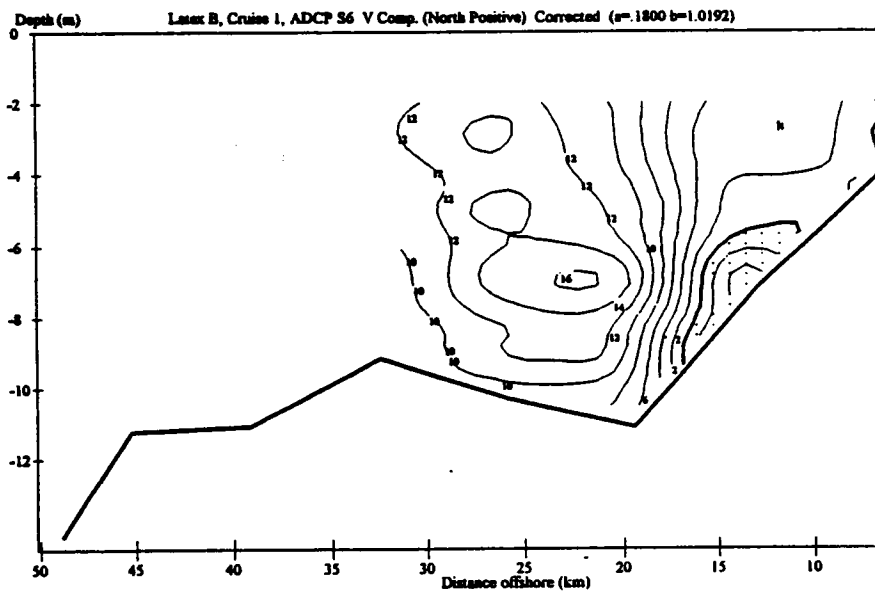
Figure 30. ADCP S6: (a) U component; (b) V component.

40
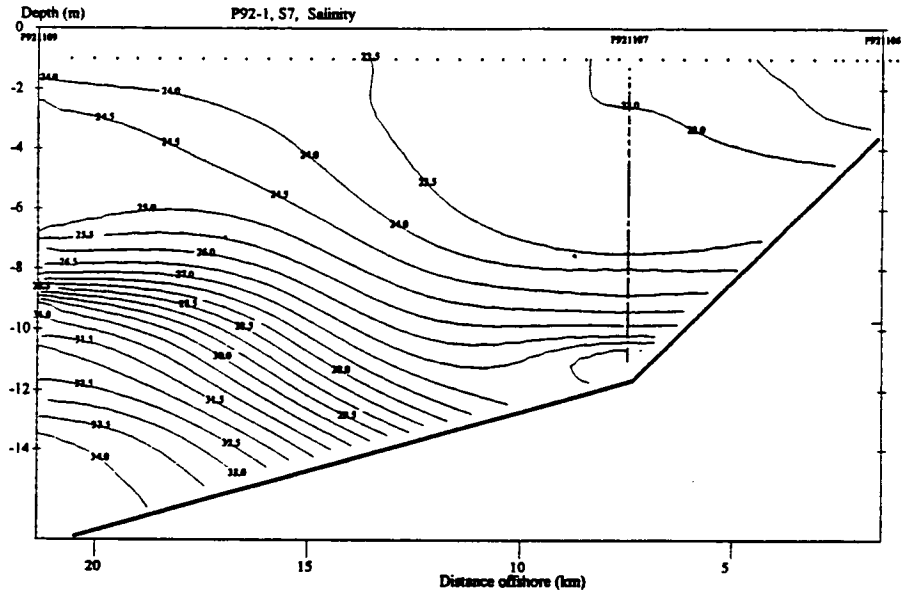
Figure 31. Salinity section S7.
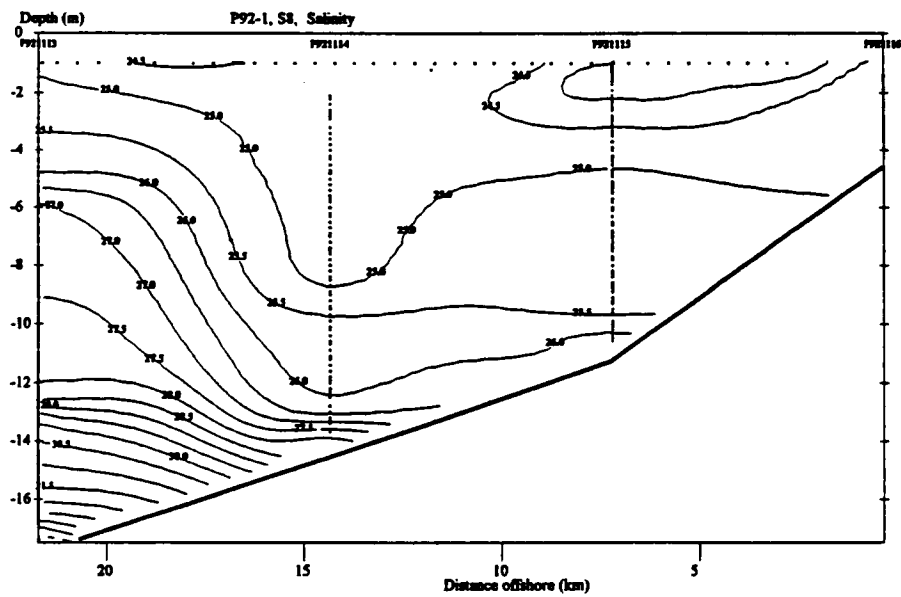
Figure 32. Salinity section S8.

layer as seen in Figures 31 and 33. The velocity sections at S7 (Figure 33) show the flow is strongly eastward (upcoast and offshore) in the surface layer above 8 m, in agreement with the salinity distribution. Below 8 m the flow is more northeastward along the bottom contours. The winds between S7 and S8 are extremely variable (see Figure 5) shifting from north-northeasterly to south-southeasterly. The velocity section at S8, shown in Figure 34, appears somewhat complex with north and northeastward flow below 8 m in the upcoast direction. Above 8 m there appears to be an eddy-like motion with westward flow at the offshore end, turning anti-cyclonically into eastward flow at the inshore end of the line.

Section T16 has no salinity section because of down time on the CTD. There is a strong eastward component to the currents above 10 m and a westward component below that level. Note that the westward (downcoast) component weakens rapidly as the ship nears the SW end of section T16. In this region, winds (see Figure 4) have shifted to blow strong from the south-southeast, which drives surface layer water in the upcoast direction.

The remaining sections normal to the coast (X1, X2, and X3; Figures 35, 36, and 37, respectively) and their long oblique tie-lines (T17, T18, and T19, respectively) were occupied during the episode of intense southerly winds off south and central Texas. A well-developed coastal plume had evidently developed before our sections, as seen in T15 (data not shown). We observed it, however, in the process of being degraded through offshore transport in the surface Ekman layer. All these normal-to-the coast sections and transit tie-lines show basically the same structure: a fairly homogeneous surface layer with salinities in the range of 24-26 psu. This layer is underlain by a broad halocline with salinity uniformly increasing from 26-32 psu. The slopes of the isohalines across the section are largely flat. Higher salinity Gulf waters (32-34 psu) can be seen intruding up the bottom slope in the 16-22 m range.

The velocity structures in this region are best examined at sections X1, X2, X3, Figures 38, 39, and 40, respectively. All these show strong northward and eastward components across the sections as a result of the strong upcoast wind driving. Note the formation of high speed jets reaching 60 cm/s near the coast in only 10-12 m of water depth (e.g., section X1, Figure 27).

Because the ship was heading directly into severe seas on T17, T18, and T19, the ADCP sled used on Cruise 1 had serious instability problems. The ADCP data in these lines failed to qualify for presentation under quality control guidelines.

A careful examination of sections S8 (Figure 32), T17, and X1 indicates this area is the location of a frontal zone between the low salinity Louisiana waters and the higher salinity waters from central and south Texas. In S8 the 27 psu isohaline is no higher than 6 m below the surface and intersects the bottom at a depth of ~13 m. Moving southwest along T17 the 27 psu is abruptly encountered at the surface, only 30 km from Section S8 and intersecting the bottom in only 6 m water. The salinity in section T17 shows the 27 psu isohaline is the leading edge of a strong frontal zone between stations P921117 and P921118, where the salinity increases 3 psu. Continuing southwest to Section X1, the 27 psu isohaline is at or near the surface over the entire section.

b. Temperature Sections. The temperature distribution in all the sections shows very little variability. The vast majority of values are confined within the range 20.5°-22.5°C. In general, the behavior of the isotherms adds little information beyond that deduced from the salinity field. We will comment here on only a few sections of interest.

Surface layer water to the east of Atchafalaya Bay is all 23°C (e.g., S1, T2, and S2). Section T3, the shallow line across the mouth of Atchafalaya Bay, shows the bay water temperature as it enters the Gulf to be >23°C. It is distinctly elevated in temperature above the coastal surface water by 1°C. This high temperature tag of the Atchafalaya outflow is also seen

(a)
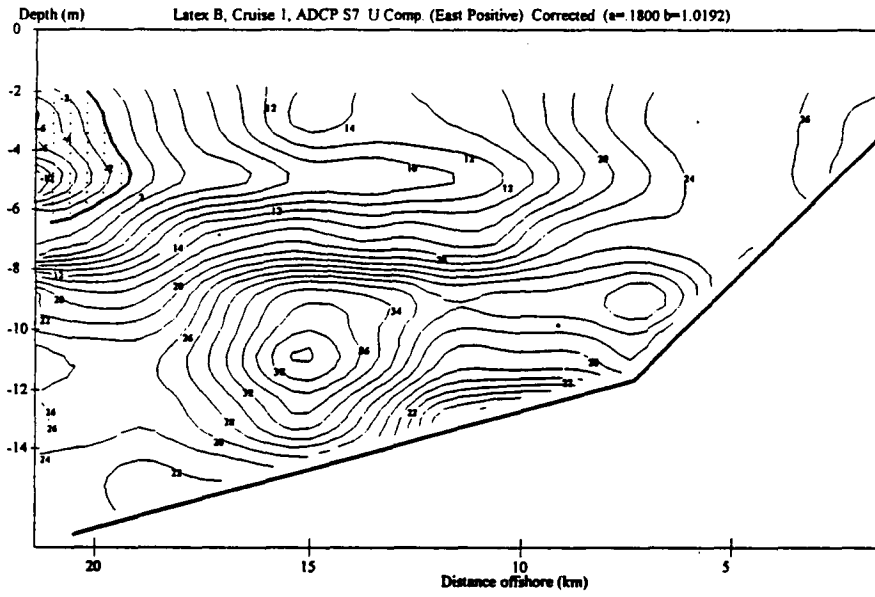
(b)
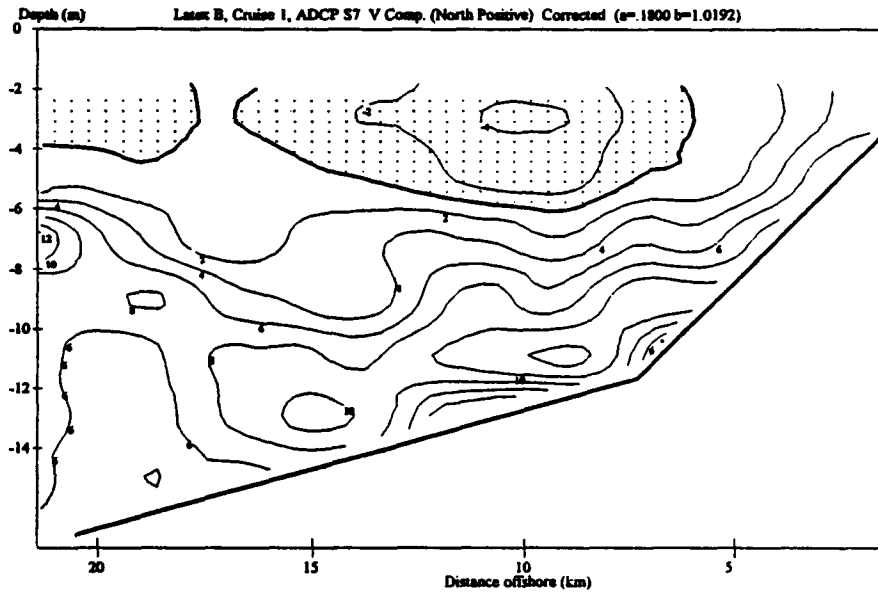
Figure 33. ADCP S7: (a) U component; (b) V component.

43

(a)

Latex B, Cruise 1, ADCP S8 U Comp. (East Positive) Corrected (a=.1800 b=1.0192)

(b)

Latex B, Cruise 1, ADCP S8 V Comp. (North Positive) Corrected (a=.1800 b=1.0192)
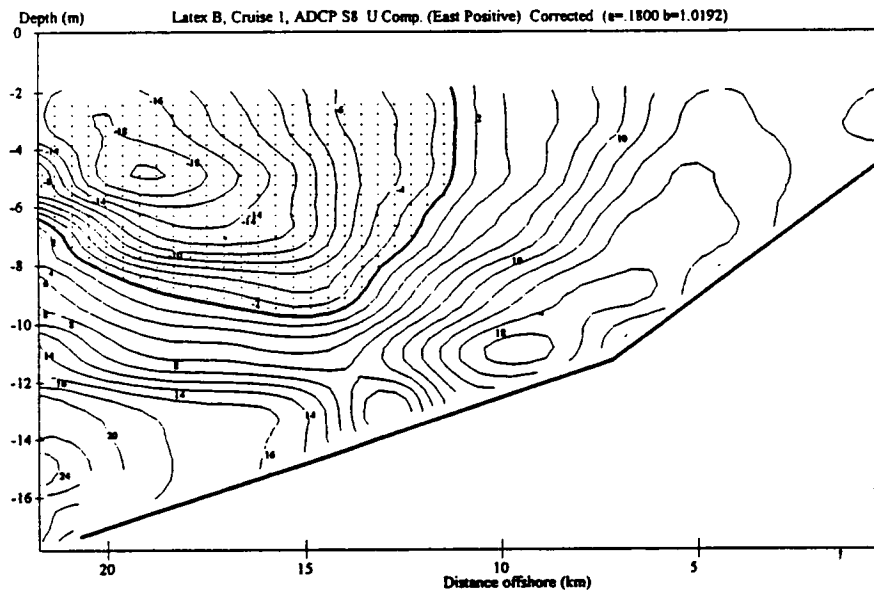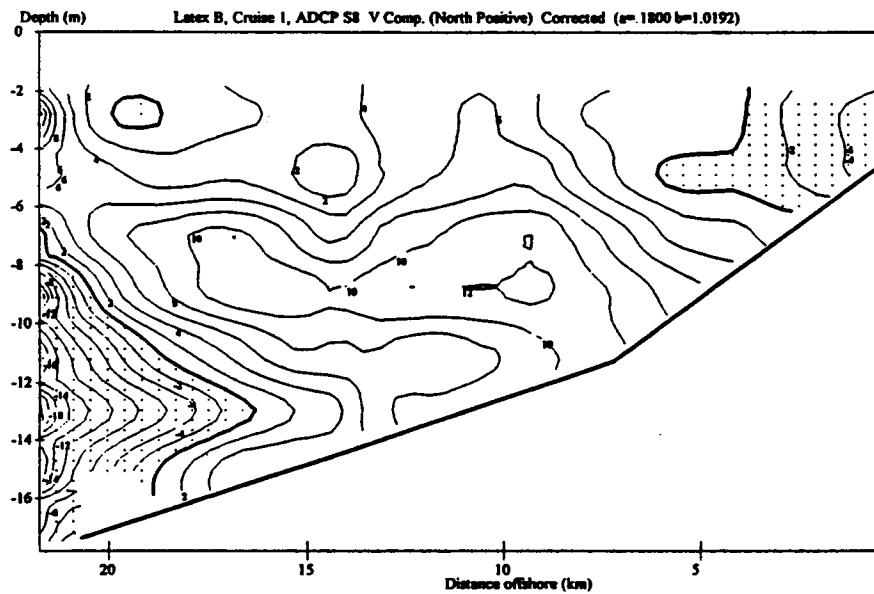
Figure 34. ADCP S8: (a) U component; (b) V component.

44

Figure 35. Salinity section X1.

Figure 36. Salinity section X2.
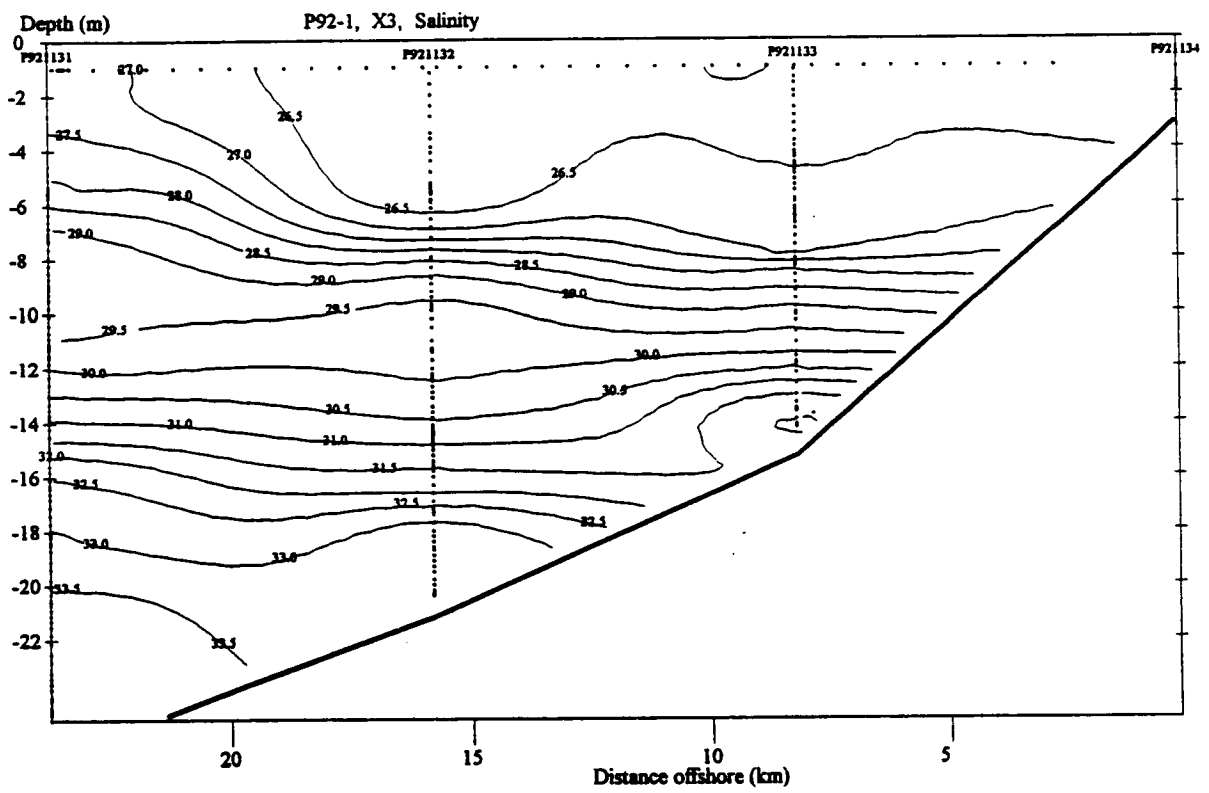
Figure 37. Salinity section X3.

46

(a)
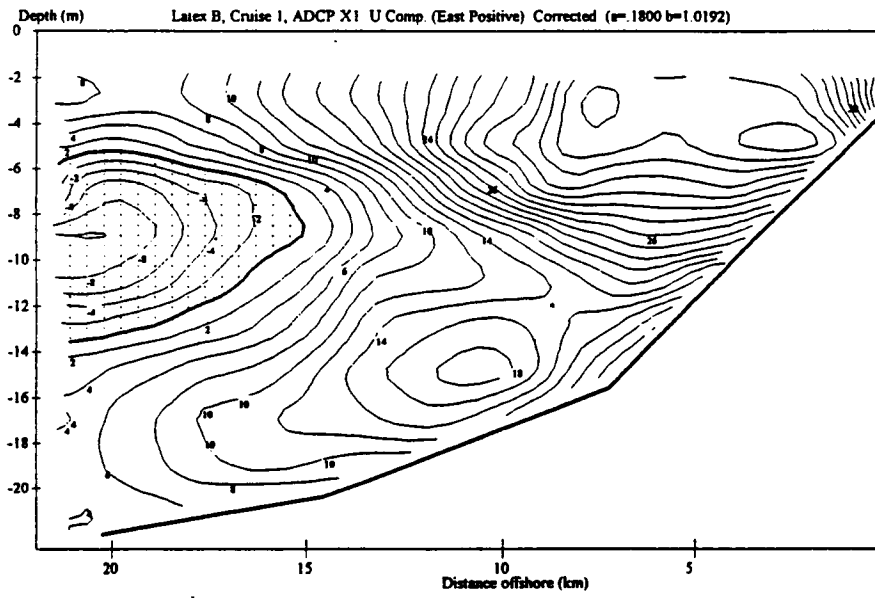
(b)
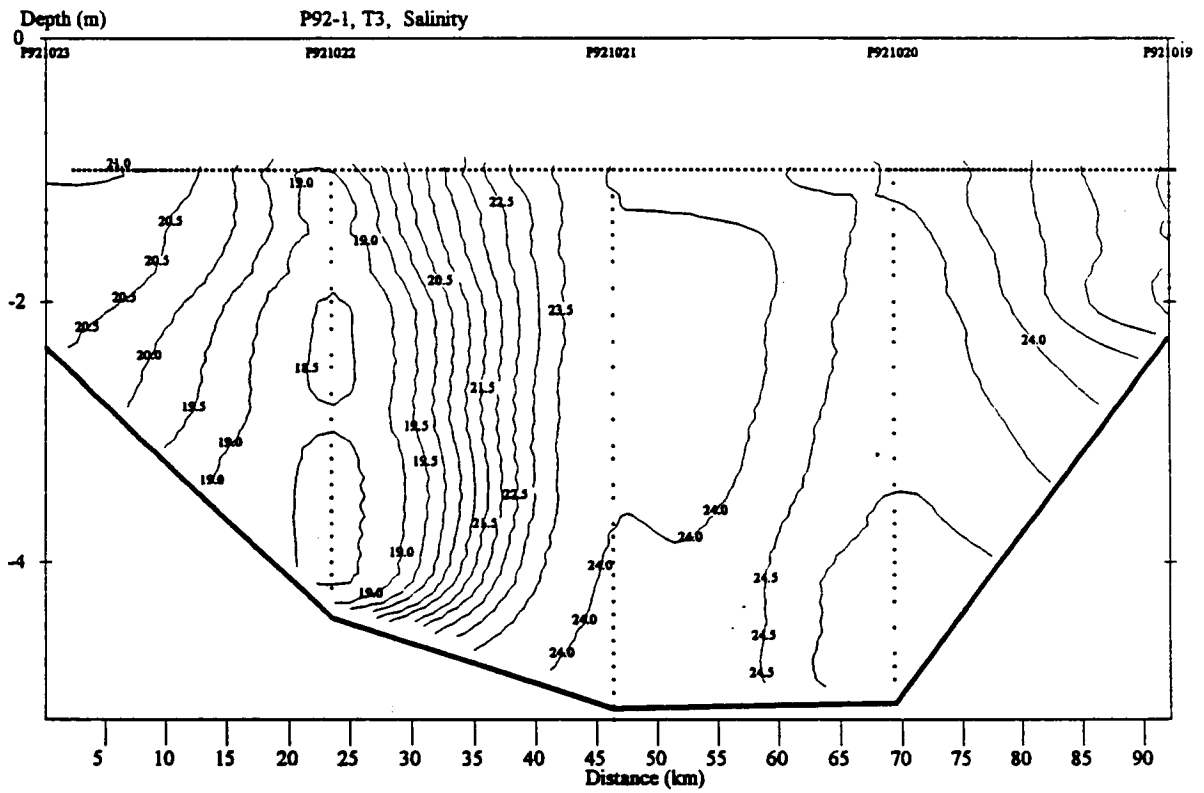

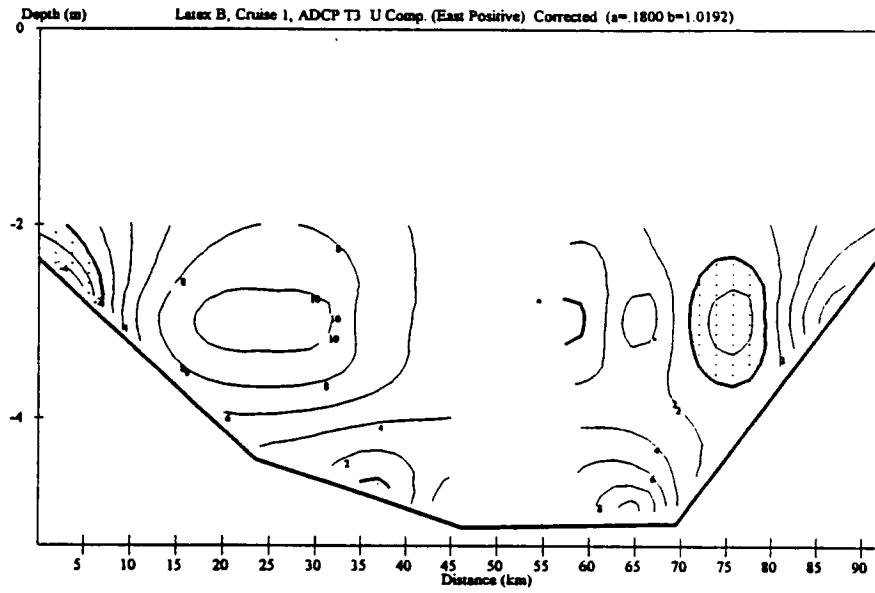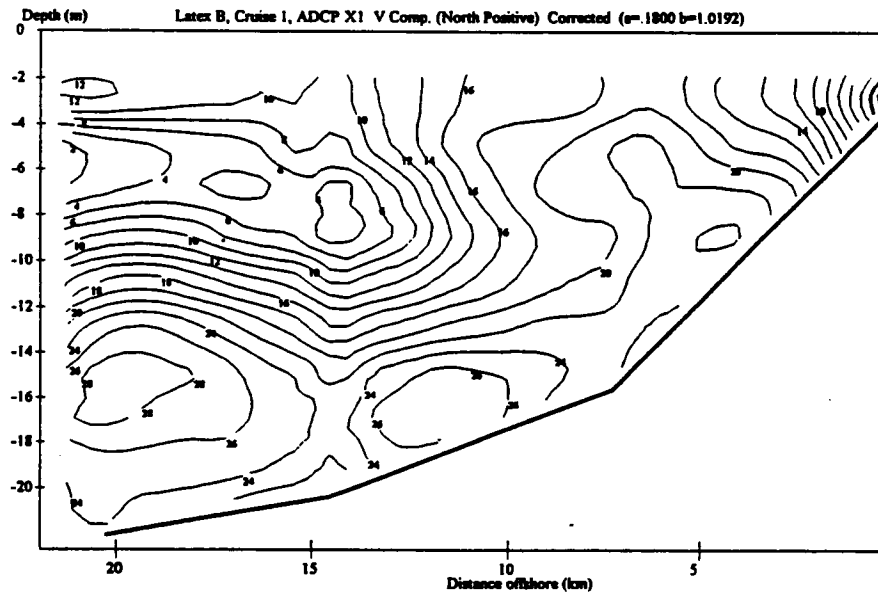Figure 38. ADCP X1: (a) U component; (b) V component.

47

(a)
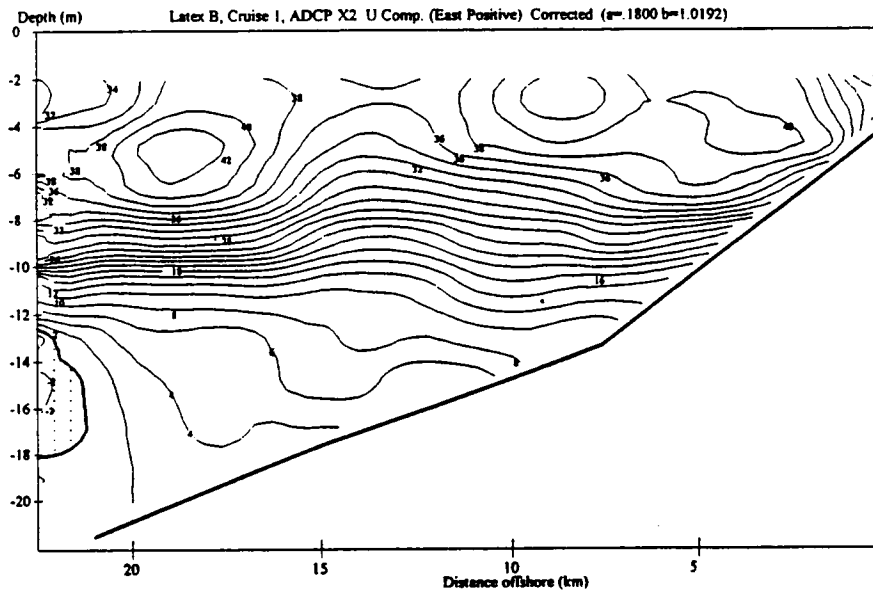
(b)
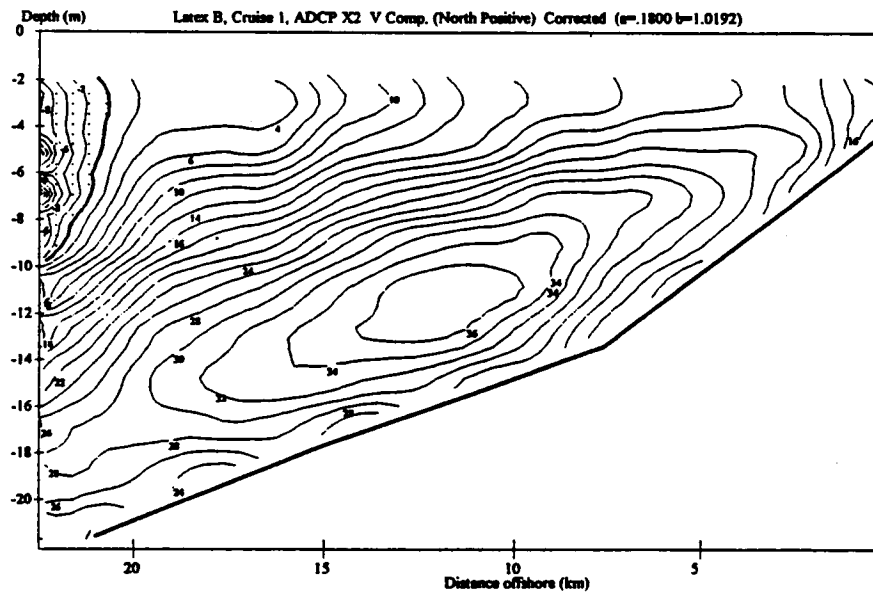
Figure 39. ADCP X2: (a) U component; (b) V component.

48

(a)
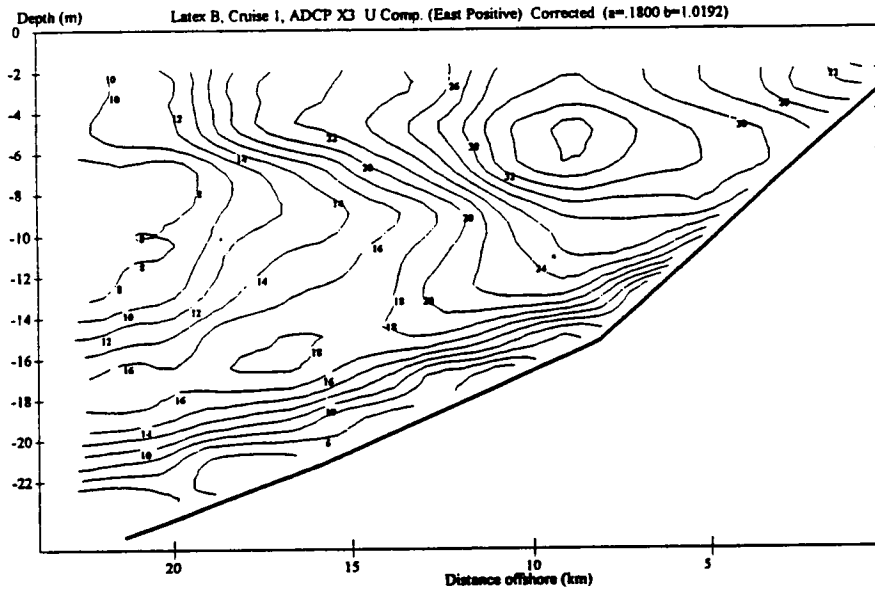
(b)
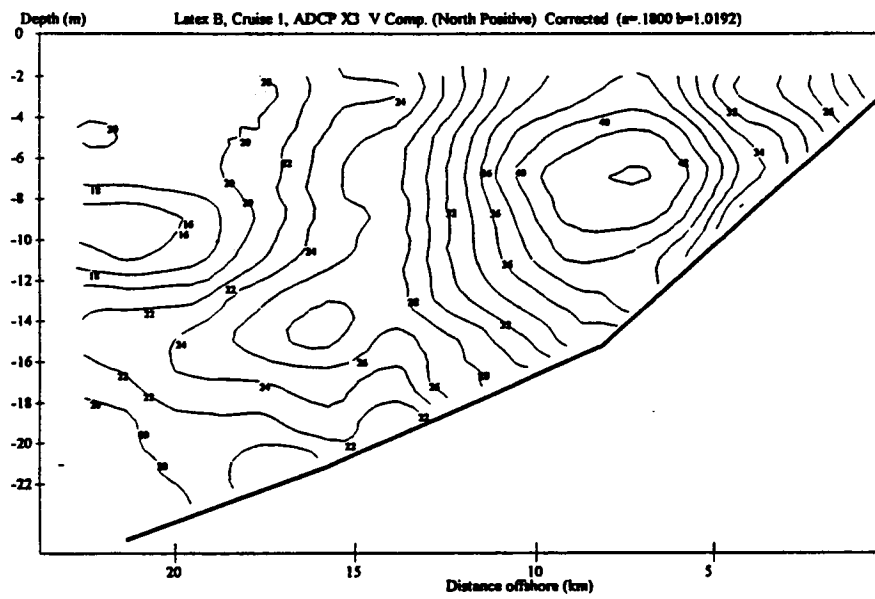
Figure 40. ADCP X3: (a) U component; (b) V component.

49

on the diagonal line T5, as well as the outer edge of the Atchafalaya box section T4 in agreement with the salinity. Note that sections T5 and S3 actually show water temperatures over 24°C, at the southwest apex of the box, i.e., the least diluted water. Water over 23.5°C can be tracked westward along T7 but has been mixed away before reaching S4.

The high salinity dome, in the area south of Sabine Pass (identified by both the MIDAS salinity data and the S5 and S6 salinity sections) also has a signature in the temperature field. At S4 the two layers of water bounded by (1) the 22-22.5°C isotherms and (2) the 22.5-23°C isotherms are only a few meters thick across the section and occupy the deepest one third of the section. In S5, the eastern border of the Sabine box, the 22.5-23°C layer occupies almost the entire section. Sections T10 and S6 are both filled with water from the deeper 22-22.5°C layer. It appears that these deeper waters have been pushed onto the inner shelf by forcing, which originates from the mid to outer shelf. Section T13, the tie-line from the Sabine box to the west, is also filled with water from the 22.0-22.5°C layer, indicating the influence of this intrusion extends at least as far as 94°W, again in agreement with the salinity distribution.

All the normal-to-the coast sections and tie-lines west and south of Galveston reveal in the temperature data the same pattern as that of the salinity sections. The strong southerly winds during the occupation of these lines drive the surface waters offshore and break down the coastal front. Isotherms are largely horizontal and widely spaced in the vertical; weak thermoclines are present at the 8-10 m level.

c. Density Sections. Our study of the temperature sections indicated there was very little thermal structure for this particular cruise and that salinity, as expected, was by far the dominant variable in determining water density. Study of the vertical sections of density indicate there are no significant differences between the structure of the sections as mapped by salinity or by density.

d. Temperature-Salinity Diagrams. Careful study of the temperature-salinity (T-S) diagrams along each section significantly assists in understanding the variability in the hydrographic structure along the coastal plume. The T-S diagrams for the stations in section S1 are good illustrations of the change in thermohaline characteristics across the plume. Station P921001 is the shallow, well-mixed freshwater end member. Stations P921002 and P921003 have a range of 10 psu in salinity but only 1.5°C in temperature, typical of the core of the coastal current. Station P921004 is the first station moving seaward to penetrate down into the Gulf water end member followed by stations P921005, P921007, P921009 in turn. The bottom water end points of these stations cluster at a salinity of 35.5-36.3 and a temperature of 20.5°C. Note *the almost right angle* shape to the T-S curve for station P921004. This implies the warm low salinity surface layer is not mixing directly with the deep high salinity layer below the pycnocline, but a third type of water, also with a high salinity is intruding into the thermocline. This is very clear with the high salinity bulge in station P921007, and the high temperature, high salinity bulges at stations P921030 and P921031 from line S3. As these stations are all at the offshore end of the survey lines, it is probable that these features are the signature of filaments advected from the shelf.

Stations P921025-P921030 also show a characteristic signature for the Atchafalaya River outflow plume. An isohaline upper layer overlaying a lower layer, weakly isothermal, but increasing rapidly in salinity, produces an L-shaped diagram at stations P921025-P9210027. The outer stations on the line, P921028 and P921030, extend the lower limb of the L into deeper, saltier water through mixing. This same type of T-S profile is seen at stations P921031 and P921033 on the outer border of the Atchafalaya box (T4) indicating the penetration of the Atchafalaya River plume out to this area.

50

The T-S diagrams from the stations on lines S5 and S6 (the Sabine Pass region) appear fundamentally different. These figures are highly elongated along the salinity axis, reflecting the quasi-isothermal nature of the water column in this region, as discussed above. Also note the temperature maximum in the 30-31 psu salinity band, again suggesting the intrusion of an offshore filament as in Sections S4 and T10. The appearance of this same type of T-S diagram along T13, T15, and S7 indicate that the dynamic processes determining the water mass characteristics in the coastal plume south of Sabine Pass extend at least as far west as Galveston Bay.

The stations in the region beginning at S8 and extending all the way southwest to X3 display similar T-S curves, which collectively appear different in kind from both the (1) Sabine Pass-Galveston grouping, and (2) the Louisiana sections further to the east (e.g., see section X1). The low salinity end member has a salinity always greater than 24-25 psu and the transition to the colder, high salinity "deep water" end water is rather sharp. Note especially the salinity of the deep end member is only 33-34 psu in marked contrast to the 36 psu deep water seen in the easternmost sections.

4. Acoustic Doppler Velocity Maps on Constant Depth Surfaces

We will conclude the presentation of Cruise I results with a discussion of the constant level velocity fields by sub-areas or sectors for the entire cruise. This allows much greater graphic resolution of the ADCP data set.

Sector 1 extends from Section S1 at 90°30' westward to about halfway between S3 and S4. It principally displays the conditions upstream (east) of the Atchafalaya River mouth and the flow pattern off the mouth itself. Figure 41 shows the ADCP velocities at the 3 m depth in Sector 1. Note again the ADCP data is of low quality and was rejected on Section S1. T2, however, shows a strong inflow of high salinity water over almost its entire length. We suspect this inflow bifurcates into east-going and west-going branches, flowing toward S1 and S2, respectively. At Section S2 the coastal current collected from S1 and T2 is a well-defined westward jet on a collision course with the southeastward flowing Atchafalaya River outflow jet. A study of the salinities along these lines indicate the coastal current is deflected sharply seaward from this impact and returns shoreward along the westward half of T4. The coastal current, augmented by the addition of the Atchafalaya River outflow, is seen flowing westward on S3 and T7. Note that S3 was run twice with ADCP coverage; the second transit is referred to as line T6. A reversal in the wind direction caused by a frontal passage produced the great variability in the current vectors on this line, as both runs are plotted in Figures 41-43.

At the 6 m level (Figure 42) the same basic flow pattern is clearly evident, except the seaward retroflection of the coastal current is less pronounced. The northward inflow of high salinity water (33-35 psu) continues through T2. The northeastward flow directions along T2 suggest that much of this water is escaping eastward through S1. Velocity vectors from the southeastward flowing Atchafalaya River plume along T5 are absent in this figure because the bottom depth is too shallow.

The flow pattern at the 10 m level (Figure 43) is less clear. The northward flow through T2 persists. It is plausible that it bifurcates at the submarine headland formed by the 10 m isobath with some flow eastward through S1 and the balance through S2 as observed. The northwestward flow along T5 under and counter to the outflow plume of the Atchafalaya River suggests strong upward entrainment into the plume. The eastern quarter of line T4 is in an onshore flow zone, but the remainder of T4 exhibits offshore flow, the source of which remains unclear. The apparent divergence in the area between T4 and T5 at this level could result from tidal aliasing or perhaps be compensated by vertical motion from above or below.

51
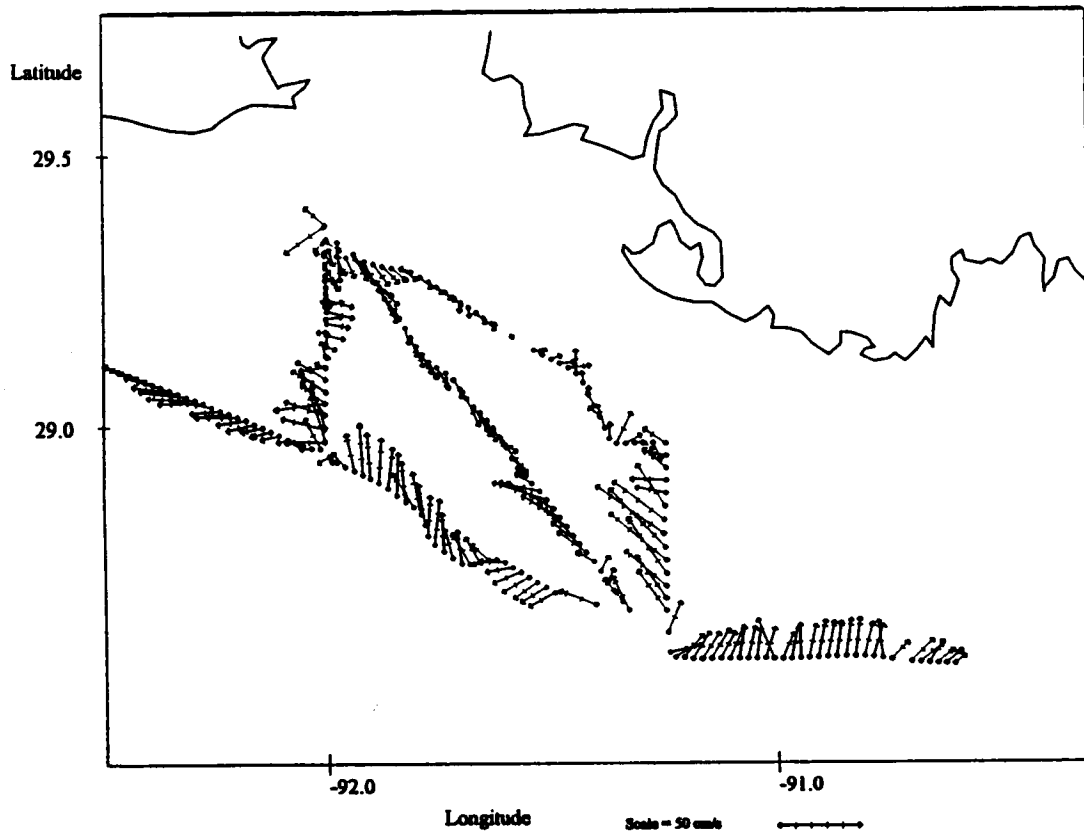
Figure 41. ADCP, 3-meter level, Sector 1.
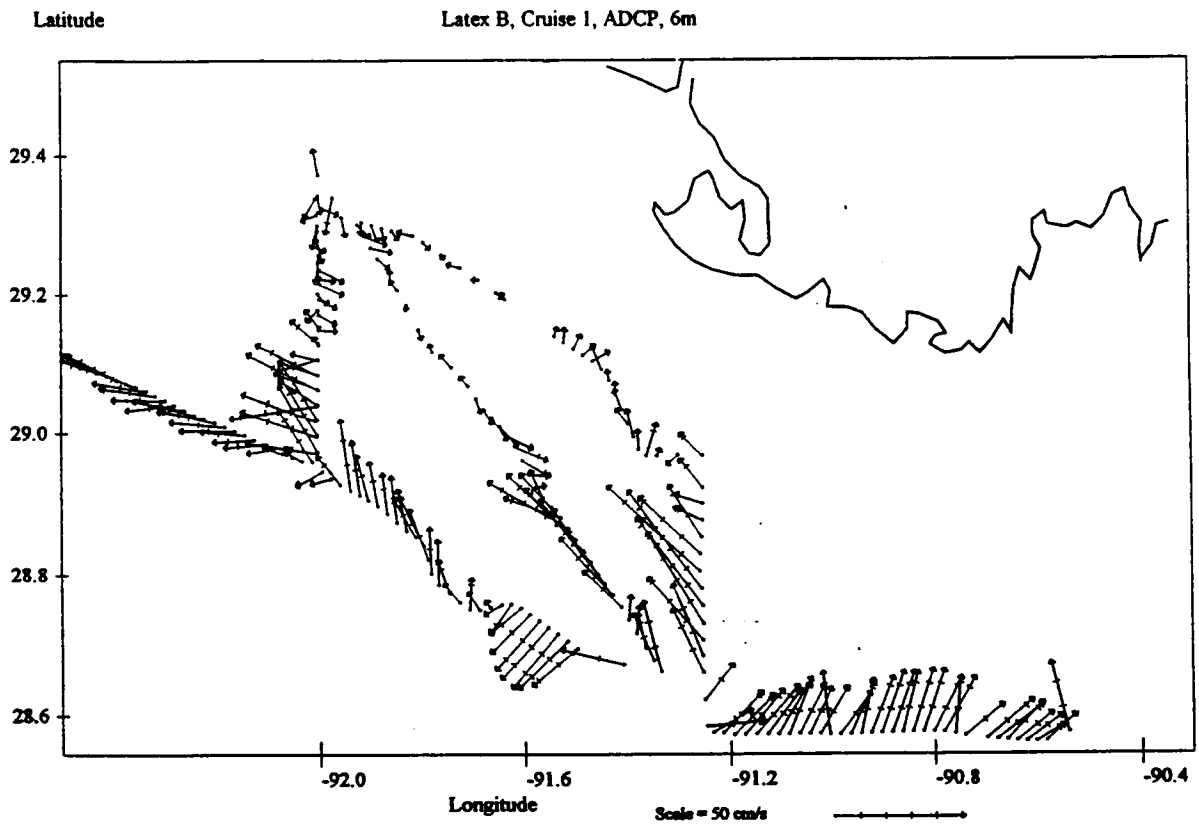
Figure 42. ADCP, 6-meter level, Sector 1.
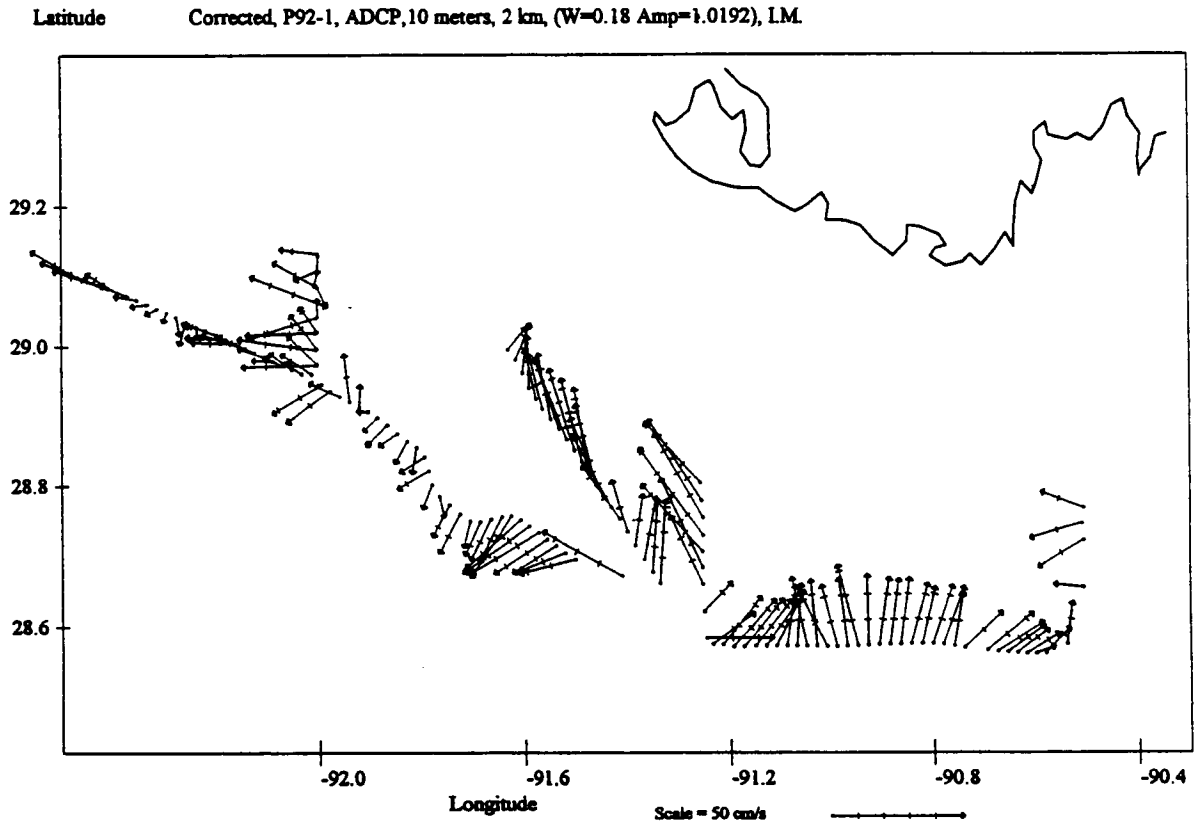
Figure 43. ADCP, 10-meter level, Sector 1.

The data at the 14 m level (Figure 44) is relatively scant, obviously caused by shallow bottom depths, but the basic flow pattern is similar to the 10 m level. It is interesting to note that all the northeastern flow coming through section T2 cannot squeeze through the short length of S2 (about 20 km) available at this depth. It must escape either by massive upwelling, downwelling or, most likely, this flow is deflected back to the northeast by the 14 m isobath headland. The southeastward outflow remains strong through T4, and its source remains unclear.

The central sector is centered at the Sabine Pass area. Figure 45 shows that the flow at S4 at the 3 m level is weak and disorganized, perhaps related to the drop-out of the southeasterly winds, which were prevalent for the previous 10 hours. S5 has degenerated into small scale flow structures with the northerly wind driving, except at its inshore end where a coherent westward current developed. There is a prevalent northward flow component at S5 against the wind stress, perhaps representing a breakdown of the coastal current into gyres of various scales under northwind conditions. The 3 m level flow at T10 appears to reflect meandering or wave-like structures.

It is surprising to note at S6 a coherent well-developed coastal current with a jet reaching 35 cm/sec in the usual location. Note that the wind (Figure 5) is strong from the northwest, in opposition to the current. Thus the driving forces for this current at S6 remain unclear. At the 6 m level (Figure 46) the flow picture remains essentially the same. At the 10 m level (Figure 47) there is good evidence for a clockwise circulation (meander or gyre) along the outer half of S5, along T6, and along the outer half of S6.

The southwestern sector extends from the Galveston Bay area southwest to line X3. The strong south-southeasterly winds of Episode V dominate the area during the cruise transect. As previously mentioned, the severe seas from the south made the ADCP data on the "into the seas" tie-line of limited use. Figure 48, the ADCP vectors at the 6 m level, shows the strong upcoast current (40-60 cm/s) at X1, X2 and X3. Section S7 south of Galveston Bay still shows the influence of Episode IV westward currents, while the vectors at S8 clearly sampled a transition period between the Episode IV and Episode V winds.

At the 12 m level (Figure 49) speeds are lower as expected, and directions are much the same as the 6 m level. Note, however, that the 12 m level currents at S8 are decidely upcoast, while the 6 m level currents are variable, indicating strong vertical shear at S8, which is absent at X1-X-3.

B. Cruise II, October 5-15, 1992 *(Curtis C. Ebbesmeyer)*

During Cruise II sections S1 through S8 were occupied as the basic grid (Figure 50). Due to a malfunction of the CTD, properties along sections S4B and S5 are not available). Five transects perpendicular to the shore were added to the basic grid and placed mid-way between sections S1 and S2 (Section S1B), S2 and S3 (Section S2B), S3 and S4 (Section S3B), S4 and S5 (Section S4B), and S5 and S6 (Section S5B) to provide higher resolution along the shore. In addition, to provide as short a synoptic time interval as possible, a longshore transect was added at the end of the cruise approximately along the 15-meter isobath (home leg) in which only parameters from the ADCP and MIDAS were sampled.

Also sampled during Cruise II were a plume off Calcasieu Lake and a front comprised primarily of salinity and secondarily of temperature variations. Descriptions of the plume and front are contained in Appendix B.

For clarity and later reference, the dates, times, and station numbers of the thirteen sections normal to the shore are provided in Table 2. The dates of the cruise reflect the interval
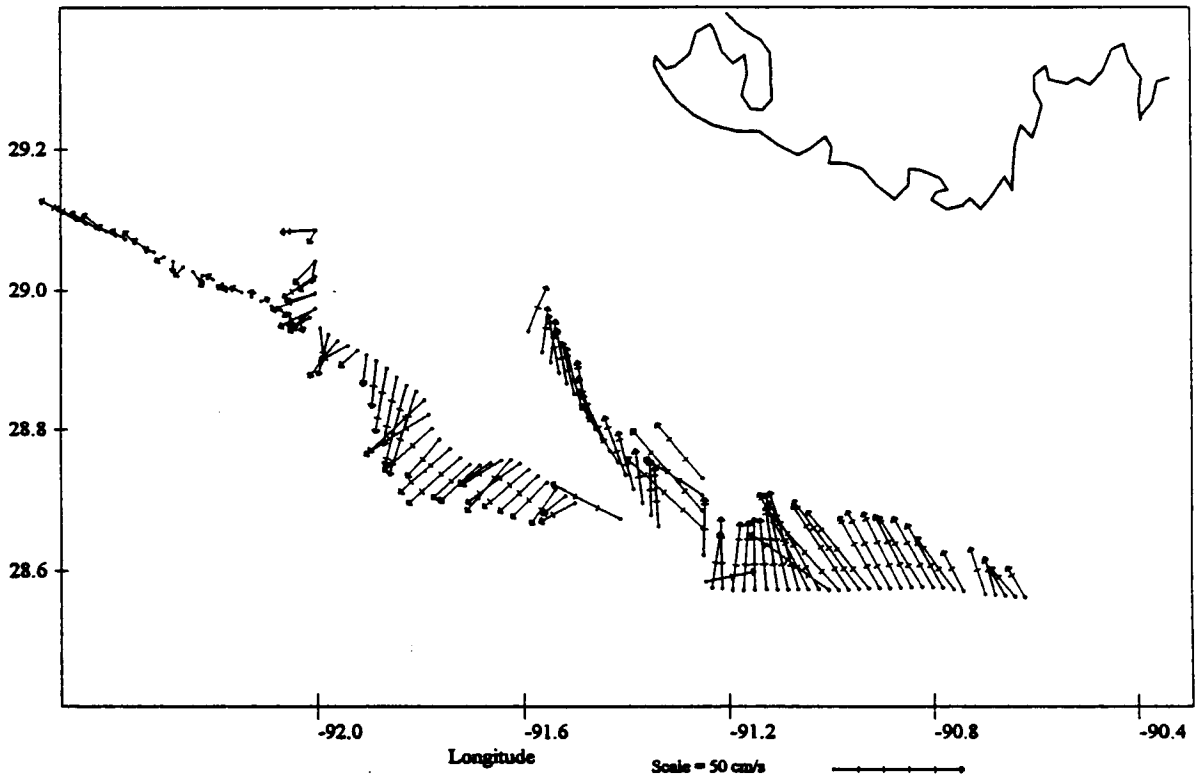
Figure 44. ADCP, 14-meter level, Sector 1.

56
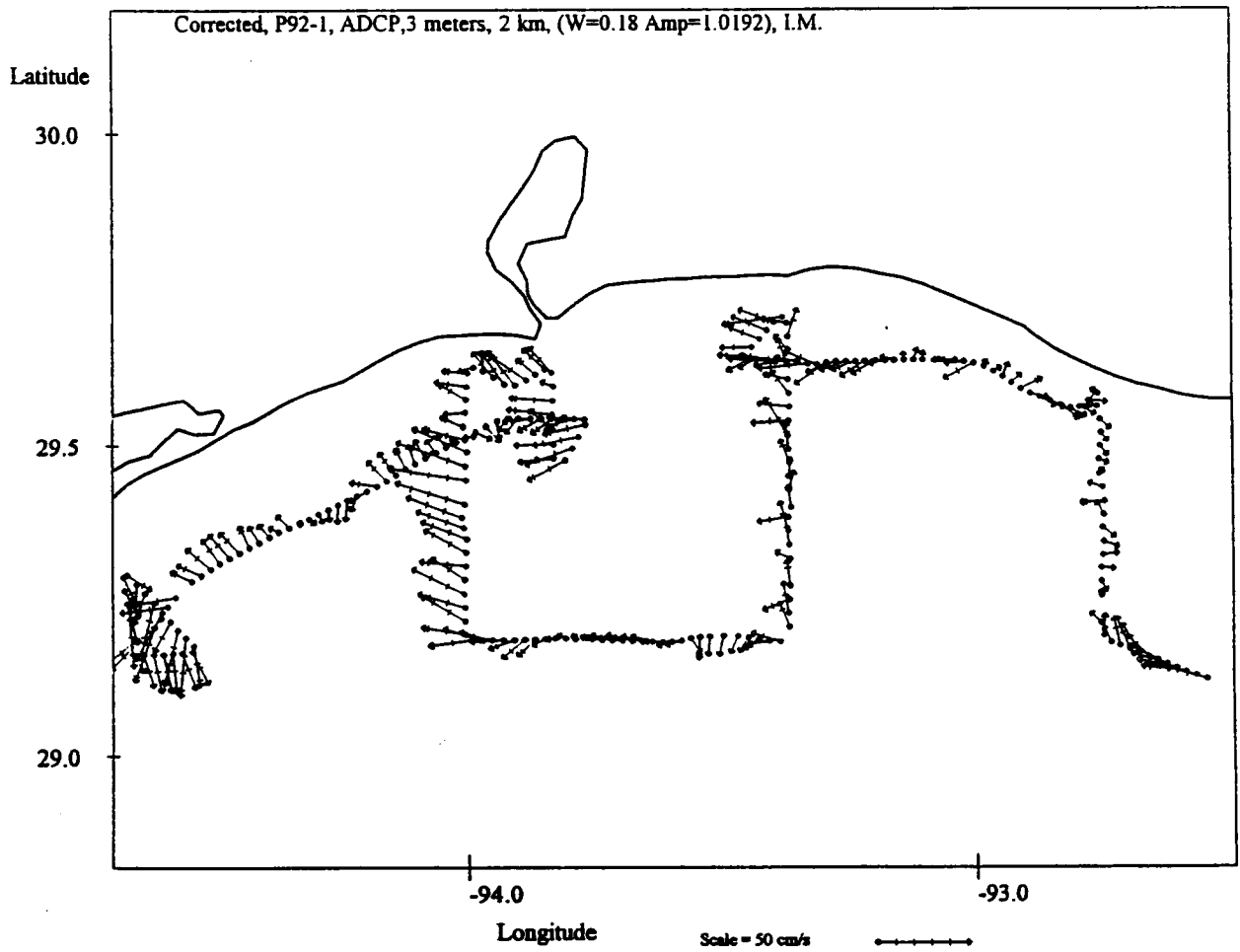
Figure 45. ADCP, 3-meter level, Sector 2.
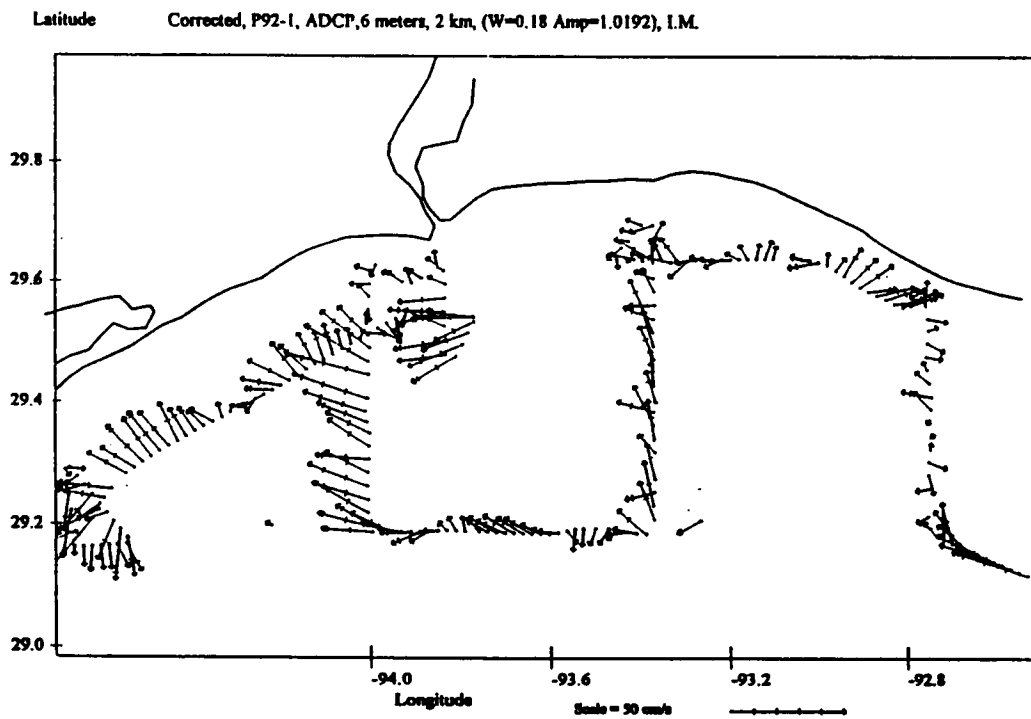
Figure 46. ADCP, 6-meter level, Sector 2.

58
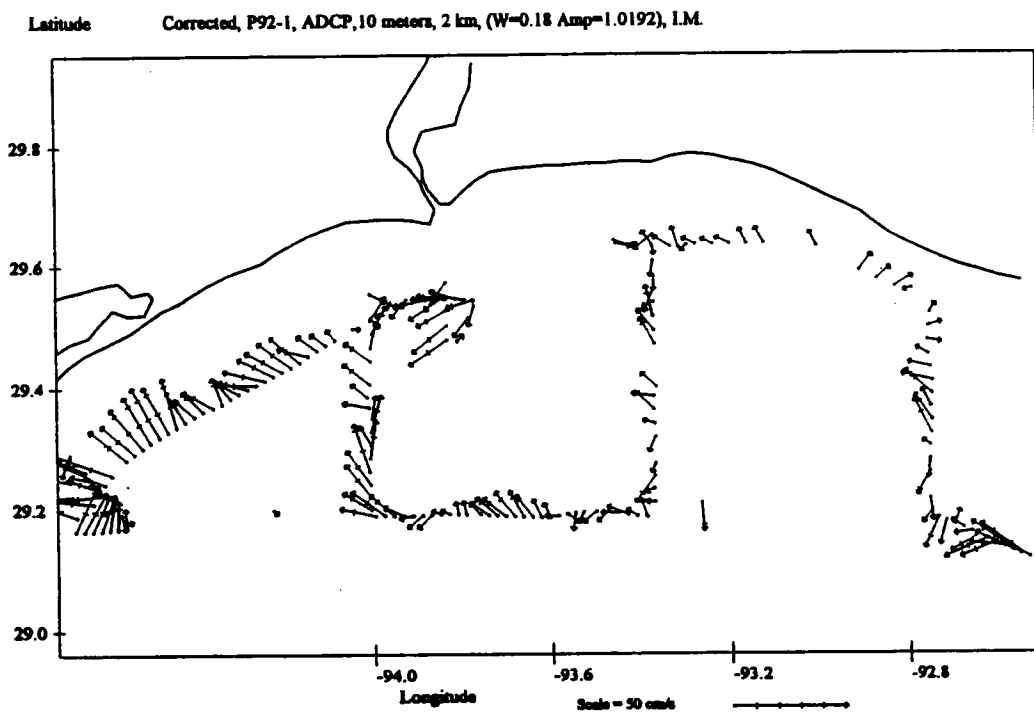
Figure 47. ADCP, 10-meter level, Sector 2.
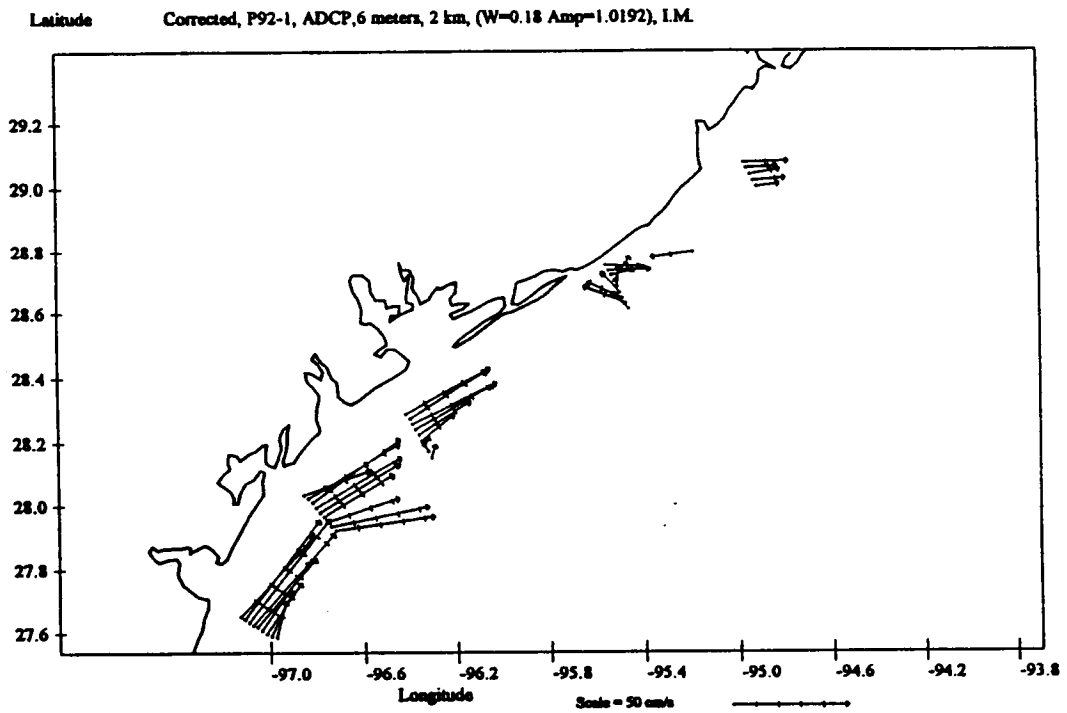
Figure 48. ADCP, 6-meter level, Sector 3.
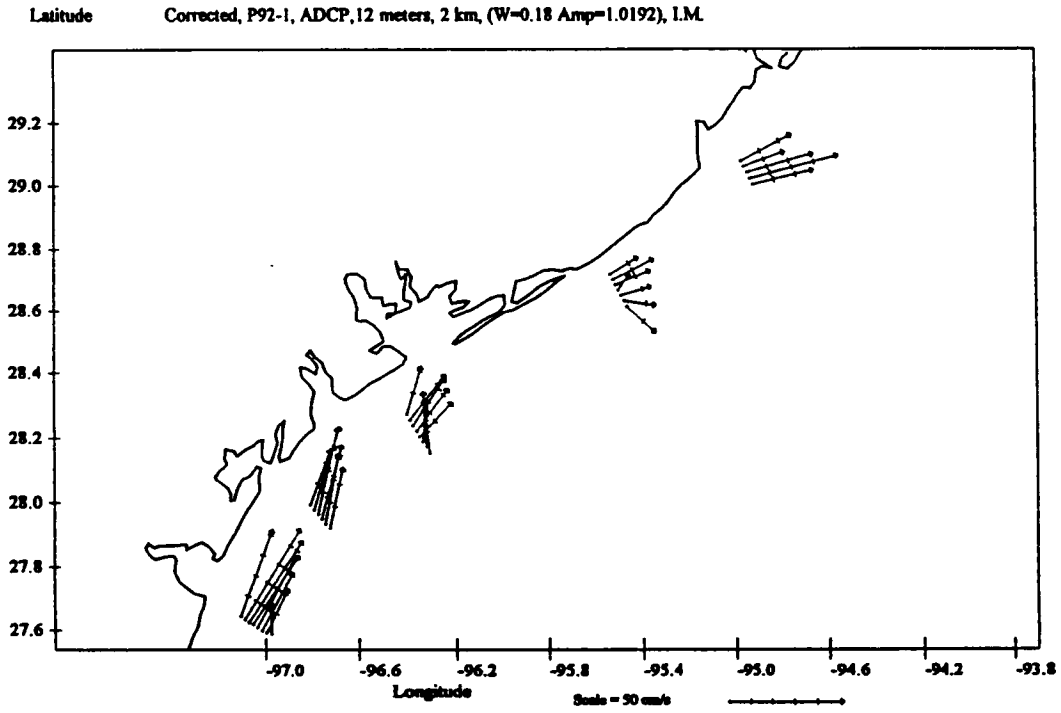
Figure 49. ADCP, 12-meter level, Sector 3.

Latex B, Cruise 2
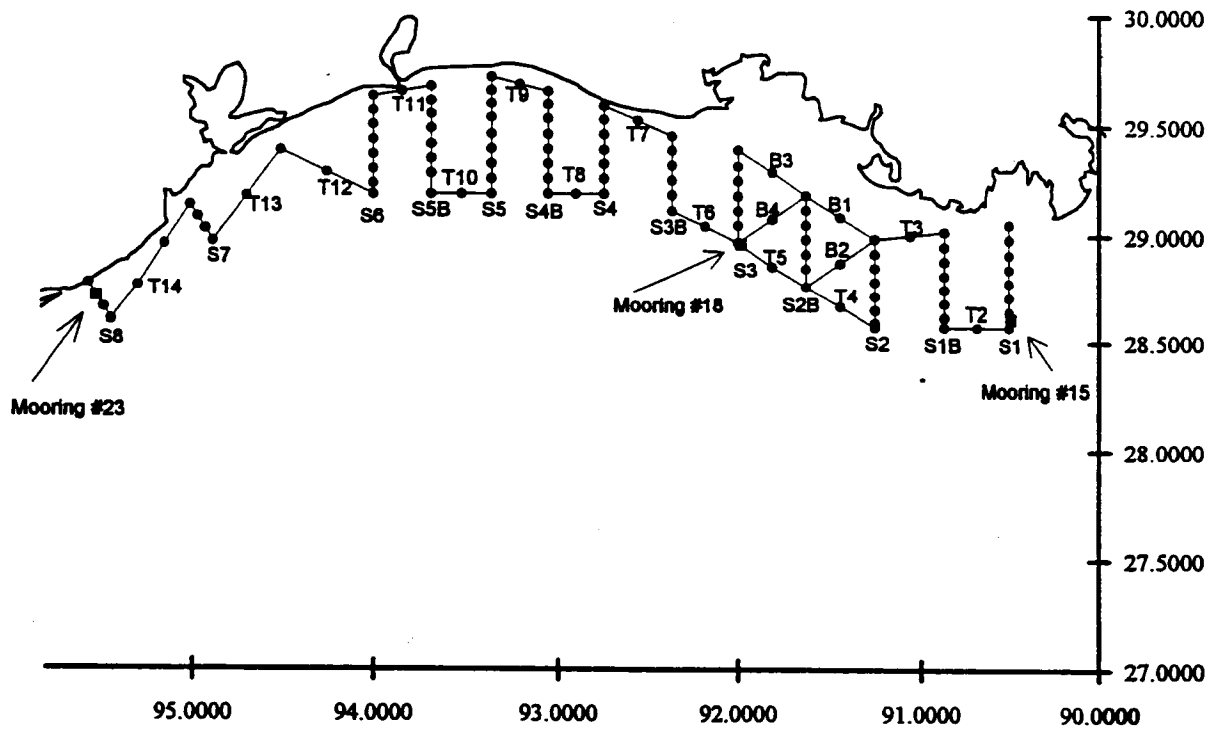
Figure 50. Map showing section designations (S1-S8; T2-T-14) of Cruise II.

over which the R/V *Pelican* was away from the LUMCON dock. Intervals required for the sampling are as follows: the synoptic interval required to occupy the thirteen stations was 6 October 0918Z through 13 October 0351Z, or a 6.77-day time interval; and the interval required for the return leg along the 15 meter isobath was approximately fourfold shorter, or 1.81 days.

Table 2. Dates, times, and station numbers of the thirteen sections made approximately perpendicular to the shore, as well as the home leg.

Section No.	Date (October)	Inshore Station		Offshore Station	
		Time	Station	Time	Station
S1	6	0918	101	2032	107
S1B	7	0639	117	0124	110
S2	7	1014	119	1539	125
S2B	7-8	0034	133	1949	127
S3	8	1835	145	1250	139
S3B	9	0952	155	0719	151
S4	9	1412	158	1956	164
S4B*	10	0430	173	0015	166
S5	11	0246	175	1004	183
S5B	11	2026	192	1322	185
S6	11-12	2332	194	0546	201
S7	12	1843	208	1604	205
S8	13	0351	214	0114	211
Home Leg	13-14	0205(13)	2130(14)		

*CTD malfunctioned; parameters from ADCP and MIDAS only.

1. Cruise Data

a. Satellite Images. *(Nan D. Walker, Oscar K. Huh, and Lawrence J. Rouse, Jr.).*
Satellite imagery obtained on October 3, 4, and 5 were analyzed and provided as color prints and GIF files prior to cruise departure. Analyses of additional imagery (October 6, 11, and 13) were faxed to the ship to assist in decision-making and to enable locating a front to be sampled in the vicinity of Atchafalaya Bay.

The October 1992 cruise was preceded by several days of exceptionally strong winds from the northeast. The main culprit for these winds was a tropical depression that moved north from the Yucatan region into the northern Gulf of Mexico. The highest wind speeds (12-16 m/s measured at Southwest Pass, Louisiana) occurred on October 2 and 3 due to the strong pressure gradient that developed between the northward moving low pressure system and a high pressure system over the east coast. As a consequence of the abnormal wind forcing, a Mississippi River jet-like plume feature was forced southwestward along the Louisiana shelf. The imagery clearly revealed that the plume consisted of cold Mississippi River water, as well as chilled inner shelf water from both the east and west sides of the Balize delta region. The relatively cold waters were "trackable" as a distinct plume feature using SST information. The satellite image of October 5 (Figure 51) clearly reveals the spatial extent of this plume feature and its source regions.

A semi-submersible drilling platform situated in 500 meters of water within the Mississippi River Canyon, owned by Ensearch Corporation, encountered severe difficulties caused by exceptionally strong currents from October 2 through 4. Although they were unable to obtain current measurements, the rig's personnel estimated peak current speeds at 3 to 4 knots
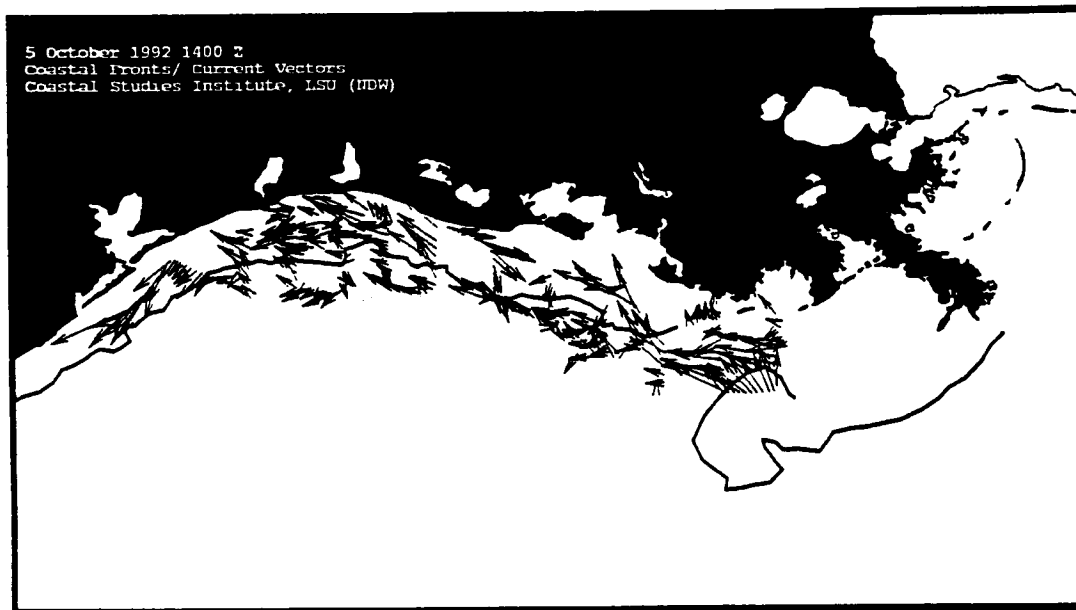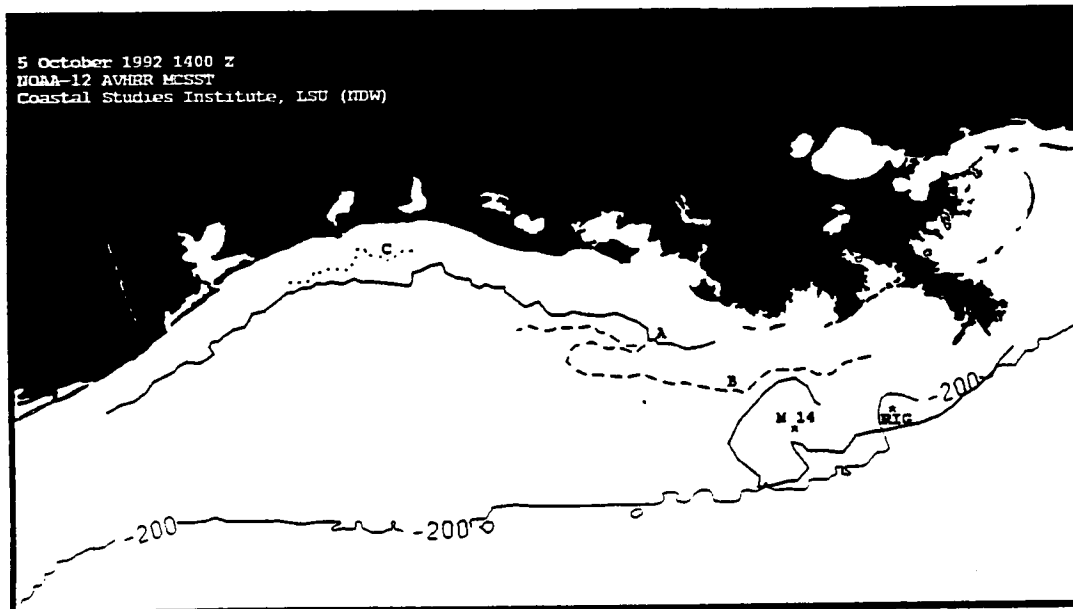
Figure 51. SST fronts as observed in the satellite image of October 5, 1992 (1400 Z). (a) The main SST front is depicted with a solid line (A) and less intense SST fronts with broken lines (B,C). Locations of the LATEX A mooring 14 and the Ensearch drilling rig are shown. (b) Selected ADCP current vectors are superimposed on the thermal fronts.

(Dennis Cox, Ensearch Corporation, pers. comm.) and reported that "the rig appeared to be under tow" (Terry Prater, Ensearch, Inc., pers. comm. to Dr. Murray Brown, Minerals Management Service) Current measurements 11 meters from the surface, from the LATEX A mooring # 14 (28.38 N, 90.49 W; Figure 56), revealed that westward currents exceeded 50 cm/s from October 2 through 5 and that maximum flow of 100 cm/s occurred on October 3 (Figure 52). The strongest currents lagged peak wind speeds by several hours. The satellite images of October 4 and 5 suggest that a narrow jet-like current converged on the drilling rig within the canyon. Thus, it is highly possible that their estimates of 3-4 knot surface currents were not far from reality. Both temperature and salinity were substantially reduced on October 3 as the plume front moved past the mooring. Temperature at 11 meters decreased from 27.2° C to 26.2° C (Figure 52), and salinity decreased from 33 to 22 ppt (Figure 52). The data suggest that the top 11 meters were virtually isothermal as the satellite temperatures were within 0.3° C of those measured at Mooring 14.

Comparison of Satellite Imagery and Cruise Data. The LATEX B cruise traversed the northern margin of the plume feature on S1 and T2 (Figure 50). The Mississippi plume feature was detected along S1 in both the salinity and temperature sections. Noticeable reductions in both salinity and temperature occurred at the outer two stations along S1. The cruise measurements suggest that the plume feature extended to at least 22 meters depth. The imagery suggests that buoyant spreading of plume water occurred shortly after it crossed back onto the shelf from the canyon region. Selected ADCP near-surface (4 meter) current measurements are superimposed on the satellite image data of 5 October 1400 Z in Figure 51. Currents along S1 were westward until the northern margin of the plume was crossed, when they changed to northwestward and northward. North and northwest currents were observed all along T-2.

On the inner shelf, the SST imagery of October 5 and 6 revealed the presence of cooler water close to the coast, warmer water offshore, and a series of SST fronts separating the water masses of contrasting temperature (Figures 51, 53). The cooler inshore water owed its origin primarily to early season cold-air outbreaks, which effectively remove heat from the shallow depth-limited coastal waters first (Huh, et al., 1984). River discharge could have also contributed to the presence of the cooler water along the coast. A relatively strong and continuous front (Figure 51) was observed, in close proximity to the 12-meter contour, extending along the inner shelf seaward of Atchafalaya Bay westward to Galveston Bay. This main SST front was situated between 30 and 40 kilometers from the coast (Figures 51, 53). The surface temperature structure across the inner shelf on October 6 is shown in Figure 53, where SST profiles have been extracted along S3 and S4. The SST front along S3 was more intense, measuring about 1° C in 2 km or 0.5 C/km (Figure 53). Temperatures ranged from 23.4° C inshore to 24.4° C on the seaward side of the front. The cool water zone extended further offshore in the vicinity of Atchafalaya Bay where freshwater is continually discharged (albeit slowly during October 1992) onto the shelf and this zone narrowed towards the west. A weaker SST front was observed seaward of the main Atchafalaya front (Figure 53), however, it was seaward of the cruise track. A secondary inner shelf front (Figure 53) was observed west of Atchafalaya Bay between Calcasieu and Sabine, inside of the main coastal front.

It is of interest to compare the near surface currents with the locations of SST fronts within the cruise area. Along lines S1 through S2B, the strongest westward currents were located in close proximity to the main SST front on the landward side. Along line S2B, two zones of accelerated currents were noted, each associated with an SST front. Surface currents southwest of the entrance to Atchafalaya Bay were weaker than those to the east or west, even though the SST front was continuous along the coastline. This observation may be attributable to passage of a weak cold front on October 8 that could have temporarily disrupted westward surface flow. West of Atchafalaya Bay (from S4B to S5B), the strongest surface currents were located closer to the coast and, generally, inside of the main SST front. The image of 11 October 2100 Z (Figure 54) is more appropriate for comparison with data collected during the latter half
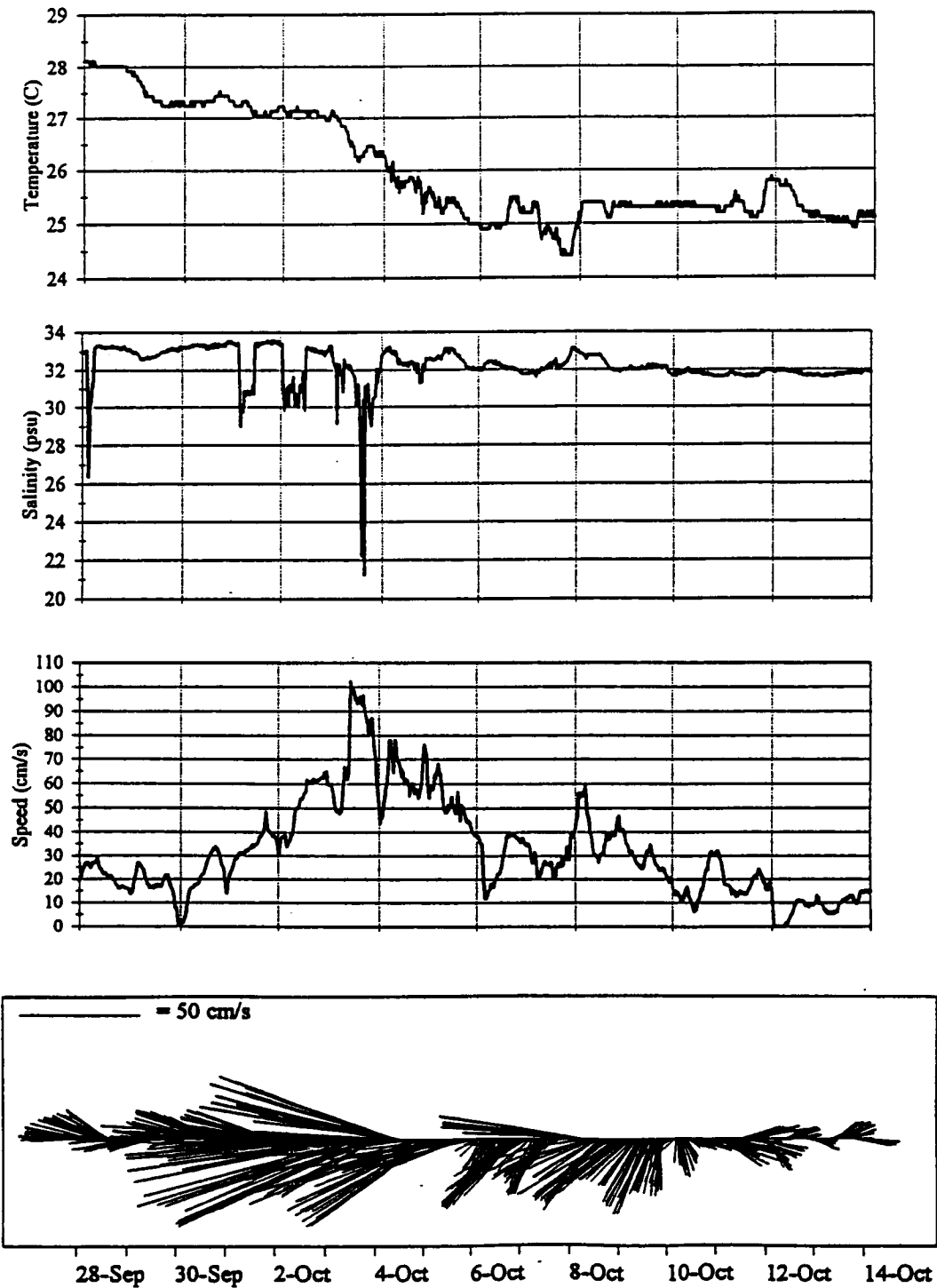
Figure 52. Time series measurements at the LATEX A Mooring 14 at 11 meters water depth (coutesy of Texas A&M). (a) Water temperature (C). (b) Salinity (psu). (c) current speed (sm/s). (d) Current vectors for the time period September 28 through October 13, 1992.
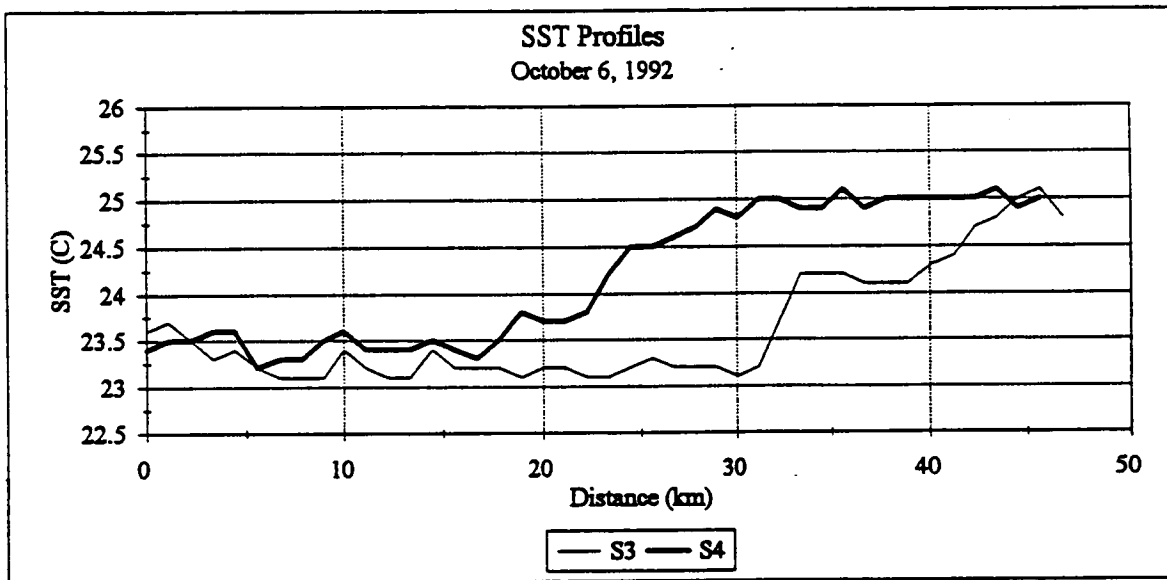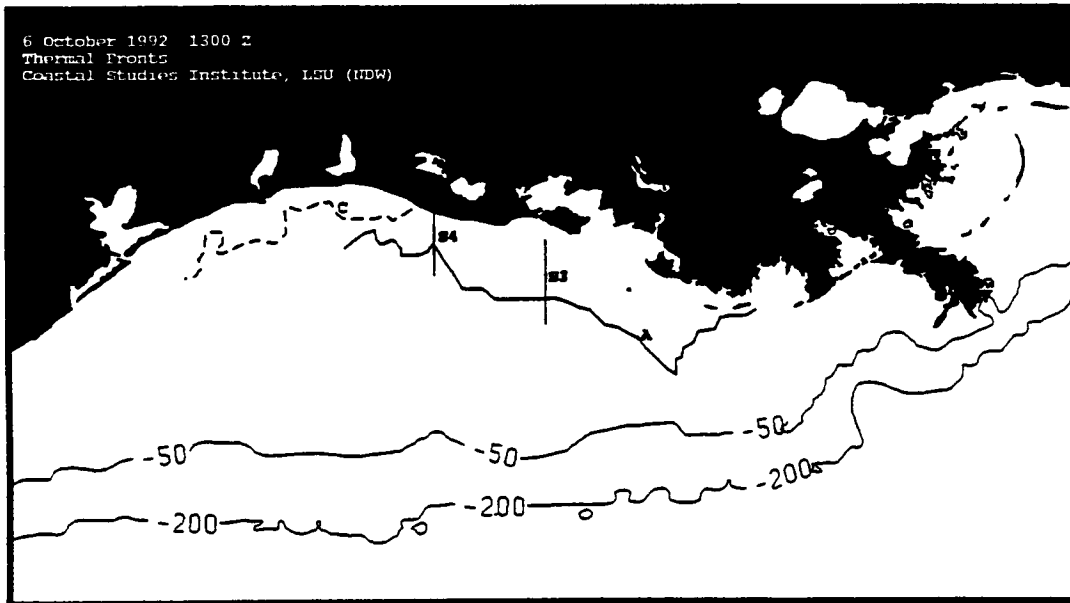
Figure 53. (a) Major (A) and minor (C) SST fronts as observed in the satellite image of October 6, 1992. (b) Surface temperatures extracted along S3 and S4.
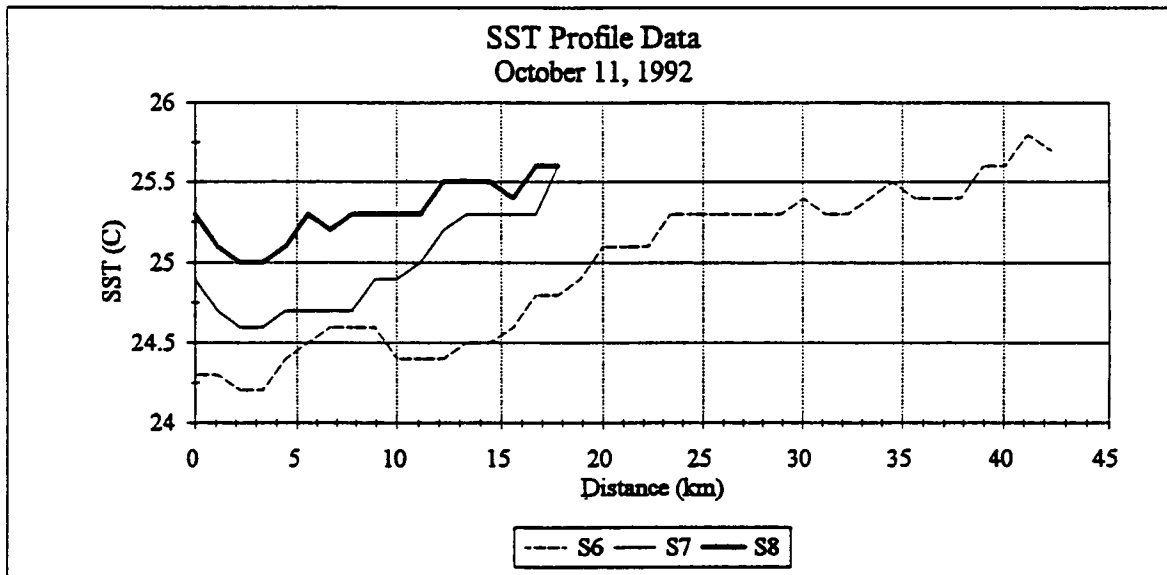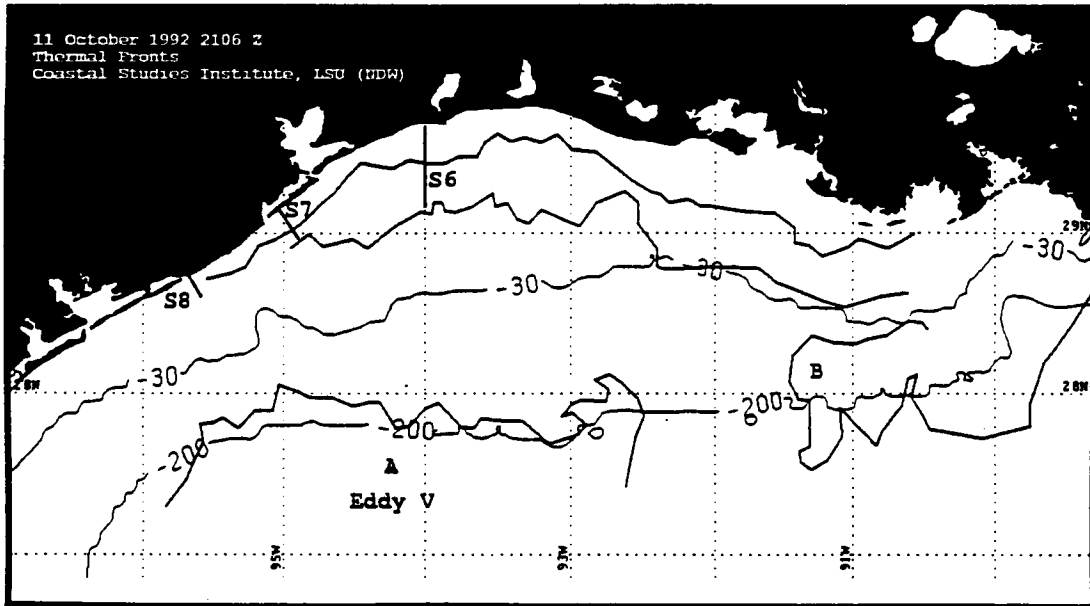
Figure 54. (a) SST fronts and oceanographic features as observed in the satellite image of October 11, 1992. (b) Temperatures extracted along S6, S7, and S8.

of the cruise. It was acquired while the ship was measuring along S6. It reveals a close correspondence between the main SST front and southwestward currents in the nearshore zone. Moving south along the Texas coast, the SST front approached the coast and diminished in intensity (Figure 54).

On the regional scale, a large warm-core Loop Eddy, Eddy Vasquez, was influencing shelf circulation during this cruise. In Figure 54, the northern edge of this eddy is depicted. Several clear-sky images were obtained from October 11 to 13 revealing the complexities of circulation within the LATEX region. Whereas inner shelf waters moved towards the west, surface flow on the outer shelf and slope and parts of the mid-shelf region were primarily eastward, as a result of the Eddy's influence on circulation. Animation of the image sequence revealed the existence of a prominent convergence zone northeast of the Eddy, from the mid-shelf region to the outer shelf region. This convergence zone forced the Mississippi plume (Figure 54, B) to mushroom out towards the north-northwest rather than continue on its westward course. The movement of plume water towards Atchafalaya Bay may have intensified fronts and currents in the region.

The suspended sediment concentrations obtained during the cruise are compared with atmospherically corrected satellite reflectance values in Figure 55. The satellite image of October 11 (Figure 54) revealed that the highest concentrations of suspended sediment were in the shallow nearshore regions seaward of Atchafalaya Bay, between Calcasieu and Galveston Bay, and from Matagorda Bay southward. The surface water samples collected and analyzed for suspended sediments revealed a similar distribution pattern, however, at a much coarser spatial resolution (Figure 55). During the cruise, the highest measurement of suspended sediment (48 mg/l) was obtained at the inshore station on S2 (Figure 54), which corresponded well with the zone of highly turbid water south of Point Au Fer island (Figure 55). The next highest values for the cruise were obtained at S2-3 (24 mg/l) and S3-1 (22 mg/l) (Figure 55). At the seaward ends of most lines, suspended sediment had dropped down to 5 or 6 mg/l. Results of Walker, et al. (1992) showed that much of the suspended sediment seaward of Atchafalaya Bay often results from wind resuspension of previously discharged river sediments. This may have been the case on October 11 as winds increased with passage of a cold front over the cruise area.

Before proceeding, the ~1.1 kilometer pixel resolution of the satellite sensors, the ~5 km resolution of the CTD stations, the 0.4 km resolution of the ADCP ensembles, and the 12-second averages of the MIDAS system should be considered. The ADCP resolution is approximately twice that of the satellite sensors. Furthermore, the flow structure in the satellite images are not resolved by the CTD stations, but are resolved by the ADCP and MIDAS records.

b. Winds. Surface winds (approximately 10 meter elevation) over the survey area were prepared using observations from the anemometer aboard the R/V *Pelican* corrected for vessel motion (Figure 56).

During most of the survey winds blew from the east at speeds averaging approximately 5 m/s. Exceptions to this condition occurred during sections S2B-S5 when winds were variable.

c. Sea Surface Temperature. Sea surface temperatures from MIDAS are contoured in Figure 57. Observed temperatures vary from a low of 23.2°C in the Atchafalaya outflow at the northernmost station of Section S3B, to a high of 24.8°C at the southernmost station of Section S5B. Colder, less saline water flowing along and nearest the coast can be distinguished by the 24°C isotherm coinciding approximately with the 28.5 psu salinity contour.

d. Sea Surface Salinity. Sea surface salinity from MIDAS is contoured in Figure 58. Salinities vary from a low of 23.0 psu off Marsh Island, to a high of 33.0 psu at the southern end of Section S5B (note that this high salinity feature is coincident with that observed during Cruise
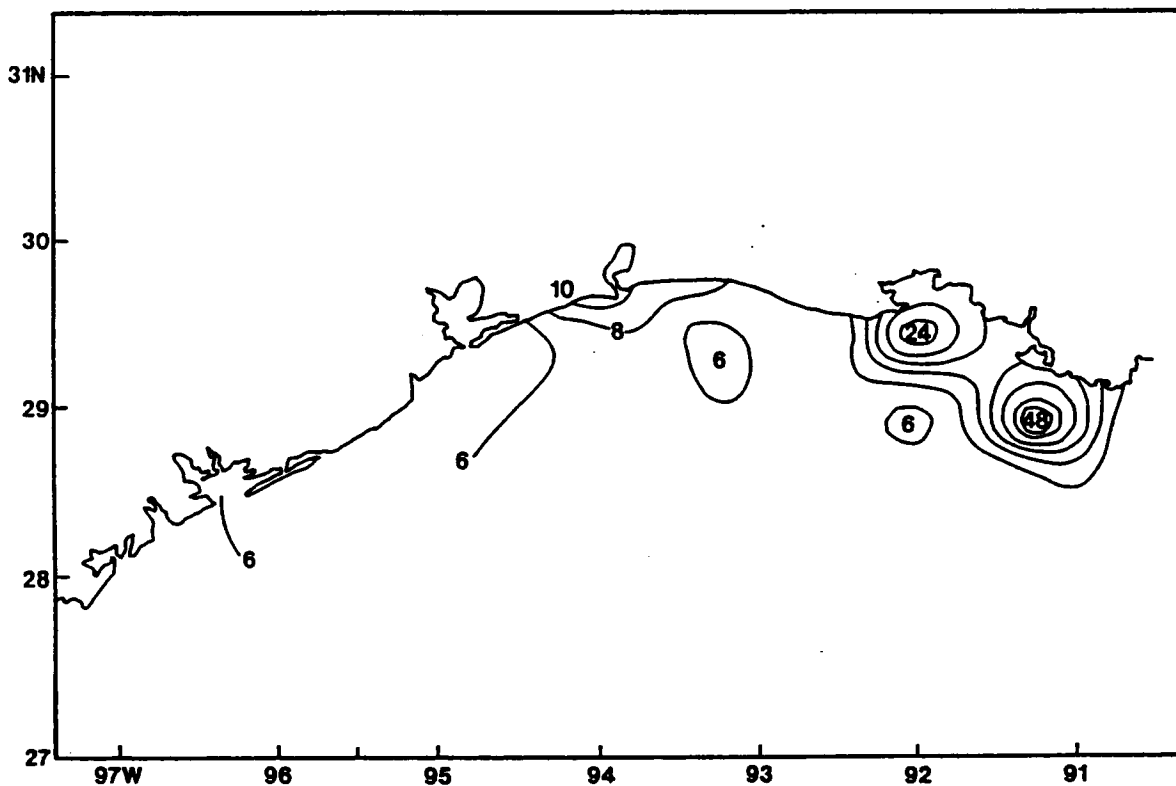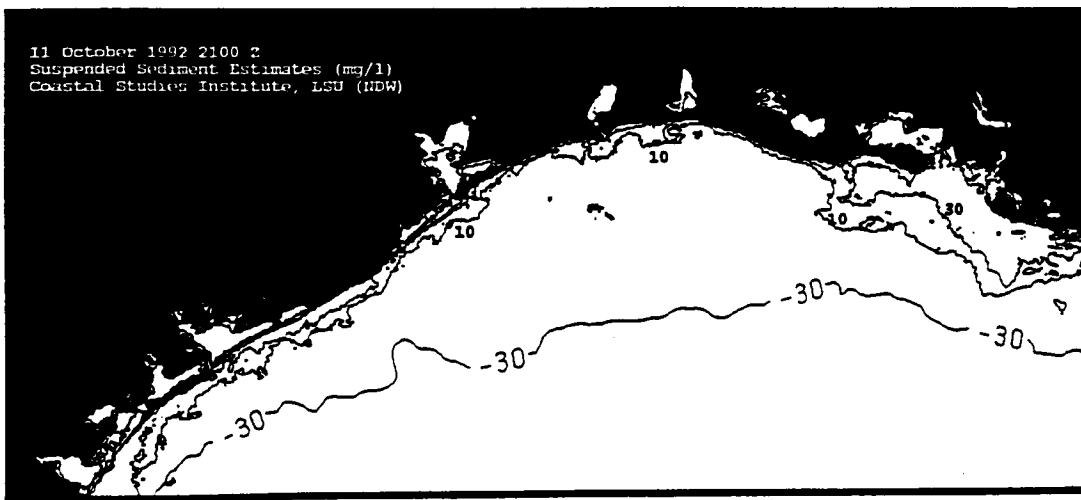
Figure 55. (a) Contour map of suspended sediment concentrations (mg/l) constructed from surface samples obtained during the cruise. (b) Surface suspended sediment estimates (mg/l) for October 11, 1992 (2100Z) derived from NOAA-11 reflectance data.

Latex B, P92-2, MIDAS, Winds
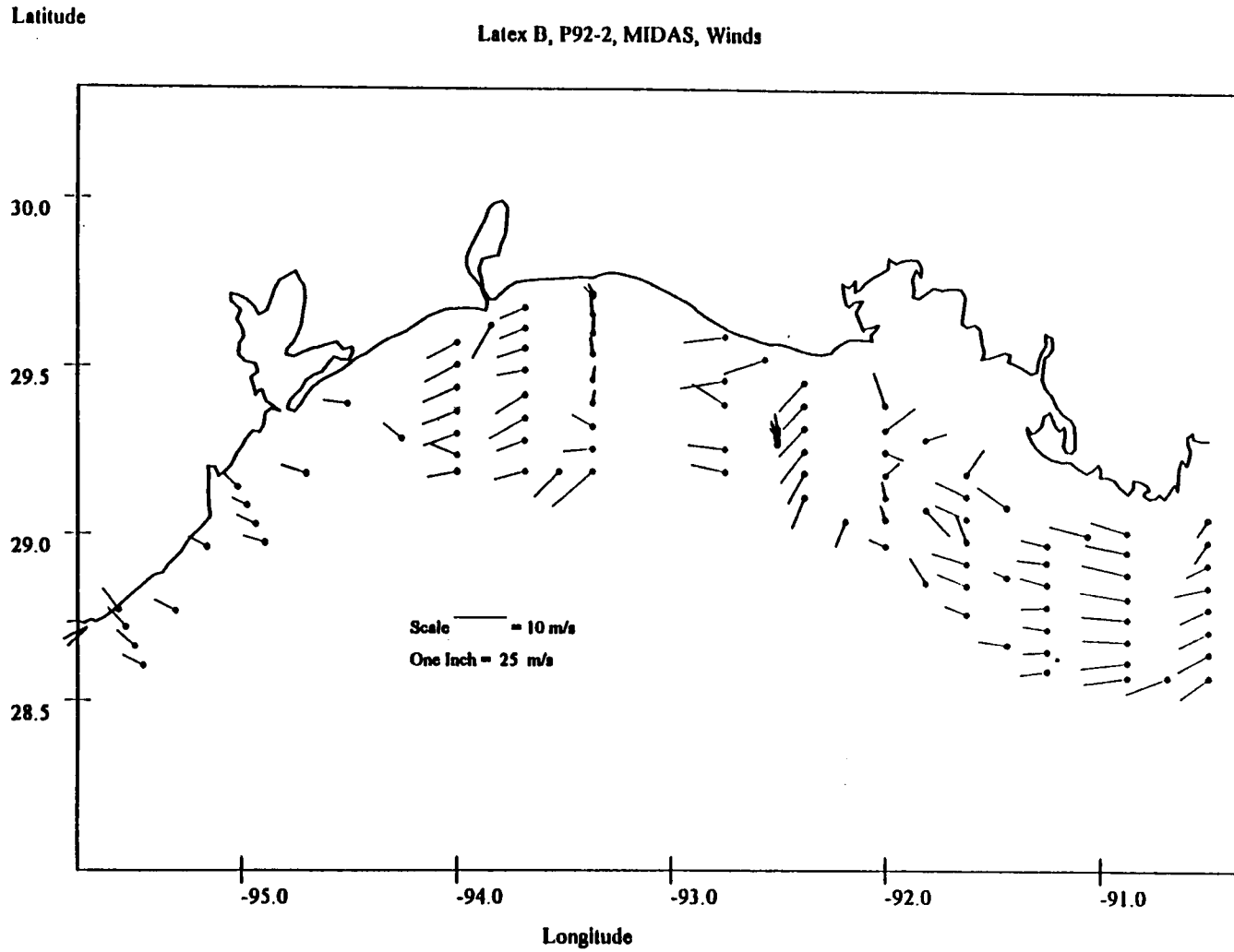
Figure 56. Map of wind vectors from MIDAS during Cruise II, October 5-15, 1992.
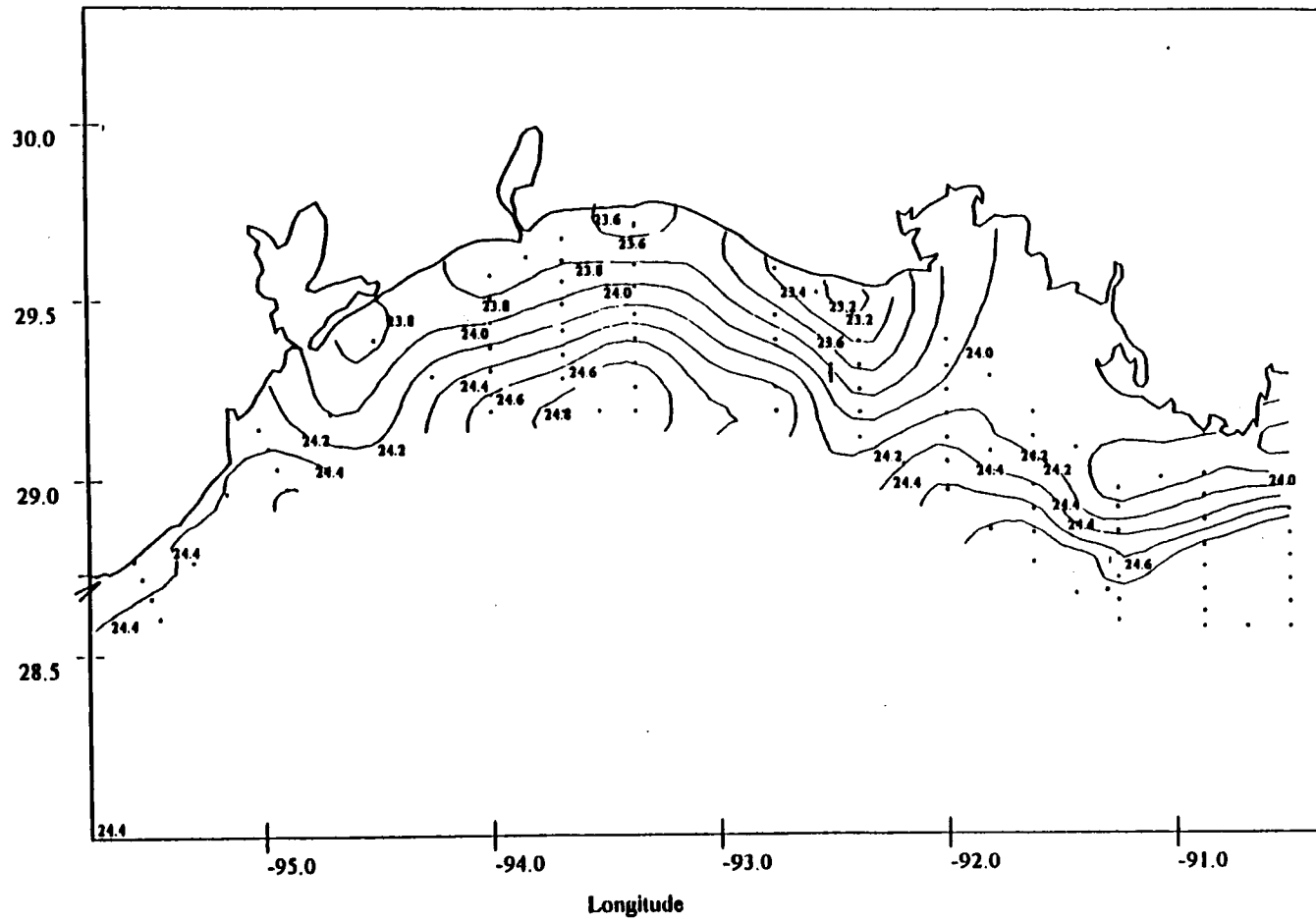
Figure 57. Map of sea surface temperature from MIDAS, Cruise II.

Latex B, P92-2, MIDAS, Salinity
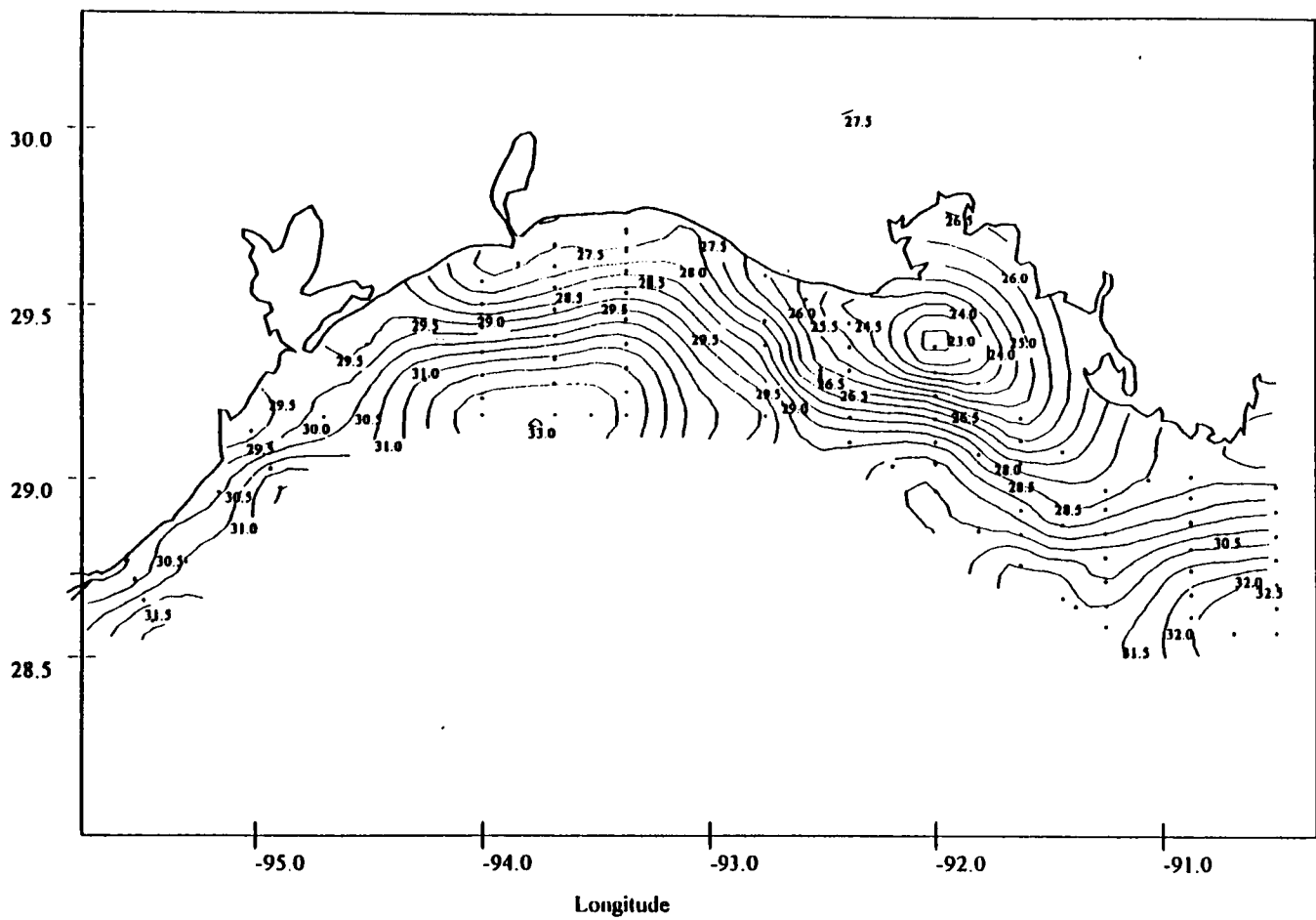
Figure 58. Map of sea surface salinity from MIDAS, Cruise II.

I). The less saline water exiting the Atchafalaya can be circumscribed approximately by the 28.5 psu contour. This contour extends parallel to the coast westward to approximately Sabine Lake. Midway between Sabine Lake and Galveston Bay, the 28.5 psu contour intersects the coast.

e. Coastal Currents. Currents along the coast were examined using maps of the current vectors from the 4-meter ADCP depth bins and time series from moored current meter records. Current vectors from the 4-meter depth ADCP bin along the cruise track are shown in Figures 59-62 (these vectors have been corrected using calibrations made at the beginning and end of Cruise II). Inspection of Figures 59-62 shows the generally westerly flow prevailing during the survey.

Overlaying these vectors on satellite thermal images amplifies the discussion given earlier to major oceanographic features. The effects of two filaments are evident (Figure 59). Along Section T2 between sections S1 and S1B, flow induced by the plume from the Mississippi River may be evident. Along Section T5 westerly currents indicate a filament between sections S2B and S3.

The transition in the flow occurring off Galveston Bay is shown by ADCP vectors along the home leg (Figure 62). To the east of Galveston Bay the current vectors are variable in direction and of lesser magnitude than those to the west. Superposing the home leg ADCP vectors on satellite images for October 11 and 13 suggests that Eddy Vasquez may approach closest to shore in the vicinity of the transition.

f. Moored Current Meters. As the coastal maps provide an overview of the study area, the time series from the current meters provides an overview of the survey's temporal domain. Locations of current meter moorings where usable data were obtained, superposed on the track of Cruise II are shown in Figure 50. Data from five current meters on three moorings near three sections were available, as follows: Mooring 15 (depths of 10, 24 meters) near Section S1; Mooring 18 (depths of 10, 21 meters) near Section S3; and Mooring 23 (depth of 9 meters) near Section S8.

Of the five time-series available, four are reasonably complete, and one (Mooring 15, depth of 10 meters) is missing for approximately half of the survey. Fortunately, at the time that the sections nearest the moorings were occupied, data were available.

Fortunately, the current meter data embrace the sections sampled during Cruise II (sections S1-S8). Though widely spaced, these three moorings illustrate differences between major segments of the cruise. At Mooring 15 (24 meters depth), near Section S1 at the eastern boundary of the cruise track the currents were episodic with mean speeds generally less than 10 cm/s. At Mooring 18 (21 meters depth), near Section S3 the currents were also episodic with mean speeds generally less than 10 cm/s. The episodic nature of the currents evident at moorings 15 and 18 was absent for the most part at Mooring 23 (9 meters depth), near Section S8 at the western end of the area surveyed. At this site the flow was, for most of the time, directed toward the southwest at speeds of approximately 10 cm/s.

2. Flow and Water Properties along 13 Sections

Characteristics of water flow and mass were described section-by-section based on contours of temperature, salinity, density and velocity components from CTD and ADCP profiles. The CTD profiles used to construct contours of temperature, salinity, and density are spaced at intervals of ~7.5 kilometers, whereas the ADCP ensembles represent averages of velocity over approximately 400 meters vessel trajectory (at typical vessel speeds of 6.5 knots, two minutes of time is equivalent to approximately 402 meters of horizontal distance). For example, if CTD stations are spaced 5 kilometers, approximately 12 ADCP ensembles will have
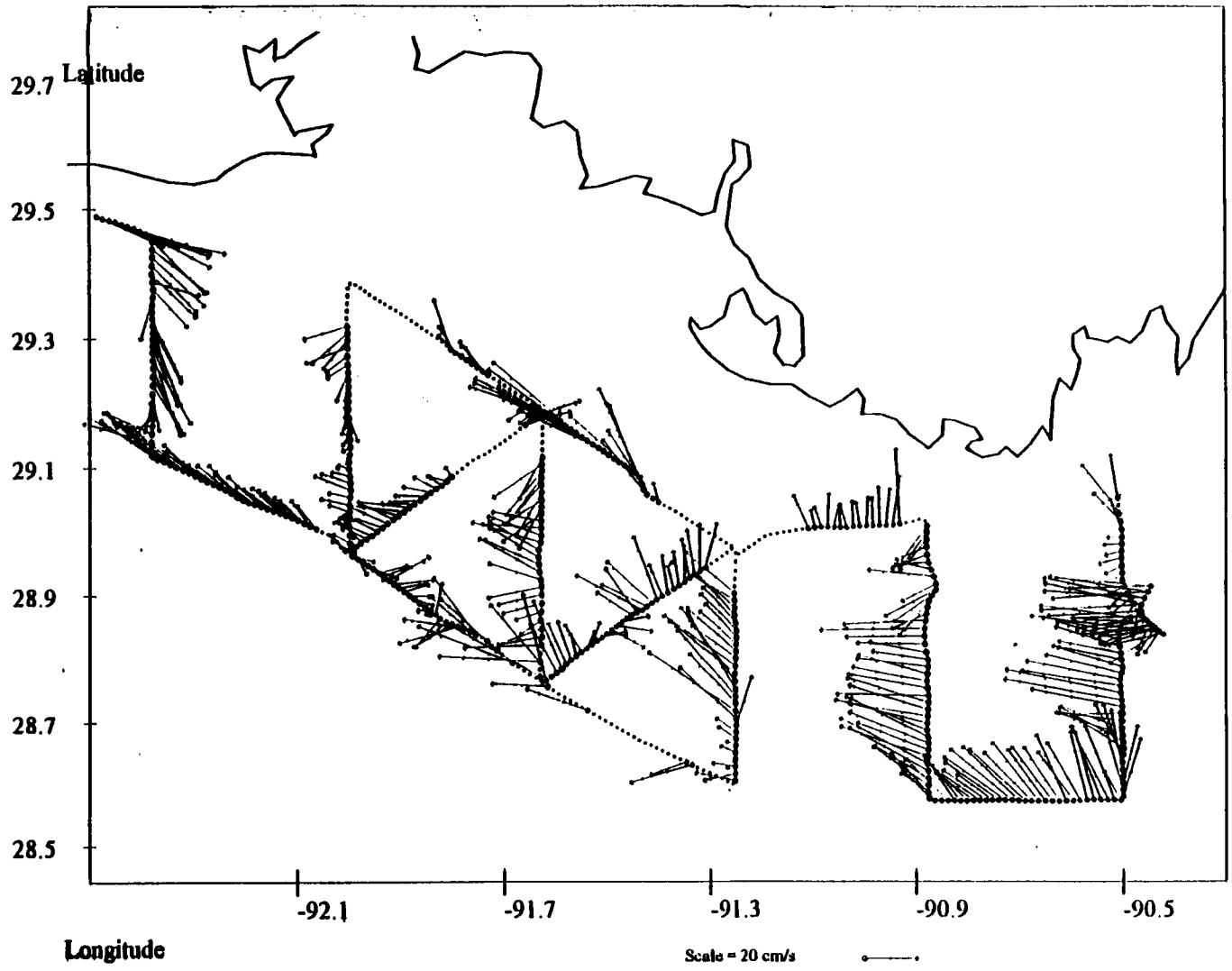
Figure 59. ADCP current vectors at 4-meter depth along sections S1-S3B.

Corrected, P92-2, ADCP, 4 meters, .5 km, (W = 0.4510   Amp=1.0103), Iterative Method

Latitude

30.1

29.9

29.7

29.5

29.3

29.1

28.9

-94.5   -94.1   -93.7   -93.3   -92.9

Longitude

Scale = 20 cm/s
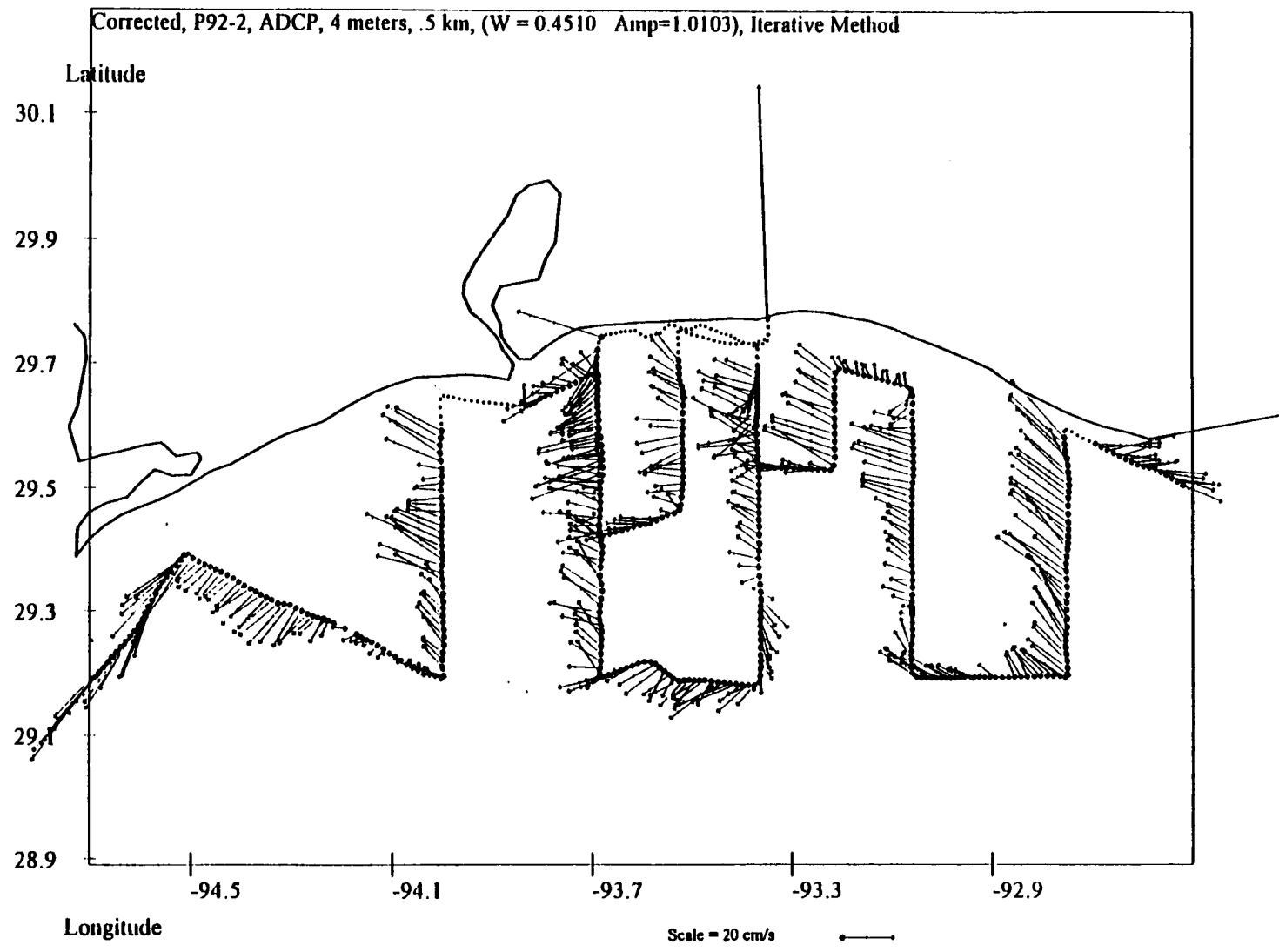
Figure 60. ADCP current vectors at 4-meter depth along Sections S4-S6.

Corrected, P92-2, ADCP, 4 meters, .5 km, (W = 0.4510 Amp=1.0103), Iterative Method

Scale = 20 cm/s
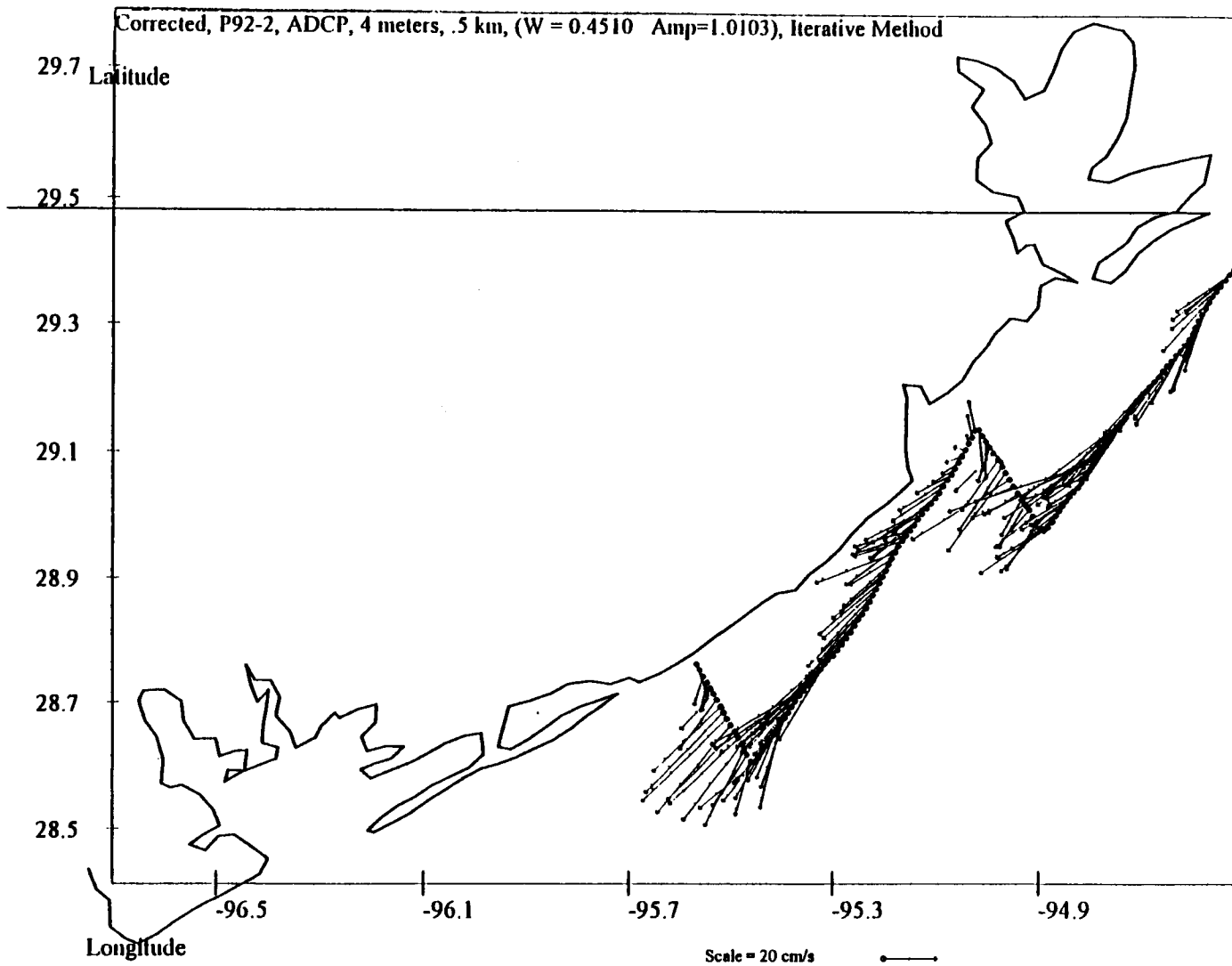
Figure 61. ADCP current vectors at 4-meter depth along Sections S7-S8.
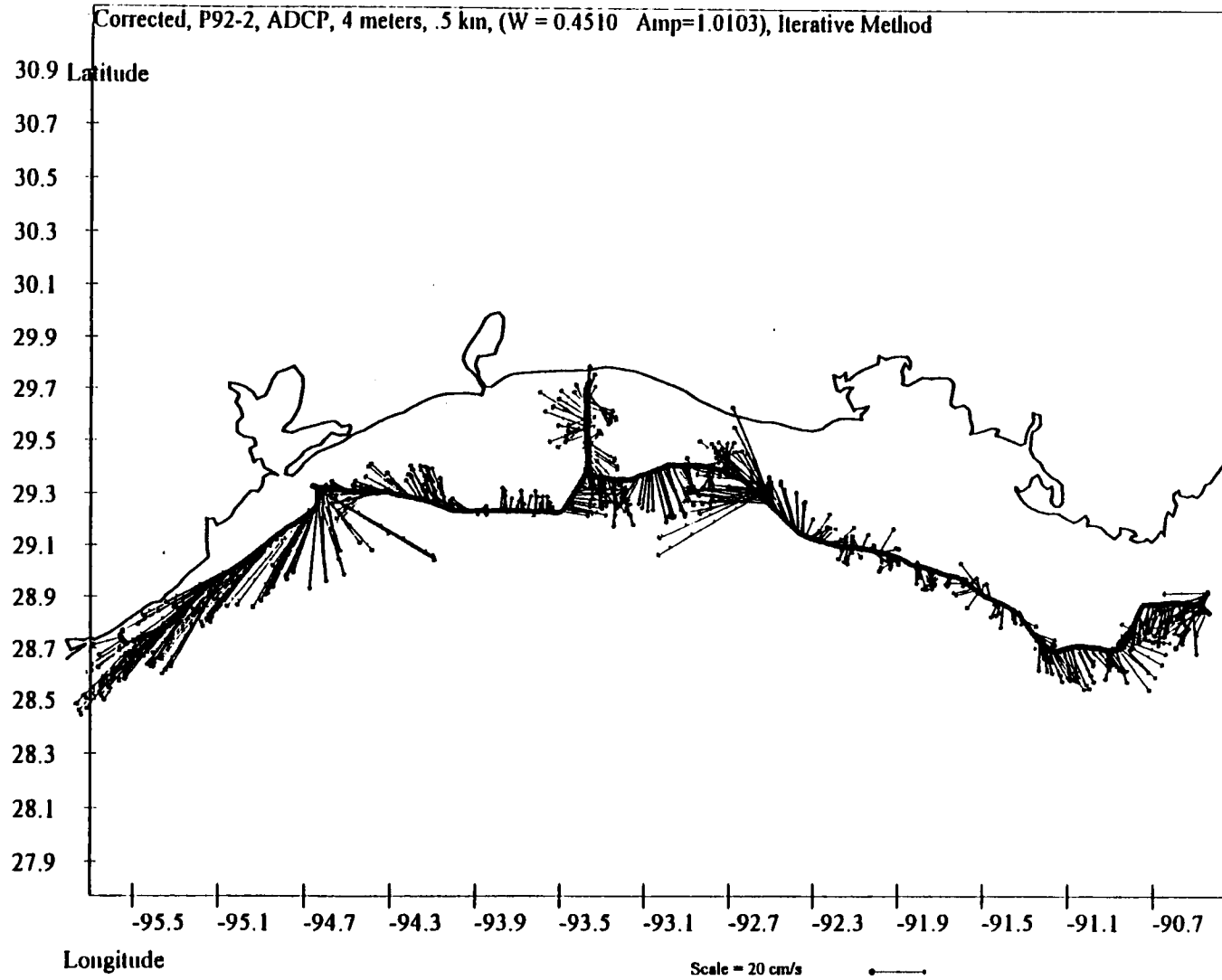
Figure 62. ADCP current vectors at 4-meter depth on the return leg.

been acquired between the pair. Therefore, filaments having widths of a few kilometers may be resolved with ADCP profiles, but not CTD profiles.

Section S1. Water characteristics along Section S1 are presented in Figures 63 and 64. The NOAA-11 MCSST image for October 5, 1992 at 0921 GMT suggests that, at the time Section S1 was occupied, a squirt of Mississippi River water apparently penetrated westward (Figure 51). Section S1 extends from a band of colder water in the northern portion of the section, southward into warmer water, and then into the cooler water filament associated with the Mississippi plume. Comparison of the satellite image with the CTD section illustrates this sequence, as follows. Water colder than 24°C occurs nearest shore and the 25.6°C contour rises from depth to the sea surface where the satellite image indicates warmer water northward of the Mississippi plume and southward of the colder coastal water.

Comparison of the satellite image with the ADCP 4-meter depth currents indicates weaker drift to the west in the colder inshore water, a band of high velocity directed to the west in the warmest water, and northeastward flow at the southernmost end of the section nearest the Mississippi plume. The warmest water at the sea surface also flowed with greatest velocity, with speeds approaching 50 cm/s.

Warm, saline water was found at depth along Section S1 where salinities exceeding 34 psu were encountered beneath the Mississippi plume and immediately inshore of the shallower jet. In both saline flows, currents had easterly components reaching approximately 10 cm/s.

Section S1B. Section S1B exhibits considerable continuity with Section S1 in that the core of strongest currents occurs in relatively warm (25.4°-25.6°C) and saline (32.5-33.0 psu) water. In both sections S1 and S1B the cores of high currents occur in regions of relatively homogeneous water. The warmest and most saline water encountered during the cruise was found at depth along Section S1B beneath and slightly offshore of the high speed core.

Section S2. In Section S2 (Figures 65 and 66) the high speed core continues westward from Section S1B, and is associated with stads of temperature (thermostad between 25.2°-25.8°C), salinity (stad between 31.5-33.0 psu), and density (pycnostad between 20.5-22.0 kg/m^3). Other stads are evident at the southern end of the section, one near the surface with strong easterly flow, and one at the sea floor with westerly flow.

Section S2B. In Section S2B the colder, fresher water extends farther from shore than in sections S1, S1B, and S2. In the satellite image for 5 October 0921Z a filament of cooler water extends westward beginning at approximately Section S2B. The root of this filament is evident in the 4-meter deep ADCP currents by the continuity between sections S2B and T5. The currents associated with this filament diverge southward from the core of high speed currents continuing along the coast. This double-core structure is evident in contours of east-west ADCP speed. Beneath the double core structure the warmest and most saline water is heading eastward.

Section S3. Section S3 (Figures 67 and 68) intersects two filaments of colder water embraced by warmer water, as evident in the satellite image for October 5. The southernmost filament which began in Section S2B extends westward and is located immediately southward of Section S3 (see satellite image for October 5). Immediately inshore of this filament lies the southern end of Section S3. In the contours of the ADCP east-west speed this warm water is apparently heading eastward. In shore of this warm water lies a core directed west in which the speeds are reduced (maximum speeds of 12 cm/s) and apparently associated with a second filament. Further inshore of this second filament lies a narrower band of warm water heading east. Toward the northern end of Section S3 the water is again cooler and directed west.
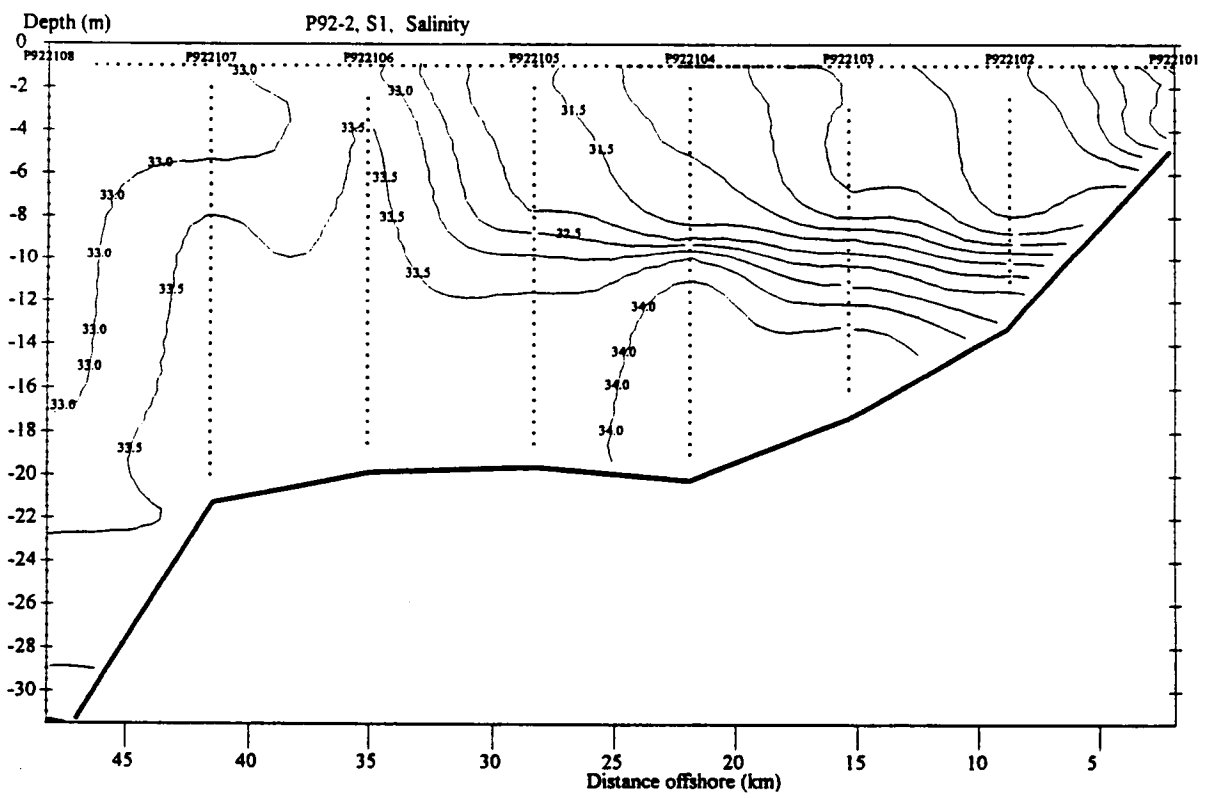
Figure 63. Section S1, salinity contours.

(a)
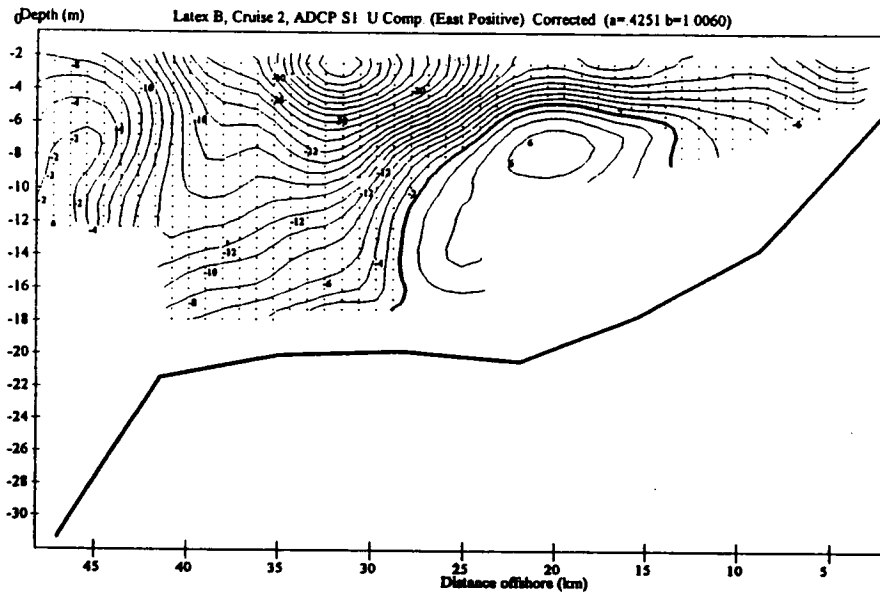
(b)
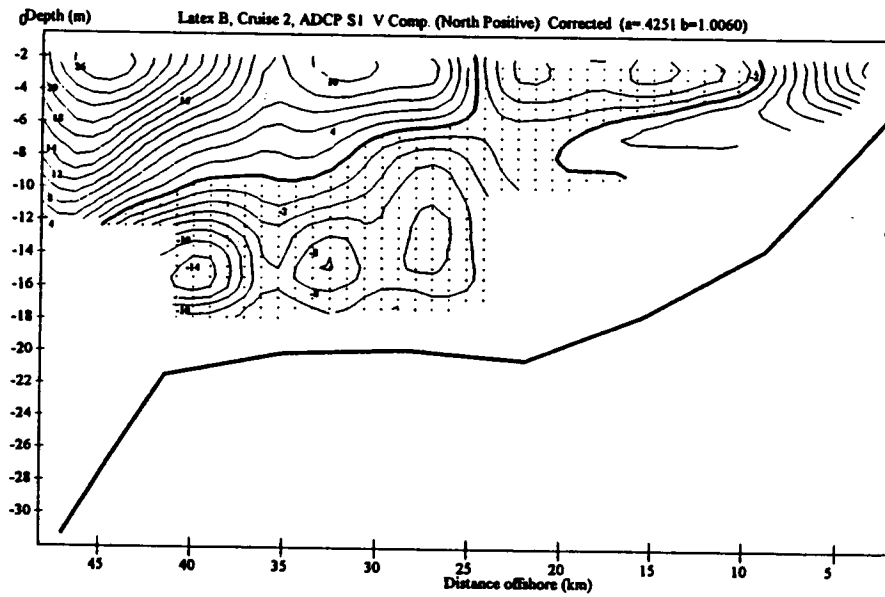
Figure 64. ADCP, Section S1: (a) U component; (b) V component.

81
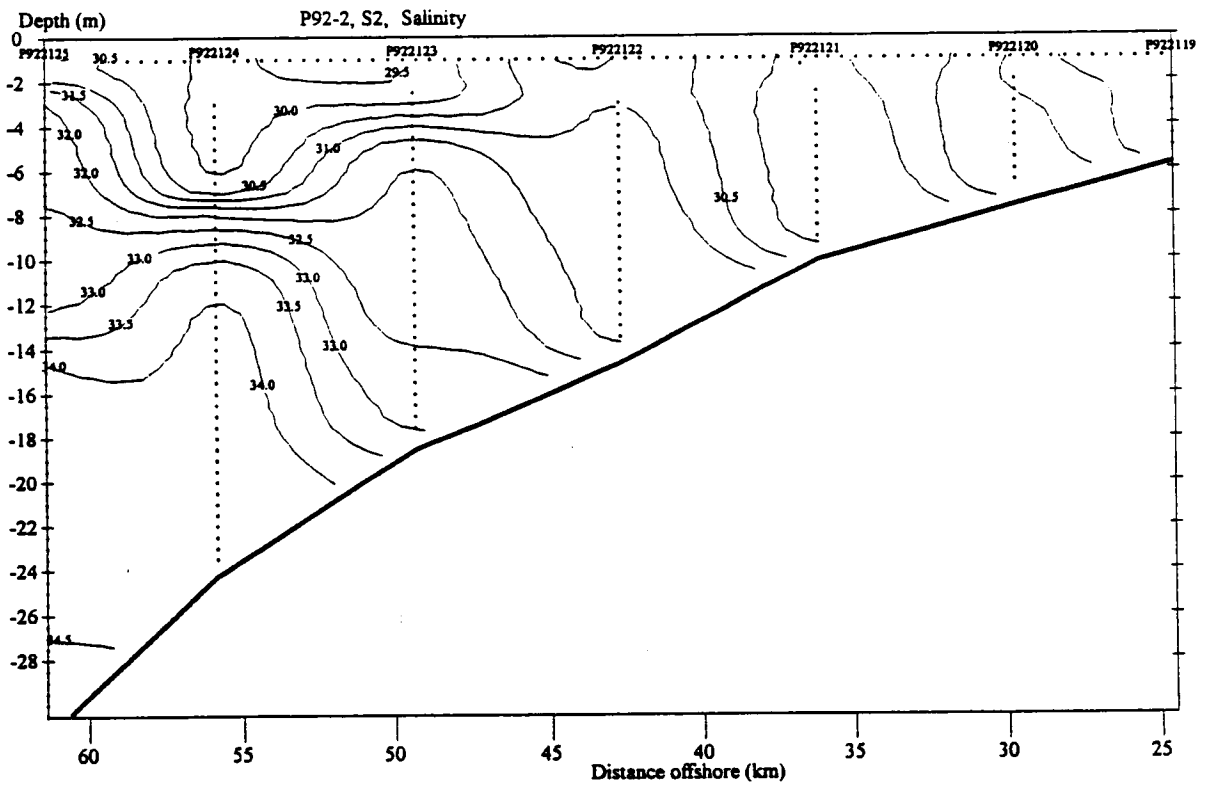
Figure 65. Section S2, salinity contours.

(a)
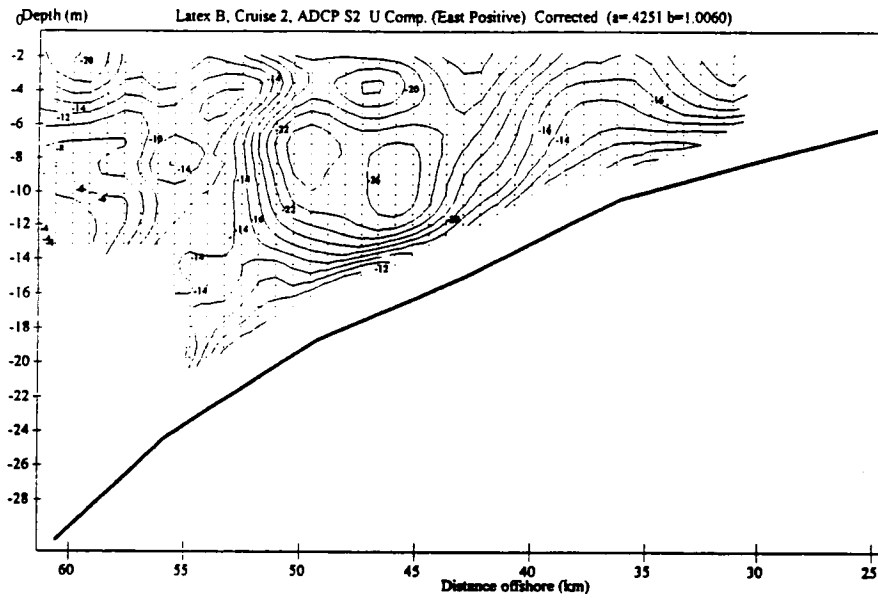
(b)
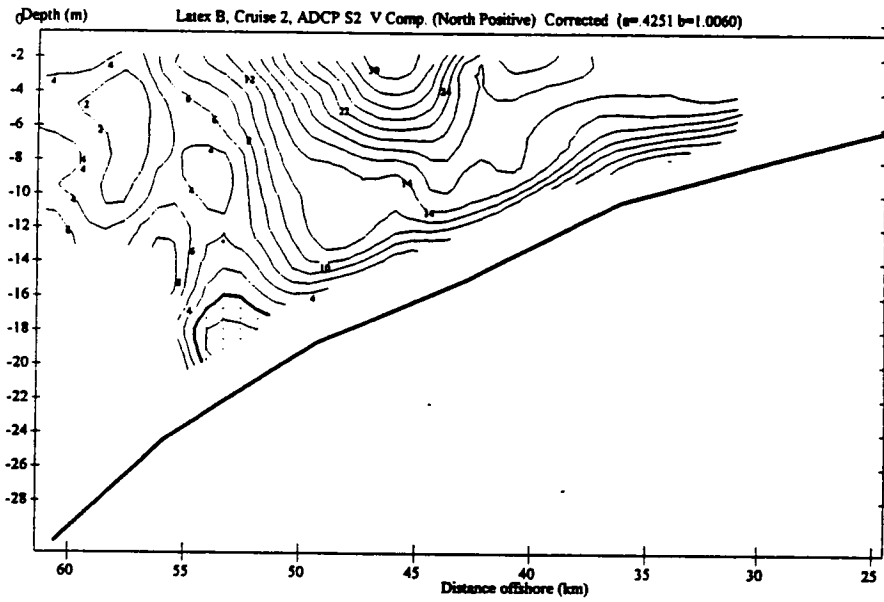
Figure 66. ADCP, Section S2: (a) U component; (b) V component.

83
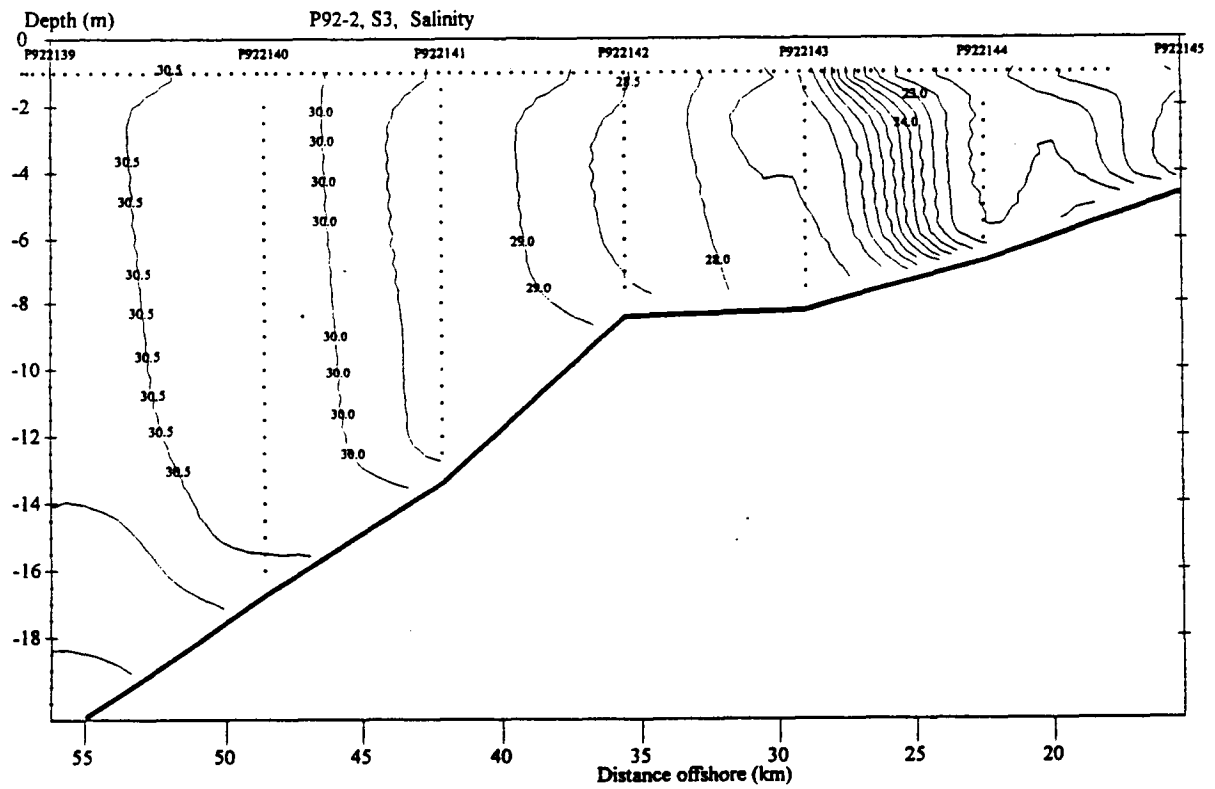
Figure 67. Section S3, salinity contours.

(a)
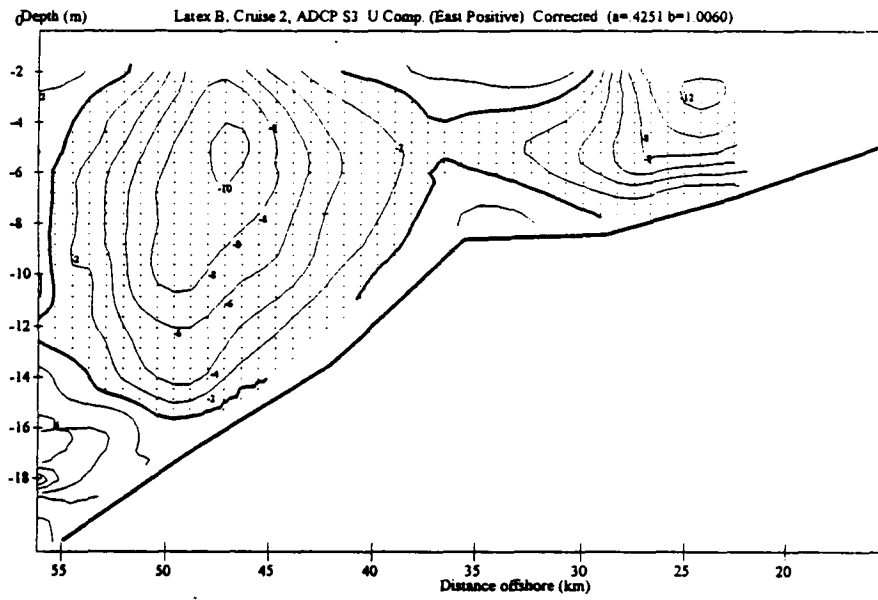
(b)
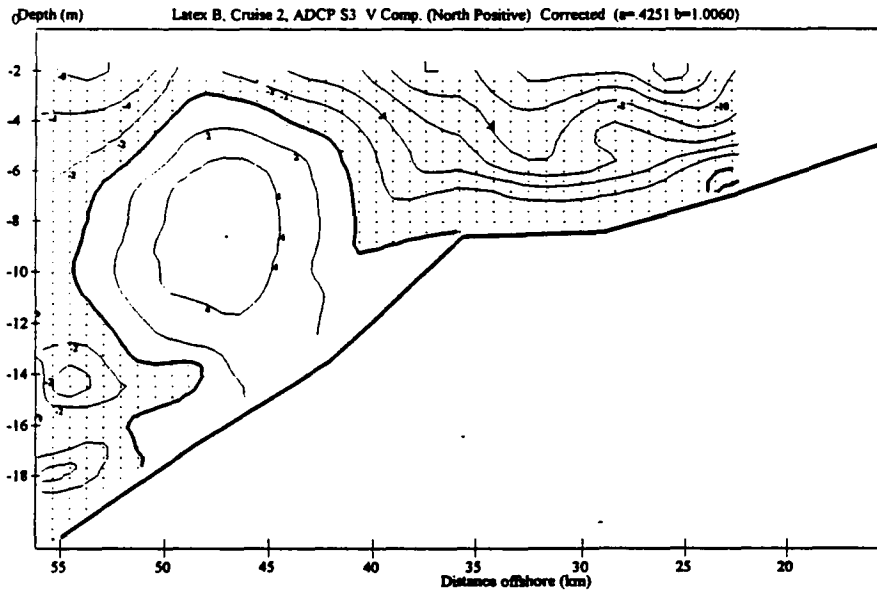
Figure 68. ADCP, Section S3: (a) U component; (b) V component.

Section S3B. In Section S3B the strongest current occurs at the southern end as a core of moderate velocity with a strong westerly component. This core occurs in a region of reduced gradients of temperature (23.8°-24.4°C), salinity (28.4-30.0 psu), and density (18.5-20.0 kg/m³).

Section S4. Along Section S4 (Figures 69 and 70) two water masses appear separated by a gradient. Centered in the gradient, a core of velocity is embedded with maximum east-west speeds of -24 cm/s (Figure 11).

Section S4B. Along Section S4B there is a well defined maximum in the east-west speed reaching -24 cm/s.

Section S5. Along Section S5 (Figure 71) a smaller core of westerly velocity was apparent, reaching a speed of -24 cm/s.

Section S5B. Along Section S5B the properties of temperature, salinity, and density were quite homogeneous in the vertical direction. A velocity core reaching a speed of 24 cm/s in the westward direction was evident.

Section S6. In Section S6 (Figures 72 and 73) the water properties were again remarkably well-mixed in the vertical direction. Three cores of velocity were evident, the largest being near the middle of the section (Figure 73).

Section S7. Properties along Section S7 are shown in Figures 74 and 75. The velocity data indicate a well-defined core of high speed centered between salinities of approximately 28.5 and 30.5 psu. Inshore of the 28 psu contour, the water is relatively homogeneous and the flow is more southerly. At the deepest, most offshore location where salinities exceed 32.5 psu the flow is weak but directed to the north.

Section S8. Properties along Section S8 are shown in Figures 76 and 77. The speed components (Figure 77) indicate a well-defined core of high speed (maximum speed in the core of approximately 43 cm/s). This core appears to lie between two water masses, one near the shore with salinities less than approximately 28.5 psu and a flow directed to the south, and a flow of more saline water (salinities greater than approximately 31 psu) with a flow also directed to the south.

3. Discussion

a. Magnitude of Transport. An important method for characterizing water flow is the computation of the net volume transport through a given section perpendicular to the shore. The volume transport in the east-west direction was computed from the ADCP data for 11 of the 13 sections (S1-S6). Total transport integrated between the offshore and inshore ends of the sections are listed in Table 3.

86
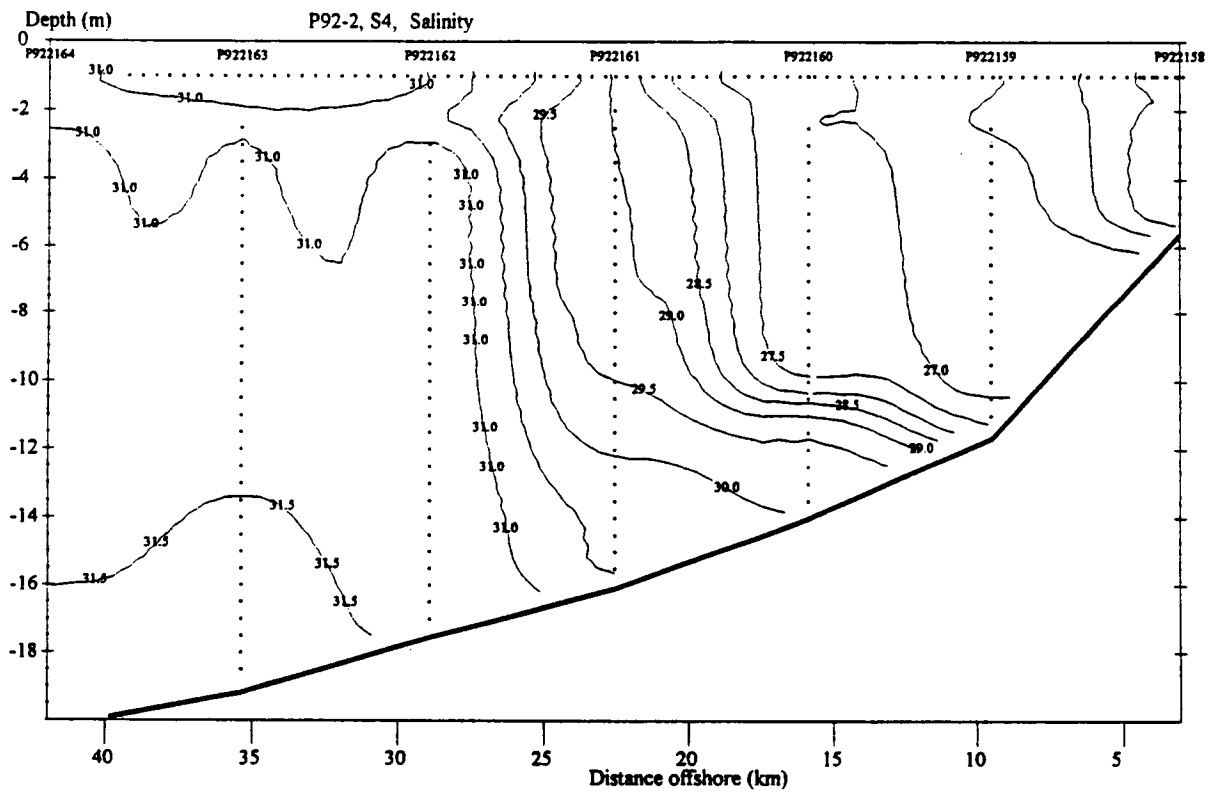
Figure 69. Section S4, salinity contours.

(a)
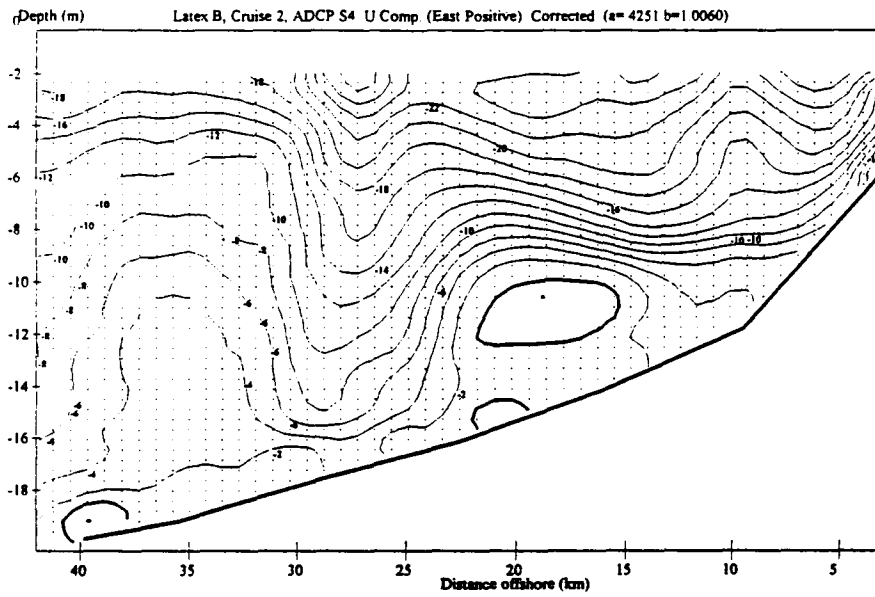
(b)
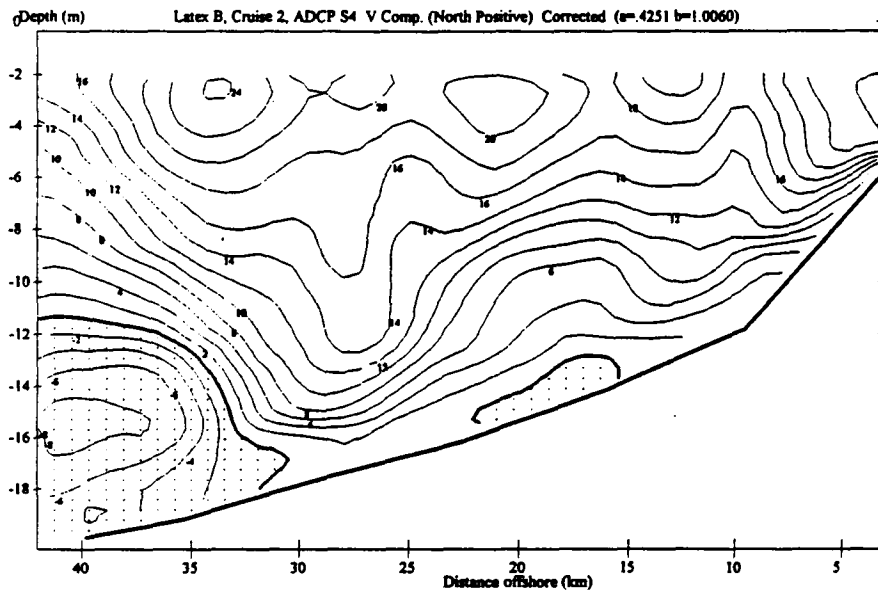
Figure 70. ADCP, Section S4: (a) U component; (b) V component.

(a)
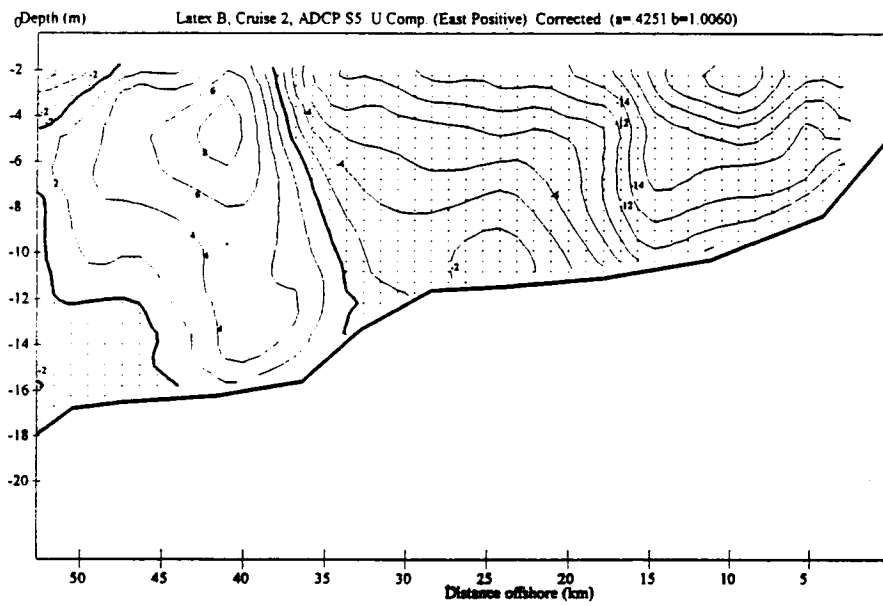
(b)
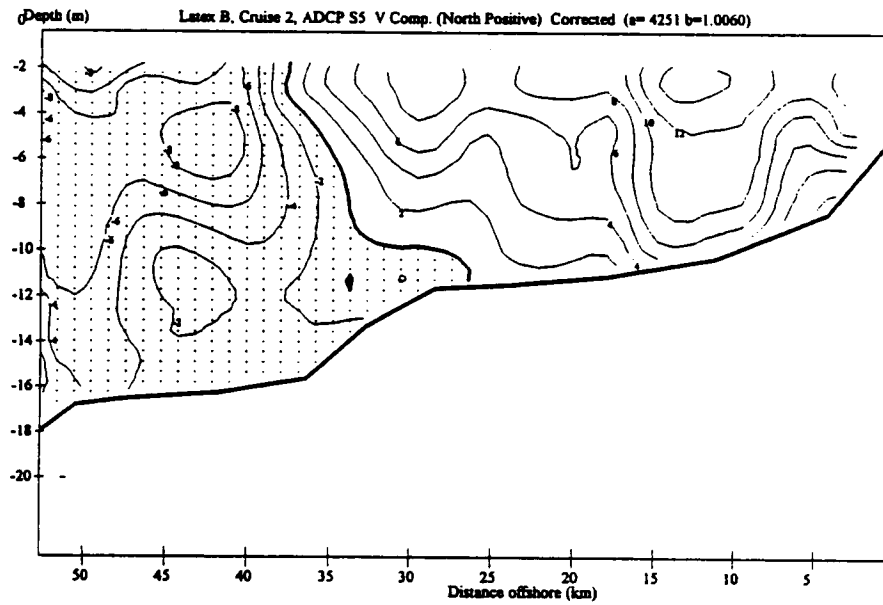
Figure 71. ADCP, Section S5: (a) U component; (b) V component.
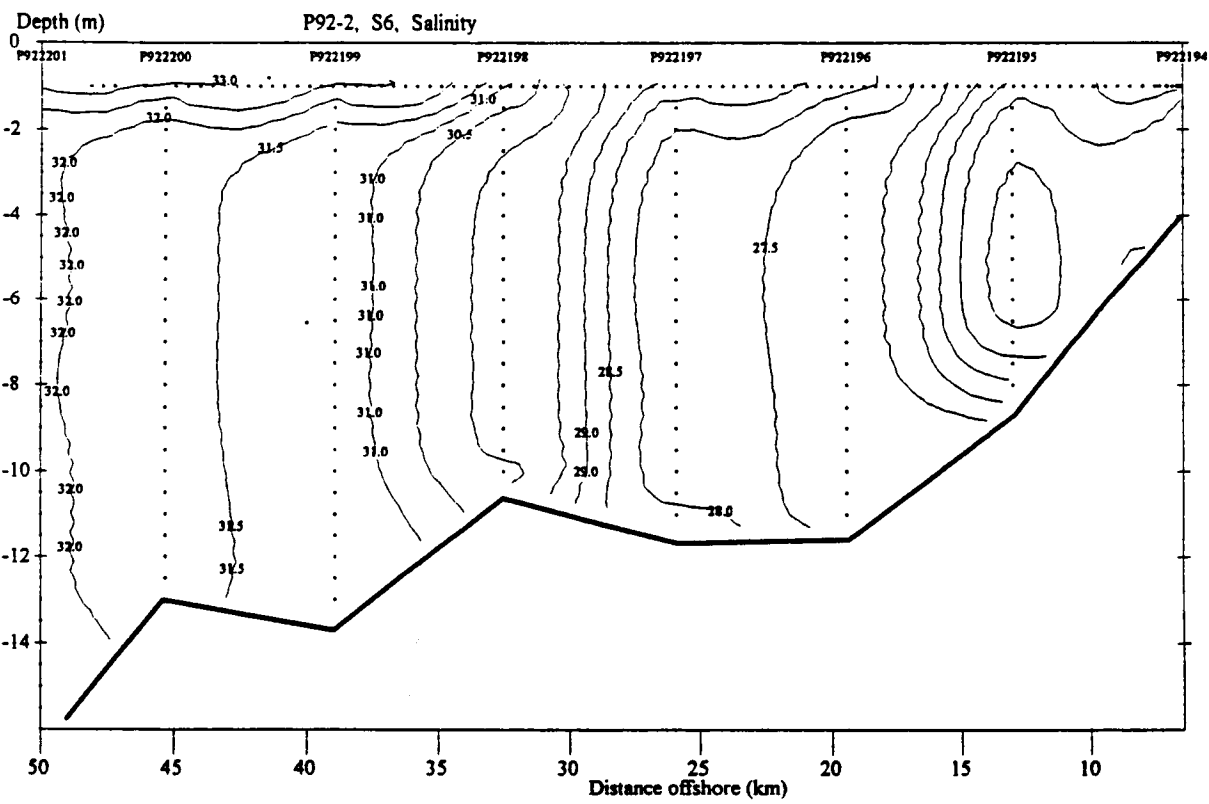
Figure 72. Section S6, salinity contours.

(a)
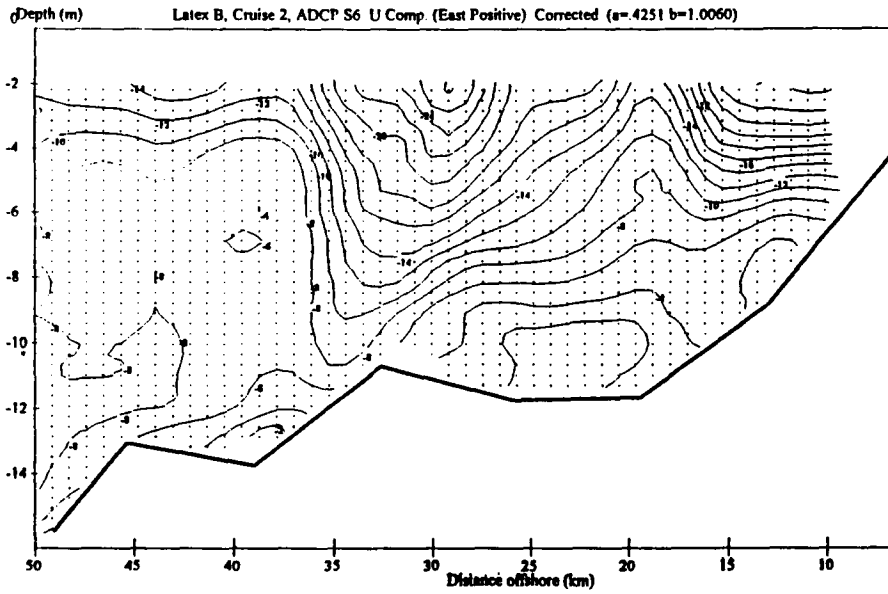
(b)
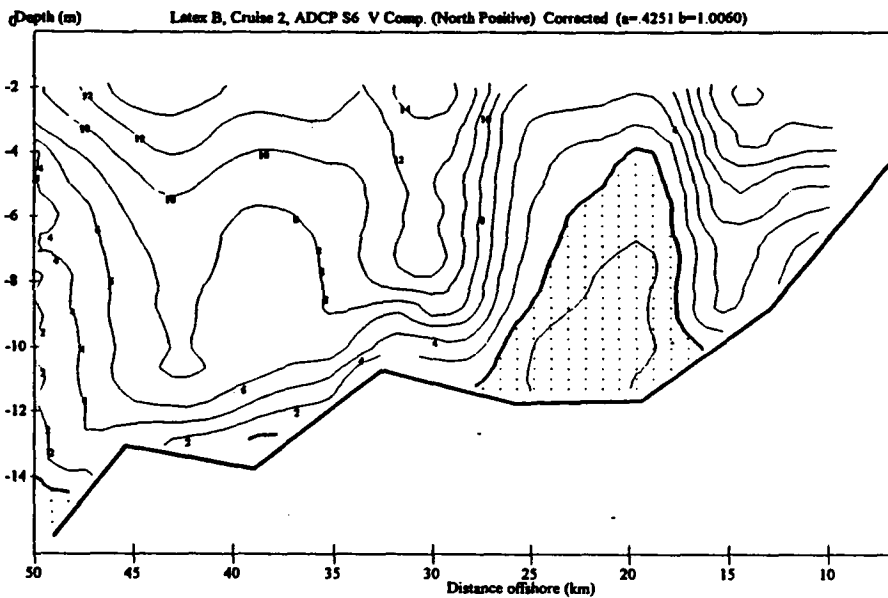
Figure 73. ADCP, Section S6: (a) U component; (b) V component.

91
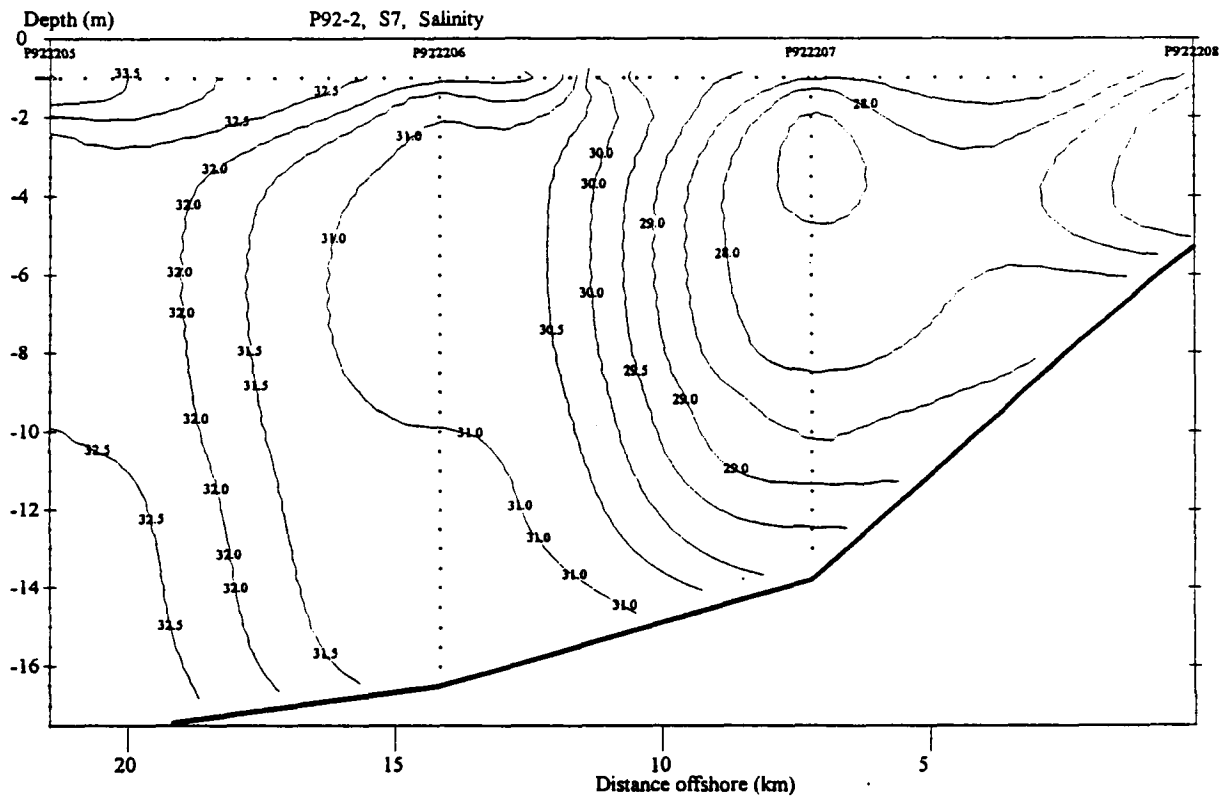
Figure 74. Section S7, salinity contours.

(a)
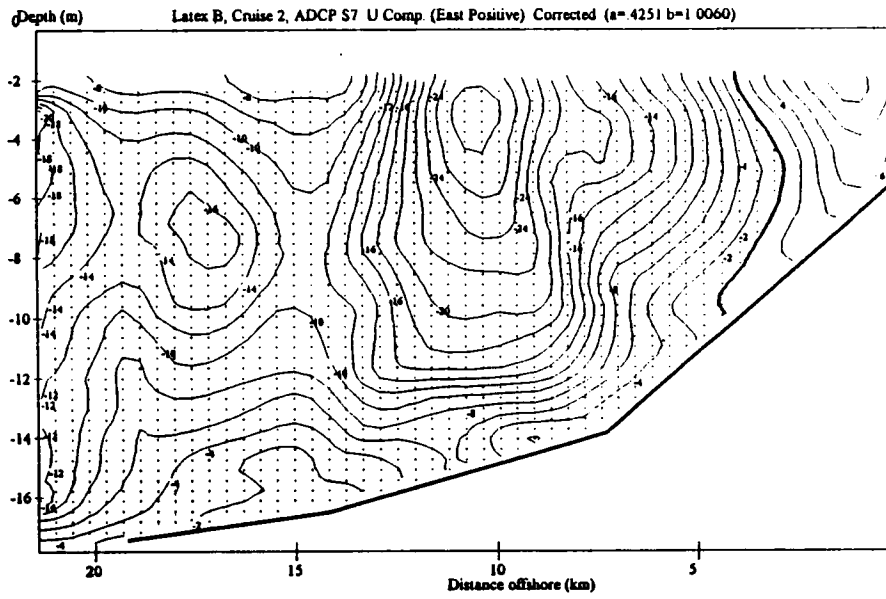
(b)
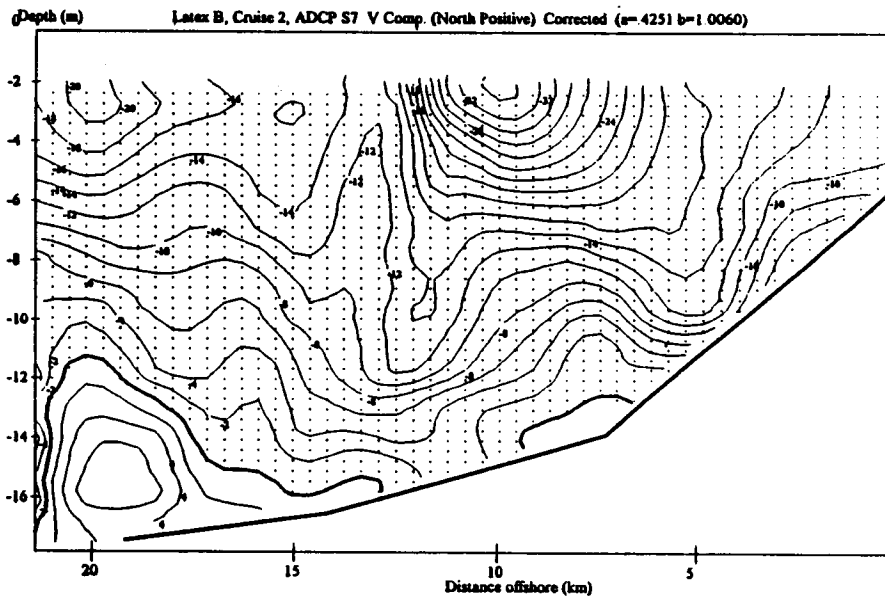
Figure 75. ADCP, Section S7: (a) U component; (b) V component.

93
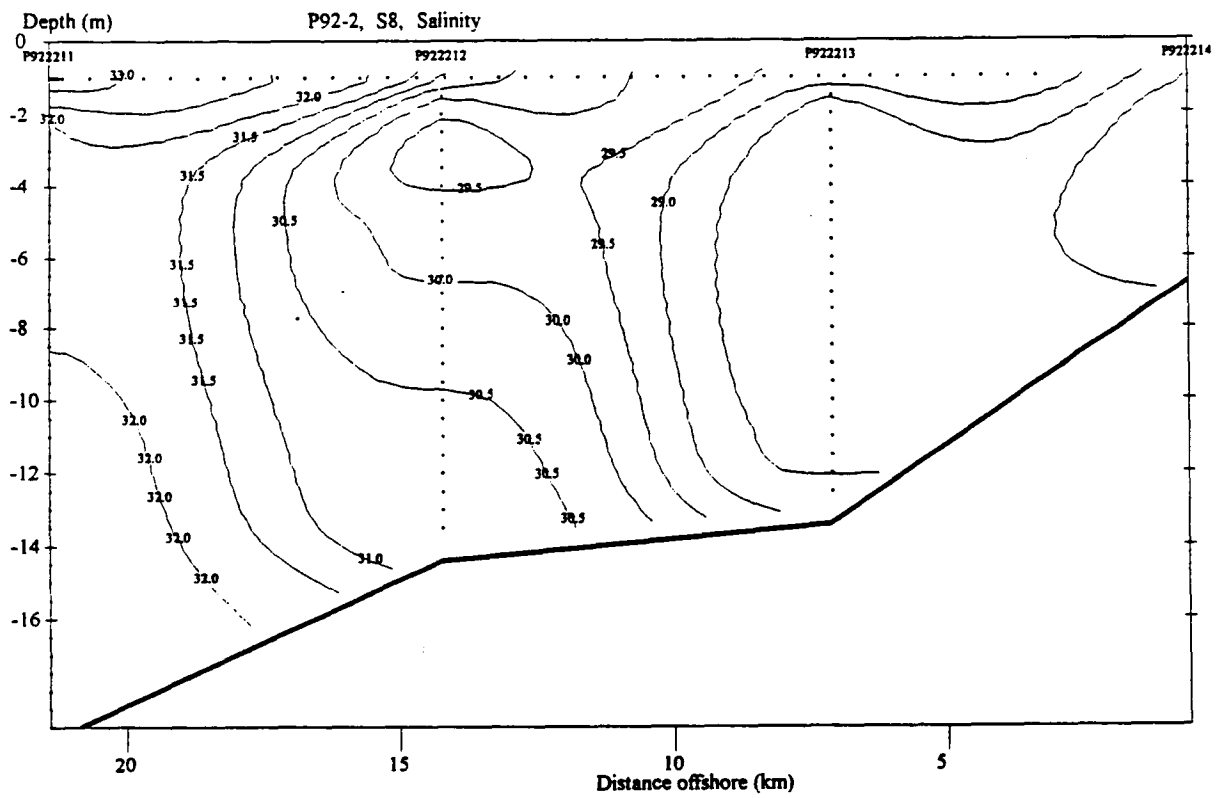
Figure 76. Section S8, salinity contours.

(a)
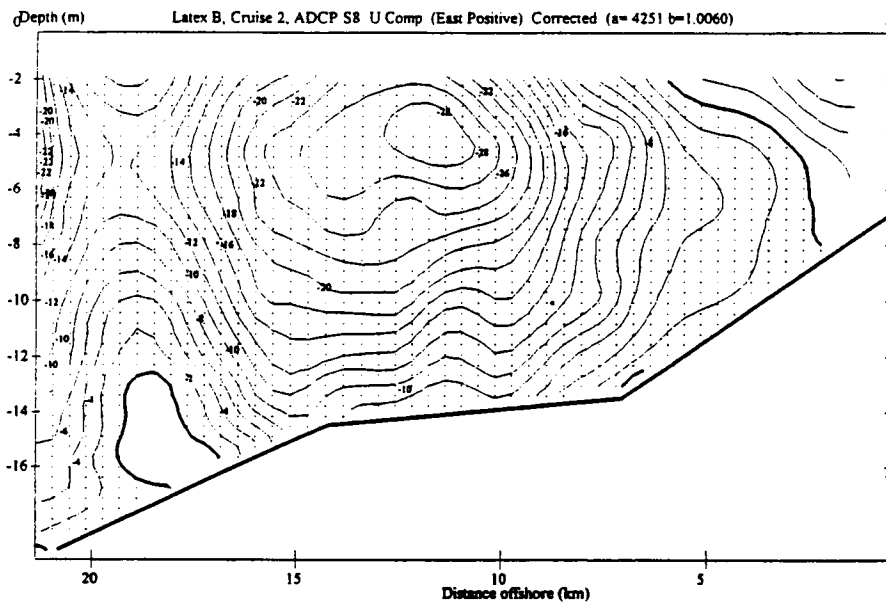
(b)
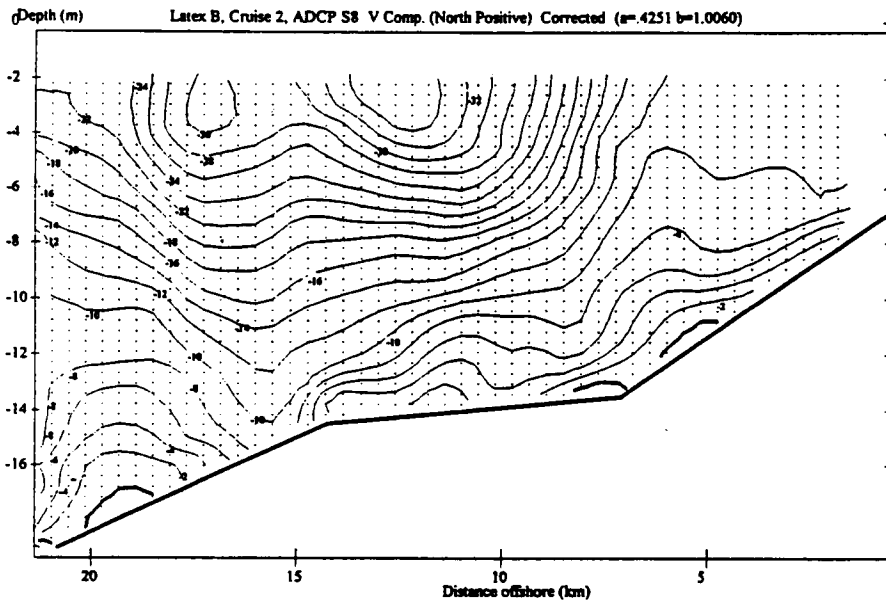
Figure 77. ADCP, Section S8: (a) U component; (b) V component.

95

Table 3. Estimates of volume east-west transport through eleven sections during Cruise II.

Section	Volume Transport (m³/s)		Mean East-West Wind Speed (m/s) (MIDAS)
	all sections	if S3 and S3B eliminated	
S1	- 77,990	- 77,990	6
S1B	-124,504	-124,504	9
S2	- 69,574	- 69,574	5
S2B	- 50,469	- 50,469	5
S3	- 14,459		0
S3B	+ 12,001		4
S4	- 64,671	- 64,671	7
S4B	- 57,320	- 57,320	
S5	- 40,281	- 40,281	2
S5B	- 82,345	- 82,345	6
S6	- 54,702	- 54,702	7
Mean	- 56,756	- 69,095	5.1
Standard deviation	35,713	24,667	2.6
Sample size	11	9	10
Standard error	10,757	8,222	0.8

For the sample of 11 the standard error equals 18.9% of the mean transport (56,756 m³/s). This fraction is reasonably small, suggesting that the volume transport differs from zero and is directed toward the west. Assuming that the transport estimates are independent and applying the t-test, it may be concluded that at the 95% level the transport was directed westward during Cruise II.

Inspection of the transport values indicates anomalous values associated with sections S3 and S3B. Earlier in this chapter it was noted that the winds during these two sections had speeds from northerly and southerly directions, whereas during the other sections the winds had predominantly east-west components. Table 3 also lists transport statistics with the elimination of transports associated with these two sections. Eliminating sections S3 and S3B leads to an increase of the mean transport by 22% to 69,095 m³/s, a decrease of the standard deviation by 45%, and a substantial decrease in transport variability, such that the standard error equals 12% of the mean transport.

b. Transport in Relation to Wind. The mean east-west wind speed component for 10 of the sections are shown in Table 3. A linear regression computed between transport and wind speed gave a correlation coefficient of $r = -0.75$, explaining 56% of the variance. With eight degrees of freedom this sample size indicates that the regression is significant at the 95% confidence level.

The linear regression based on data in Table 3 may be expressed as

$$T \ (10^3 m^3/s) = -1.1 - 10.9 \ W \ (m/s),$$

where T represents volume transport in thousands of cubic meters per second, and W represents the east-west wind speed component in meters per second. Applying the regression the following estimated transports at selected wind speeds were obtained: 1,100 m³/s at zero wind

speed; 55,000 m³/s at 5 m/s; and 110,000 m³/s at 10 m/s. During the survey, the mean wind speed in the east-west direction equalled approximately 5.1 m/s, implying a mean transport of approximately 57,000 m³/s compared with the average of the transport estimates equalling 57,000 m³/s.

The relation developed between winds and transport suggests that the sections surveyed can be divided according to the characteristics of the wind that occurred at the time of the section. Inspection of the MIDAS winds (Figure 56) indicates that relatively steady westerly winds prevailed during seven of the sections: Sections S1-S2 in the eastern portion of the survey area; and Sections S5B-S8 in the western portion of the survey area. Between these eastern and western groups of sections the winds were considerably more variable. Therefore, the discussion has been divided into narratives according to wind characteristics.

   c. Sections during Steady Westerly Winds. During the eastern and western portions of the survey area the winds were relatively steady. A characteristic common to the seven sections surveyed under prevailing westerly winds (sections S1, S1B, S2, S5B, S6, S7, S8) is the presence of a core of high current with maximum speeds on the order of half a knot (~ 30 cm/s). This may be seen by comparing contours of east-west current speed along these sections. To summarize the attributes, maximum speeds in the cores are presented in Table 4, as well as the presence of counter currents.

Table 4. Characteristics of the velocity cores under prevailing easterly winds.

Section	Core Characteristics		Counter Currents
	Width (km)	Max. Speed (cm/s)	
S1	17	-46	Inshore easterly
S1B	17	-32	None
S2	7	-26	Easterly offshore
S5B	12	-24	None
S6	17	-30	None
S7	7	-30	Inshore & offshore
S8	8	-30	Inshore & offshore
Mean	12	-31	Sometimes present

Under prevailing, reasonably steady winds the velocity structure tends to organize itself as a core of high velocity sometimes accompanied by counter currents. On average, the core measures 12 kilometers in the cross-shelf direction, with a maximum velocity of approximately 30 cm/s.

   d. Sections during Variable Winds. In the middle section of the survey area, when winds were variable, the velocity structure becomes quite complex and the velocity core becomes much weaker and difficult to distinguish from other currents (see east-west speed contours in Figures 49, 60, 66, 70, 72).

   e. Temporal Flow Variability Observed with Current Meters. Current meters moored near the eastern and western ends and near the middle of the survey area give further indications of flow variability. In the eastern half of the survey area, currents were episodic with a net mean current indistinguishable from zero. In contrast, currents in the western portion had significant net mean current directed toward the southwest at speeds on the order of 5 cm/s. Given the near-zero mean currents in the eastern portion and the strong southwest current in the western portion

of the study area, a divergence in the long-shore current field may have occurred, with onshore flow at some locations in the western half of the survey area.

Because of wide spacing, the current meter data at present cannot be used to infer the location of the transition between episodic and strong along-shore flow. The most synoptic view of the transition to strong long-shore flow was obtained by displaying the ADCP current vectors at 4 meters depth the transit between sections S8 and S1 at the end of the cruise (Figure 62). A transition occurred in the vicinity of Galveston Bay: to the south the speeds at 4 meters depth were consistently on the order of 30 cm/s; whereas, to the east speeds were generally less and the directions were variable.

Superposing the 4-meter ADCP currents (Figure 62) on maps of surface temperature and salinity (Figures 57, 58) indicates that the transition occurred at approximately the western extent of the main Atchafalaya plume. Superposing the ADCP transect on the sea surface salinity map it can be seen further that the termination of the plume occurs approximately onshore of the cell of high salinity and that currents apparently circulate in the clockwise direction around this salinity feature. During Cruise I, this salinity feature was also present at approximately the same location.

f. Inferences for Box Model Computations. Filaments and eddies appear to interact with the flow and properties in the survey, thereby influencing the interpretations of fluxes computed with box models. In the eastern portion of the survey area three filaments mentioned at the outset of this chapter appear to transport water across the box boundaries parallel to the shore, i.e., the filaments cross at angles to the box boundaries drawn nominally parallel to the shore. In the western portion of the survey area, a large Loop Current eddy (Eddy Vasquez) may affect the flow and properties westward of approximately Galveston Bay. The strong southwesterly flows noted in the fastest currents also imply transport of materials across the boundaries drawn for the boxes parallel to the shore.

III. Biological Characteristics Survey

A. Light Conditions and Nutrients in the Coastal Plume *(R. Eugene Turner)*

1. Introduction

The coastal plume is characterized by strong turbidity gradients and well-defined density structure responsive to local winds, freshwater supplies, and weather fronts. It therefore has a relatively unstable structure over periods of days to weeks, as shown by remotely sensed images of turbidity in the surface layer. Visual observations of only the surface layers are substantially inadequate descriptions of the coastal plume, for the physical structure is not homogenous with depth. Light conditions within the coastal current vary temporally along the 3 spatial axes and, when defined, can be used to both define its location and to quantify its variability.

The light field within the coastal plume, regardless of cause, has important biological consequences. Microbes, zooplankton and fish are dependent on the phytoplankton whose accumulation and production is responsive to the same forces delimiting its physical structure. Low oxygen zones, or hypoxia (<2 mg/l), on the Louisiana shelf are extensive and are the largest in the U.S. One of the tasks of LATEX B is to define the light field of the coastal plume and to establish quantitative relationships between the physical and biological components. We have begun this investigation using traditional methodology: i.e., data from transmissometers, secchi disks, PAR sensors, suspended sediment measurements, and satellites. Data from moored instruments, and other data, are being obtained from the Nutrient Enhanced Coastal Ocean Productivity, Mississippi-Atchafalaya River Outflow Study (NECOP) and historical records. Other tasks include determination of nutrient concentrations to assist interpretation of the biological variability. This is the first data reduction exercise and is therefore limited to discussion of a few examples of the variability found on the first two cruises.

The light field of the coastal current is, of course, strongly structured because of the density gradients. The extinction coefficient varies tremendously with depth, and turbidity layers are often found at the surface and bottom of a water column. Also, the light conditions at one station, even within one month, vary. The noontime light available for photosynthesis ranged 20-fold during one month at the moored light meter, south of Terrebonne Bay.

2. Methods

Data obtained from an in situ light meter and nutrient sampling are two observations made to supplement the hydrographic data reported in previous sections of this report.

The light meter is a hand-held Biospherical Instruments, Inc., meter equipped with a deck reference PAR sensor, and a submersible PAR sensor within a wired instrument package, including sensors for depth, natural fluorescence, and temperature. The lowering cable is attached to a portable computer that displays results while on station. The computer software computes the estimated extinction coefficient, with depth, the percent irradiance at depth, and a relative estimate of phytoplankton production. The latter estimate is made using an empirical conversion factor to convert the natural fluorescence values and PAR to instantaneous phytoplankton production rates. Because of potential interference from red light (absorbed completely below 3 m), care must be used in estimating phytoplankton production rates in the upper 1-3 meters. This is under investigation for these turbid waters.

The nutrient samples are analyzed in routine fashion, on frozen samples, using a Technicon AutoAnalyzer. Secchi disk measurements and light meter readings are done on the lighted side of the vessel, within 3 hours of local apparent noon.

3. Preliminary, Descriptive Results

a. Descriptions of Nutrient Concentration and Light Conditions along a Salinity and Longitudinal Gradient. Nutrients are plotted in two different ways for the data from the April and October 1992 cruises: nutrient concentration versus longitude and nutrient concentration versus salinity. The vertical axes are generally (but not always) the same scale for each nutrient on different nutrients.

Cruise I. April 21-May 1. 1992. Ammonia concentrations were generally highest near the 92° W region, near the two major riverine sources, the Mississippi and Atchafalaya rivers (Figure 78). The bottom concentrations were frequently as high as the surface layers. It appears that there is a bimodal peak, downstream of each of the riverine sources.

Nitrate concentrations were higher (Figure 79) and also peaked (perhaps with a bimodal distribution with longitude) downstream of the two riverine sources. Bottom concentrations of nitrate were generally equal to those in the surface waters.

The total dissolved inorganic nitrogen forms (Figure 80) are dominated by nitrate. Phosphate did not rise so dramatically downstream of the riverine sources, but did increase somewhat (Figure 81). Silicate concentrations (Figure 82) followed the same pattern.

Nitrate and silicate concentrations were generally higher at lower salinities, but only silicate concentrations showed a possible dilution gradient with salinity changes. Plots of samples within 2° of the Mississippi River demonstrate a more conservative mixing gradient (not shown).

The nitrogen:phosphate atomic ratios (an indicator of nutrient limitation) were quite high at the 30 ppt range indicating potential phosphorous limitation for phytoplankton growth. In contrast, the Si:N ratio was near the threshold for silicate limitation for diatoms. The plots of N:P and Si:DIN atomic ratios show the potential limitations highest immediately downstream from the two river sources.

Light conditions in April, for these samples, showed a typical decline in extinction coefficient and deepening of the secchi disk depths with increasing salinity. The secchi disk depth average about 10% of the incident surface radiation.

Cruise II. October 5-15. 1992. Similar plots for the October cruise are shown in Figures 83-96. In general, the same conditions were observed, but the concentrations of nutrients were, in almost every instance, at a lower concentration. Also, the data distribution for Cruise II was restricted to mostly off the Louisiana shelf, rather than the more extended sampling from Cruise I.

Ammonia concentrations were about one-half that observed in April, 1992 (Figure 83). The nitrate concentrations (Figure 84) were about one-fifth the concentrations observed in April but remained the dominant form of inorganic dissolved nitrogen (Figure 85). Phosphate concentrations (Figure 86) were at about the same concentration in the surface and bottom layers, whereas the silicate concentrations were about the same level (Figure 87). A distinctive peak in dissolved inorganic nitrogen occurred at 30 ppt (Figure 88). However, the salinity gradient sampled was restricted to a narrow range (Figure 89-90) for phosphate and silicate. In contrast to the April cruise, the N:P and N:SI ratios were quite low and high, respectively, (Figures 91 and 92), indicating no P or Si limitation on phytoplankton growth. The highest ratios were observed south of the Atchafalaya River (Figures 93 and 94).
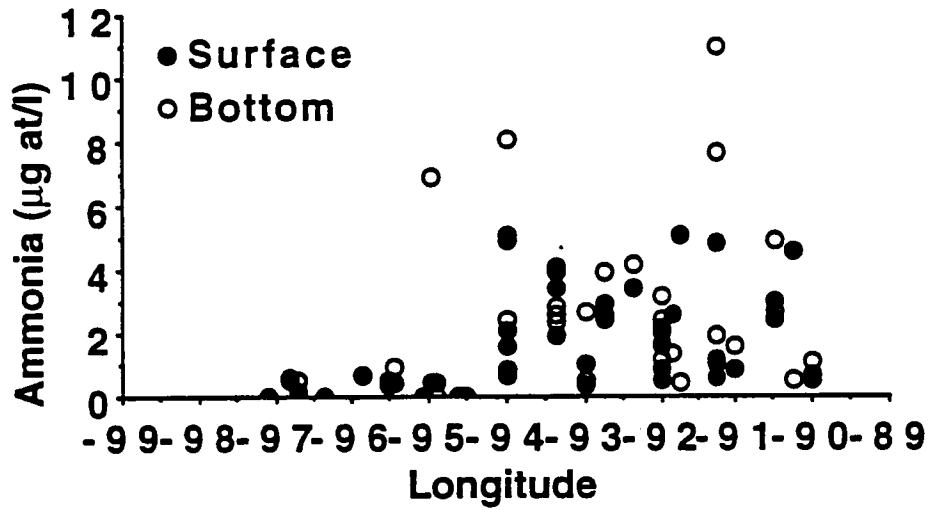
Figure 78. Ammonia concentration (μg at/l) in the surface and bottom waters for stations sampled on Cruise I.
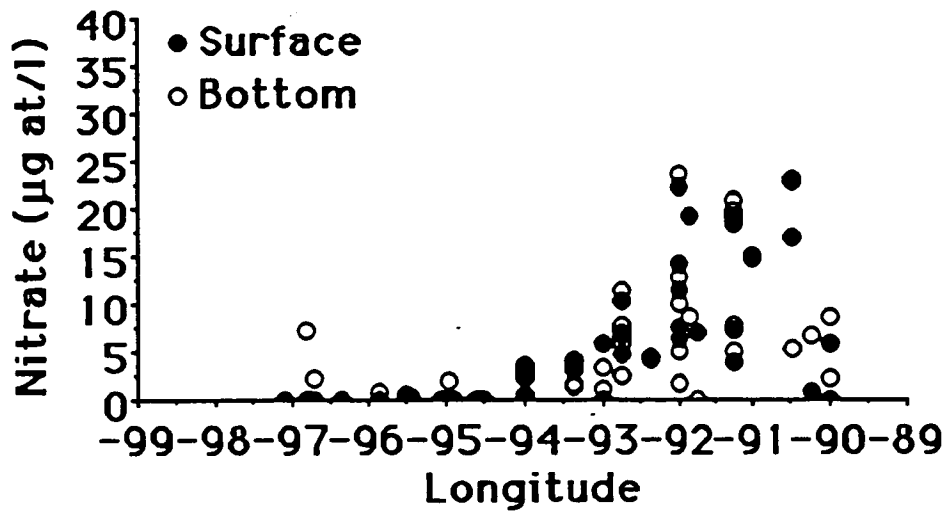
Figure 79. Nitrate concentration (μg at/l) in the surface and bottom waters for stations sampled on Cruise I.

101
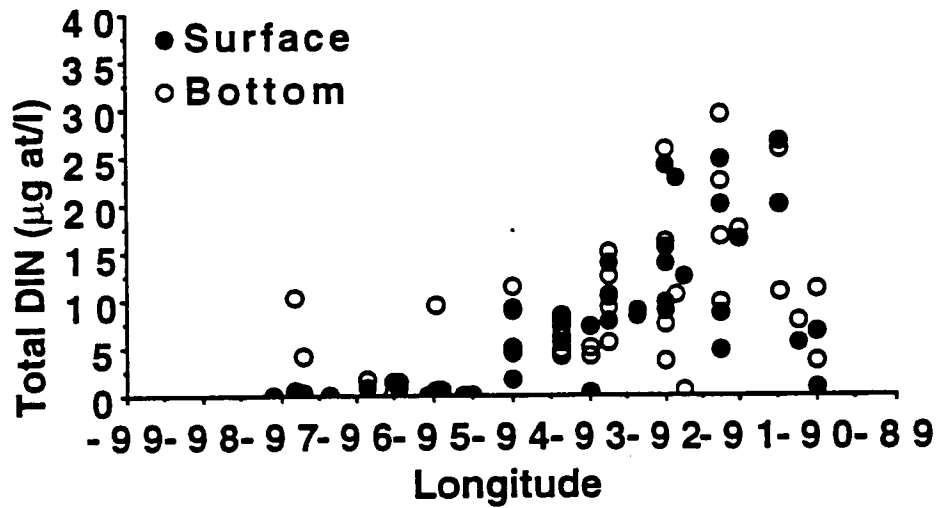
Figure 80. Total dissolved nitrogen concentration (µg at/l) in the surface and bottom waters for stations sampled on Cruise I.
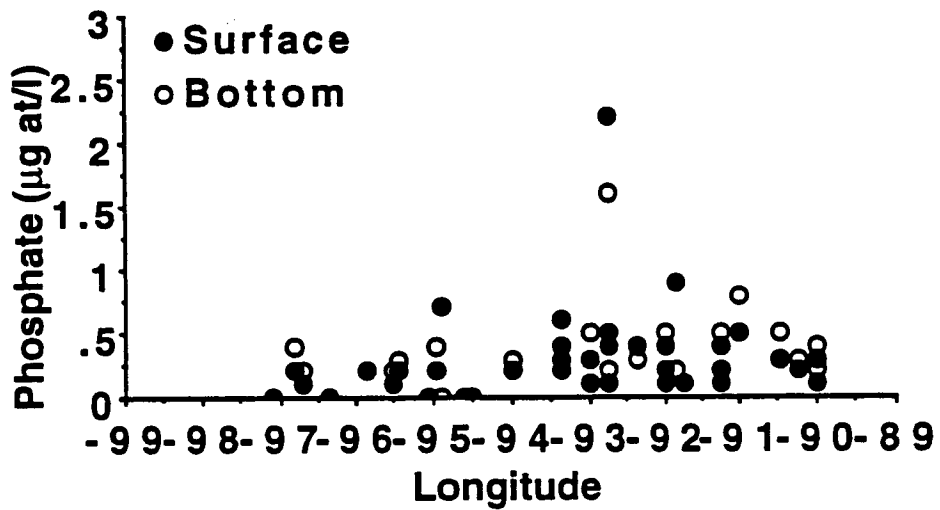
Figure 81. Phosphate concentration (µg at/l) in the surface and bottom waters for stations sampled on Cruise I.
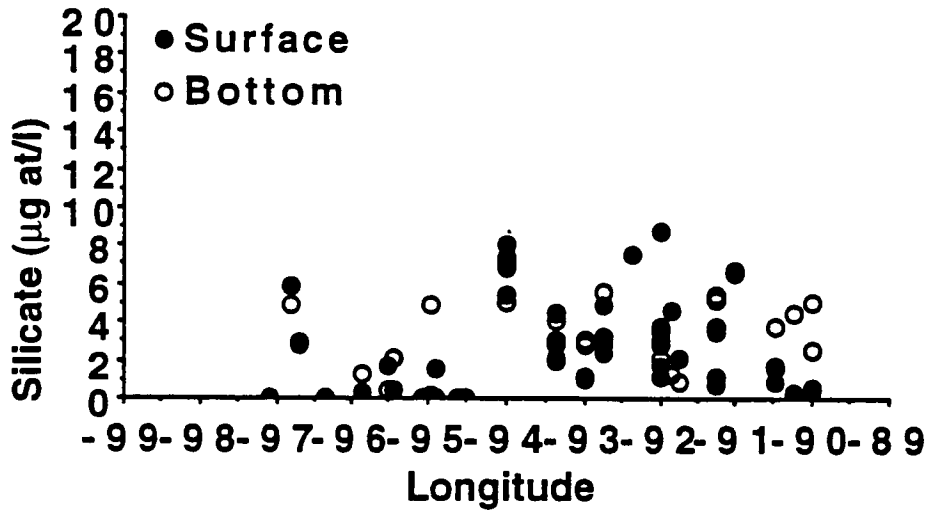
Figure 82. Silicate concentration (µg at/l) in the surface and bottom waters for stations sampled on Cruise I.
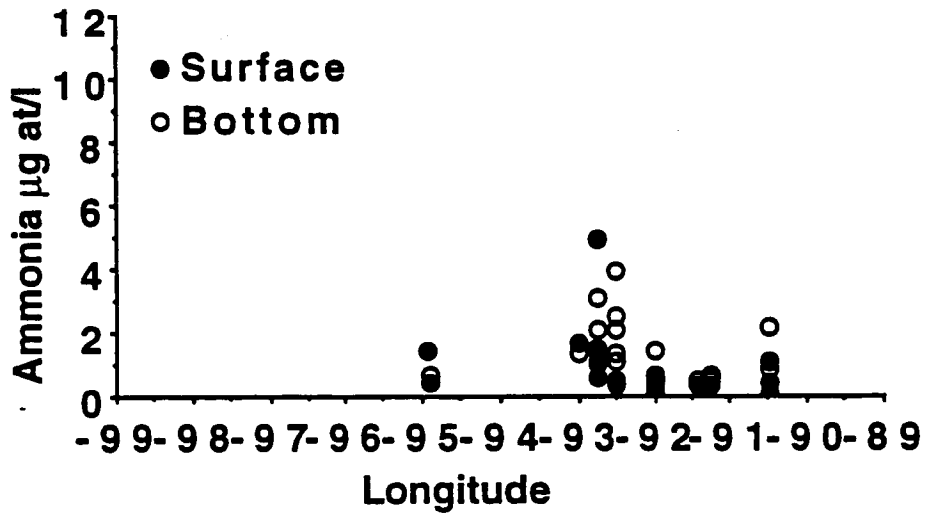
Figure 83. Ammonia concentration (µg at/l) in the surface and bottom waters for stations sampled on Cruise II.
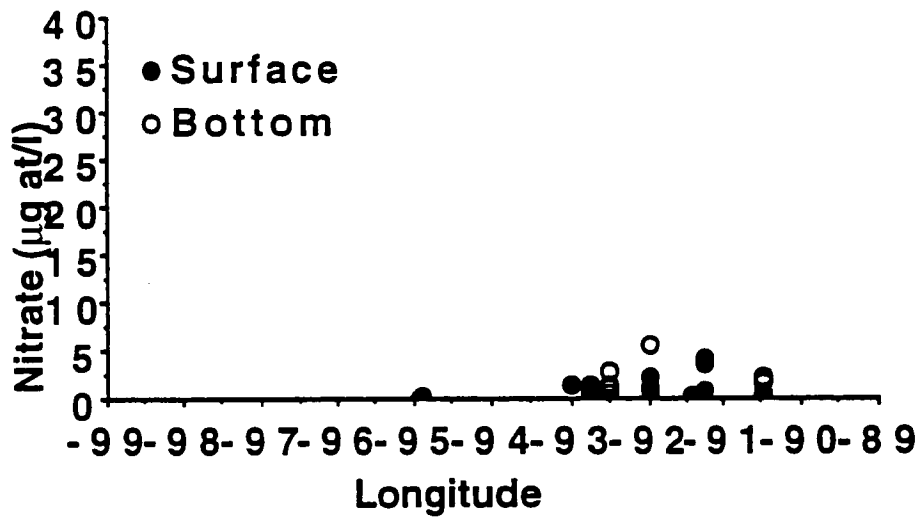
Figure 84. Nitrate concentration (μg at/l) in the surface and bottom waters for stations sampled on Cruise II.
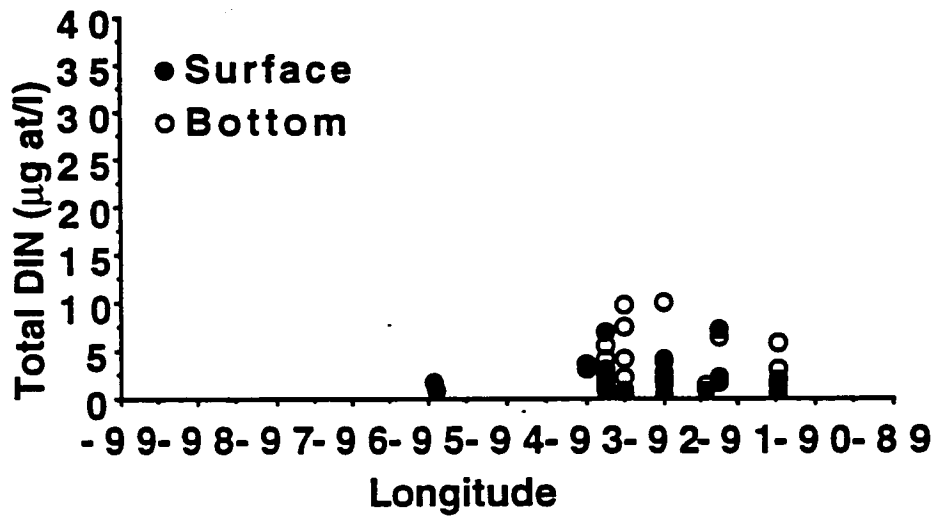
Figure 85. Total dissolved nitrogen concentration (μg at/l) in the surface and bottom waters for stations sampled on Cruise II.
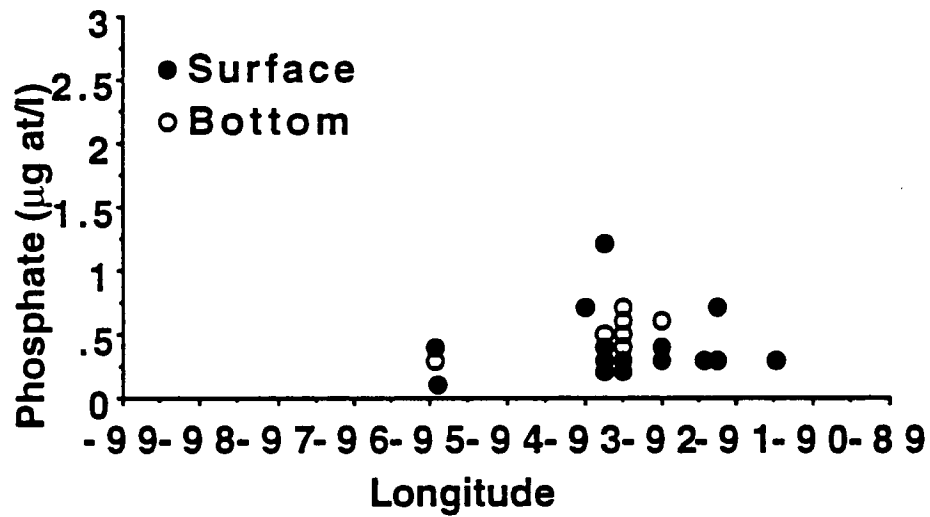
Figure 86. Phosphate concentration (µg at/l) in the surface and bottom waters for stations sampled on Cruise II.
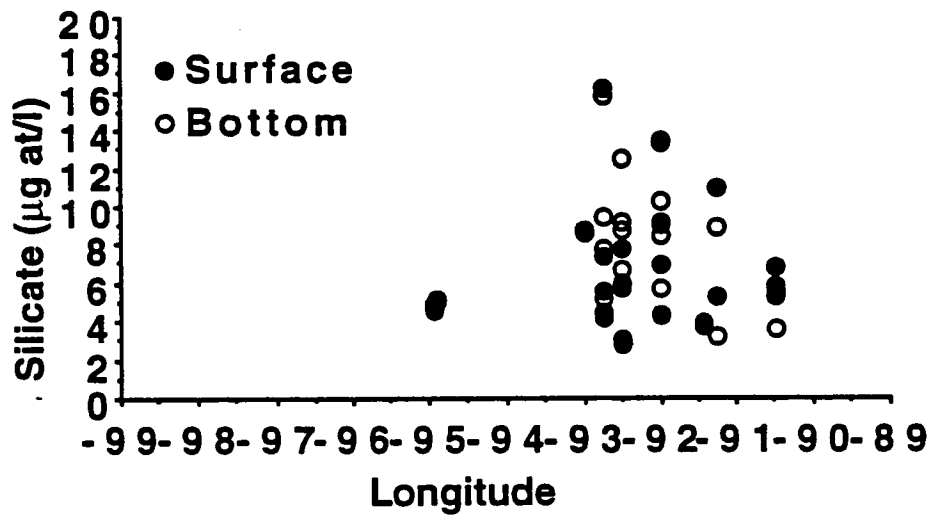
Figure 87. Silicate concentration (µg at/l) in the surface and bottom waters for stations sampled on Cruise II.
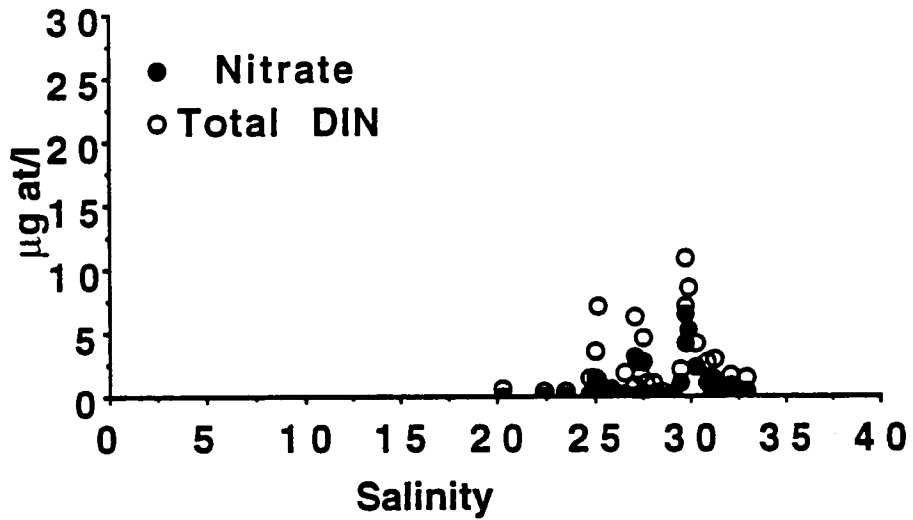
Figure 88. Nitrate and total dissolved inorganic nitrogen concentrations (μg at/l) plotted against salinity in the surface waters for stations sampled on Cruise II.
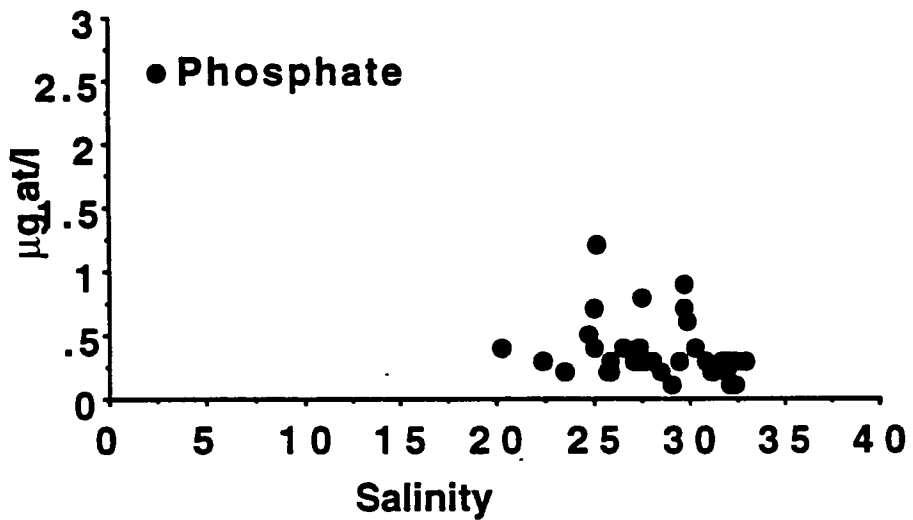
Figure 89. Phosphate concentration (μg at/l) plotted against salinity in the surface waters for stations sampled on Cruise II.
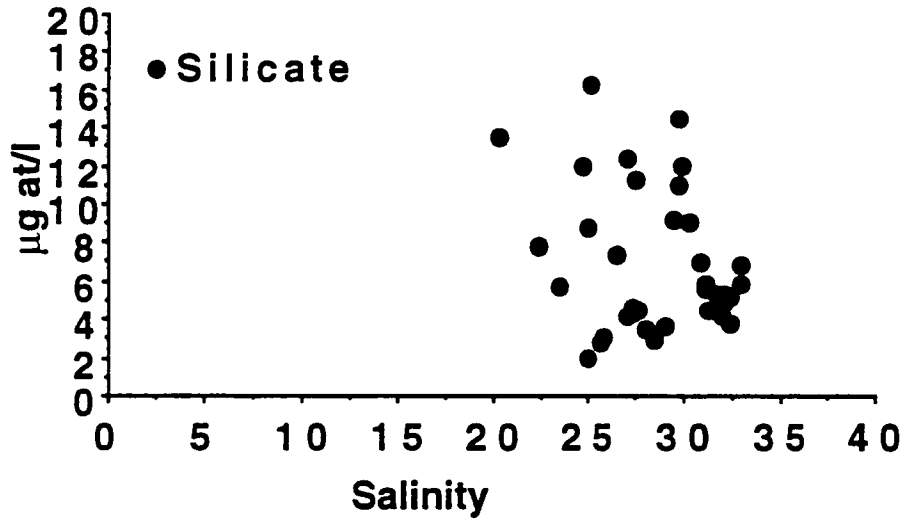
Figure 90. Silicate concentration (µg at/l) plotted against salinity in the surface waters for stations sampled on Cruise II.
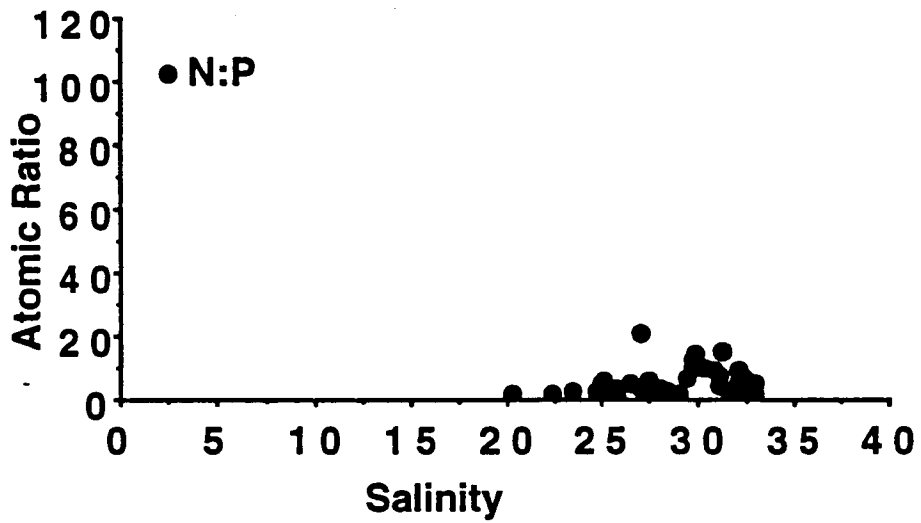
Figure 91. The atomic ratio of dissolved nitrogen and phosphate plotted against salinity in the surface waters for stations sampled on Cruise II.

107
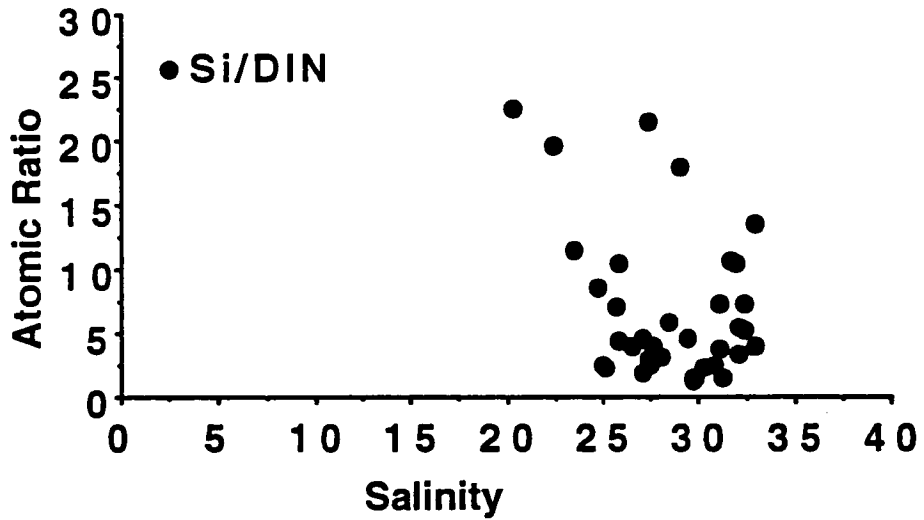
Figure 92. The atomic ratio of dissolved nitrogen and silicate plotted against
salinity in the surface waters for stations sampled on Cruise II.
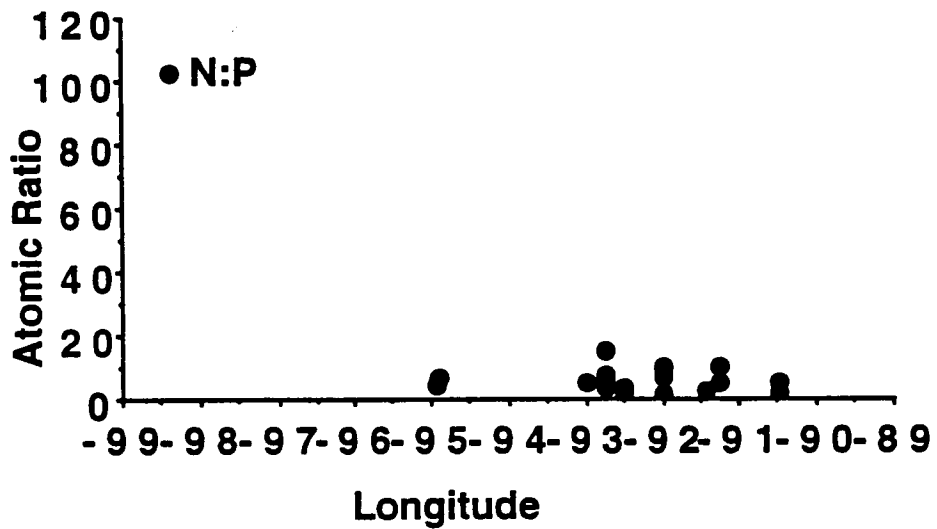
Figure 93. The atomic ratio of dissolved nitrogen and phosphate plotted against
longitude in the surface waters for stations sampled on Cruise II.

108
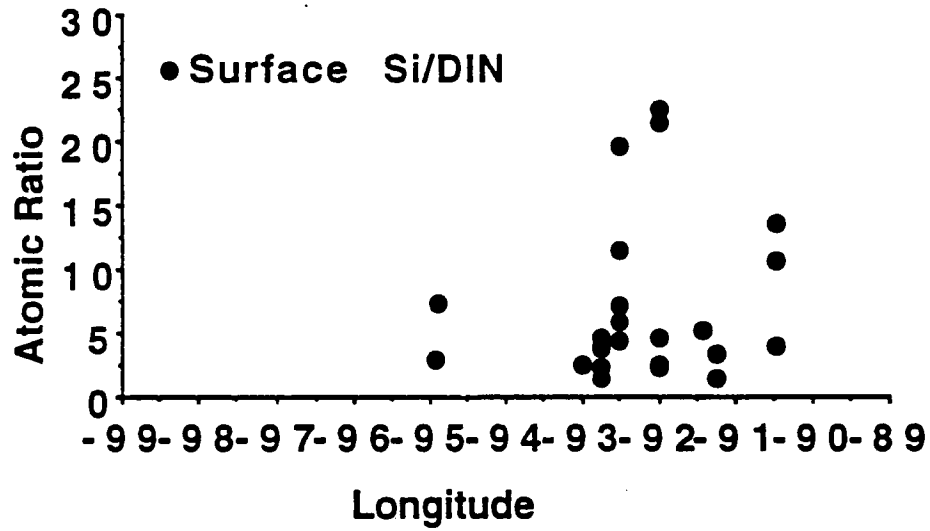
Figure 94. The atomic ratio of dissolved nitrogen and phosphate plotted against longitude in the surface waters for stations sampled on Cruise II.
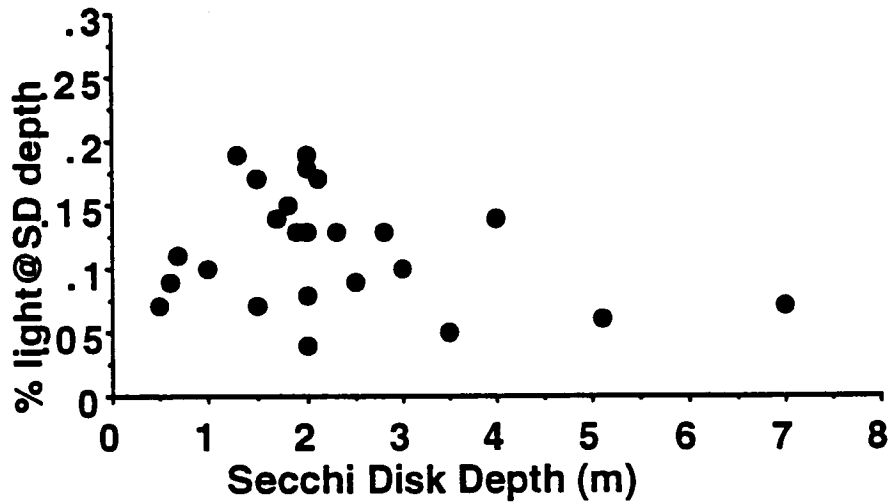
Figure 95. The relationship between the percent of light and secchi disk depth for stations sampled on Cruise II.

Extinction Coefficient (k) Transect A 4/92

K Par

Phytoplankton production

Unscaled Primary Production Rates
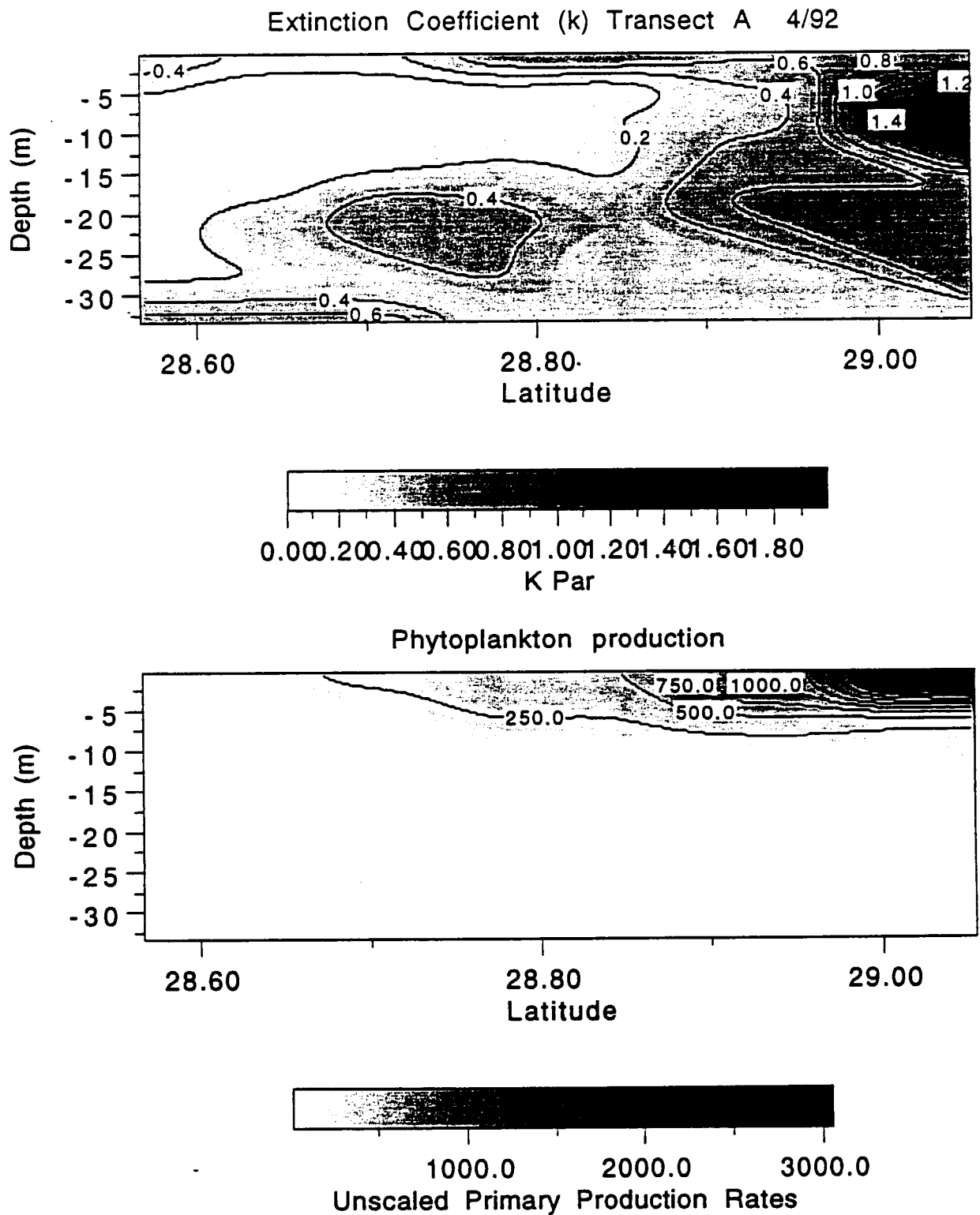
Figure 96. Changes in the extinction coefficient (k) and primary production rates along a transect south of Grand Isle, in April 1992.

110

Turbidity along the longitudinal lines showed no patterns. As in April, the October 1992 distribution of secchi disk depths showed an average incident radiation of about 10% at the secchi disk depth (Figure 95).

b. Contours of Phytoplankton Pigments versus Secchi Disk Depths and Salinity. The highest concentrations of phytoplankton are located in the region of intermediate salinity where the light conditions are beginning to improve. The seaward side of coastal current fronts are therefore sites of intense phytoplankton activity. Here the nutrients are relatively high and the phytoplankton are basically light limited.

c. Cross-shelf Contours. An example of the extinction coefficient across a transect south of Grand Isle, LA, is shown in Figure 96. The coastal plume is shown on the right side, looking westward. Light at the surface does not penetrate below 10 m anywhere along the transect. Placed between the turbid layer and the illuminated water column further offshore is a region of high phytoplankton production.

d. 20-m Isobath Contours of Light Conditions. The 20 m isobath was chosen as an example of changes along the edge of the coastal plume, from the Mississippi River to the Texas coastline (Figure 97). At no place is light impinging on the bottom. This is an important observation, for the extensive hypoxic zones that form during the spring (and last throughout the summer) may be limited on their seaward edge by the oxygen produced in situ on the seafloor (by benthic microalgae, for example).

4. Discussion

This is only the first annual report of several planned reports, and the results are necessarily descriptive. Some of the data sets are not merged (from the hydrographic surveys, for example), and the extensive statistical analyses are just beginning as the data are entered and merged, and more data is collected. The advantage of this project is that a geographically diverse data collection effort, combined with interdisciplinary interactions, will allow us to quantitatively summarize the variability, physical-biological interactions, and structure of the coastal plume.

The secchi disk, whose measurement is a variable depth estimate of a variable source strength (sunlight), has been around longer and used routinely, compared to the newer instrumentation. Its simplicity, low cost and frequent use has provided many measurements of turbidity that should not be ignored for superficial reasons. Measurements from secchi disk depths and optical measurements (from an in situ light meter) are well-correlated. In situ measurements of the compensation depth (defined as where phytoplankton production is zero) are also well-correlated (not shown). Secchi disk measurements are therefore potentially valuable sources of information on the light field within the CBL. It is one of the goals of the LATEX B study to summarize the historical data sets of secchi disk measurements, to determine long-term changes in the turbidity regime (if any), and to offer an empirical conversion factor for this particular locale to convert from Secchi disk depths to % light penetration along a salinity gradient.

Turbidity—quantified as light transmitance, attenuation, and extinction coefficients—has both physical and biological components. Suspended sediments and phytoplankton pigments are the main contributors to the extinction coefficient (K) in coastal systems, although dissolved materials, such as humics, may be significant inhibitors to light transmittance at some wavelengths. The biological components may be less responsive to variations to the forcing functions than the physical components, because, for example, growth and decay rates are involved. Some geophysicists may view the biology as a regrettable complication to elegant mathematical modeling of the coastal plume, but the facts show that the light attenuation by

Latex Cruise 10/1992, 18-20 m isobath
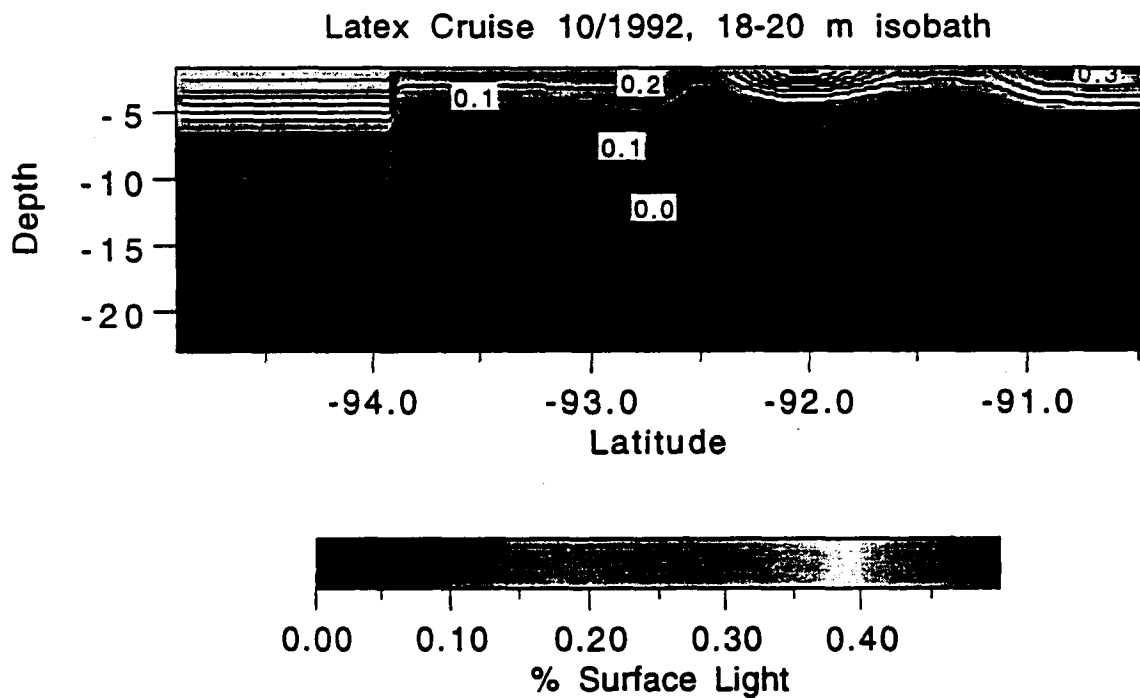
Figure 97. The percent surface irradiance with depth along the 20-meter isobath from the Mississippi River bight to the south Texas coastline. The Mississippi River is approximately on the right hand border, and the Atchafalaya River inputs arrive about one inch to the right.

112

phytoplankton may be significant, even within and near the Mississippi River delta coastal plume. The LATEX B sampling includes other measures of factors contributing to light attentuation, including dissolved fluorescence (humics) and suspended matter that will enable us to discriminate between the phytoplankton, dissolved and non-living particulate components contributing to light attenuation.

The light regime in the LATEX B study area shows substantial variability across the shelf in three directions: over days, weeks, and seasonally. There is also the possibility that there has been decadal changes in the light regime, for two basic reasons. First, the suspended load of the Mississippi River has changed with land-use, water control structures and water delivery patterns. Land-use changes began in the 1800s with European settlement and soon led to flood protection measures, including dam construction. Water diversions from the Mississippi River to the Atchafalaya River began in the 1920s. Thus the seasonal timing, the quantity and the allocation of water supplies and therefore sediment supplies changed in the last 200 years. The second basic influence on decadenal light regime changes involve the nutrients necessary for phytoplankton growth, largely following agricultural practices. The concentration of nitrogen in the Mississippi River doubled since the 1950s, whereas the concentration of silicate declined by 50%. These nutrient changes affected the quantities and qualities of phytoplankton in the coastal plume and therefore the pigments.

This is the first year of LATEX B. We are working to integrate the various measures of light field in the CBL and to quantify the contribution of phytoplankton to the light field. The opportunity to couple the variability of the physical and biological elements within one field study is a large challenge for such a dynamic area.

B. Phytoplankton Pigments (Nancy Rabalais)

A useful, standard, and easy method for the determining phytoplankton biomass in seawater is to estimate the amount of chlorophyll (usually as chlorophyll *a*). Our methods followed those of Parsons et al. (1984) fluorometric determination. Chlorophyll degradation products, phaeopigments, were also determined fluorometrically after acid treatment of the chlorophyll extract. Fluorometry is not a good indicator of phycocyanin- or phycourobilin, phycoerythrin-containing organisms in the phytoplankton community, individuals of which may often be abundant. The small coccoid cyanobacteria have less chlorophyll and more of the other photosynthetic pigments than the larger-sized phytoplankton. And, while fluorometric measurements do not provide the detail of pigment speciation available from high performance liquid chromatography (HPLC), most of the larger-sized fractions of phytoplankton, which contribute proportionally more to phytoplankton biomass, do contain chlorophyll *a*. Thus, the fluorometric method of estimating phytoplankton biomass is suitable for comparison to electronic measures (CTD and MIDAS) and for comparison with salinity and nutrient data, to identify trends in biological communities.

1. Methods

Water samples were collected by bucket for the surface or by 5-liter Niskin bottles for near-bottom or selected depths. The middle of the Niskin bottle was approximately 1-m above the CTD Sea Tech fluorescence probe. MIDAS samples were collected from tubing (outflow or inflow) closest in proximity to the point of measurement of *in vivo* fluorescence in the system (Turner Designs fluorometer). The volume of water filtered through GF/F filters was 100 ml, or less if turbid. If a backlog of filtered samples was anticipated on a cruise, the filters were frozen in liquid nitrogen until further processing. The filters were extracted in 5 ml of 40/60 DMSO (dimethyl sulfoxide)/90% acetone solution for a minimum of 1 hour and not more than 5 hours. Extracts were measured, before and after acidification, on a Model 10 Turner fluorometer. The

fluorometer was calibrated with a chlorophyll a standard (Sigma, *Anacystis* chlorophyll a) on a Varian DMS80 UV, visible spectrophotometer. Calculation of chlorophyll a and phaeopigments were according to the following formulae:

$$\text{Chlorophyll } a = \frac{K\,(\,Fo - Fa)\times vol.\ extr.}{vol.\ filt.}$$

$$\text{Phaeopigments} = \frac{K\,(rFa - Fo)\times vol.\ extr.}{vol.\ filt.}$$

Total Pigments = Chlorophyll a + Phaeopigments

where,   K = constant determined from calibration
r = acid ratio
Fo = fluorescence before acidification
Fa = fluorescence after acidification

Electronic measurements of *in vivo* fluorescence were collected from the LUMCON SeaBird CTD Sea Tech fluorometer, and the LUMCON MIDAS system Turner Designs fluorometer. Surface water salinity values for Cruise I were obtained onboard from the LUMCON Beckman RS5, calibrated by the LUMCON Marine Technician. Surface salinity values for Cruise II were determined on an AutoSal, maintained and calibrated by the LSU Coastal Studies Institute Shop.

2. Results

   a. Cruise I, April 1992. Surface and near-bottom water chlorophyll a, phaeopigments, and total pigment distributions indicated strong cross-shelf gradients, indicative of the Louisiana coastal current, as far west as longitude 95.0°W (Figures 98 and 99). Differences between the concentrations in surface and near-bottom waters were minimal at the nearshore stations and became greater with distance offshore and increased water depth (Figures 98 and 99). South of Galveston Bay, pigment distributions did not indicate cross-shelf gradients, but rather north-south differences that persisted across the short cross-shelf distances sampled on the South Texas extension.

   Extremely high concentrations of chlorophyll a were obtained from surface waters at the second sampling of the nearshore station (P921039) on the S3 line (Atchafalaya Bay). Values exceeded 200 µg l^{-1} and were associated with a dinoflagellate bloom. When this same location was sampled 1 day earlier (P921023), chlorophyll a concentrations were high (44 µg l^{-1}), but not extraordinarily so. For this report, discussions of pigment concentrations mostly exclude P921039, or note its abnormally high concentration.

   Peaks in nearshore concentrations of phytoplankton pigments (both surface and near-bottom) were greatest at Atchafalaya Bay, with lesser peaks at the Sabine Estuary and Galveston Bay (Figure 100). These peaks in pigment concentrations were associated with lower surface salinities indicative of the freshwater outflows of the three systems. The extensive freshwater signature off Galveston and Sabine was related to the flooding in east Texas following heavy spring rains in 1992.

   Surface pigment totals were composed primarily of chlorophyll a. Phaeopigments composed mostly less than 25% of the total pigments and were distributed on an east-west gradient similar to chlorophyll a (Figure 101). Higher percent phaeopigment concentrations were usually associated with oxygen-depleted near-bottom waters.

114
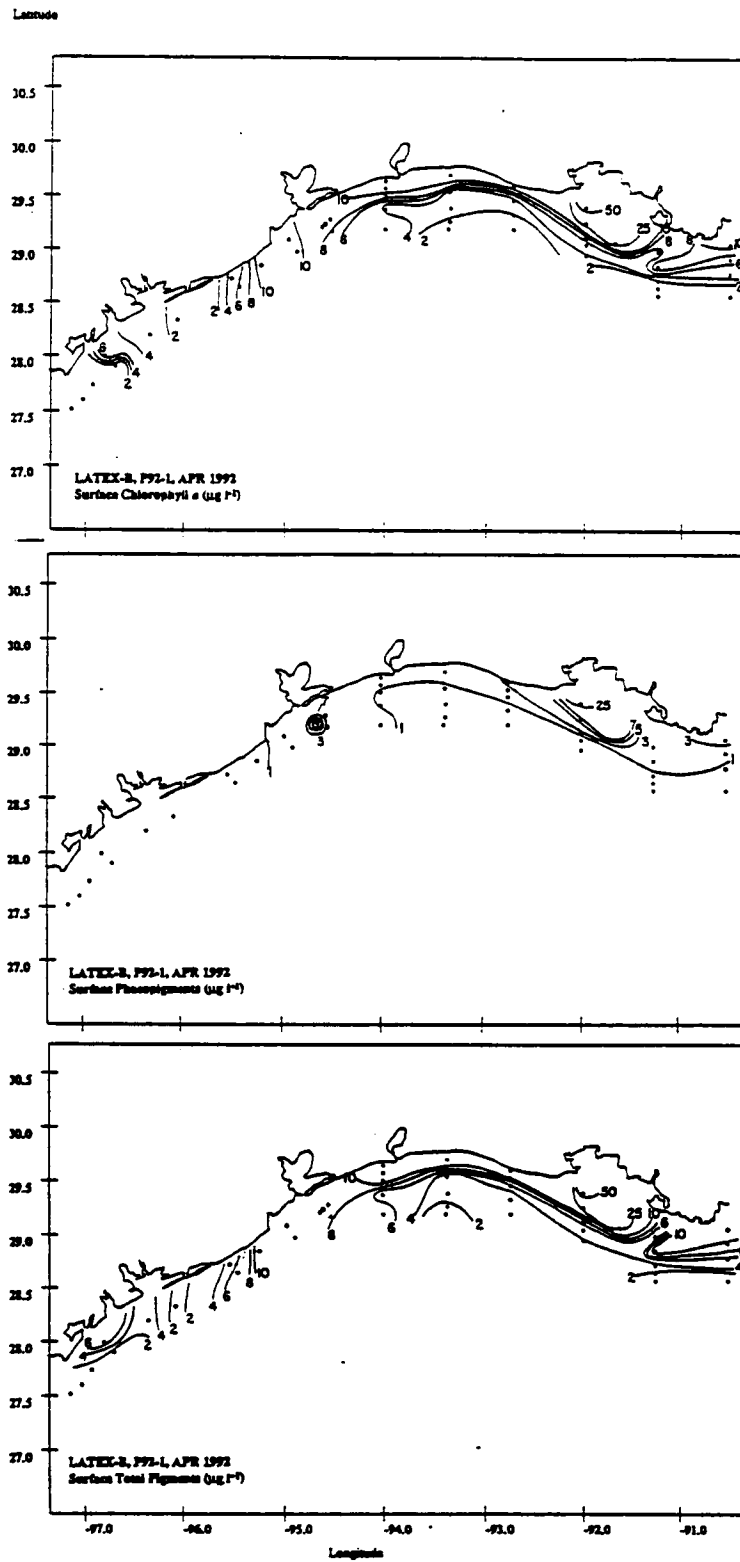
Figure 98. Distribution of surface water chlorophyll *a*, phaeopigments and total pigments for Cruise L

115
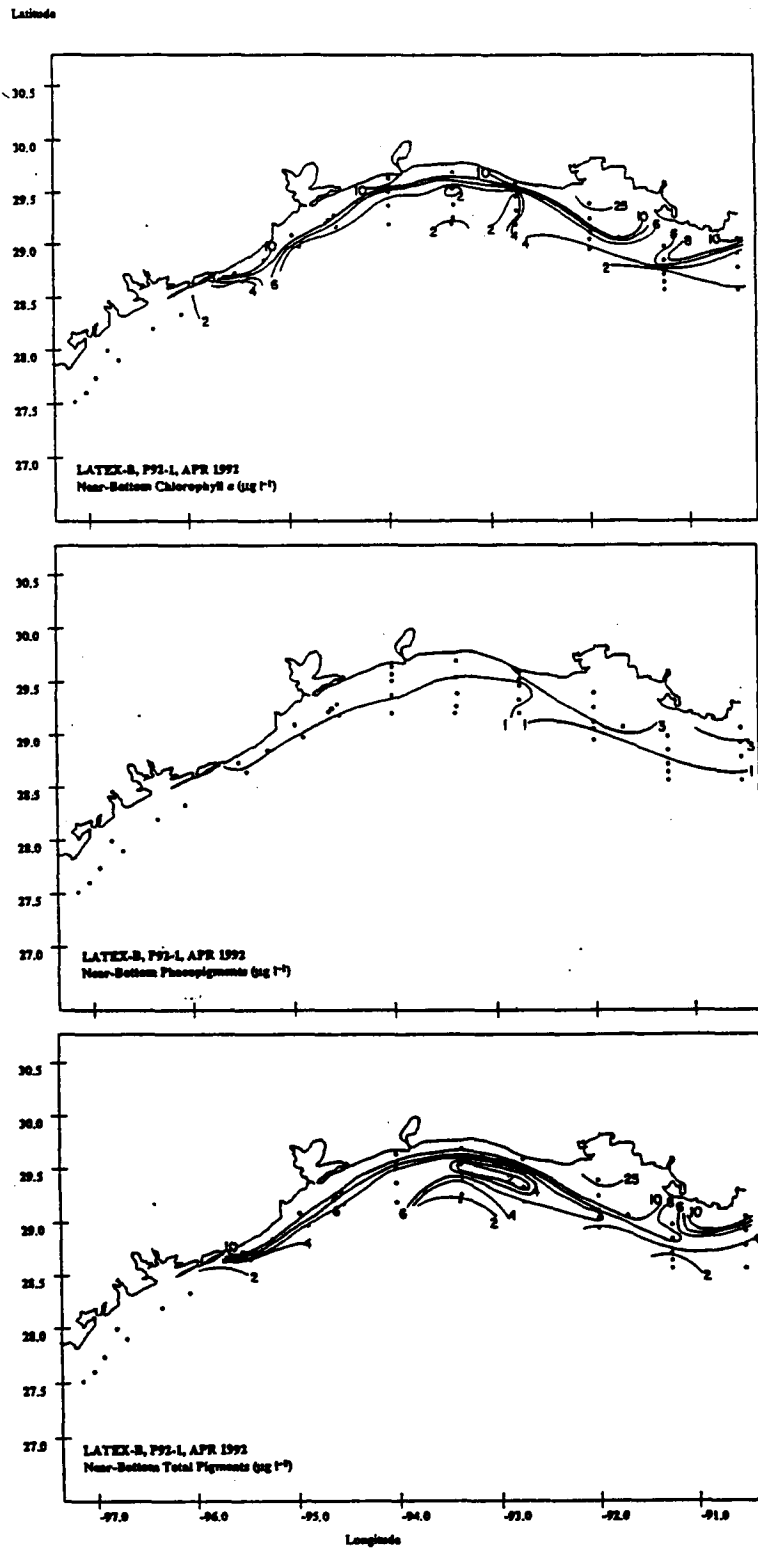
Figure 99. Distribution of near-bottom water chlorophyll *a*, phaeopigments, and total pigments for Cruise I ("near-bottom" is 2-3 meters above the seabed).

116

Mean Surface Chlorophyll A vs Longitude
LaTex B   April 1992
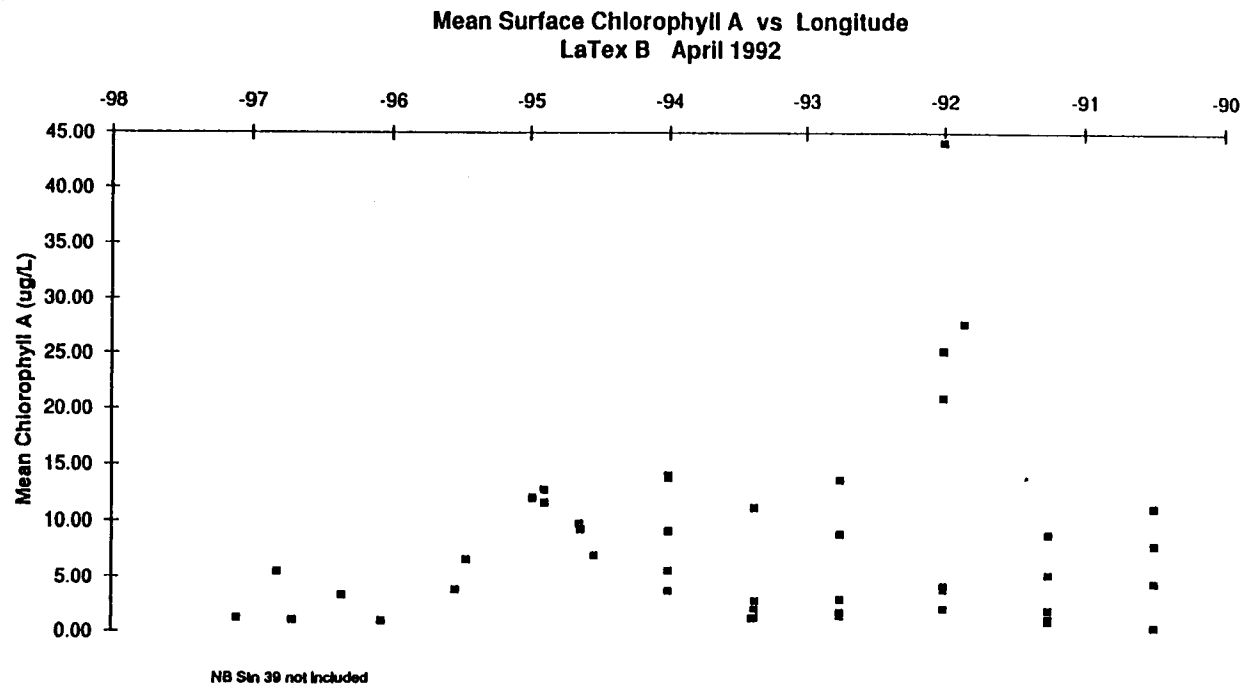
Figure 100. Distribution of surface water chlorophyll *a* by longitude for Cruise I.
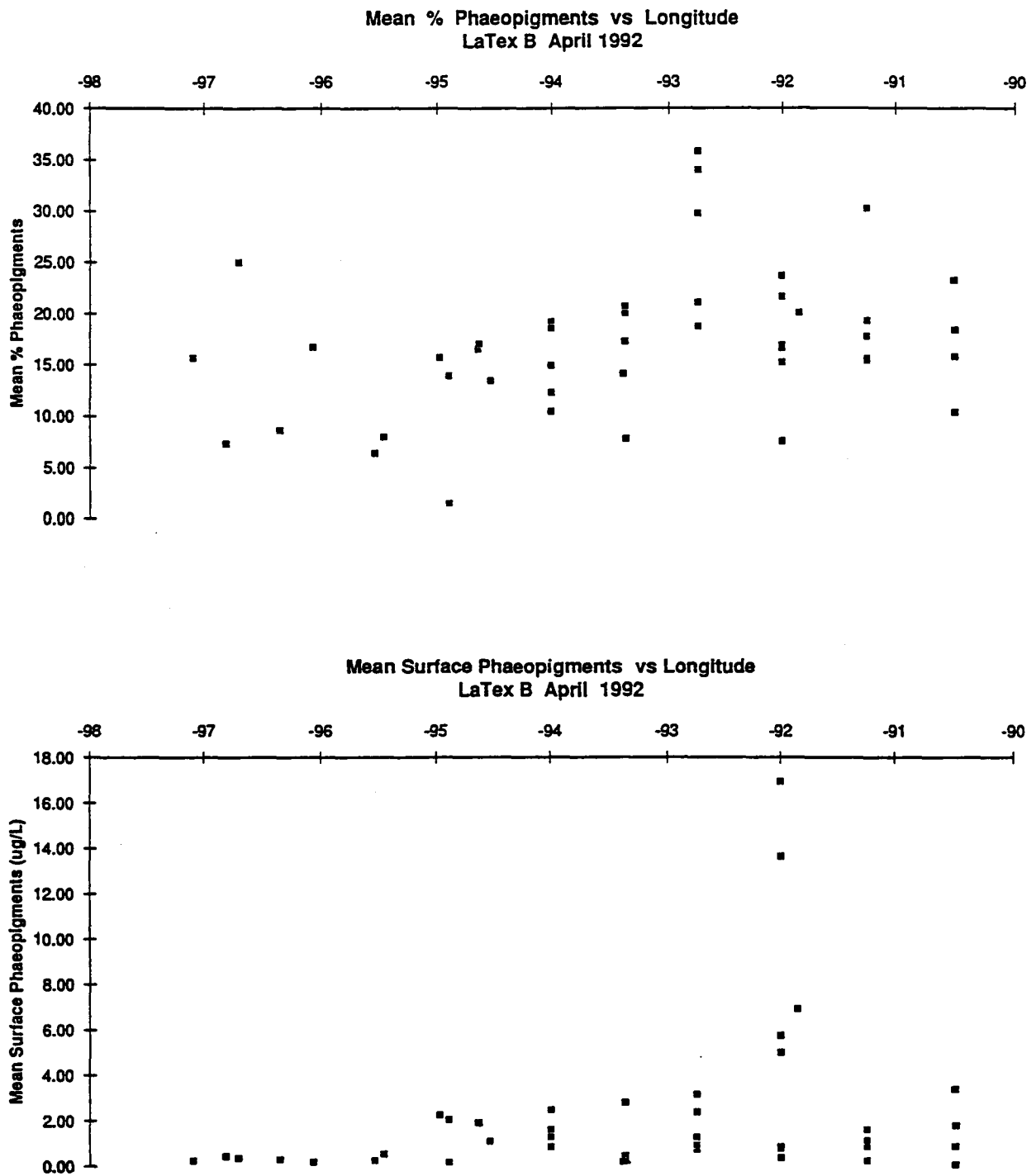
Figure 101. Percent phaeopigments of total pigments (upper) and phaeopigments (lower) in surface waters by longitude for Cruise I.

118

Chlorophyll *a* concentrations in surface water samples (bucket-collected) were very similar to those obtained from the MIDAS flow-through system (Figure 102). This indicates that the flow-through system was collecting the same water mass as the bucket from the surface. On the other hand, the continuously-recording, electronically-derived *in vivo* chlorophyll *a* values from the MIDAS system did not correspond well with the absolute values obtained from the water samples . The function for this relationship [as well as those from most other cruises, e.g., NOAA NECOP, July 1992] was parabolic, with the fluorometer voltage tailing off on the upper end of the absolute chlorophyll *a* concentrations. The distribution for Cruise I also indicated two groups of samples (those below 10 volts and those above 20 volts). Because there was no clear relationship between the absolute chlorophyll *a* values and the scaled *in vivo* fluorometer voltage, cross-shelf contours of phytoplankton biomass were illustrated (Figures 98 and 99) based on discrete water samples rather than the MIDAS data.

A similar comparison of the LUMCON CTD *in vivo* fluorescence probe to absolute concentrations of chlorophyll *a* obtained from water samples showed a much better relationship than the MIDAS comparison. Although the linear relationship does not fall through the origin, it is offset from the 1:1 relationship by a uniform value. Cross-shelf contours of CTD *in vivo* fluorescence will be good representations of the chlorophyll *a* biomass in the study area.

With the exception of a few values above 32 ppt, the salinity of bucket-collected surface waters compared well with the MIDAS system salinity. We feel confident, therefore, that the values obtained from the Beckman RS5 were representative of the water samples from which phytoplankton pigments and nutrients were determined. The peak chlorophyll *a* concentration (209 µg l^{-1}) was associated with the lowest salinity water (13.7 ppt). Other surface water salinities exceeded 21 ppt. Surface water chlorophyll *a* biomass peaked in the 21 to 25 ppt range; these results are consistent with many other chlorophyll *a* biomass vs. salinity distributions. Phytoplankton biomass peaks at 20-25 ppt where turbidity of the waters is reduced and light limitation does not affect phytoplankton growth, but where nutrient concentrations have not been diluted to the point where they may become limiting.

The dissolved nutrients generally decreased with an increase in salinity away from the freshwater sources (see Section III.B), but the relationships were far from simple. The dissolved inorganic nitrogen pool was dominated by nitrate, and DIN was usually much greater than silicate concentration so that the silicate:nitrate ratio was mostly below 1:1. Chlorophyll *a* biomass was high across a broad range of nutrient concentrations but generally decreased as nutrients were diluted on the seaward end of the plume.

b. Cruise II, October 1992. Surface and near-bottom water chlorophyll *a*, phaeopigments, and total pigment distributions indicated strong cross-shelf gradients, indicative of the Louisiana coastal current, as far west as longitude 95°W (Figures 103 and 104). Differences between concentrations in surface and near-bottom waters were minimal at all stations, reflecting the well-mixed nature of the water column at most stations. Nearshore concentrations were, in general, much lower for October 1992 than for April 1992 (cf. Figures 98 and 99). The overall trend for chlorophyll *a* concentrations was also lower in October 1992 than in April 1992 (mean = 4.39 µg l^{-1} ± 0.41 SE, n = 79, October 1992; mean = 7.54 µg l^{-1} ± 0.11 SE, n = 74, April 1992).

The peaks in nearshore chlorophyll *a* concentrations (both surface and near-bottom waters) were located at the most nearshore station (P922145) off Atchafalaya Bay (Section S3) (Figure 105). Lesser peaks were located at the mouth of Terrebonne Bay and the Calcasieu Estuary. Higher chlorophyll *a* concentrations were associated with lower surface salinities from the Atchafalaya River outflow and the shoreward edge of the Louisiana coastal current.

119

Chlorophyll A: Bucket Sample vs Midas Tap-in

Latex B   April 1992

NB Sta. p921039 not included

■ Midas Tap-in

Midas Tap-in Chlorophyll A (ug/L)

Bucket Sample Chlorophyll A (ug/L)
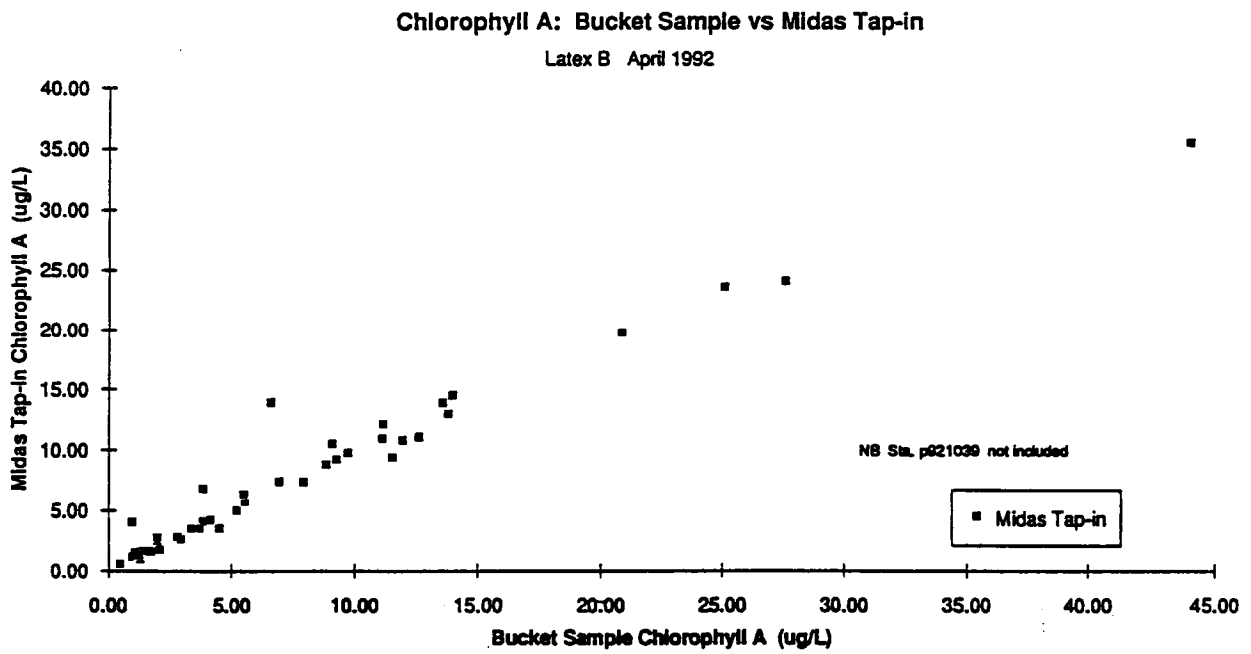
Figure 102. Relationship between chlorophyll *a* concentrations in MIDAS tap-in
samples and surface water collected by bucket for Cruise I (with
station P921039 excluded).
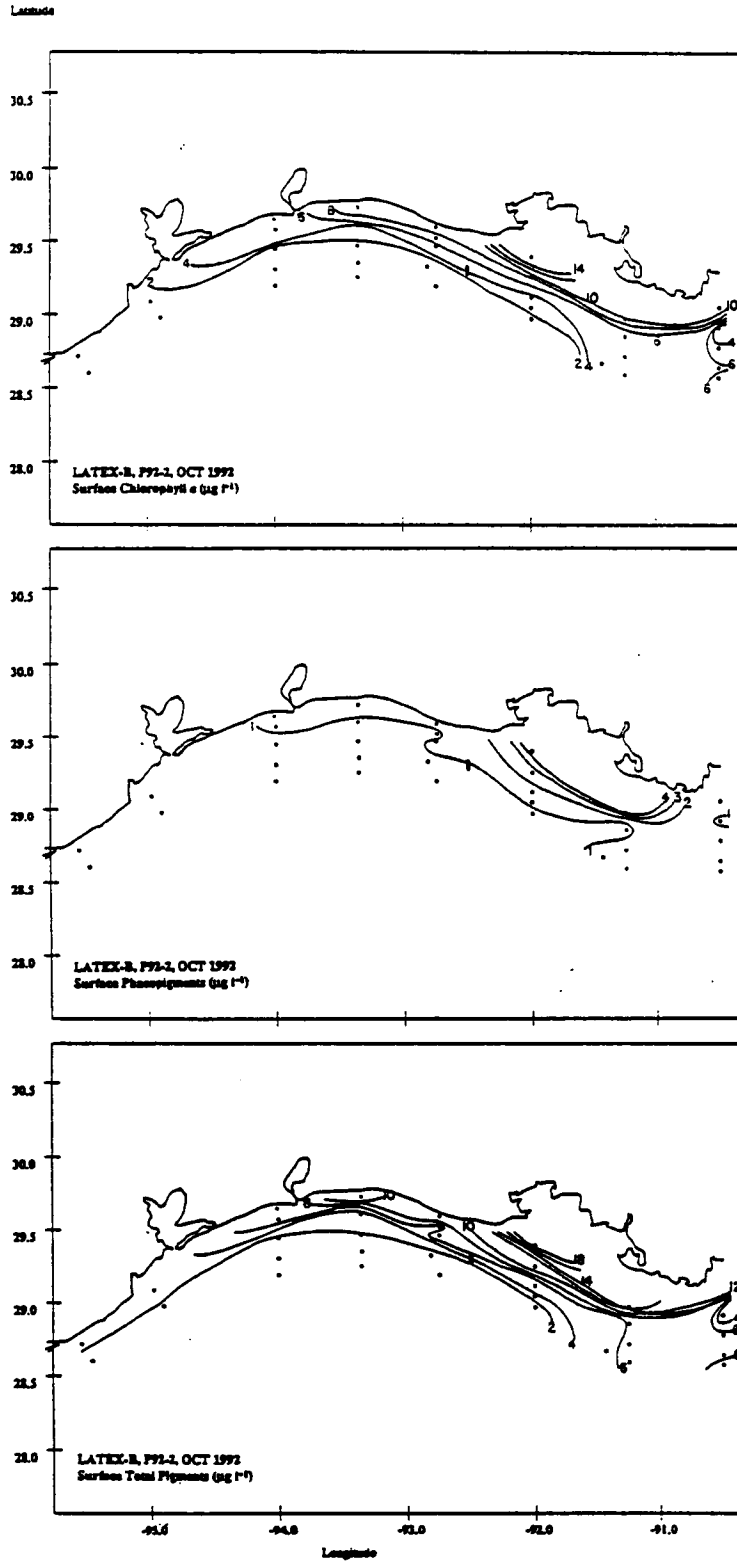
Figure 103. Distribution of surface water chlorophyll *a*, phaeopigments and total pigments for Cruise II.

121
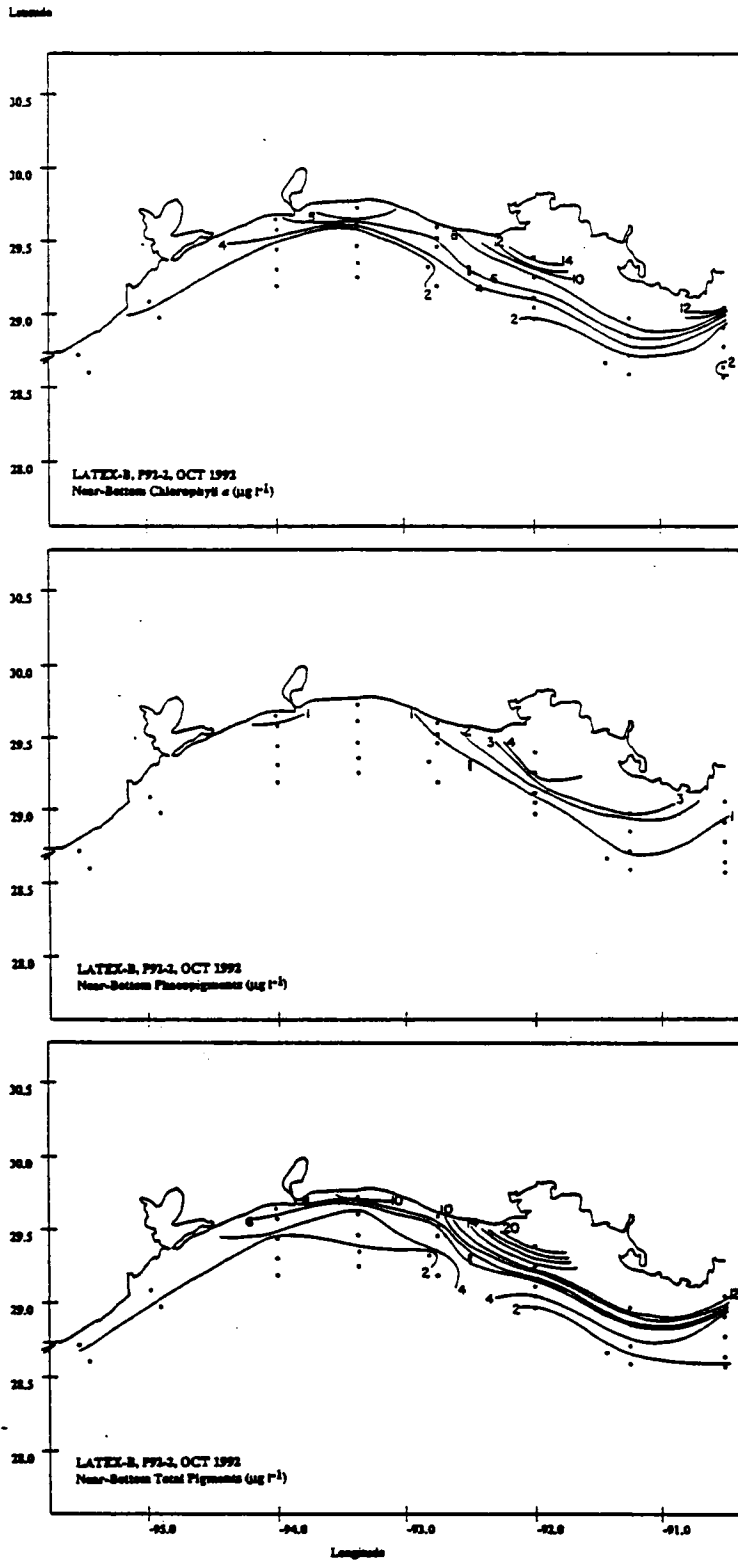
Figure 104. Distribution of near-bottom water chlorophyll a, phaeopigments and total pigments for Cruise II ("near bottom" is 2-3 meters above the seabed).

122

Mean Surface Chlorophyll A vs Longitude
LaTex B   October 1992
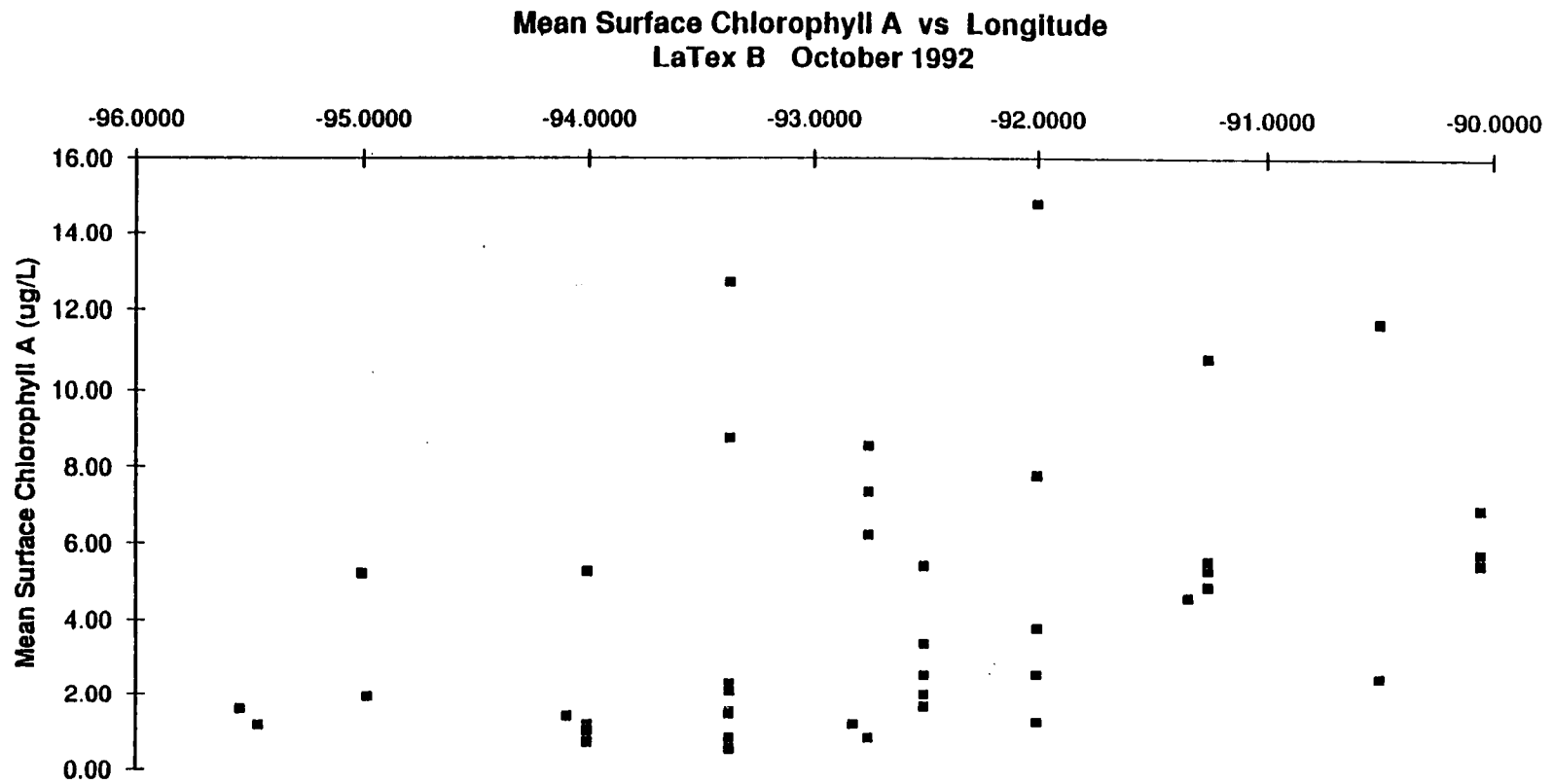
Figure 105. Distribution of surface water chlorophyll *a* by longitude for Cruise II.

As on Cruise I, surface pigment totals were composed primarily of chlorophyll a. Phaeopigments composed mostly less than 20% of the total pigments (Figure 106) and were distributed on an east-west gradient similar to chlorophyll a (Figure 106). Higher % phaeopigment concentrations, as observed in some oxygen-depleted, near-bottom waters in April 1992 were also present in some near-bottom waters in October 1992, but most near-bottom waters (Stations P922101-P922164) were near oxygen saturation in October 1992.

As on Cruise I, chlorophyll a, phaeopigment, and total pigment concentrations in surface water samples (bucket-collected) were very similar to those obtained from the MIDAS flow-through system. This indicates that the flow-through system was collecting the same water mass as the bucket from the surface. On the other hand, the continuously-recording, electronically-derived *in vivo* chlorophyll a values from the MIDAS system did not correspond well with the absolute values obtained from the water samples. The function for this relationship (as well as those from other cruises) was parabolic, with the fluorometer voltage tailing off on the upper end of the absolute chlorophyll a concentrations. Because there was no clear relationship between the absolute chlorophyll a values and the scaled *in vivo* fluorometer voltage, cross-shelf contours of phytoplankton biomass were illustrated (Figures 103 and 104) based on discrete water samples rather than the MIDAS data.

A similar comparison of the LUMCON CTD *in vivo* fluorescence probe to absolute concentrations of chlorophyll a obtained from water samples showed a positive, strong, linear relationship offset from the 1:1 relationship by a uniform value. Cross-shelf contours of CTD *in vivo* fluorescence will be, therefore, good representations of the chlorophyll a biomass in the study area.

With the exception of one value, the salinity of bucket-collected surface waters compared well with the MIDAS system salinity. Comparison of this value with the near-surface CTD salinity values indicated that the bucket value was in error, and it was deleted from the data base. We are confident, therefore, that the remaining surface salinity values obtained from the AutoSal were representative of the water samples from which phytoplankton pigments and nutrients were determined. The peak chlorophyll a concentration (14.8 µg l^{-1}) was associated with the lowest salinity water (20.2 ppt) collected on Cruise II. Other surface water salinities exceeded 23 ppt. Surface water chlorophyll a biomass peaked in the 20 to 27 ppt range; these results are consistent with many other chlorophyll a biomass *vs.* salinity distributions.

Cruise II nutrient concentrations, in general, were approximately half the concentrations measured for Cruise I. The dissolved nutrients generally decreased with an increase in salinity away from the freshwater sources (see Section III.A), but the relationships were far from simple. Unlike April 1992, silicate concentrations generally exceeded nitrate concentrations, and the silicate:nitrate ratio consistently exceeded 1:1. Chlorophyll a biomass was high across a broad range of nutrient concentrations. There were no clear relationships of chlorophyll a concentration with nutrient concentration, with the exception of a general decrease in chlorophyll a with a decrease in silicate concentration.

C. Phytoplankton Survey (Quay Dortch)

There were three primary purposes for measuring phytoplankton species composition as part of the LATEX B program: (1) to use phytoplankton as indicators of water sources and mixing; (2) to trace phytoplankton from surface to bottom layers, where their decomposition contributes to oxygen depletion; and, (3) to extend our understanding of processes affecting phytoplankton abundance and composition from the extensively studied near-plume areas to the unstudied, extended plume areas. In this report, the focus will be on the first goal because (1) no cruises have been conducted yet during the summer when hypoxia is prevalent and (2) with only
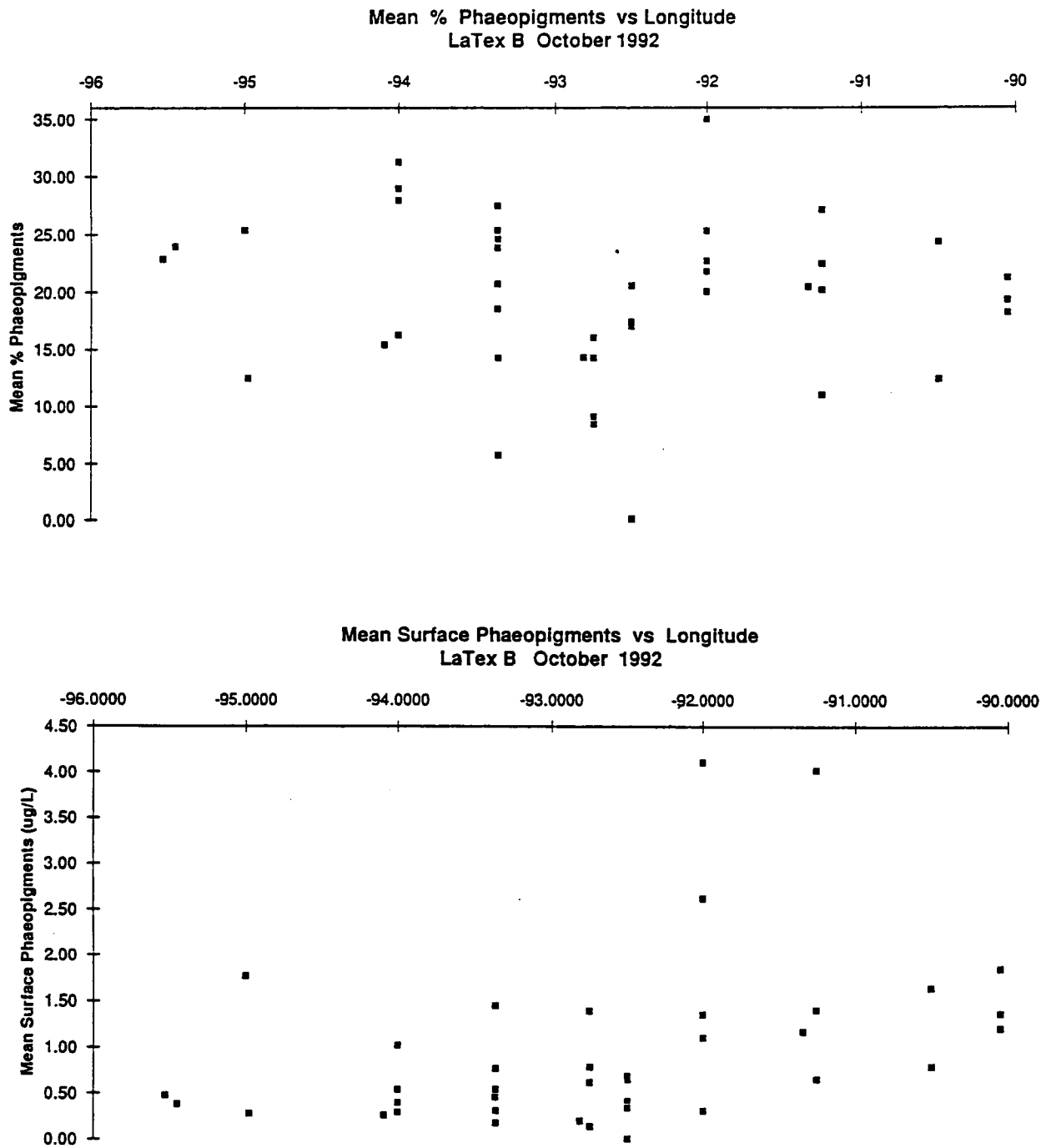
Figure 106. Percent phaeopigments of total pigments (upper) and phaeopigments (lower) in surface waters by longitude for Cruise II.

two cruises in the extended plume there is too little data from which to draw meaningful conclusions. Finally, although it was not a goal of the research, this data greatly expands the data base concerning the distribution of phytoplankton species that cause toxic and noxious blooms on the Louisiana and Texas continental shelves. These blooms, which have increased world-wide, perhaps in response to increasing coastal eutrophication (Smayda, 1989, 1990; Shumway, 1990; Hallegraeff, 1993), can have major economic consequences.

Using phytoplankton as water mass tracers or indicators of mixing is a novel approach, possible only where there is sufficient background information to establish recurrent patterns, whose cause is reasonably well understood. With the data which has been or will be collected as part of this program and others (NOAA NECOP; LaSER/NSF EPSCOR; LEQSF) from 1989-1994, sufficient background data will be available (>3000 samples). These indicators are based in part on obvious distributional differences and in part on a mechanistic understanding of the factors controlling phytoplankton distributions in regions influenced by large rivers (Figure 107). An alternate approach will be to perfom statistical analyses to determine specific groupings, but, because the factors controlling the groups may not be known, interpreting the results will be more difficult. However, when all the data are compiled, this approach will also be taken to find possible relationships which have been missed.

1. Phytoplankton as Indicators

a. Indicators of Fresh Water Input. River waters contain a variety of specifically fresh water phytoplankton, most of which disappear at very low salinities. However, a few are sufficiently halotolerant that they can survive for some time at higher salinities and serve as a marker of freshwater input. The small (1-2 μm), coccoid cyanobacteria of the species *Synechococcus* have a variety of photosynthetic pigments besides chlorophyll *a*, which give them distinctive colors under epifluorescence microscopy (Table 5). One group, containing the pigment phycocyanin (PC), is usually the only cyanobacteria at low salinities (Waterbury et al., 1986; Vaulot and Ning, 1988). Not quite as halotolerant is one diatom species, *Asterionella formosa*, and several genera of colonial green algae, *Scenedesmus* and *Pediastrum*, which are often seen near river mouths during periods of high river flow.

Table 5. Appearance of different pigment groups of cyanobacteria (0.2 to 3 μm size fraction) under epifluorescence microscopy with blue and green excitation light.

Pigment Group	Blue Light	Green Light
Phycocyanin	Dull Red	Bright Red
Low Phycourobilin/Phycoerythrin	Orange*	Orange
High Phycourobilin/Phycoerythrin	Yellow*	Orange

*Difficult to distinguish because the amounts of phycourobilin are quite variable and represent a continuum rather than distinctly different types. The low PU/PE includes a range of hues, but the high PU/PE contains only cells which are distinctly yellow under blue light. Further, very high phycourobilin cells may fluoresce green (Olson et al., 1988) and may not be counted because they cannot be distinguished from green fluorescing, heterotrophic bacteria (stained slightly by glutaraldehyde).

b. Indicators of Offshore, Oligotrophic Waters. Phytoplankton in offshore waters are generally small and dominated by one group of small coccoid cyanobacteria, the high phycourobilin phycoerythrin-containing *Synechococcus* (High PU/PE) (Table 5) (Olson et al.,

126

Conveyor Belt

Mississippi River Plume

River Input
High Nutrient
Freshwater
Phytoplankton

Nutrient   Regenerated Production   Chl   Nutrients and Light   Light Limited

Limited ·   Max   Sufficient   Low Chl

Low Chl   High zooplankton and bacteria   Low zooplankton

Small Flagellates   Large Diatoms

C flux to benthos
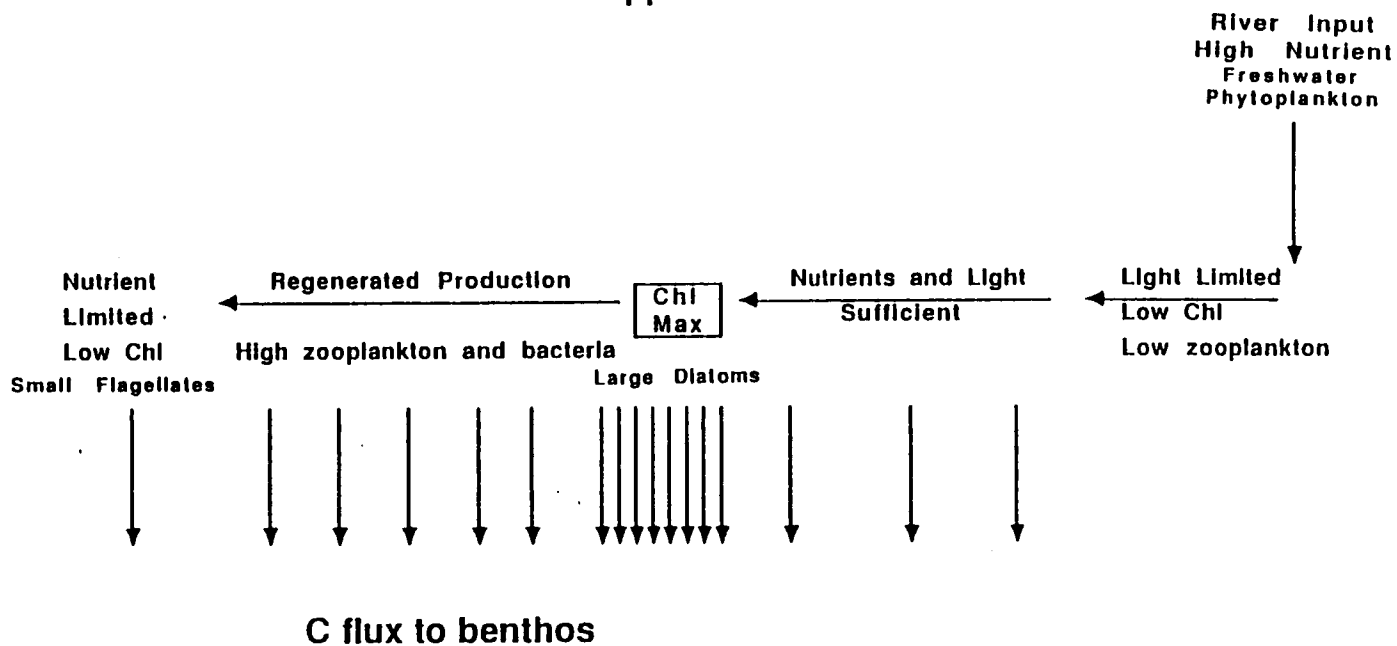
Figure 107. Conceptual model of phytoplankton processes in the plume and
extended plume of the Mississippi River.

1988). Due to the very low silicate concentrations in offshore waters, there are very few diatoms, especially in the large size fractions. The large size fraction does contain green-fluorescing heterotrophic dinoflagellates (Shapiro et al., 1989; Carpenter et al., 1991), which are a distinctive marker of oligotrophic waters in the Gulf of Mexico.

   c. Riverine Plume Indicators. Phytoplankton biomass and growth is usually maximal at some distance from the river mouth because it is necessary for the sediment to settle out so there is enough light to stimulate photosynthesis (Figure 107). The first species to respond is almost always *Skeletonema costatum,* an opportunistic, fast-growing diatom. Growth of this species is then followed by that of other diatoms. Further down the axis of the plume, the nutrients become depleted, and although there is plenty of light, there are insufficient nutrients to support high phytoplankton biomass. Thus, it can be hypothesized that high numbers of *S. costatum* will indicate the high productivity core of the plume, but that diatoms will dominate along the axis of the plume until the nutrients become depleted or diluted. As mentioned above, PC cyanobacteria will also indicate the path of the river plume.

   d. Indicators of Mixing. Displacement of any of these species or groups from their usual pattern might indicate mixing between dissimilar water types. For example, a squirt might inject coastal diatoms into oligotrophic waters. The most reliable indicator at present are the small coccoid cyanobacteria, two groups of which have already been described. A third group, low-phycourobilin, phycoerythrin-containing cyanobacteria (Low PU/PE), which appears to be intermediate, is also observed (Table 5). The pigment differences may be related to either salinity or light quality (Wood et al., 1985; Waterbury et al., 1986; Vaulot and Ning, 1988; Pick, 1991), but, regardless, because they are halotolerant and persist when the salinity changes, they are specific indicators. Thus, the degree to which the high-PU/PE or PC cyanobacteria dominate and are mixed with each other and the low-PU/PE cyanobacteria can indicate what types of water are mixing. Unfortunately, a time-scale cannot yet be put on the mixing because we do not yet have any data on survival rates after mixing.

2. Method

   The method for preserving and counting phytoplankton was adapted from Murphy and Haugen (1985), Shapiro and Haugen (1988), and Shapiro et al. (1989). Phytoplankton samples were collected at the surface using a bucket and at the bottom using 10-liter Niskin bottles on a CTD Rosette. If there was a mid-water fluorescence maximum (Sea Tech Fluorometer on SeaBird CTD), samples were also taken with a Niskin bottle. Between 0.1 and 1 liter was preserved with 50% glutaraldehyde to a final concentration of 0.5% (by volume) and refrigerated for at least 1 hour and not more than 24 hours prior to size fractionated filtration. Polycarbonate filters were used throughout. Phytoplankton in the 3-8 μm and > 8 μm size fraction were stained with proflavine monohydrochloride (Sigma P-4646, 0.33 g/200 ml distilled, deionized water). Before staining samples < 25 ml were made up to 25 ml using 0.2 μm filtered seawater of approximately the same salinity. If possible samples were filtered without vaccuum, but if necessary < 100 mm vacuum was applied. The filters were transferred to slides and mounted with low fluorescence, low viscosity immersion oil. The 0.2-3 μm size fraction was counted immediately, the 3-8 μm size fraction was stored in the refrigerator and counted within several days. The > 8 μm filters were stored frozen and counted back in the lab within 60 days. Phytoplankton were counted on a BH2-RFA epifluourescence microscope with blue and green excitation (excitation filters BP-490 and BP-545, barrier filters 0-515 and 0-590, and dichroic mirrors DM500 and DM580). Table 6 outlines the types of organisms counted in each size fraction.

128

Table 6. Common phytoplankton groups counted in each size fraction.

Size	Phytoplankton Groups
0.2 - 3.0 μm (count immediately on ship)	Coccoid cyanobacteria—mostly Synechococcus Autotrophic flagellates Heterotrophic flagellates
3.0 - 8.0 μm (count on ship within several days)	Photosynthetic flagellates and non-flagellates Heterotrophic flagellates and non-flagellates Cryptomonads Athecate dinoflagellates Diatoms Coccoid cyanobacteria
> 8.0 μm (freeze and count in lab, detailed taxonomy to species where possible)	Diatoms Dinoflagellates Ciliates Cryptomonads Colonial cyanobacteria Colonial, freshwater chlorophytes

3. Results

a. Cruise I, April 1992. Distribution of Different Size Classes. The total numbers of phytoplankton of all sizes was high at the surface and there were no strong cross-shelf gradients, indicative of the coastal boundary current (Figure 108). The highest concentrations were associated with the Atchafalaya River, Sabine Pass, and Corpus Christi Bay. Some of these same areas showed high chlorophyll concentrations, but others did not match the chlorophyll distributions. For example, the high phytoplankton concentrations off Sabine Pass are not reflected in the chlorophyll data. Most of the high phytoplankton patches are associated with areas of low salinity. Off the Louisiana coast the bottom concentrations and distributions were similar to that at the surface, whereas off Texas, the bottom concentrations were lower and generally constant over wide areas. There are no major differences in water depth or stratification which can explain the differences in bottom water phytoplankton concentrations.

The same basic patterns were observed for the two smallest size fractions, 0.2-3 μm and 3-8 μm, with some minor differences. This is to be expected since they make up the bulk of the phytoplankton in terms of numbers. However, the numbers of phytoplankton > 8 μm are quite different. The highest values are found in the plume of the Atchafalaya River. The values are generally high along the shelf and decrease off of south Texas. There is no sharp break which would indicate the presence of the coastal boundary current. In general the pattern of large cell numbers is similar to that for chlorophyll concentrations because (1) although they are numerically less abundant, they are larger so they make up more of the biomass and (2) the small coccoid cyanobacteria, which make up most of the total phytoplankton numbers, have less chlorophyll and more of other photosynthetic pigments than the diatoms.

Distribution of Specific Groups or Species. The % cyanobacteria (0.2-3 μm)/total phytoplankton at the surface (Figure 109) was lowest in the plumes off of the Atchafalaya, Sabine Pass, and Corpus Christi. It tended to increase toward the west and offshore. At both the eastern and western ends of the study area, there were substantial cross-shelf gradients of the type expected when crossing the coastal boundary current. Similarly, the cyanobacterial pigment groups display the location of fresh water plumes (high % PC and low % High PU/PE), the
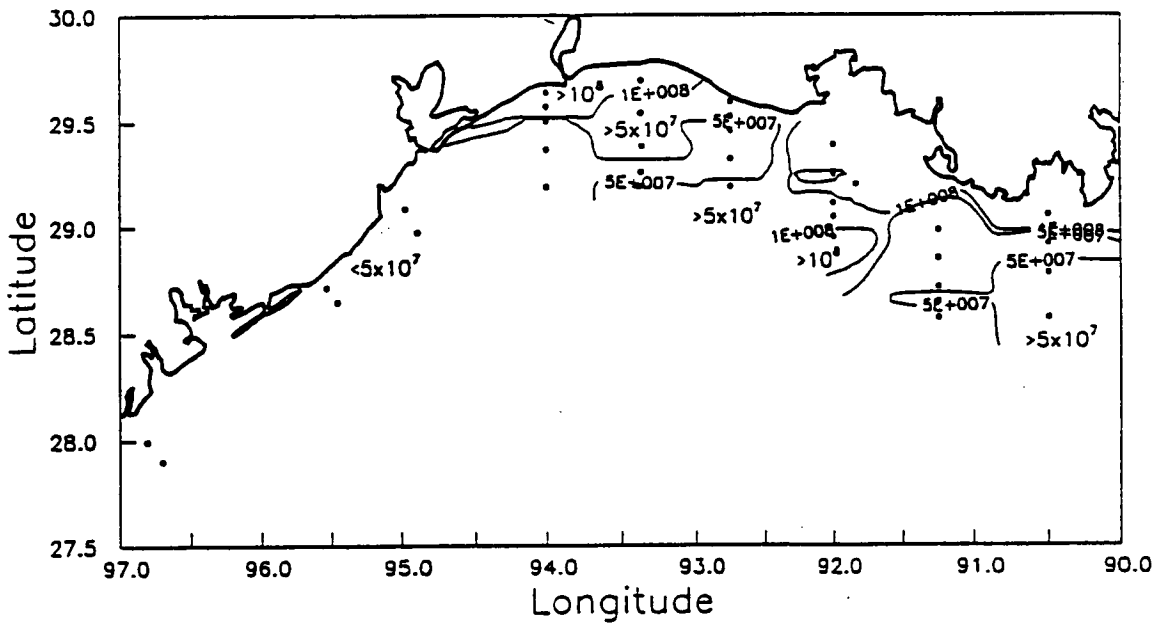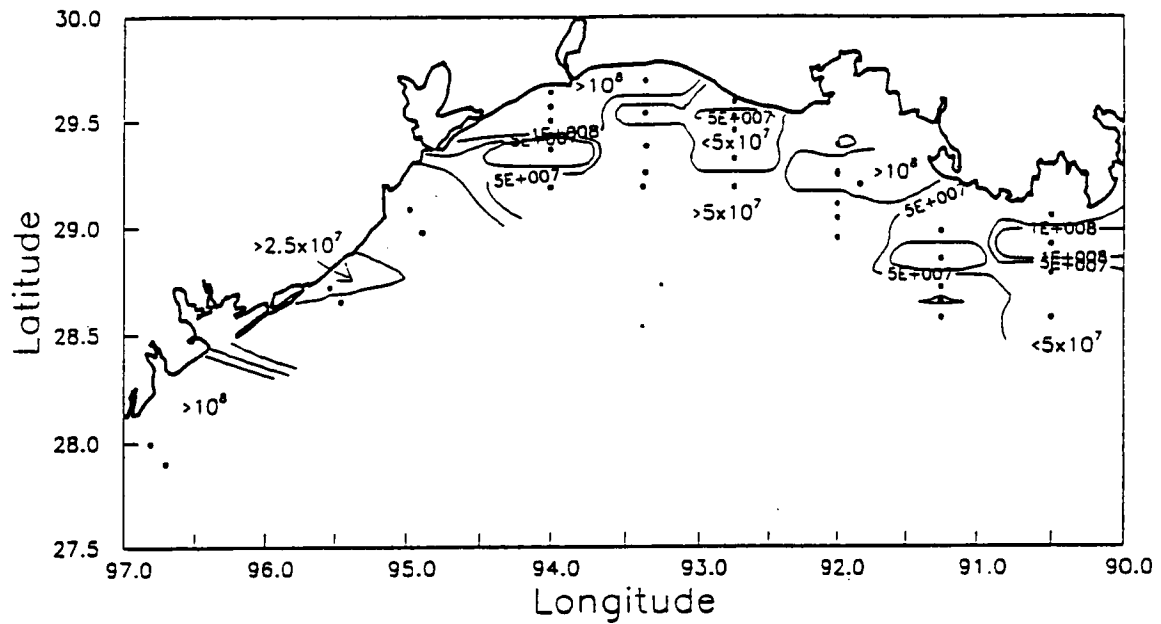
Figure 108. Contours of total numbers (number/liter) of phytoplankton in all size
fractions during Cruise I: surface (upper); bottom (lower).
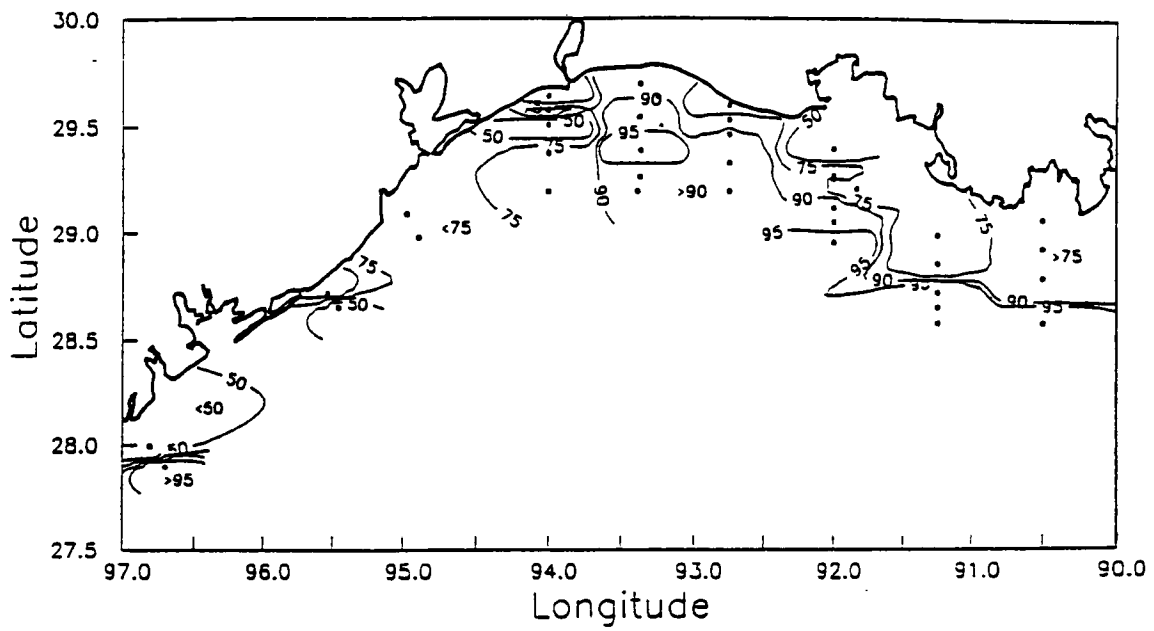
Figure 109. Surface contours of percent cyanobacteria (0.2-3.0 μm)/total
phytoplankton during Cruise I.

131

extended plumes and the gradient toward offshore water (Figures 110 and 111). Despite the strong gradients, especially along the Louisiana coast, values approaching the 100% High PU/PE expected for offshore waters are never observed. Thus, sampling did not extend beyond the coastal boundary current.

Diatoms comprise a small portion of the total phytoplankton numbers, but a large fraction of the phytoplankton > 8 μm. The extended plumes of the Mississippi River and an area off Galveston Bay are particularly diatom-dominated and somewhat higher diatom numbers are associated with the Sabine Pass and Atchafalaya plumes. Again, there is no sharp cross-shelf gradient in the % diatoms indicating the position of the coastal boundary current.

None of the freshwater indicator species were observed on this cruise. Since river runoff in Louisiana was low and salinities during the cruise exceeded 20%, except at one station, this is not surprising. Green-fluorescing dinoflagellates were observed at only one station off the south Texas coast since sampling did not extend beyond the coastal current.

High numbers of *Skeletonema costatum* were observed, especially on the Louisiana shelf, which is typical of spring conditions. However, the highest concentrations clearly delineate the river plumes, especially the Mississippi and Atchafalaya Rivers.

Toxic and Noxious Algae. On April 24, 1992 at the station nearest shore on the S3 line (Atchafalaya Bay line), reddish, discolored water was observed. Chlorophyll concentrations were in excess of 200 μg/liter, an extraordinarily high number. Although a variety of diatoms and dinoflagellates were present, the dominant organism was a dinoflagellate, identified as a *Scrippsiella* sp. Concentrations of this species alone at both the surface and bottom exceeded 2×10^7 cells/liter. The bloom was a small-scale, ephemeral feature because the *Scrippsiella* sp. was present only in very low numbers at a few adjacent stations and was not there on other days. There is no evidence at present that species of this genera produce toxins, but because many of them produce calcereous cysts (Taylor, 1987), which is a mechanism leading to persistent blooms, there is potential for continued blooms in this area.

A number of other possibly toxic and noxious algae were observed on this cruise, sometimes in high concentrations. Particularly notable was *Nitzschia pungens*, a diatom that in its toxic form can cause amnesiac shelf fish poisoning (ASP) (Shumway, 1990; Hallegraeff, 1993). It occurred at all stations across the entire shelf at concentrations up to 2×10^6 cells/liter, with the highest concentrations in the plume of the Atchafalaya River, the extended plume of the Mississippi River, and off of Galveston. Three dinoflagellates implicated in causing outbreaks of Diarrhetic Shelfish Poisoning (DSP), *Dinosphysis caudata*, *Prorocentrum micans*, and *Procentrum minimum* (Shumway, 1990; Hallegraeff, 1993), were also observed, but the concentrations were generally less than 2×10^4 cells/liter and the observations were widely scattered.

b. Cruise II, October 1992. Distribution of Different Size Classes. The total numbers of phytoplankton were higher in the fall than in the spring (Figure 112). The bottom concentrations were generally lower, but showed the same patterns as the surface concentrations. As in the spring, there were no clear cross-shelf or along-shore gradients and only some correspondence with the distribution of chlorophyll in the same area. Only the Atchafalaya plume was clearly delineated.

Since the 0.2 to 3.0 μm and 3.0 to 8 μm size fractions made up most of the phytoplankton numbers, their numbers were up in comparison with the spring, and the pattern was very similar to that of the total phytoplankton. In contrast, the numbers of phytoplankton > 8 μm were less in the fall (Figure 113) than in the spring. In fact, the decrease in phytoplankton > 8 μm was similar

132
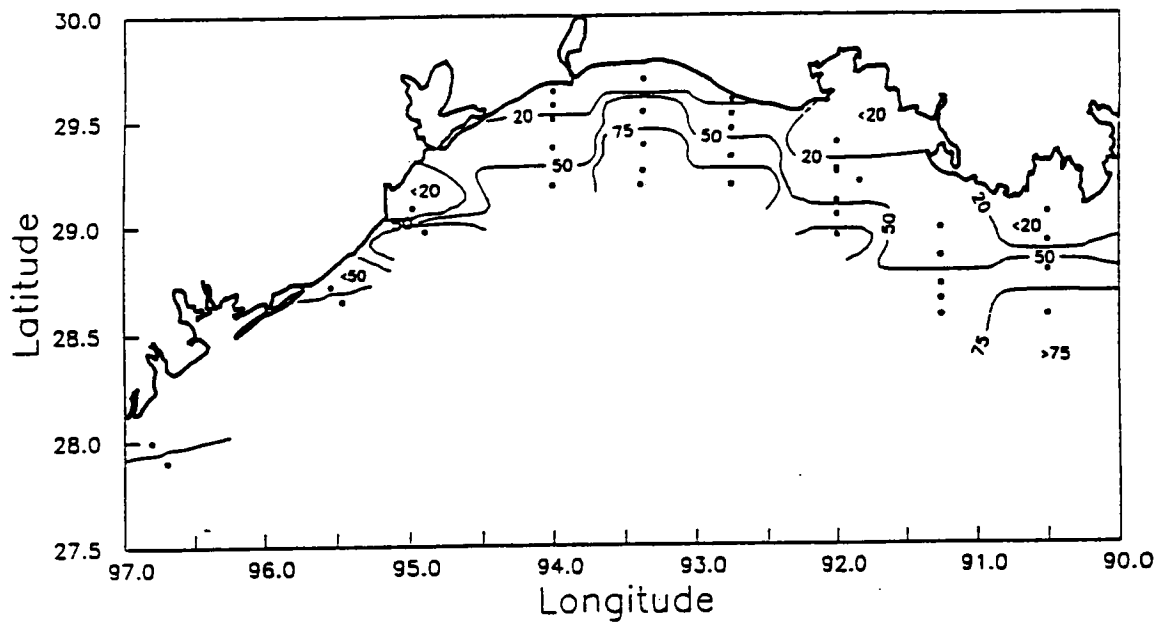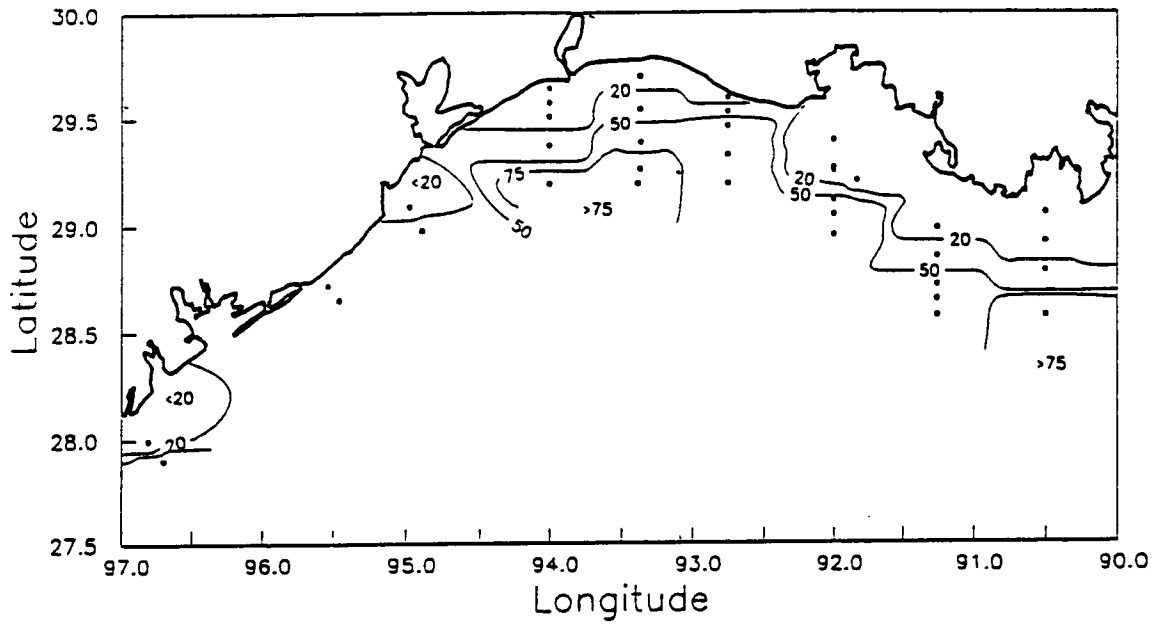
Figure 110. Contours of percent High PU/PE cyanobacteria/total cyanobacteria
(0.2-3.0 μm) during Cruise I: surface (upper); bottom (lower).

133
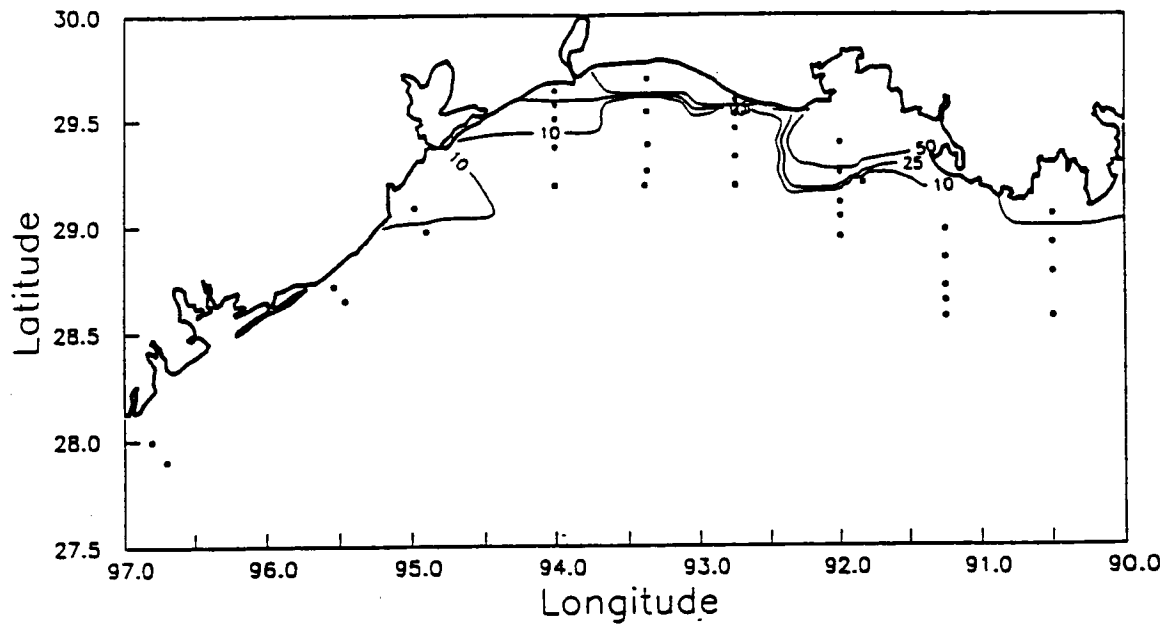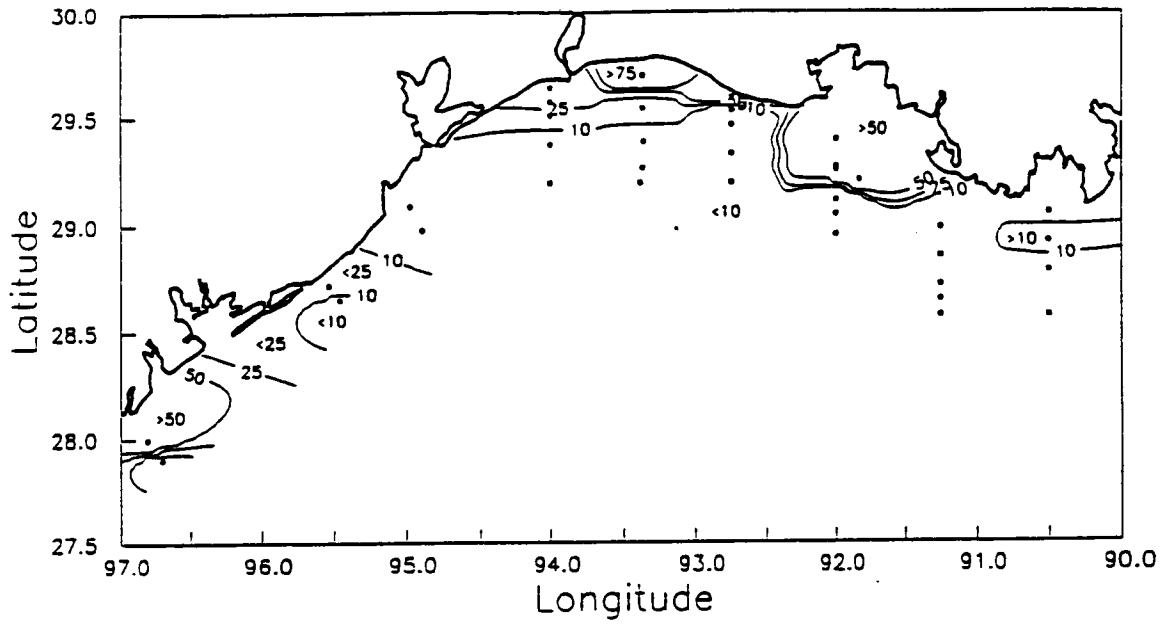
Figure 111. Contours of percent PC cyanobacteria/total cyanobacteria (0.2-3.0 μm) during Cruise I: surface (upper); bottom (lower).
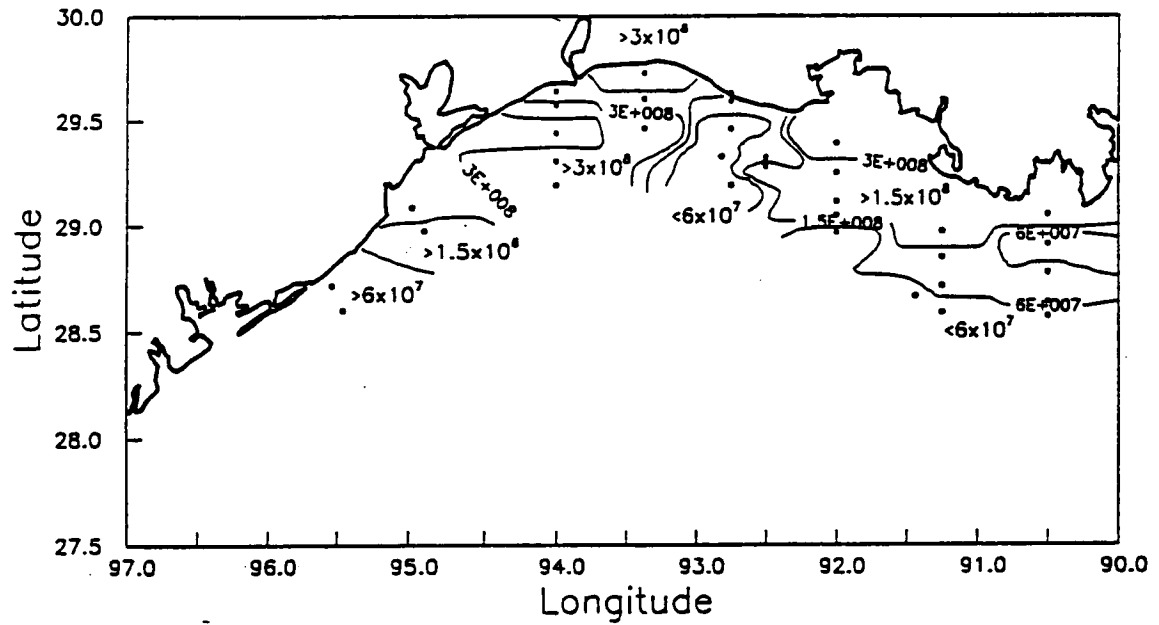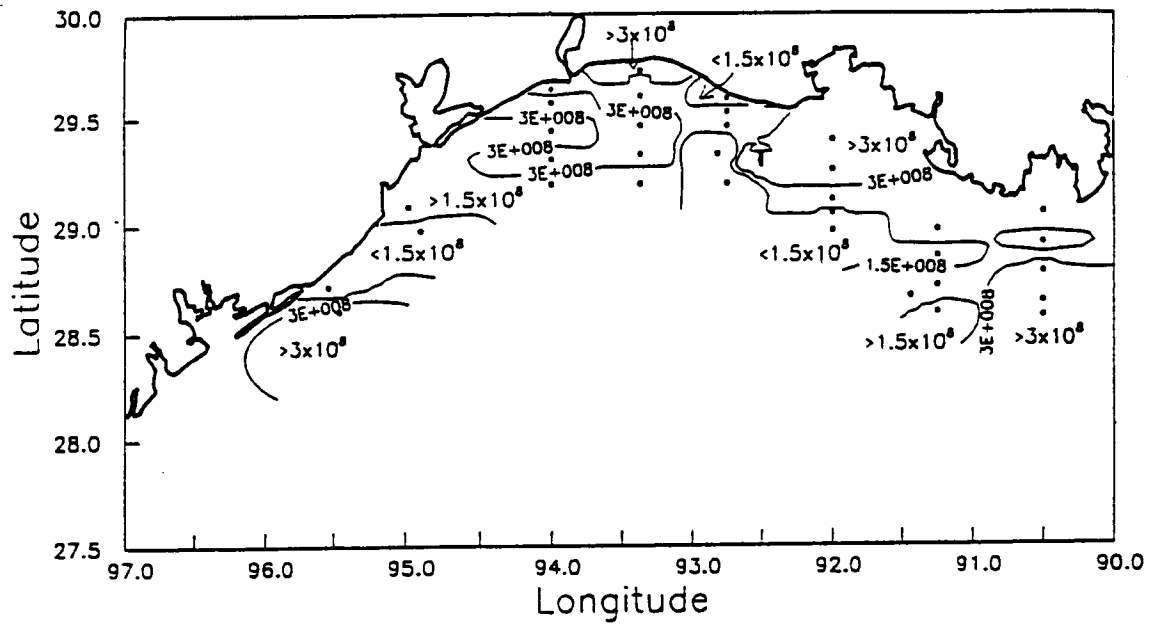
Figure 112. Contours of total numbers (number/liter) of phytoplankton in all size
fractions during Cruise II: surface (upper); bottom (lower).
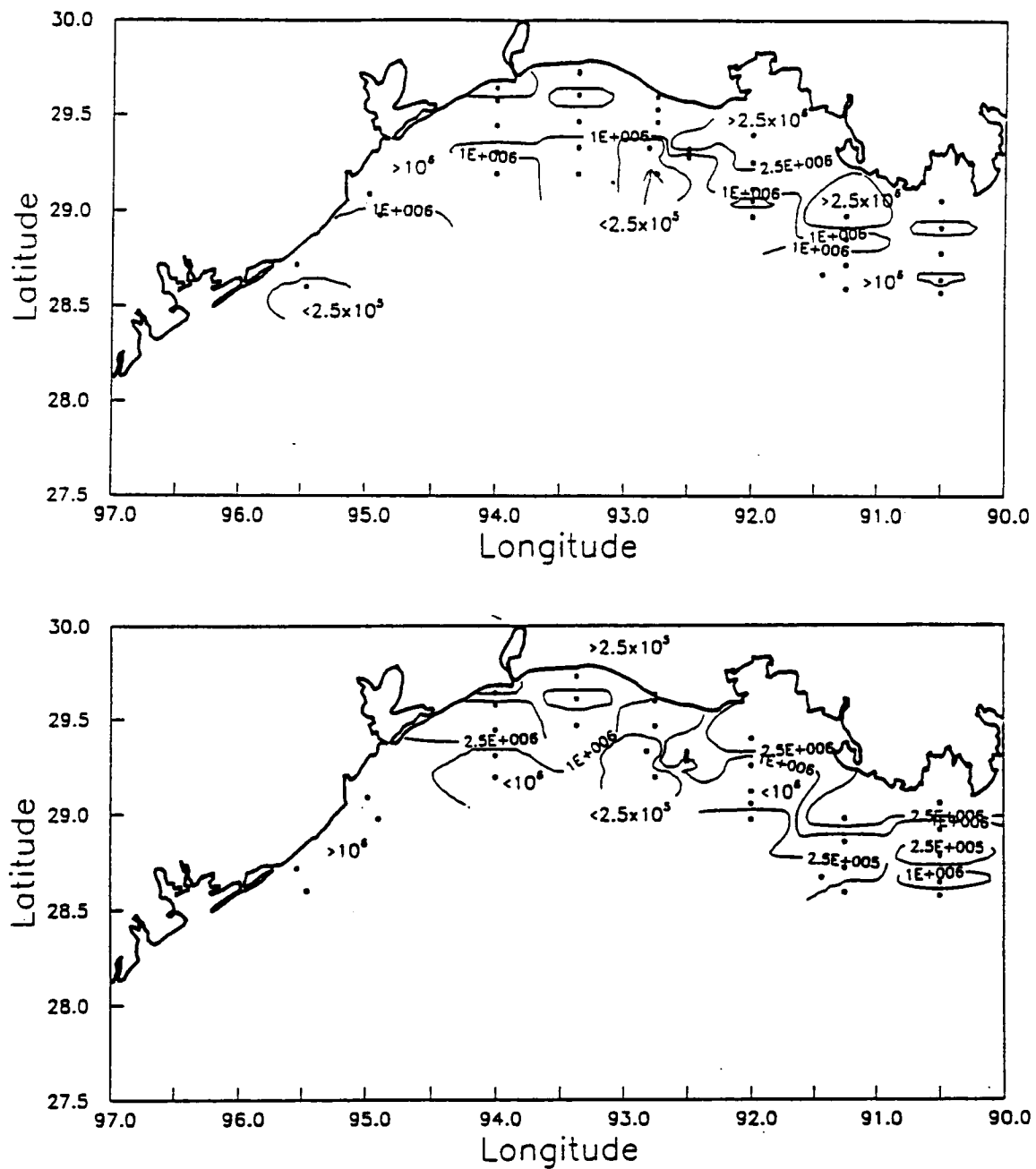
Figure 113. Contours of numbers (number/liter) of phytoplankton >8 μm during Cruise II: surface (upper); bottom (lower).

136

to the decrease in chlorophyll values between spring and fall, suggesting again that chlorophyll concentrations were a good indication of the biomass of large phytoplankton. There was no clear cross-shelf gradient, but the numbers of phytoplankton > 8 μm decreased to the west. The plume of the Atchafalaya River was evident from the higher numbers of large phytoplankton in that area.

Distribution of Specific Groups or Species. The small coccoid cyanobacteria were so dominant that it was impossible to interpret contours of their distribution. The same inverse relationship was observed between the % PC and % High PU/PE cyanobacteria (Figures 114 and 115) that was seen in the spring (Figures 110 and 111). The distribution of the two groups clearly showed the extended plume of the Mississippi River and the Atchafalaya River. There was no evidence of freshwater inputs off the Texas coast.

Since the cyanobacteria dominated so completely, the relative numbers of all other groups of organisms are very low. Thus, the diatoms made up < 1% of the total numbers (Figure 116). Even in the > 8 μm fraction, they generally made up less than 25% of the autotrophs (Figure 117). Low numbers of diatoms are typical of fall, low runoff conditions. Both the extended Mississippi River plume and the Atchafalaya plume had elevated concentrations of diatoms, and the relative concentrations of diatoms decreased along the Texas shelf.

Skeletonema costatum concentrations were highest on several transects on the Louisiana shelf, which are under the influence of the Mississippi and Atchafalaya Rivers, although overall they were much lower than in the spring. In the fall *Skeletonema costatum* distributions did not define the plume as well as other groups such as the cyanobacterial pigment groups. No green-fluorescing dinoflagellates were observed during this cruise, which is not surprising since the relatively low % High PU/PE cyanobacteria at the offshore stations indicate that oligotrophic waters beyond the coastal boundary current were not sampled. Due to the low river flow and generally high salinities (> 20%) the phytoplankton indicators of very high freshwater input were not observed.

Toxic and Noxious Algae. There were no blooms observed visually during Cruise II. *Nitzschia pungens*, the diatom associated with ASP, was again widely distributed along the Louisiana/Texas shelf. Concentrations were generally lower than in the spring, with a maximum of 4 x 10^5 cells/liter during the front study. There was no clear pattern to the distribution on the shelf. The dinoflagellates associated with DSP outbreaks, *Prorocentrum micans* and *Dinophysis caudata*, were also observed at widely scattered stations, the former at concentrations up to 1 x 10^5 cells/liter, but the latter at very low concentrations. Finally, two other dinoflagellates, which have caused sudden episodes of anoxia when they bloomed and sedimented out, *Gymnodinium splendens* (Harper and Guillen, 1989) and *Ceratium tripos* (Shumway, 1990), were observed at a few stations, but not in concentrations high enough to cause concern.

c. Discussion. Using Phytoplankton as Indicators of Water Masses and Mixing. Remote sensing images of, for example, turbidity in the coastal zone show a strong gradient at approximately the location of the coastal boundary current. It can be hypothesized that a number of the phytoplankton parameters which are sensitive to differences between coastal and offshore water, will also show a strong gradient in that region. For the most part, none of them did, suggesting that the transects were not extended far enough to sample beyond the coastal boundary current. The exceptions are the stations at the southern extent of the eastern two transects on Cruise I and the first transect on Cruise II. On these transects the 33% water, which is now known to indicate the approximate location of the coastal current, intersected the surface. On both cruises, at the eastern end of the study area, some of the indicators showed the beginning of strong cross-shelf gradients, which might correspond to the coastal current. On subsequent cruises, this problem was remedied by extending the sampling grid out into the Gulf.

137
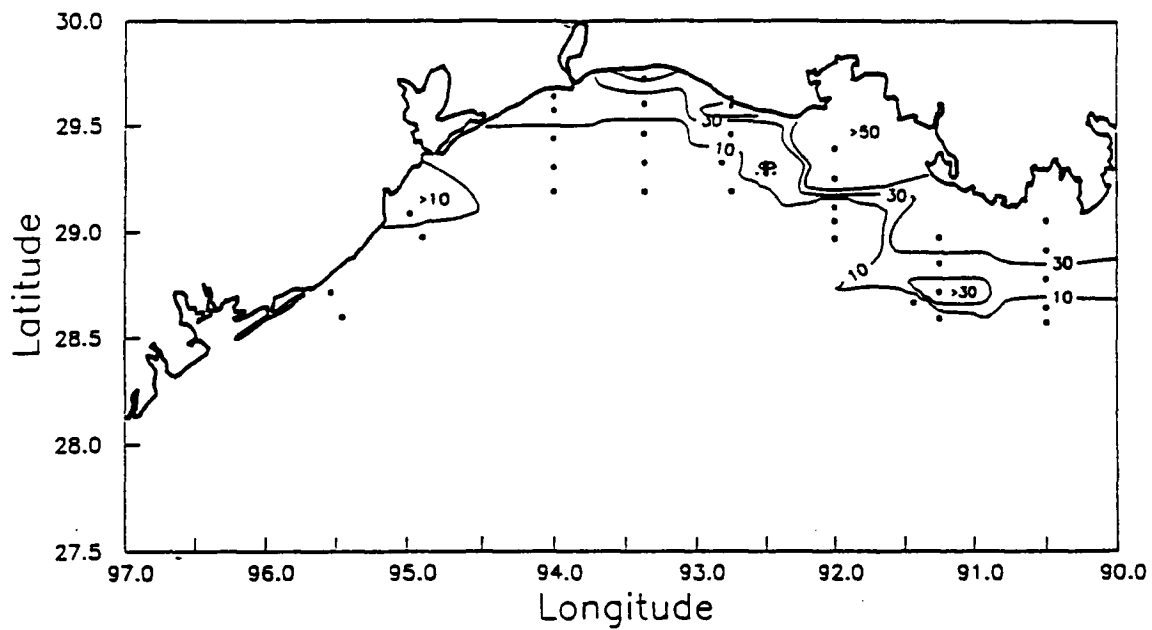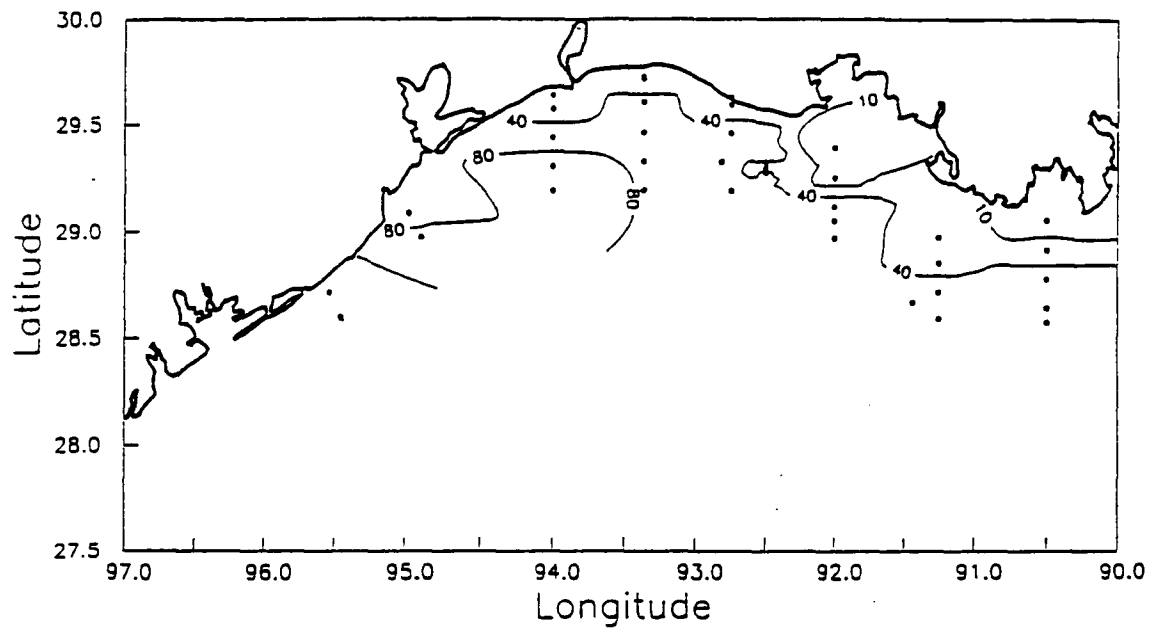
Figure 114. Contours of percent High PU/PE cyanobacteria/total cyanobacteria
(0.2-3.0 μm) during Cruise II: surface (upper); bottom (lower).
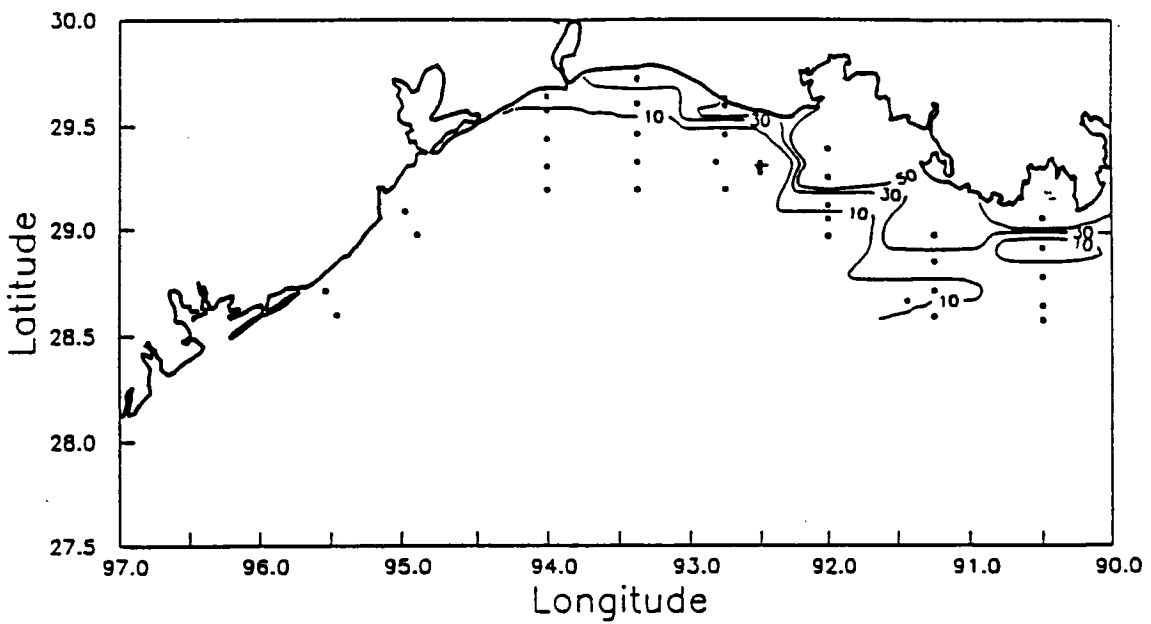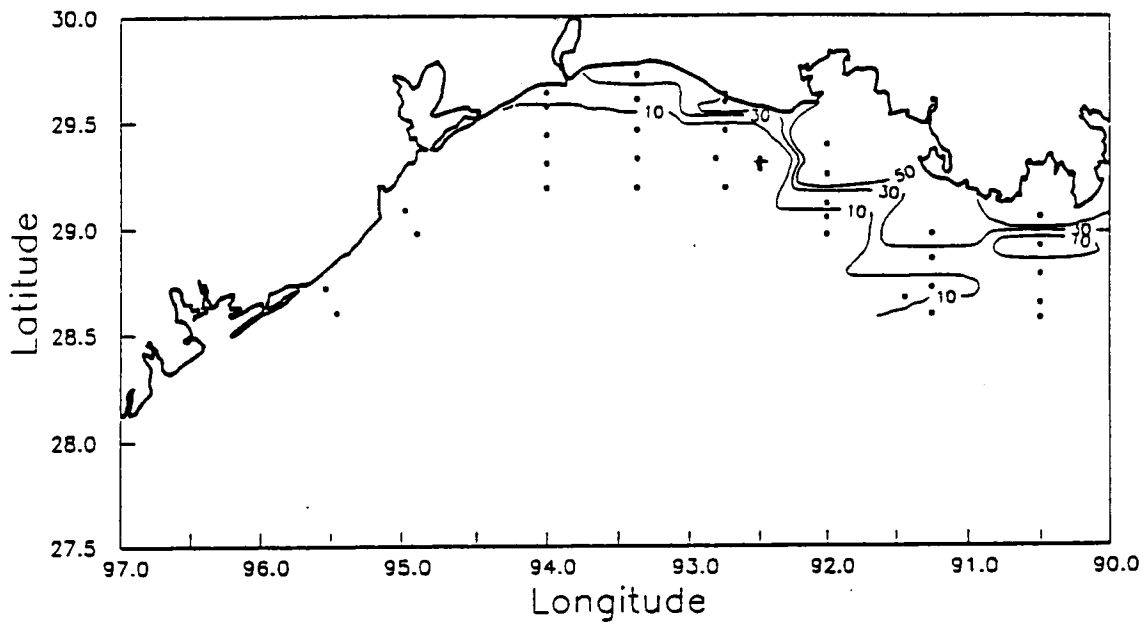
Figure 115. Contours of percent PC cyanobacteria/total cyanobacteria (0.2-3.0 μm) during Cruise II: surface (upper); bottom (lower).
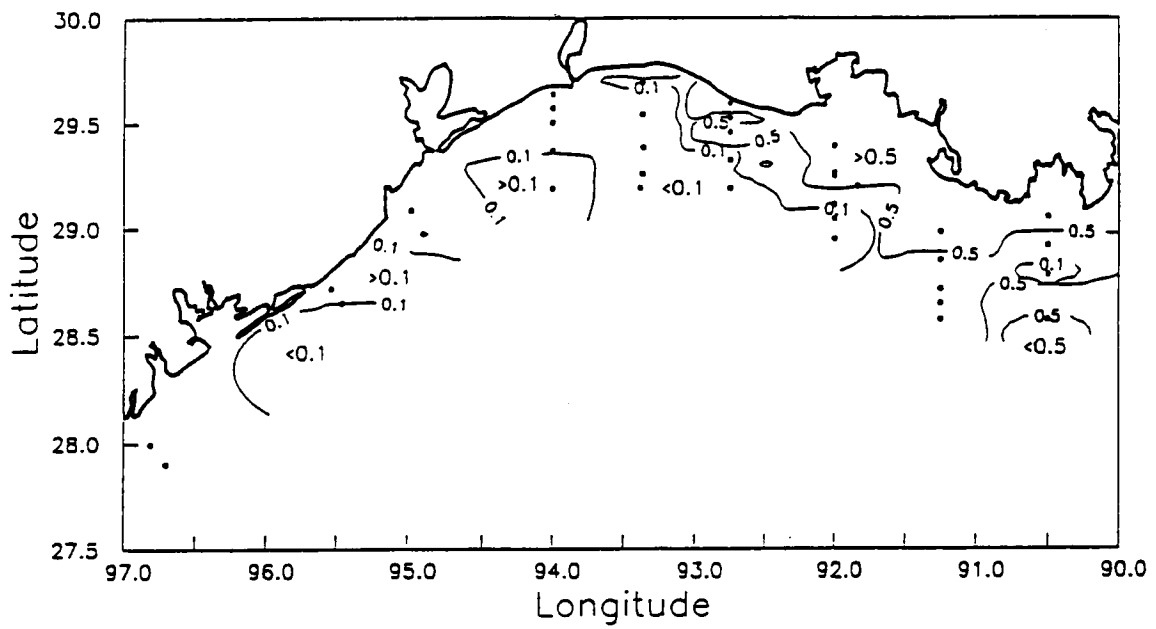
Figure 116. Surface contours of percent diatoms/total phytoplankton during
Cruise II.
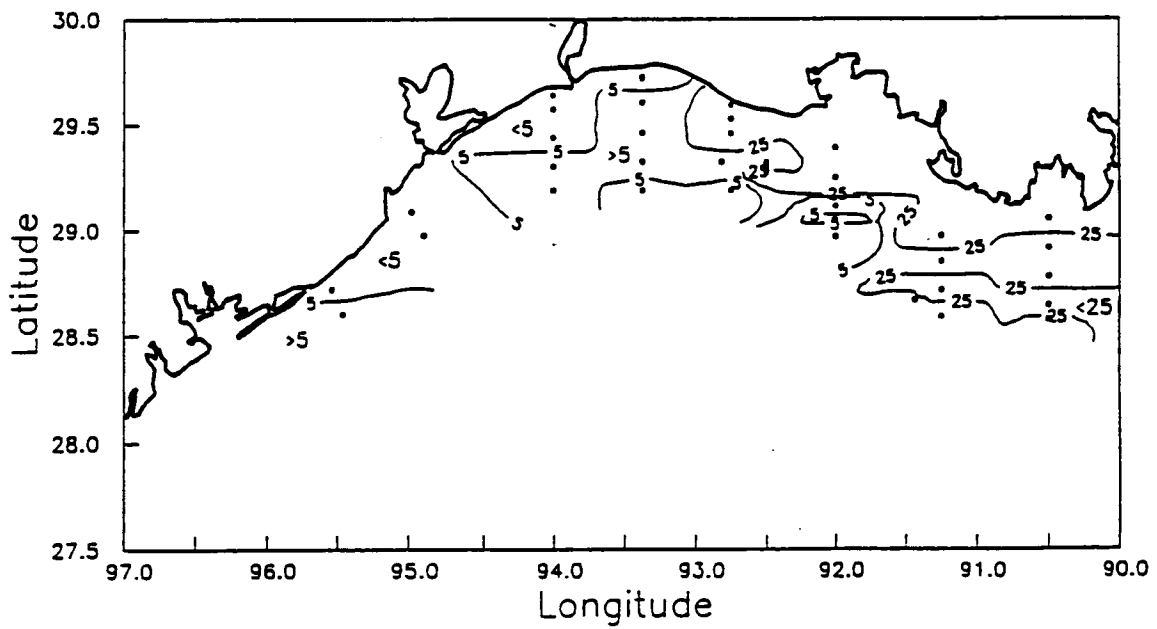
Figure 117. Surface contours of percent diatoms/phytoplankton >8 μm during
Cruise II.

The inputs of fresh water, river plumes, and extended plumes, were delineated clearly by several of the phytoplankton indicators. Most definitive were the cyanobacterial pigment groups, the % diatoms/autotrophs > 8 μm, and numbers of *Skeletonema costatum*. Multiple plumes and inputs of freshwater were indicated in the spring when runoff was high, especially on the Texas shelf. The data suggested that some of the plumes had high numbers of small phytoplankton, expecially the Atchafalaya River, Sabine Pass, and Corpus Christi plumes, and others had high numbers of diatoms, including the Mississippi River extended plume, the Atchafalaya and Galveston Bay plumes. On Cruise II the only plumes which were observed were the extended plume of the Mississippi River and the Atchafalaya River plume. The Mississippi River extended plume appears as a band of distinct phytoplankton composition, which joins the Atchafalaya plume from the east and is enhanced by the growth of phytoplankton stimulated by the Atchafalya River.

Because the sampling grid did not extend beyond the coastal boundary current and no sampling was conducted during the summer period when the water column is stable and mixing is minimal, it was not possible to test the feasibility of using phytoplankton as indicators of mixing. The success using the cyanobacterial pigment groups as markers for freshwater inputs and offshore waters suggests their probable utility as markers of mixing between dissimilar water masses. To test this, the cyanobacterial pigment data for these spring and fall cruises can be compared with similar data from a summer cruise in the same year (Dortch and Rabalais, unpublished). The geographic distribution of the data is somewhat different since the summer cruise started at the Mississippi River and went to approximately the Texas border, but about half the data are from overlapping stations. Cyanobacterial numbers are much higher in summer, and they are dominated by the intermediate pigment group, the Low PU/PE. Dominance by this group and decreased co-occurence of the other two groups may indicate stability and reduced mixing.

Seasonal Differences. There were distinct differences overall between the two cruises (Table 7). Phytoplankton numbers were higher in the fall. The increase was due to increased numbers of small phytoplankton (0.2 to 3.0 and 3.0 to 8.0 μm) because the numbers of large phytoplankton decreased. In the spring diatoms dominated the large size fraction and were a substantial portion of the total phytoplankton, but in the fall they were a miniscule fraction of the total and no longer dominated the large size fraction. The relationship of these differences to environmental factors, such as runoff, salinity, temperature, and nutrient availability, will be tested in later reports.

Table 7. Seasonal comparison of Mean and Standard Deviation of phytoplankton counts (autotrophs, cells/liter) and various phytoplankton groups for Cruises I and II.

| | SPRING | | | | FALL | | | |
| | Surface | | Bottom | | Surface | | Bottom | |
Autotrophs	Mean	Std. Dev.	Mean	Std. Dev.	Mean	Std. Dev.	Mean	Std. Dev.
0.2-3μm	7.73×10^7	7.37×10^7	8.73×10^7	7.22×10^7	2.54×10^8	1.44×10^8	1.55×10^8	1.73×10^8
3.0-8 μm	6.18×10^6	8.18×10^6	9.14×10^6	5.58×10^6	1.09×10^7	1.23×10^7	1.36×10^7	1.14×10^7
>8 μm	4.73×10^6	7.15×10^6	3.95×10^6	7.60×10^6	1.42×10^6	1.00×10^6	1.31×10^6	1.18×10^6
Total	8.87×10^7	7.71×10^7	8.18×10^7	9.49×10^7	2.66×10^8	1.48×10^8	1.86×10^8	1.65×10^8
% Diatoms/Autotrophs								
>8 μm	61.77	25.72			17.52	17.95		
Total	9.20	11.16			0.97	0.43		
% Cyanobacteria/Autotrophs								
Total	77.01	21.89			95.90	3.65		
% Autotrophs/(Autotrophs+Heterotrophs)								
Total	88.80	15.06	86.16	15.38	99.16	0.90	98.86	1.12
# of Samples	39		38		42		37	

Potential for Blooms of Toxic and Noxious Algae. The Louisiana and Texas continental shelves have not had the kinds of problems with persistent blooms that many other areas of the U.S. and the world have had (Smayda, 1989, 1990; Shumway, 1990; Hallegraeff, 1993). Over the years there have been sporadic blooms (Parsons et al, 1992) similar to, although more extensive than, the *Scrippsiella* sp. bloom observed off the Atchafalaya River on Cruise I. Of more concern are several phytoplankton whose toxicity has only recently been recognized and which are frequently observed in coastal waters of Louisiana and Texas. These include the diatom, *Nitzschia pungens*, associated with outbreaks of ASP, and various *Dinophysis* and *Prorocentrum* species, associated with DSP.

During a recent bloom of what we have called *Nitzschia pungens*, a sample was isolated and samples prepared for Scanning Electron Microscopy (SEM), to determine if it was the toxic form. According to G. Fryxell (pers. comm., who did this work, that particular isolate was the species *Pseudonitzschia pseudodelicatissima*, which was the species responsible for the first outbreak of ASP in Canada (Martin et al., 1990). Since we may have a mixture of species (Fryxell, pers. comm.), which we cannot distinguish using epifluorescence microscopy, we will continue to use the term "*Nitzschia pungens* " until more identifications have been made with SEM. The data from these two cruises indicate that this species or group of species is present, often at very high concentrations, throughout the region.

The toxin causing DSP has been isolated from oyster tissue in Mobile Bay (Dickey et al. 1992). Dinoflagellates that produce this toxin were present during both cruises although not in bloom concentrations. However, blooms of these phytoplankton have been observed on other cruises (Parsons et al., 1992). These data sets provide an opportunity to define more precisely the conditions that foster the growth of toxic dinoflagellates.

142

D. Zooplankton Survey (Richard F. Shaw)

1. Materials and Methods

Oblique plankton tows were made with a 60-cm diameter paired-bongo frame modified to accommodate a 20-cm ring. Bongo-net meshes were 153- and 335 μm, while a 63-μm mesh net was lashed to the ring. The 153- and 335-μm nets were fitted with a torpedo-type flowmeter for volume-filtered estimates. Volume-filtered estimates were not determined for the 63-μm net because of the potential of clogging (Taylor, 1976; Tranter and Smith, 1968). Upon retrieval, nets were thoroughly rinsed from the outside, concentrating the sample within the cod-end. The 63- and 153-μm samples were initially preserved in 4% formaldehyde and transferred to 70% ethanol after 24 hours. The 335-μm samples were preserved in 70% non-denatured buffered ethanol, placed on ice, and transferred to fresh 70% ethanol 24 hours later. This method is suitable for larval fish otolith and growth analysis (Butler, 1992; Methot and Kramer, 1979).

Biomass estimates were performed on halves of all samples. All plankton splits were made with a Folsom plankton splitter (McEwen, et al., 1954). Halves were randomly selected for analysis. The three mesh sizes used in the study were analyzed in order to get an idea of zooplankton-size fractionations. To determine the relationship between volumetric and gravimetric techniques, volume displacements (Yentsch and Hebard, 1957) were conducted on a randomly-selected third of the stations from each cruise prior to dry weight determination. Dry weights were determined for all samples by oven-drying at 60°C to constant weight (Lovegrove, 1966). Zooplankton density was calculated for both gravimetric (g/m^3) and volumetric (ml/m^3 when present) biomass estimates for the 153- and 335μm samples as:

$$\text{zooplankton density} = \text{biomass estimate/volume filtered,}$$

where volume filtered equals volume filtered (m^3) by the net. Zooplankton density was not determined for the 63-μm samples because volume filtered estimates were not recorded for these samples.

Invertebrate composition of a fraction of the 153-μm samples was determined for half of the stations sampled. Identifications were made to family level when possible, although distinctive species and some target species (i.e., copepods and decapods) were identified to higher taxonomic levels. At least 150 organisms were identified in each sample analyzed.

Larval fish and squid were removed from halves of all 335-μm samples and were identified to the lowest taxonomic level possible. If a 335-μm mesh sample was not taken at a particular station, the 153-μm sample was sorted if present. For each station, larval density ($\#/100 \, m^3$) was calculated for each species as:

$$\text{density} = (\# \text{ species}_x \, / \text{ volume filtered}) \times 100,$$

where # species$_x$ equals the number of larvae of the xth species at that station. For each cruise, percent catch was calculated for each species as:

$$\% \text{ Catch} = (\# \text{ Species}_x \, / \, \_(\# \text{ Species}_x)) \times 100.$$

Kendell τ correlation coefficients (SAS Institute, Inc., 1985) were calculated between station densities of the most abundant species collected for each cruise (as determined by percent catch) and of zooplankton biomass and various environmental variables (α=0.05). Values of CTD

variables, ADCP water current, and chlorophyll a and phaeopigment concentrations were averaged through the water column before use in the correlation analysis.

All halves (minus the fraction used in the zooplankton analysis for the 153-µm samples and larval fish and squid for the 335-µm samples) not used for biomass estimates were archived in 70% ethanol for future ecological studies.

2. Results

Two hundred and twenty samples were obtained from 76 biological stations during on Cruise I (April 1992) and Cruise II (October 1992). The total number of larval fish collected was 8,773, and the number of squid was 18 within a maximum depth of 40 m. Twenty-eight families, composed of 45 larval fish and 2 squid genera, were identified collectively.

Mean biomass densities were higher in April than in October for both the 153- and 335-µm samples. The correlation between zooplankton dry weight and volume displacement was highly significant for both the 153- (N=27) and 335-µm (N=28) samples. The regression intercepts were not significantly different from zero (ANOVA, p=0.528). Thus, the two biomass determinations appear to be linearly related; however, dry weight estimates tend to be less variable, more reproducible, and more useful for ecological studies from an energetic standpoint than volume displacement estimates (Laurence, 1976).

a. Cruise I, April 1992. Ninety-five samples from 34 biological stations were obtained during Cruise I, a high-river period. Samples were collected from the Mississippi Delta to near Corpus Cristi, the southwestern-most portion of the plume's range. Temperature ranged from 22°-24°C while salinity ranged from 18 to 34‰.

Zooplankton biomass tended to be high in the western portion of the study area for both the 153- and 335-µm samples during Cruise I (Figures 118 and 119). Zooplankton dry-weight density for the 153-µm samples ranged from 0.002 to 0.112 g/m³ (=0.014, s.d.=0.020), while the 335-µm samples ranged from less than 0.001 to 0.015 g/m³ (=0.004, s.d.=0.004). Dry-weight densities were highly correlated between the 153- and 335-µm samples.

During Cruise I, 6396 larval fish and 12 squid were collected . Larval fish densities were highest off Atchafalaya Bay and westward to Sabine Lake (Figure 120), ranging from 2 to 695 larvae/100 m³ (=94.7, s.d.=123.6). No significant correlation was seen between larval density and both the 153- and 335-µm biomass estimates; however, high larval densities were significantly correlated with the warm water column temperature. April samples were dominated by *Anchoa* spp. (% catch=61.5%), although *Cynoscion arenarius* (14.4%), unidentified engraulids (8.4 %), *Etropus crossotus* (3.8%), and *Symphurus* spp. (3.7%) were also abundant. Including all genera, the family Engraulidae made up 74% of the total catch. Listed below is a breakdown of the cruise by transect.

S1. 153-µm dry-weight density increased with increasing distance from shore, ranging 0.002-0.011 g/m³. 335-µm biomass ranged from less than 0.001 to 0.003. Larval densities were fairly low, ranging 1.5-41.7 larvae/100 m³.

S2. No trend was observed for the density variables. 153-µm zooplankton densities were relatively high, ranging 0.006-0.017 g/m³. The range for 335-µm dry weights was 0.002-0.009 g/m³. Larval densities ranged 7.0-135.2 larvae/100 m³.

S3. Biomass for the 153-µm samples tended to increase with increasing distance from shore, while the opposite held true for the 335-µm samples and larval density. Dry weight for the
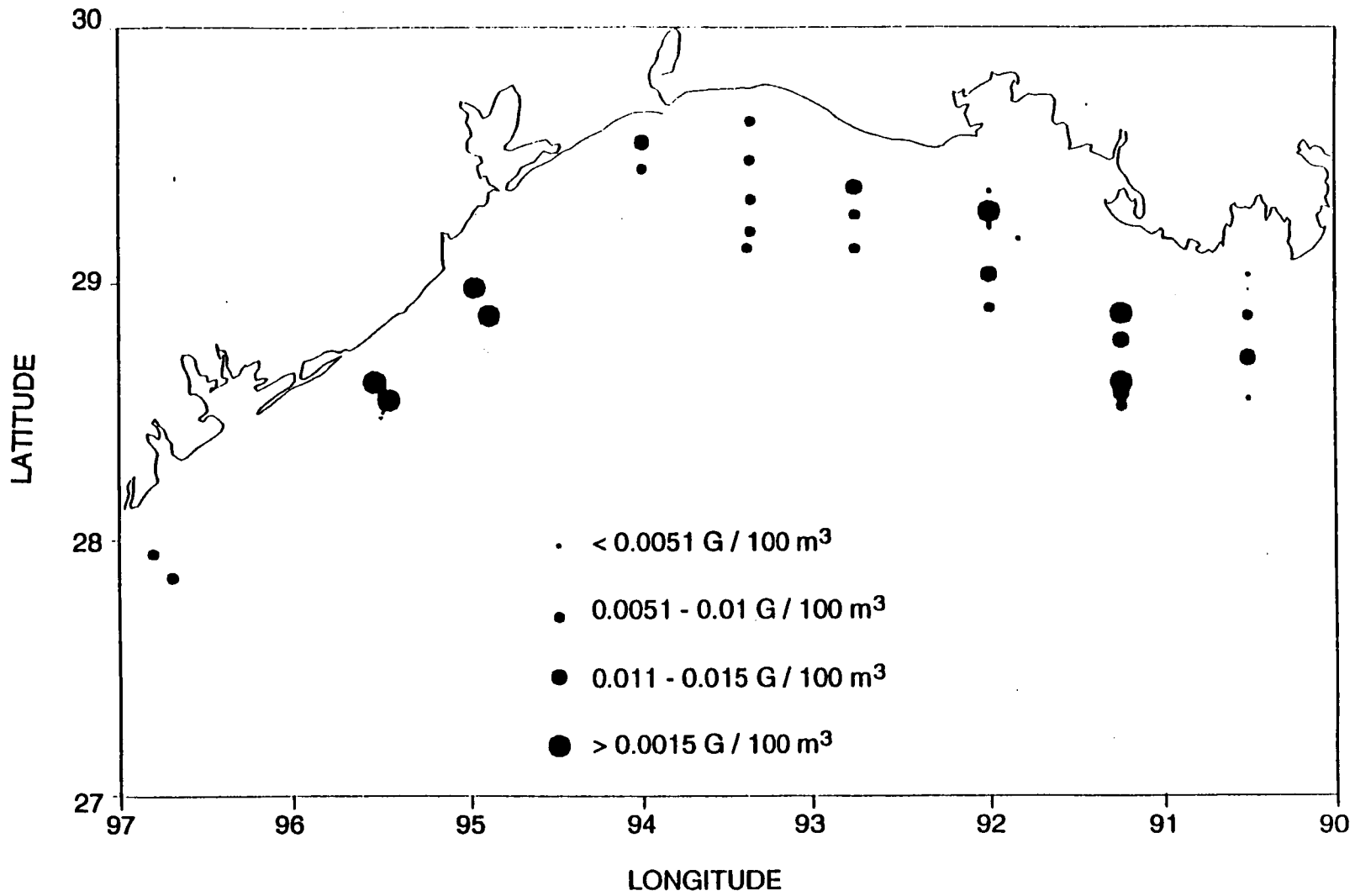
Figure 118. Plankton biomass (g/m³) for 153-μm mesh samples collected during Cruise I.
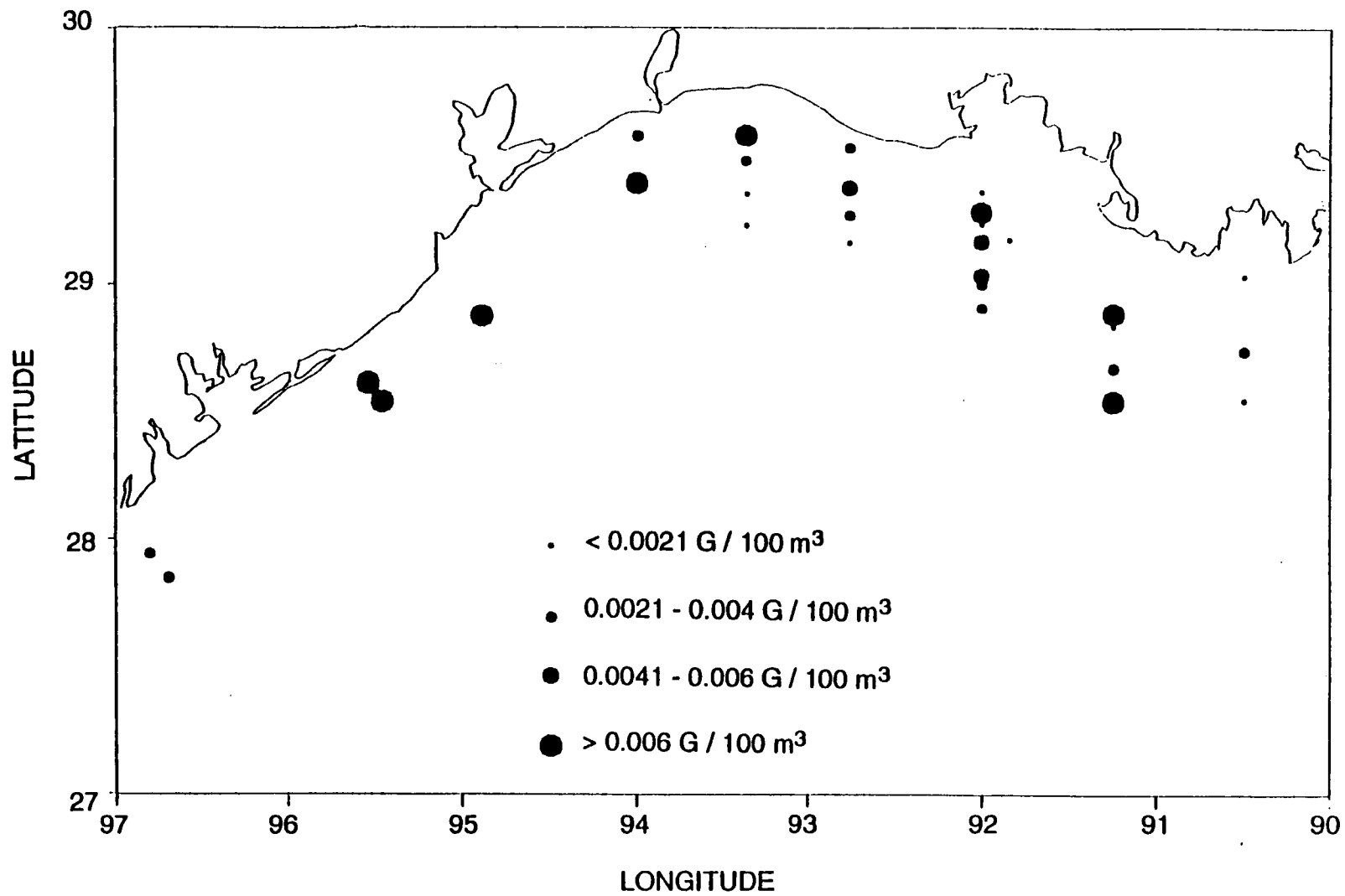
Figure 119. Plankton biomass (g/m³) for 333-μm mesh samples collected during Cruise I.
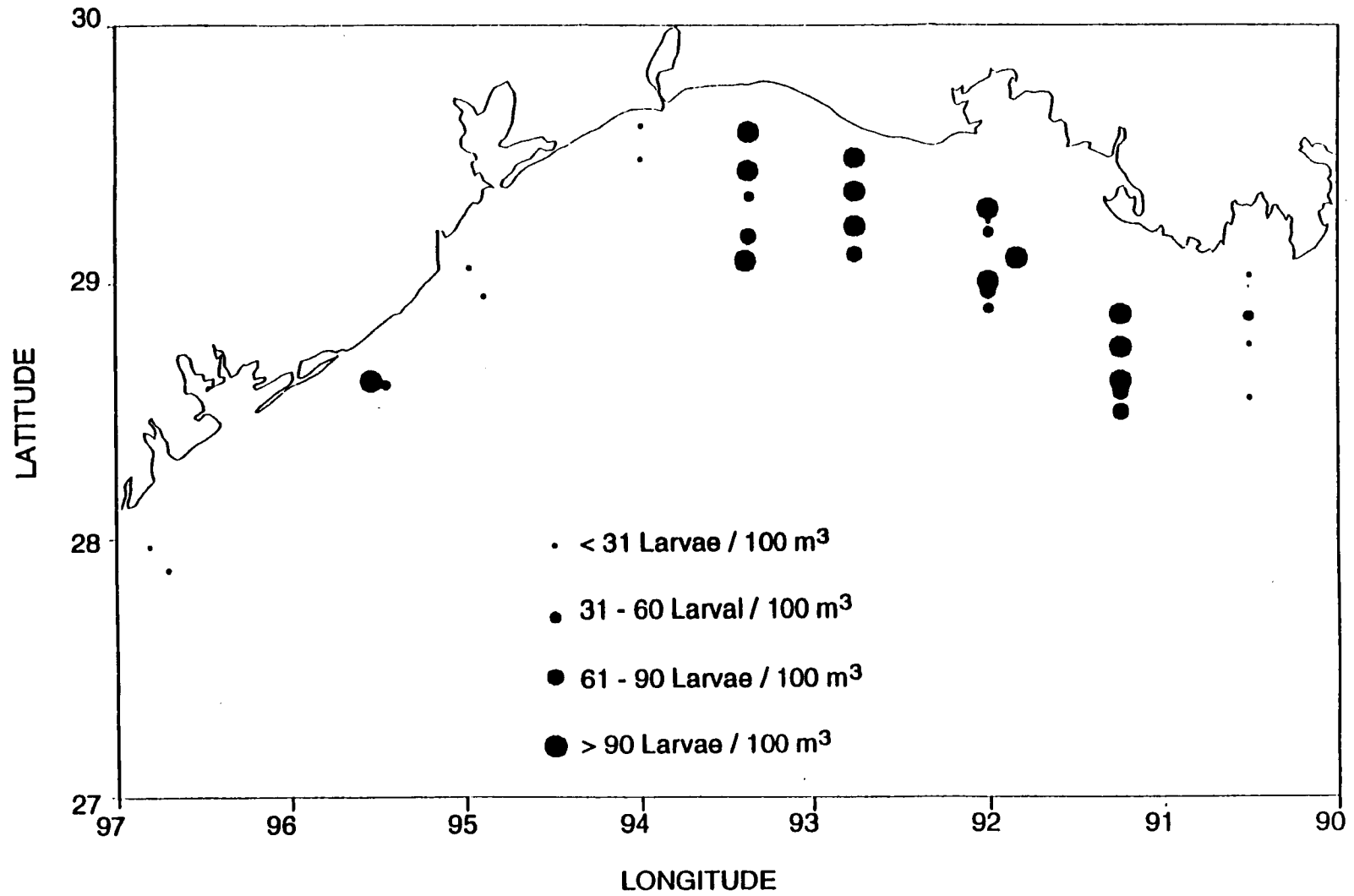
Figure 120. Larval fish density (#/100 m³) for Cruise I.

153-μm samples ranged 0.003-0.015 g/m³, while the 335-μm samples ranged from less than 0.001 to 0.006 g/m³. Larval densities ranged 3.2-247.6 larvae/100 m³.

S4. 153-μm biomass ranged 0.012-0.006 g/mμ. 335-μm biomass and larval density decreased as distance from shore increased. Biomass for the 335-μm fraction decreased from 0.005-0.002 g/m³, while larval density decreased from a cruise maximum of 695.5-63.6 larvae/100 m³.

S5. Zooplankton biomass tended to decrease with increasing distance from shore, ranging from 0.006 - 0.009 g/m³ for the 153-μm samples and 0.001-0.006 g/m³ for the 335-μm samples. Larval density revealed no clear trend and ranged from 36.4-166.2 larvae/100 m³.

S6, S7, S8, and X2. Zooplankton density was high in the southwestern portion of Cruise I. 153-μm samples ranged 0.006-0.112 g/m³, a cruise maximum which occurred along Section S7. 335-μm biomass ranged 0.002-0.015 g/m³, a cruise maximum which also occurred along transect S7. Larval densities remained low except along transect S8 and ranged 6.7-137.7 larvae/100 m³.

b. Cruise II, October 1992. One hundred and twenty-five samples were collected from 42 stations during Cruise II, a low-river period. Samples were collected from Mississippi Delta to Galveston Bay. Temperature ranged from 23° to 26°C and salinity ranged from 20-34 ‰.

Zooplankton biomass for the 153-μm mesh tended to be high west of Atchafalaya Bay (Figure 121), while 335-μm samples were highest between Atchafalaya Bay and Sabine Lake (Figure 122). Biomass for the 153-μm samples ranged from 0.001-0.074 g/m³ (=0.009, s.d.=0.012) and 335-μm samples ranged from less than 0.001-0.008 g/m³ (=0.002, s.d.=0.002). As before, both mesh dry-weight densities were highly correlated; however, negative correlations were noted between biomass for the 153- and 335-μm samples and both water column salinity and temperature.

During Cruise II, 2377 larvae and 6 squid were obtained. Larval fish densities were highest off Sabine Lake and at offshore stations, ranging from 0-130 larva/100 m³ (=18.7, s.d.=25.3; Figure 123). Again, no significant correlation was noted between larval density and zooplankton biomass. Larval density was positively correlated with both water column temperature and salinity; however, an inverse relationship existed between larval fish density and chlorophyll concentration ([chl *a*]=0.52-15.43 μg/l). *Micropogonias undulatus* was the dominate species (% catch=48.3%) collected. *Anchoa* spp. (17.3%), *Symphurus* spp. (6.6%), *Etropus crossotus* (6.4%), *Sciaenops ocellatus* (2.6%), and unidentified gobiids (2.4%) were also common in October samples. Listed below is a breakdown of the cruise by transect.

S1. No trend was observed for the zooplankton biomass estimates. Dry weight for the 153-μm samples ranged 0.001-0.006 g/m³, while the 335-μm samples ranged from less than 0.001-0.001 g/m³. Larval densities tended to increase with increasing distance from shore, ranging 5.0-20.8 larva/100 m³.

S2. Biomass for the 153-μm samples was higher at near-shore stations, ranging 0.002-0.004 g/m³. 335-μm biomass ranged 0.001-0.002 g/m³ while larval density ranged from 0-20.2 larva/100 m³.

S3. Zooplankton biomass increased with increasing distance from shore. 153-μm samples increased from 0.002-0.080 g/m³ and the 335-μm fraction increased from 0.001-0.002 g/m³. Larval density ranged 0-20.2 larvae/100 m³.

148
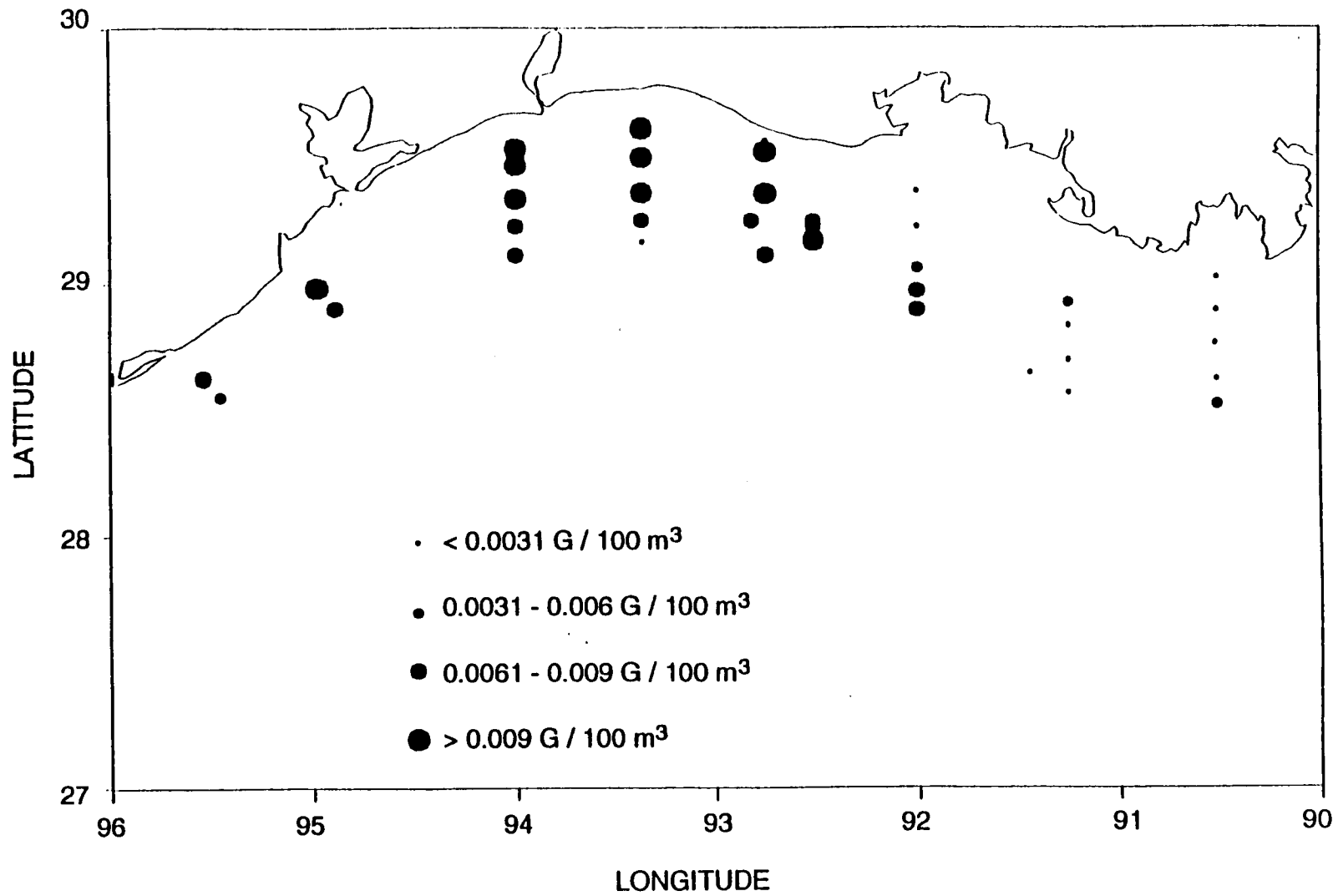
Figure 121. Plankton biomass (g/m³) for 153-µm mesh samples collected during Cruise II.
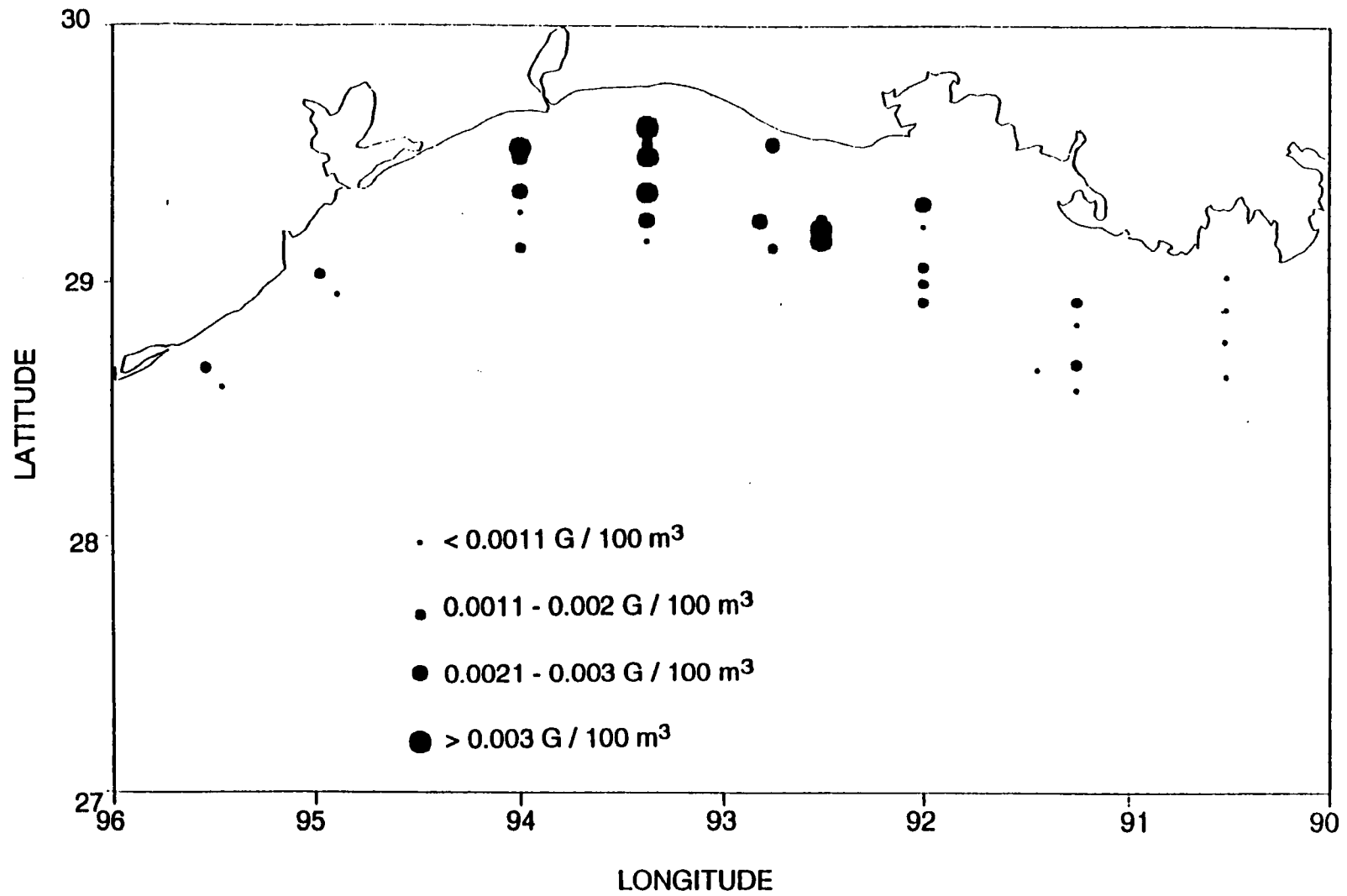
Figure 122. Plankton biomass (g/m³) for 333-μm mesh samples collected during Cruise II.
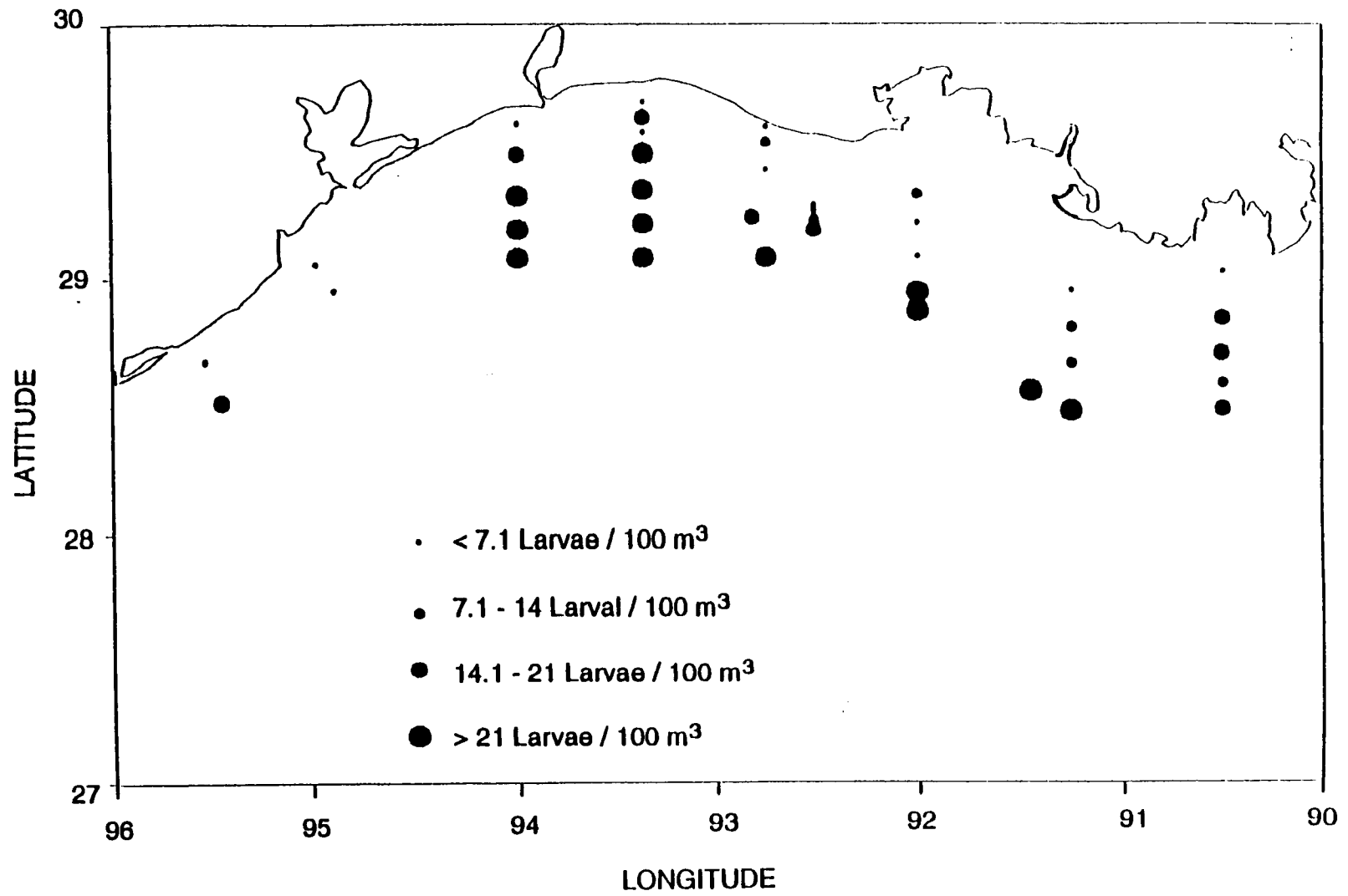
Figure 123. Larval fish density (#/100 m³) for Cruise II.

S4. Zooplankton biomass for the 153-μm fraction decreased from 0.003-0.016 g/m^3 as distance from shore increased. 335-μm biomass estimates ranged from 0.001- 0.003 g/m^3. Larval density increased with increasing distance from shore, ranging 1.0-25.3 larvae/100 m^3.

S5. Zooplankton biomass decreased, while larval density increased, with increasing distance from shore. The 153-μm fraction decreased from 0.037- 0.002 g/m^3 and 335-μm samples decreased from 0.007-0.001 g/m^3. Larval density increased from 14.0-129.6 larvae/100 m^3, a cruise maximum.

S6. Again, zooplankton biomass decreased, while larval density increased, with increasing distance from shore. The 153-μm biomass decreased from 0.017- 0.006 g/m^3 and 335-μm samples decreased from 0.004- 0.001 g/m^3. Larval density increased from 0-80.9 larvae/100 m^3.

S7 and S8. Zooplankton biomass decreased as distance from shore increased; larval density was variable in the western portion of the cruise. Biomass for the 153-μm fraction ranged 0.006-0.009 g/m^3, while the 335-μm fraction was approximately 0.001 g/m^3 at the western stations. Larval density ranged 1.5-18.3 larvae/100 m^3.

IV. Sediment Flux
(Wilford D. Gardner and Mary Jo Richardson)

A. Introduction

In order to measure the particle settling and resuspension fluxes, sediment traps were deployed at six sites across the Louisiana shelf along two transects (90.5° W and 92° W), which straddled a region of known summer hypoxia (Rabalais et al., 1991). These samples also provided material for compositional and particle size analysis to assess pollutant transport and the impact on the biological community.

Trap collections are integrations of the material collected at one point over the time of deployment. This adds a temporal extension to point sampling during hydrographic cruises, providing the opportunity to assess conditions and variations between cruises. It is important to remember, however, that traps collect the large, settling particles, which are the greatest contributors to the vertical settling of particles, rather than the total load of particles, which is heavily dominated by the small, slowly settling particles. The resulting profiles of sediment fluxes may be very different from the instantaneous profiles of particle concentrations determined optically or by water bottle filtration.

B. Methodology

Sediment traps were attached to LATEX A current meter moorings 14, 15 and 16 along 92° W and 17, 18, and 19 along 90.5° W during the first year of deployments (Figure 124). Traps were located 1 m above bottom (mab) at each site.

The traps were 76 cm tall butyrate cylinders with a 7.3-cm inside diameter, resulting in an aspect ratio (H/D) of 10. The upper 5 cm of the trap contained a honeycomb baffle made of epoxy-impregnated nylon. The purpose of the baffle was to exclude large swimmers from the trap (those < 1 cm) and to stabilize the turbulent flow within the trap. No poisons or preservatives were used in the traps. Divers exchanged the traps except on moorings 14 and 19 where the moorings were recovered using an acoustic release and redeployed. Some trap samples were lost during this procedure because of the difficulty of keeping the traps upright during recovery.

Additional traps were attached at depths indicated in Table 8 to be above the bottom boundary layer or as close to the surface plume as possible. Mooring and safety requirements usually necessitated that the uppermost trap was 6 m below the surface. Moorings were generally serviced every 45 days to minimize biofouling, but occasionally traps were out for 90 days. In addition to the traps on current meter moorings, an independent mooring with 5 or 6 traps was deployed near the VIMS tetrapod during the boundary layer studies in May 1992 and June 1993. Another trap was attached to the base of one leg of the tetrapod with the trap top at 0.76 mab. These fluxes will be compared later with the predicted resuspension rates from the tripod to estimate the sediment fluxes from the river plume versus resuspension of bottom sediments.
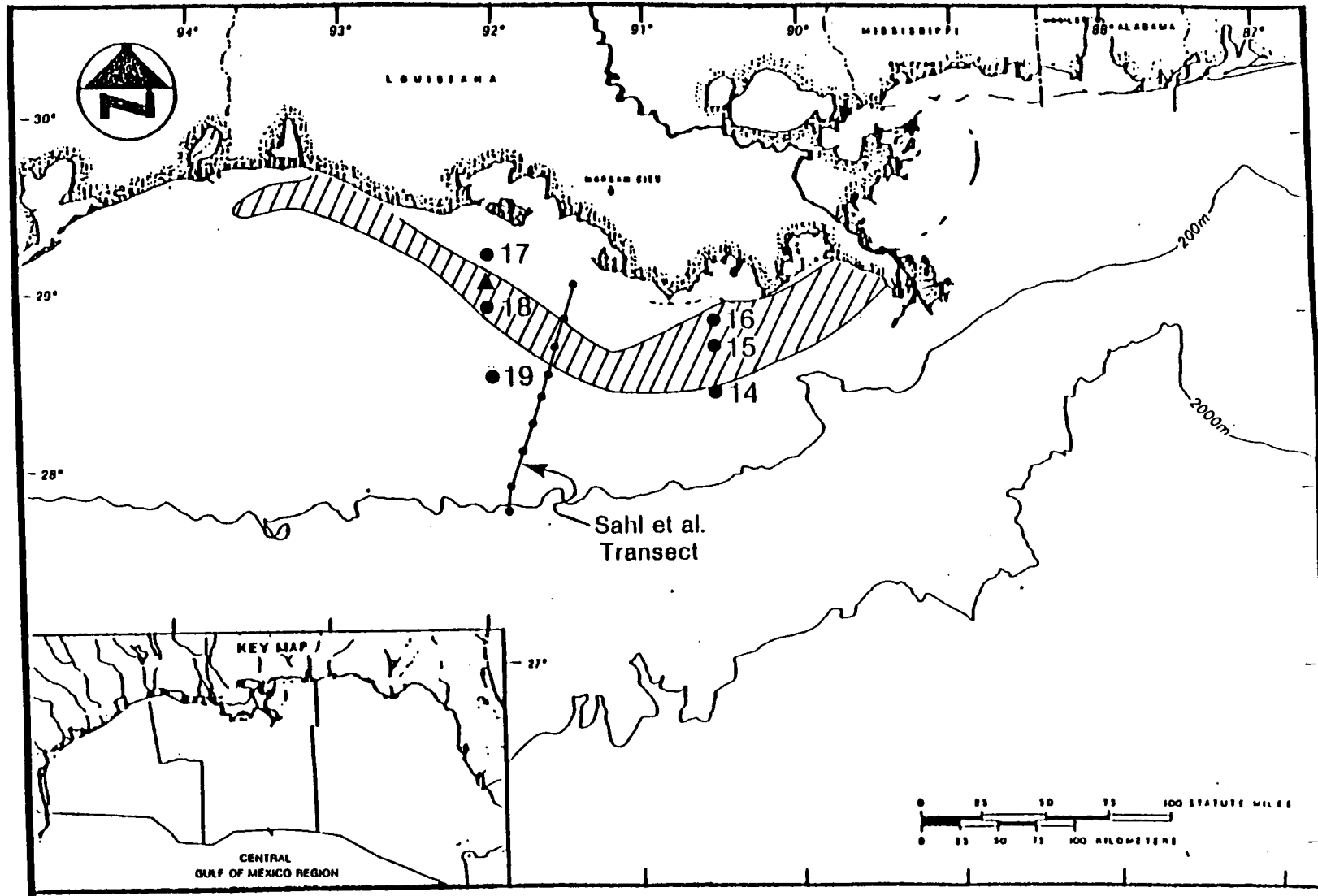
Figure 124. Location of moorings on which sediment traps were located. Triangle denotes site
of VIMS tetrapod deployment. Hatchured area is region of bottom hypoxia during
1987.

Table 8. Mooring data for sediment traps

Mooring	Water Depth (m)	Trap Depth (m)	m above bottom	Attachment Point
17	7.6	6	1	Base of Minispec
18	22	13	9	Mooring wire
		17	5	Mooring wire
		21	1	Base of Minispec
19	50	13	37	Mooring wire
		41	9	Mooring wire
		45	5	Mooring wire
		49	1	Anchor
16	20	13	7	Mooring wire
		19	1	Base of Minispec
15	27	21	6	Mooring wire
		23	4	Mooring wire
		26	1	Anchor
14	48	13	35	Mooring wire
		39	9	Mooring wire
		43	5	Mooring wire
		47	1	Anchor

Sample analysis was contracted to include only total mass, particle size distribution and percent organic carbon. In addition, we have measured the percent carbonate in trap samples. Portions of selected samples will be shipped to LSU for analysis of a suite of chemical pollutants. Trap samples were carefully wet-sieved through a 1 mm mesh and swimmers were removed from the sample. The sample portion less than 1 mm was split using a fast, high-precision splitter that uses air pressure to discharge a continuously-mixed particle suspension into six sub-samples (Tennant and Baker, 1992). Grain size distributions were obtained by wet-sieving samples into fractions < 63 μm, 63-125 μm, 125-250 μm, 250-500 μm and 500-1000 μm. Size fractions are sucked onto pre-weighed 0.4 μm Poretics filters, dried and reweighed.

Carbonate content was determined for one sample split by freeze-drying, weighing, acidification by dilute HCl, drying and reweighing for calculation of weight loss. Corrections were made for salt content based on water content and salinity. A portion of this sample was then analyzed for organic carbon content with a Carlo Erba NA 1500 Analyzer.

It is important to note some caveats in the use of sediment traps in shelf environments. Studies suggest that traps are unbiased collectors in currents where Reynolds' numbers (R = $p*u*D/\upsilon$, where p is water density, u is the velocity past the trap opening with diameter D, and υ is viscosity) are less than 30,000 with a cylindrical trap aspect ratio (A = trap height to diameter ratio-H/D) of 8 (Baker, et al.,1988). This would allow unbiased collections of particles in flows up to 40 cm/s for the 7.3 cm diameter cylinders we used. Data from adjacent current meters will be used to interpret and correct (if necessary or possible) calculated fluxes.

Another caveat in using traps in shelf environments is the overlap of the surface and bottom boundary layers. Turbulent planetary boundary layers have turbulent diffusion and

155

secondary flow that can circulate particles through the boundary layer (on the shelf, this can be the entire water column depending on stratification and current velocities) more than once before they settle to the layer below or to the seafloor. Therefore, trap measurements may yield overestimates of vertical flux in boundary layers (Gardner and Richardson, 1992). At the very least the trap samples yield relative fluxes in time and space, and provide samples for compositional and size analyses in different segments of the boundary layer.

C. Results

1. Moorings

The fluxes considered reliable from moorings 14-19 during deployments 1-5 (April 13-December 13, 1992) are graphed on a semi-log plot (Figure 125). Fluxes increase exponentially with depth by one to two orders of magnitude. Fluxes vary spatially by nearly three orders of magnitude among the sites over the same time period (deployment 4) and temporally by more than two orders of magnitude at the same site (site 14), though the temporal variability is usually closer to one order of magnitude at a given site.

The center of Hurricane Andrew went right between moorings 14 and 15 on August 26 during deployment 3 (July 21-September 1, 1992). A few days after passage of the hurricane, the moorings were serviced. A total of four traps, including all those at mooring 15, were torn off the mooring lines and one mooring with a single trap could not be found. One of the traps was on a minispec current meter frame that rests on the seafloor, weighted with a railroad wheel. The divers found the frame on its side and half buried in the mud. After attaching a cable and bringing it to the surface, the trap contained 15-20 cm of sediment, but the integrity of the sample is too suspect to be reliable.

The trap samples that have been analyzed for organic carbon and nitrogen show a decrease with depth in the percent of organic carbon from 2-5% at 6-9 mab to about 1% at 1 mab (Figure 126), even though the apparent flux of organic carbon increased with depth. The C/N ratio (by atomic weight) increases with depth from about 9 at 6-10 mab to as much as 15 at 1 mab.

During each deployment the carbonate percentage of trap samples decreased substantially with depth from as much as 40% at 6 mab to only 20% at 1 mab (mooring 14). As with organic carbon, the apparent flux of carbonate increased with depth.

The wet-sieved size distributions of the trap samples collected at each mooring site during deployment 5 reflects the same general trend as earlier deployments.

2. Tetrapod

During the May, 1992 deployment of the VIMS tetrapod, fluxes increased from about 9 g m^{-2} d^{-1} in mid water to 90 g m^{-2} d^{-1} at one meter above the bottom (Mooring ST1). The apparent flux measured with the trap attached to the leg of the tetrapod was 192 g m^{-2} d^{-1}.

D. Discussion and Interpretation

Trap samples are integrations of conditions over the time of deployment, with the mooring samples integrating over 6 weeks and the tetrapod samples integrating over a few days. The mooring samples provide spatial coverage over different shelf regimes relative to the plume. As noted earlier, trap fluxes measured in boundary layers are maximum fluxes because particles may cycle several times in the boundary layer before they are deposited. We await further

156
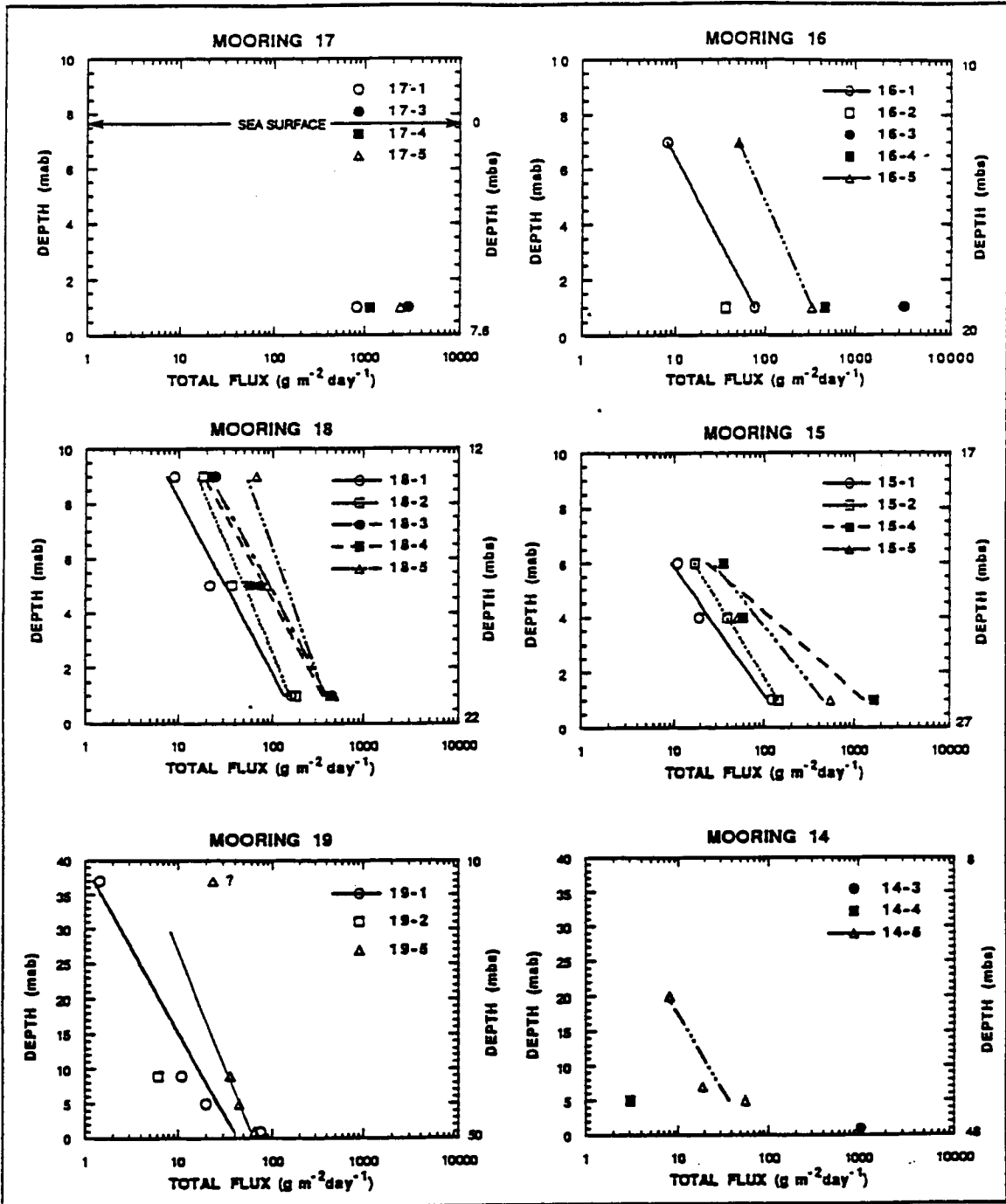
Figure 125. Fluxes calculated for sediment traps on LATEX A moorings 14-19 during Deployments 1-5 (April 13-December 13). Trap depths are plotted as meters above bottom (mab) on the left axis and in meters below the sea surface (mbs) on the right axis. To maintain uniform scales only the bottom 10 m are plotted except for moorings 19 and 14. Flux scales are the same on all moorings.

157
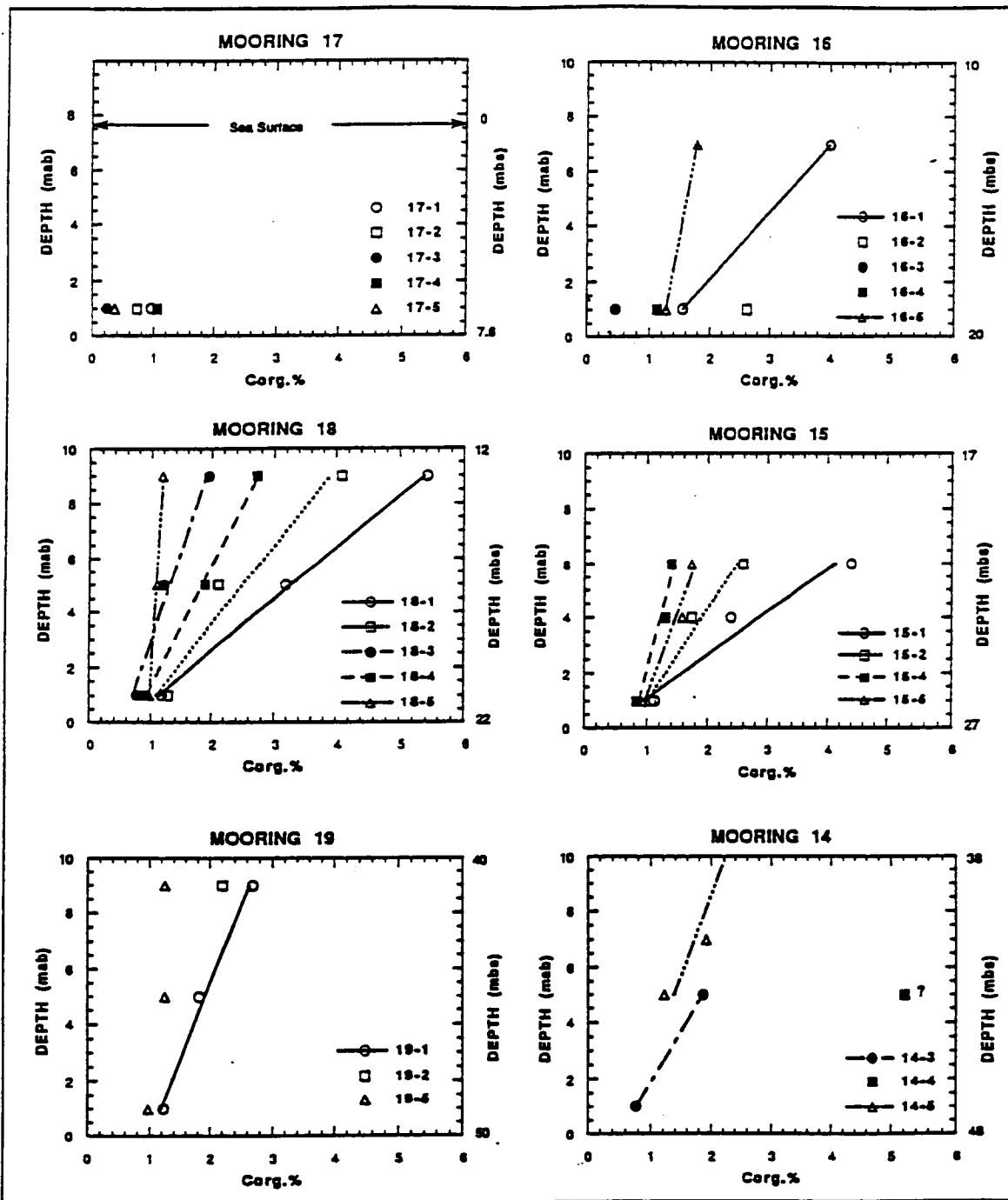
Figure 126. The percentage of organic carbon in the fraction less than 1 mm (usually >95% of the total samples was < 1 mm) was determined for each sample and is plotted as in Figure 125.

information about current speeds and hydrography during the deployment before final analysis can be made of which traps were likely to be within a boundary layer and for how long.

Pending further information on currents and hydrography, it seems reasonable to conclude that the large increases in flux with depth reflect the resuspension and recycling that occur near the seafloor in this region. The wet-sieved size analysis demonstrates that most of the resuspended material is very fine-grained or is composed of aggregates that are easily broken up in the sample handling. Material collected further up in the water column is larger in size and has an abundance of biogenic aggregates that do not break down during wet sieving. The decrease in the percentage of organic carbon with depth in trap samples is further evidence that the increase in flux with depth results from resuspension of bottom sediments, which are likely to have low organic carbon contents. The increase with depth in the C/N ratio is also evidence that the material collected contains older material that has had time to decompose, probably at the seafloor, thus increasing the C/N ratio.

The spatial variation in bottom fluxes reveals a sharp decrease with distance off shore (Figures 125 and 127). The high fluxes at mooring 17 are presumably caused by the close proximity to the Atchafalaya River. During the passage of Hurricane Andrew the total settling flux in near-bottom traps increased by up to an order of magnitude near the hurricane path (Figures 125 and 127). The currents were so high at mooring 15 that all the traps were torn from the mooring line and lost. Mooring 18 was 150 km west of the eye of the hurricane, and the bottom trap registered no increase during that time, suggesting an intense, but rather localized effect of the hurricane on resuspension. Again, we await the current meter data to reach final interpretation of the trap data.

A seasonal signal in the percentage of organic carbon collected in sediment traps is also beginning to emerge. The trap samples away from the seafloor are least likely to be contaminated by resuspended sediment and should best represent the composition of material settling from surface waters. Primary production in surface waters would be expected to be highest in the spring and decrease during the year. Thus, the percentage of organic carbon in the traps away from the seafloor should be highest in the spring and decrease during the year as seen in Figure 128a. It also appears that the percentage of organic carbon in mid-water traps from the area of hypoxia (moorings 15, 16, and 18) is greater than from outside the hypoxic area. This mid-shelf region may be an area of higher primary production because of increased water clarity and high nutrients. The particulate carbon could then quickly settle to the seafloor and utilize oxygen during degradation. The flux of organic carbon increases by as much as a factor of two over that same time period (Figure 128b), but that results from the 5-10-fold increase in total flux (Figure 125). The decrease in percent organic carbon provides a clearer picture of the changing seasonal conditions in the composition of settling material.

To determine whether or not there is a seasonal trend in resuspension of bottom sediments we have plotted the flux measured by all bottom traps versus time (Figure 129). Resuspension seems much lower in the late spring to early summer than during the rest of the year, but the intense resuspension during the passage of Hurricane Andrew during August may bias that impression. We might expect to have less resuspension with the greater stratification that would develop during the summer, but a comparison also needs to be made with the intensity and frequency of storm and wind events.

E. Relationship to Other Studies Areas

The marked vertical variations in total and organic carbon fluxes, percent organic carbon and C/N ratio are consistent with massive resuspension of bottom sediments in the bottom boundary layer due to large bottom shear stresses in this shelf area. Bottom fluxes decreased

159
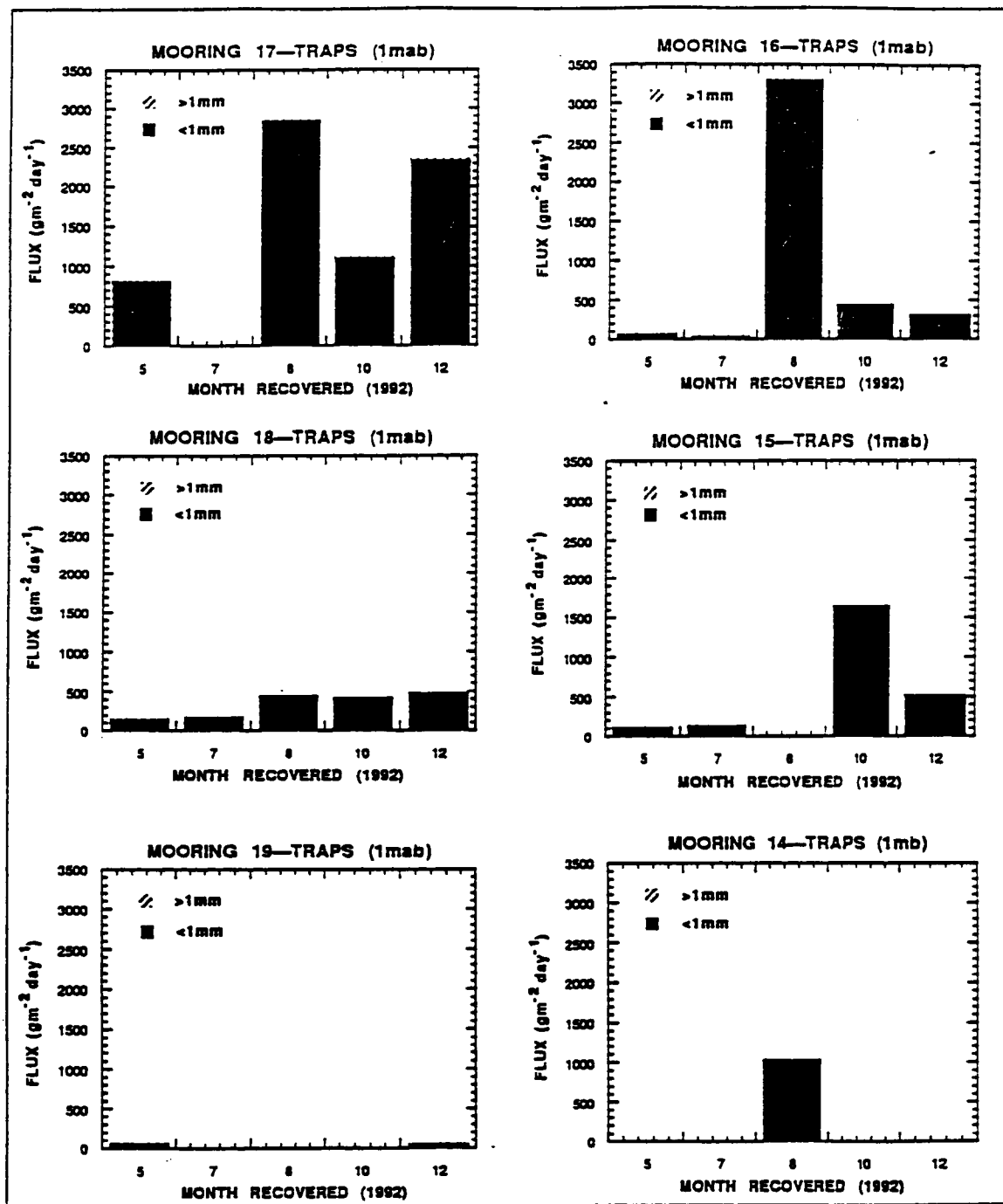
Figure 127. Fluxes at 1 meter above the seafloor calculated from the first 5 deployments of sediment traps at all mooring sites. Note the decrease in flux across the shelf (down the page), though several samples are missing. The passage of Hurricane Andrew near mooring 16 greatly increased the flux at that site, but less so at other deeper sites..

160
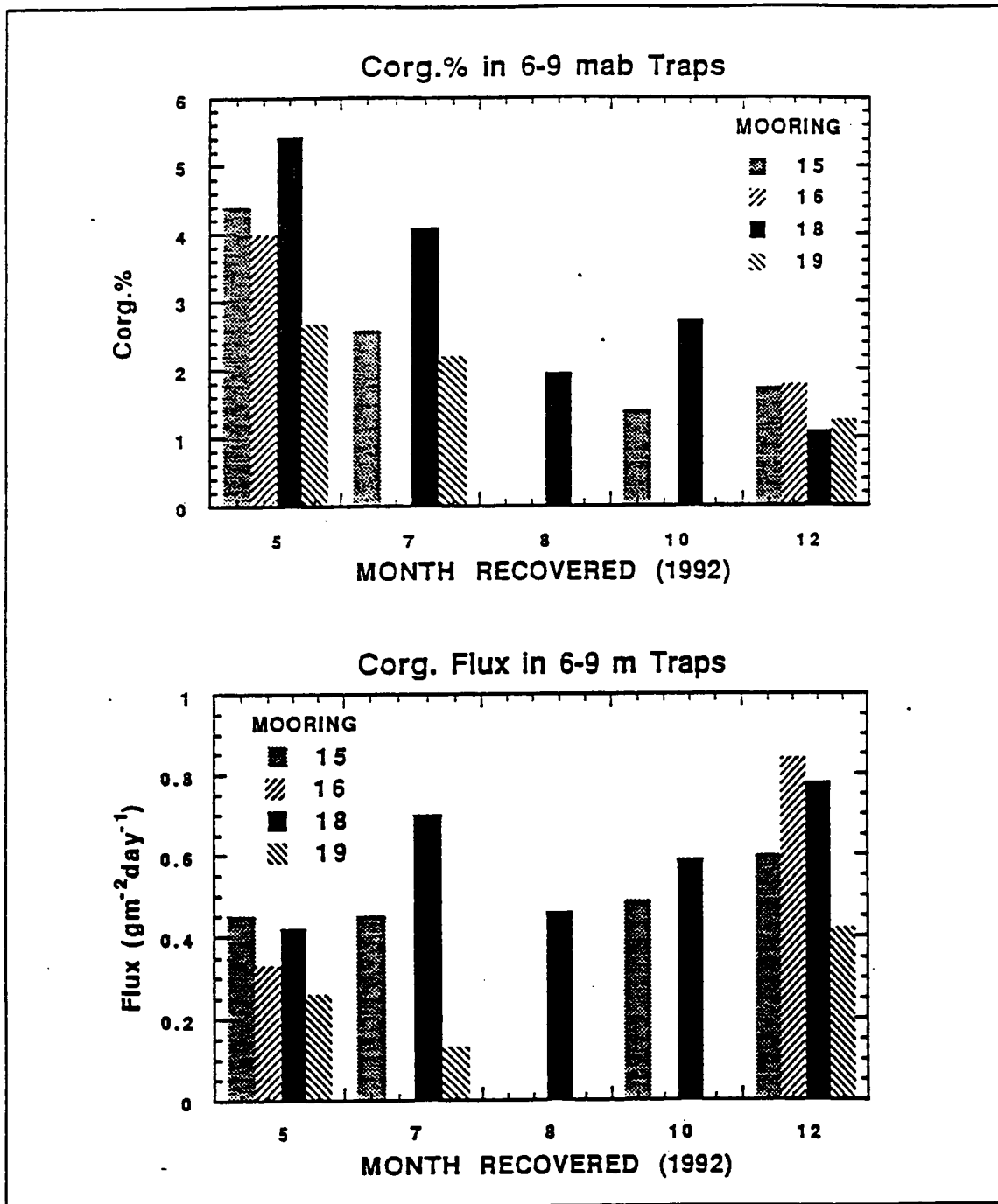
Figure 128. Traps 6-9 mab: percent organic carbon as a function of time of year (upper); flux of organic carbon as a function of time of year (lower).

TOTAL FLUX IN 1 mab TRAPS
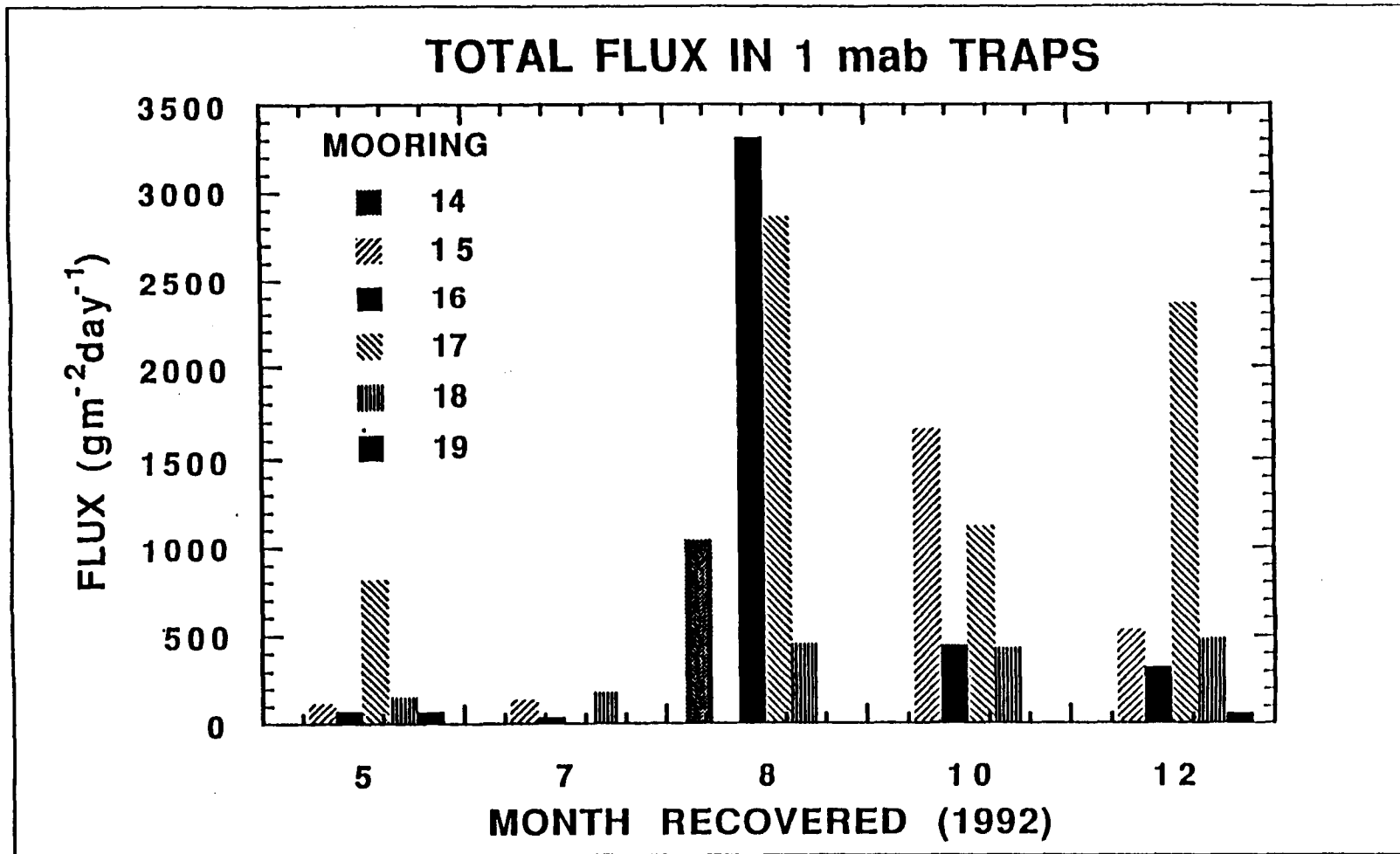
Figure 129. Total flux of material in bottom traps as a function of time of year.

with distance off shore as a result of decreased bottom stresses as the water deepens, increased distance from sources or river sediment, or both. Fluxes increased near the Atchafalaya River.

The mid-shelf area of summer hypoxia may result partially from an increase in the flux and organic carbon content of material settling in that region.

The passage of Hurricane Andrew increased the near-bottom fluxes (resuspension fluxes) by up to an order of magnitude near the path of the hurricane, but not at all away from the hurricane, suggesting a rather localized effect on resuspension.

V. Hypoxia
(Nancy Rabalais)

A. Introduction

Hypoxia (≤ 2 mg/l dissolved oxygen) is a seasonally dominant feature of the inner- to mid-continental shelf of Louisiana, most widespread and severe during June-August, but occurring as early as February and as late as October (Rabalais et al., 1991, 1992). Hypoxia forms and is maintained by a combination of physically controlled density structure (mediated by high freshwater inputs of the Mississippi and Atchafalaya Rivers) and biological processes that contribute to productive coastal waters and oxygen depletion of the lower water column. The configuration of hypoxic water masses can be related to large-scale circulation patterns, river flow, hydrographic structure (in particular salinity, temperature and density), and biological features (in particular chlorophyll *a* and phaeopigments concentrations and phytoplankton distributions). In addition, the distribution of hypoxic water masses detailed on the LATEX B plume cruises can be compared to data obtained from the NOAA NECOP Hypoxia Monitoring Studies of Rabalais et al. (1992)(where stations overlap suitably in time and space).

B. Methods

Dissolved oxygen concentrations were recorded electronically by the LUMCON SeaBird CTD unit. The precision of measurements for the SeaBird oxygen probe is 0.1 ml l^{-1}. The upper and lower dissolved oxygen limits of the probe were determined by the LUMCON Marine Technician prior to each cruise and incorporated into the configuration files for the SeaBird software (SeaSoft Vers. 3.4H). Calibration of the oxygen probe was accomplished by Winkler titrations on water collected in 5-liter Niskin bottles from the CTD/rosette across the range of values observed. Replicate titrations from replicate 300-ml BOD bottles were made on a Mettler DL21 automatic oxygen titrator. Mean chemically-derived values were compared to the SeaBird oxygen data for the oxygen probe stabilized at the depth at which the water sample was collected. A regression equation was developed by which the SeaBird oxygen data were corrected or not, depending on the goodness of fit of the regression equation and its deviation from a 1:1 relationship. An example of a suitable Winkler versus CTD regression is given in Figure 130.

A protocol was developed for extracting usable oxygen data from the SeaBird CTD unit. This methodology was used to delete oxygen data from the upper parts of CTD casts where the oxygen probe had not stabilized adequately prior to the downcast, where the oxygen probe had not stabilized adequately prior to the collection of a near-bottom water sample, and where the oxygen data for the entire cast were suspect. The remaining oxygen data were processed by the same protocols for the other SeaBird parameters. "Near-bottom" oxygen values are defined as those concentrations recorded at the end of the downcast, after the oxygen probe stabilized, and just prior to the tripping of Niskin bottles or just prior to the beginning of the upcast. "Near-bottom" values for Cruises I and II were as much as 2-3 m above the seabed, because rough sea conditions precluded taking the CTD unit within 1 m of the bottom.

Comparative hydrographic data were available from the NOAA NECOP Hypoxia Monitoring and Related Process Studies of Rabalais, Turner and Wiseman (e.g., Rabalais, et al., 1992). These data were collected with a Hydrolab Surveyor 3 (accuracy of 0.2 mg l^{-1}). Transect C of Rabalais et al. parallels the nearshore end of the LATEX-B S1 transect, then turns to the southeast (Figure 131). Similar station depths are occupied along the two transects and provide suitable data to examine temporal and/or small-scale spatial variability. LATEX-B station 104 was comparable in location and water depth to station C6B of the NOAA NECOP study.

Comparison of CTD and Winkler Oxygen Concentrations
NECOP - July 1992

$y = 0.29153 + 0.86469x \quad R^2 = 0.990$

CTD Dissolved Oxygen (approx. mg/l)

Winkler Dissolved Oxygen (mg/l)
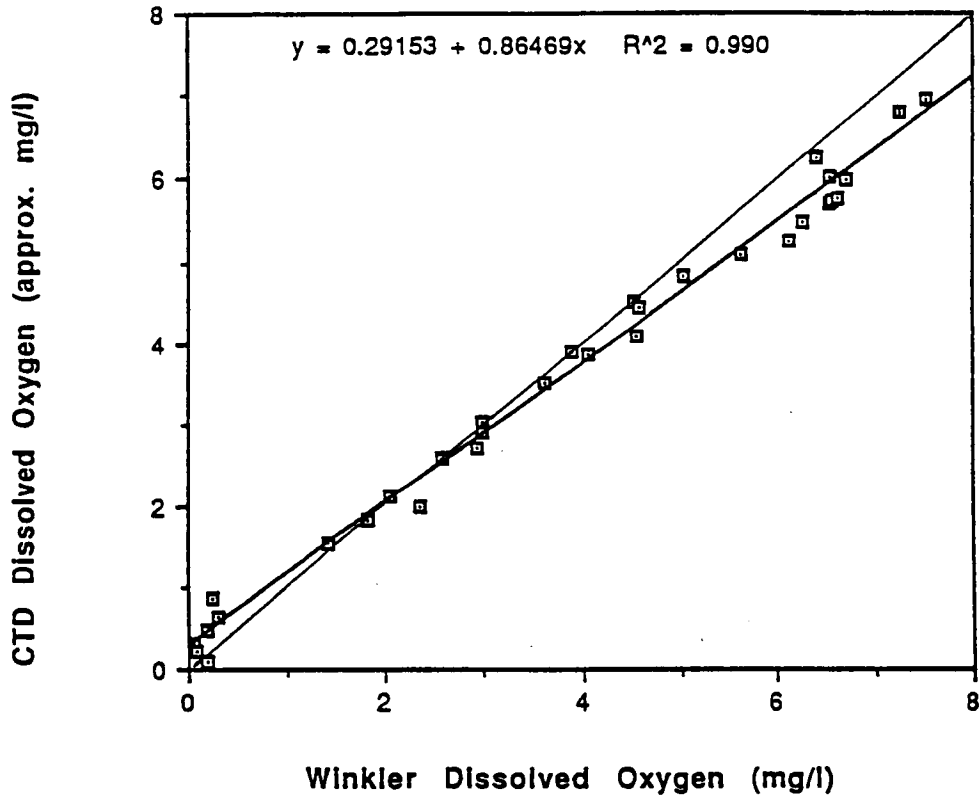
Figure 130. Comparison of dissolved oxygen data obtained from the LUMCON SeaBird oxygen probe and a series of Winkler titrations from the NOAA NECOP Hypoxia Monitoring and Related Studies (Rabalais, et al., unpubl. data).

166
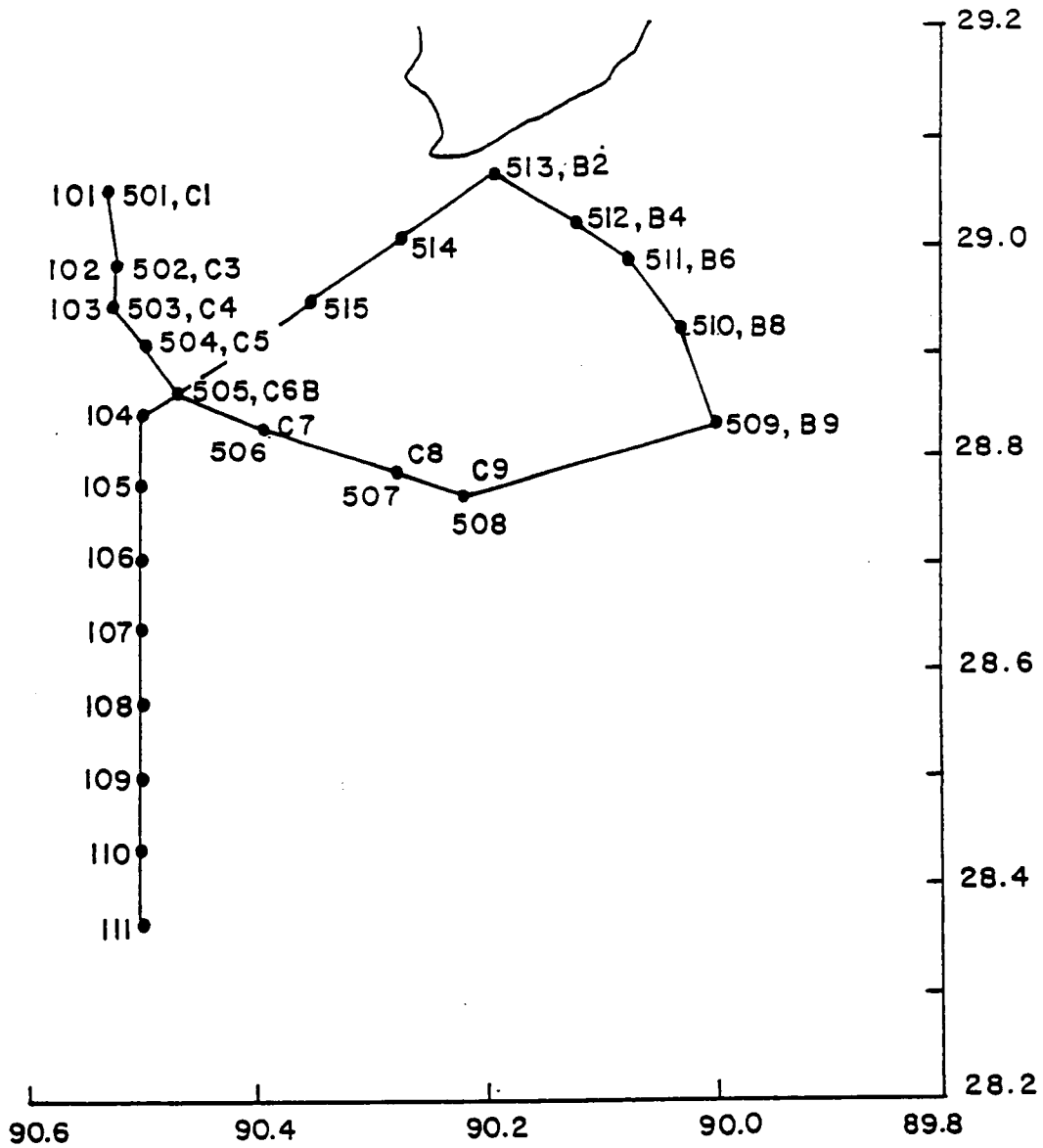
Figure 131. Map of LATEX-B stations along the S1 transect, the "Hypoxia Extension" of Cruise II, and the names for the NOAA NECOP Hypoxia Monitoring stations (Rabalais, et al., unpubl. data).

C. Results

1. Cruise I, April 1992

A broad range of dissolved oxygen concentrations (2 to 9.5 mg l^{-1}) was obtained for the development of a regression equation of CTD oxygen values versus Winkler titrations. In general, above 2 mg l^{-1}, the CTD oxygen probe was giving higher values for dissolved oxygen than determined by Winkler titrations (Figure 132). The CTD oxygen data were corrected by the following equation (R^2 = 0.985, n = 6):

$$y = 0.50215 + 0.82164x,$$

where y = recalculated CTD oxygen value, and x = CTD oxygen value measured during cruise.

The CTD protocol in use for Cruise I did not allow an adequate soak time for the oxygen probe, a slow enough lowering speed, and a suitable start depth. Very often the upper 2 to 8 m of the CTD cast did not provide suitable oxygen measurements, and these data were deleted. For stations P921048, P921050, P921057, and P921093, all oxygen data were deleted. Near-bottom values were deleted for P921005 and P921015. A revised CTD protocol was employed for Cruise II, and most of the SeaBird CTD oxygen data were usable (Stations P922101-P922164).

An area of near-bottom hypoxic waters was documented along the mid to outer stations on the S1 and S2 lines, respectively, from Terrebonne Bay to Point au Fer Island (Figure 133). Other near-bottom waters low in oxygen, but not hypoxic ($2.5 \leq x \leq 4$ mg l^{-1} dissolved oxygen) were located off the Sabine and Galveston estuaries (Figure 133). The hypoxic water mass was confined to the lower 2 m of the measured water column, compared to a much thicker hypoxic zone usually seen in mid-summer, and was not severe, oxygen values of 1.5 to 2 mg l^{-1} compared to values usually less than 0.5 mg l^{-1} in mid-summer.

A comparison of dissolved oxygen data and density structure for LATEX-B transect S1 (April 22, 1992) was made with the NOAA NECOP transect C data for April 10-11, 1992. The near-bottom oxygen depletion feature was evident mid-transect on both dates (Figure 134). Density structure of the water column was very similar on the two collection dates and indicates the persistence of the hypoxic zone and the density structure. Hydrographic data from P921004 and C6B for the same date show somewhat different salinity and temperature structure, but very similar oxygen profiles.

2. Cruise II, October 1992

A revised CTD protocol that allowed for a longer surface "soak" time, a slower lowering speed, and a shallower start position, provided a better and more complete dissolved oxygen data set derived from the SeaBird CTD unit. Complete oxygen profiles of SeaBird data, which started in the upper 2 to 3 m of the water column were obtained for stations P922001-P922164. Problems with the SeaBird CTD unit precluded obtaining any usable oxygen data from stations P922165-P922185. A SeaCat CTD unit was used for stations P922186-P922414, but the dissolved oxygen concentrations were too high to be realistic and did not match real-time oxygen concentrations recorded from the SeaBird CTD display. The oxygen data for the SeaCat casts were deleted.

Because the sea conditions prior to and during Cruise II were rough, the water column was well-mixed and a limited range of oxygen concentrations was encountered. This prevented us from obtaining a broad range of dissolved oxygen concentrations for the development of a regression equation of CTD oxygen values versus Winkler titrations. Values between 4.5 and 6

Comparison of CTD and Winkler Oxygen Concentrations
LaTex - April 1992
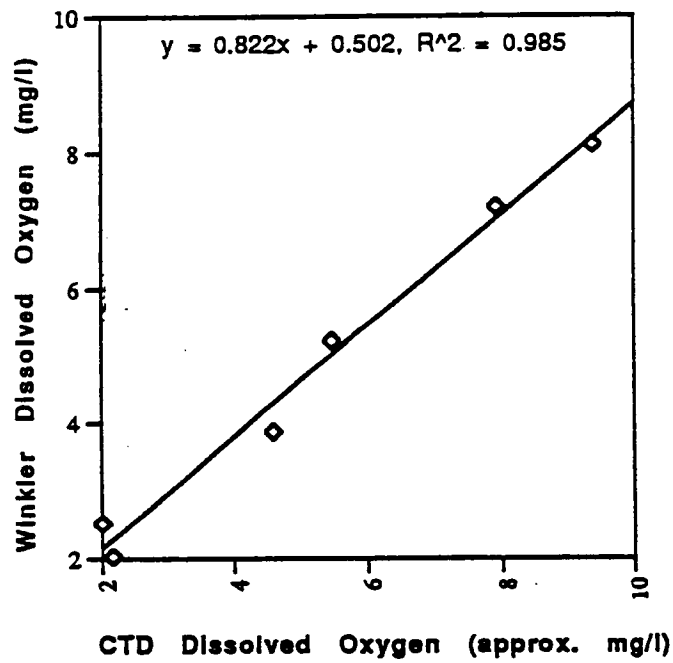
Figure 132. Comparison of dissolved oxygen data obtained from the LUMCON SeaBird oxygen probe and a series of Winkler titrations for Cruise L

LATEX-B, P92-I, APR 1992
Near-Bottom Dissolved Oxygen (mg/l)
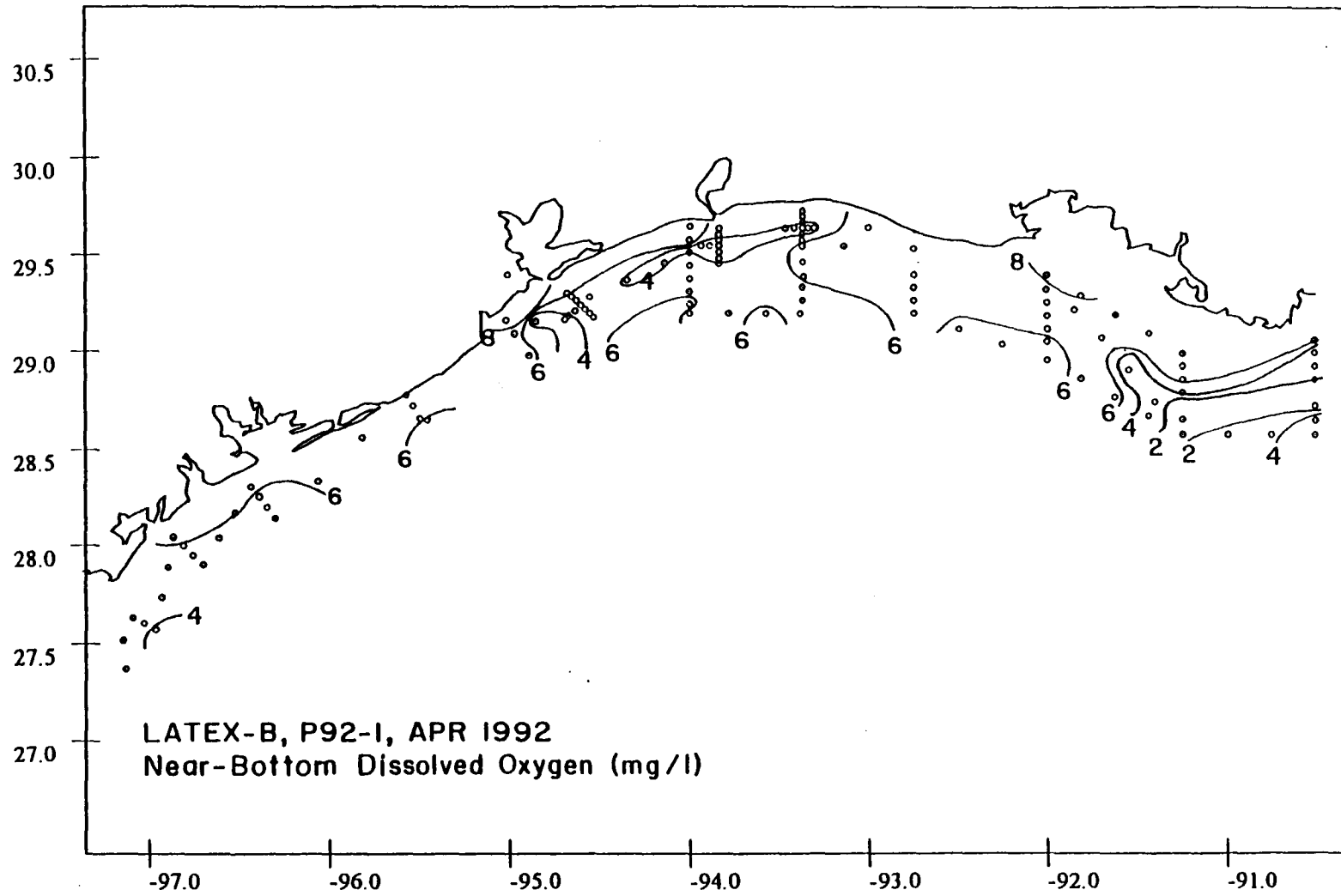
Figure 133. Distribution of near-bottom dissolved oxygen (mg l⁻¹) for Cruise I ("near bottom" is 2 to 3 meters above the seabed).
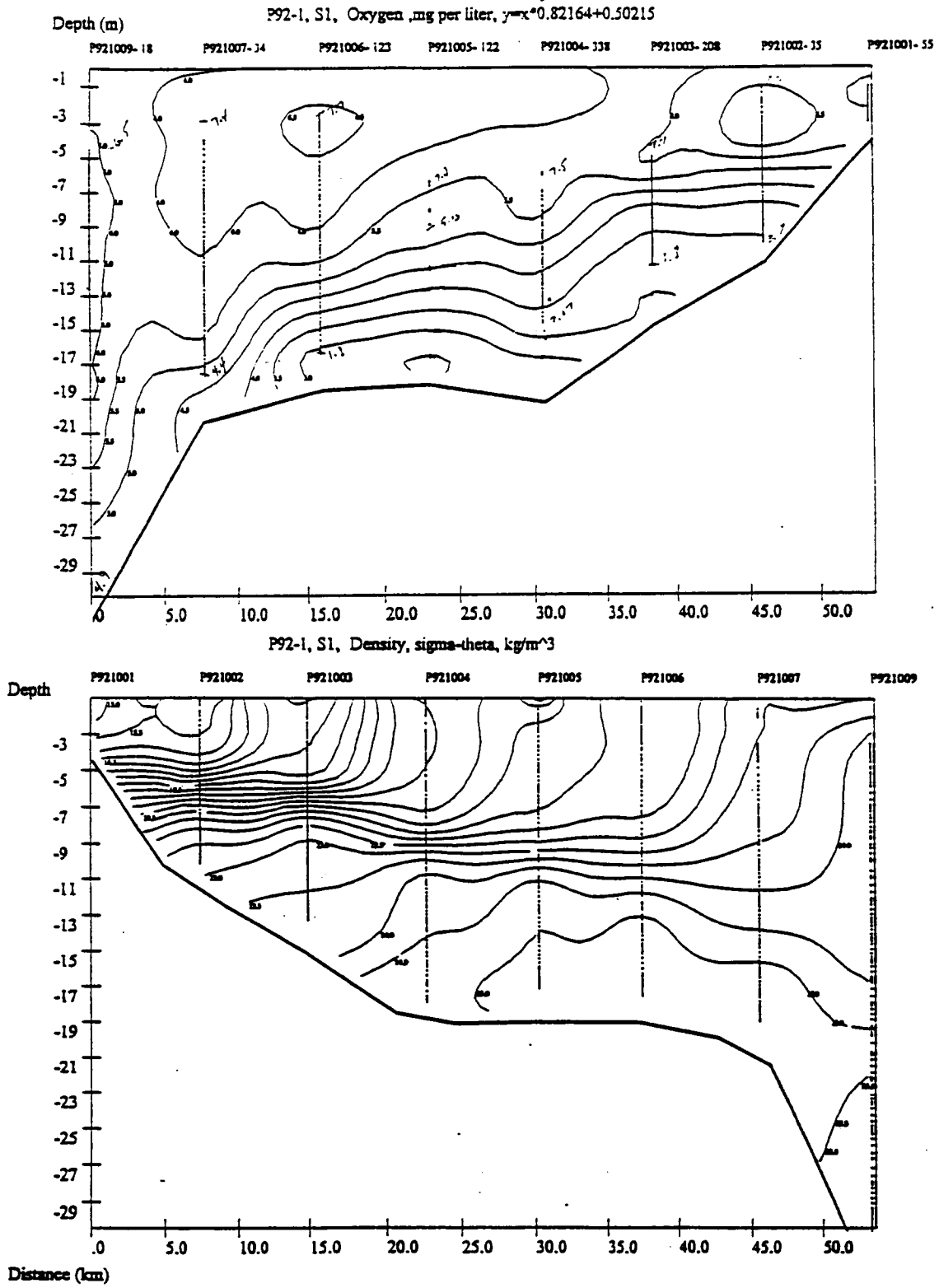
Figure 134. Cross-shelf contours of dissolved oxygen (upper) and density (lower) for Cruise I, S1.

171

mg/l were obtained, but the number of points was not adequate for a correction of the SeaBird dissolved oxygen data. In general, the CTD oxygen probe was giving lower values for dissolved oxygen than determined by Winkler titrations, and values reported are probably low by as much as 1 mg l^{-1}. Because the number of data points in the regression was so low, it was not possible to correct the CTD oxygen data. Comparison of the CTD data at P922104 with station C6B (NOAA NECOP studies of Rabalais, et al., 1992) for the same data indicated that the CTD values were probably low. It was not possible to calibrate the oxygen values for the SeaCat CTD unit. Niskin bottles were fired from the SeaBird rosette system, which displayed real-time data, and the pressure sensor recorded on the SeaCat, so that the depth and oxygen concentration of a water sample could not be cross-referenced to an oxygen reading on the SeaCat. Thus, the dissolved oxygen data for Cruise II are limited and not absolute.

The water column was fairly well-mixed with regards to salinity, temperature, and dissolved oxygen. There were no areas of near-bottom hypoxic waters (Figure 135).

LATEX-B, P92-2, OCT 1992
Near-Bottom Dissolved Oxygen (mg/l)
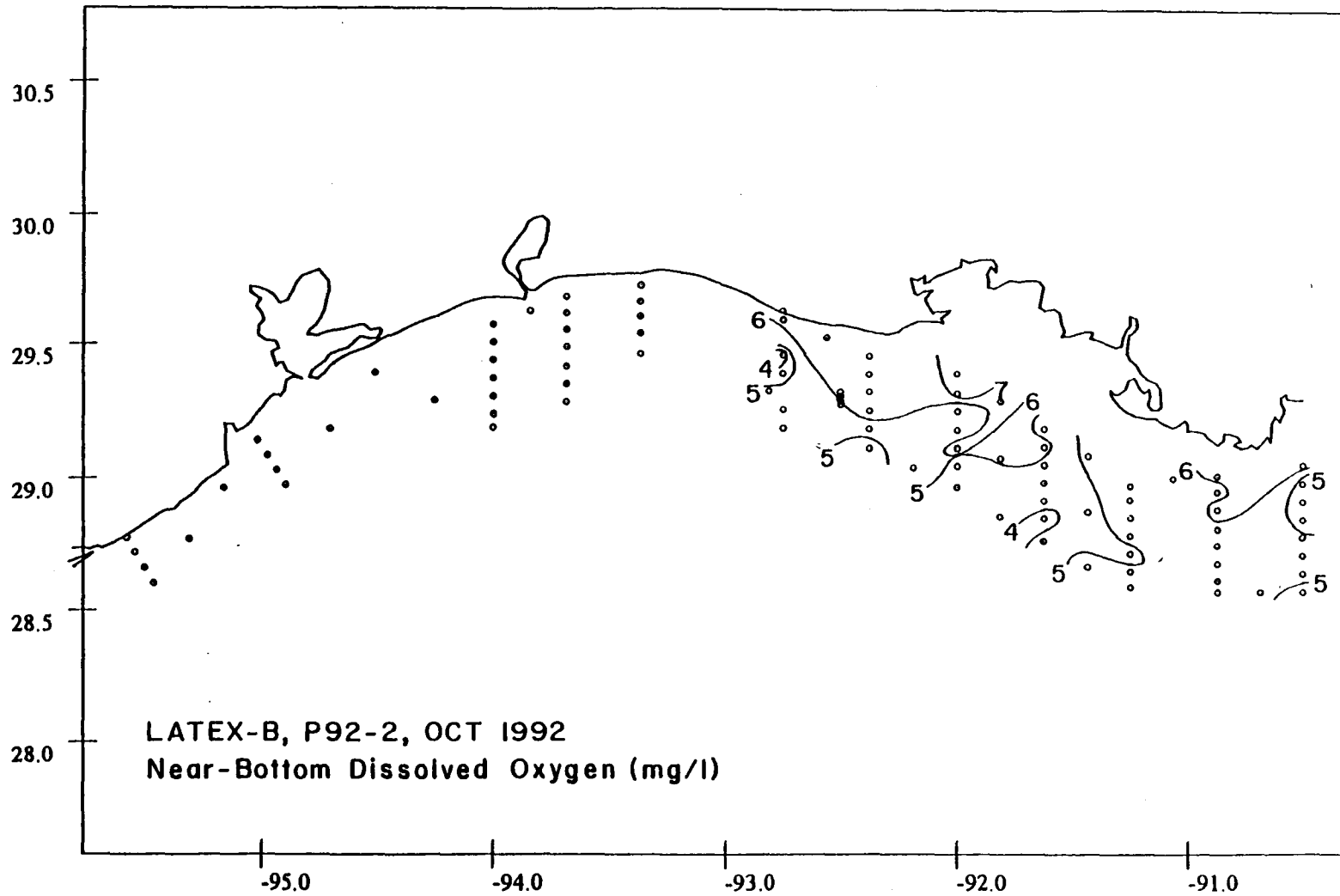
Figure 135. Distribution of near-bottom dissolved oxygen (mg 1^{-1}) for Cruise II ("near-bottom" is 2 to 3 meters above the seabed).

173

VI. Pollutant Chemistry
Transport and Three-phase Partitioning
in the Shallow Coastal Shelf of the Gulf of Mexico
(Jay C. Means and Debra J. McMillin)

A. Introduction

The Minerals Management Service is charged with the responsibility to determine and evaluate environmental impacts of the development and production of oil and gas in the Outer Continental Shelf (OCS) regions of the nation's coasts. Historically, the Gulf of Mexico has been an area of intensive exploration and production of oil and gas and is therefore a region where impacts might be expected to be the greatest if they occur. Impacts of production may result from chronic discharges of drilling muds, surfactants, produced waters and other chemicals used in the production process or they may result from accidental or catastrophic releases of oil as the consequence of spills, blowouts, fires or breaks in transportation lines.

In order to investigate the potential fate of chemicals discharged into Gulf of Mexico waters, a fairly complex set of physical and chemical oceanographic processes must be elucidated and understood. Among these are the bulk transport or advective processes of the water masses themselves. This includes mixing of fresh and saline waters, current direction and velocities, and temperature and salinity gradients and stratification. All of these forcing functions drive the dilution of chemical species in discharges. Along with these bulk phase physical processes, pollutant chemicals may undergo partitioning processes with suspended particulates (Means, et al., 1980), which may have their origins in either allocthonous (riverine) or autochthonous (resuspension/biological production) sources. The partitioning of both metals and organic compounds that occurs in this dynamic hydrologic environment is a function of compound/metal solubility and changes in salinity, temperature and redox potential. Sedimentation of particulates to the sediment bed is the major removal process of chemicals that may be introduced in discharges. Resuspension and bed load transport of materials may also occur in tidally energetic areas or as the result of strong weather events. Photolysis and hydrolysis reactions resulting in the decomposition of the chemical may be important for some chemical classes.

In recent years, a competing partitioning process with colloidal-sized, organic-rich micro-particulates has been recognized as a potential factor in the facilitation of transport processes in aquatic systems (Sigleo and Means, 1990). Because these colloidal solids can bind both metals and organic compounds and because they are relatively stable in the water column, they result in increasing the apparent "dissolved phase" transport of bound substances. The present study represents the first large geographic scale evaluation of the three-phase partitioning model that was developed in the laboratory.

Attempts to study such a complex array of transport processes using the low level chronic discharges from single sources in the Gulf of Mexico have been only partially successful in determining the fate of chemicals. At most, the range of reliable information has extended only a few hundred meters from the discharge source (Rabalais, et al., 1991). In the present study, the large and relatively intense chemical signatures of the Mississippi River and Atchafalaya River plumes, as well as other smaller riverine inputs to the Gulf of Mexico from the Calcasieu, Sabine and Galveston estuaries, have been used to investigate transport processes over much greater distances and may provide the necessary information to develop long-range fate and transport models for the Gulf of Mexico. These models can be used by MMS in fulfilling their mandate to assess real and potential environmental impacts of chronic and catastrophic chemical releases during oil and gas production.

B. Objectives

The objectives of this subtask are:

(1) To make pollutant chemical measurements on samples collected on the hydrographic cruises whose geographic focus is the Mississippi-Atchafalaya plume, which gives rise to the Louisiana/Texas coastal current, from the Mississippi River to the south Texas coast, with special attention given to the area from the Atchafalaya River to the north Texas coast. The pollutant samples for measurements were acquired at 34 selected stations and two depths.

(2) To use these measurements to characterize the pollutant plume in the study area.

(3) To trace the movement and mixing of pollutants in particular water masses within the plume in conjunction with the data from the other parts of the study, particularly the remote sensing and current data.

(4) To assist in the interpretation of the importance of changes in water mass characteristics within the plume and offshore to pollutant and sediment transport.

(5) To use phytoplankton and zooplankton systematics to determine the source of the organic material controlling colloidal phase biogeochemistry.

(6) To identify and trace specific chemical pollutants as they enter into and mix and advect through the plume.

Based on our knowledge of the hydrography of the LATEX shelf, we designed and undertook a hydrographic sampling plan to meet the above objectives. We have begun to characterize—chemically, physically, and biologically—the hydrographic conditions of the plume and to determine the pollutants present in the plume and their speciation between the dissolved, colloidal and particulate phases in the plume. In addition, we collected and analyzed 52 sediment samples from coastal areas adjacent to estuaries between the mouth of the Mississippi River and the Galveston Bay estuary. The goal of sediment analyses was to characterize the scope of pollutants being deposited in surficial sediments in the coastal current region.

During Cruise I, a total of 68 samples of plume water were collected for pollutant analysis. These samples were fractionated on board the ship using filtration and ultrafiltration techniques into a total of 204 dissolved, colloidal or particulate samples. In addition, 2-liter dissolved fraction water samples were extracted for organic pollutant analysis on the ship using solid phase extraction (SPE) techniques. This approach to the sampling of the plume had several advantages:

(1) The time between sampling and extraction was minimized to prevent degradation and changes in phase distribution of the pollutants.

(2) Contamination of the samples was minimized.

(3) Storage of large volumes of water on the ship was eliminated. Typically, a 20-liter water sample could be reduced to the following in 3-5 hrs:

(a) A set of 0.4 μm filters containing the particulate sample fraction, stored in a small glass jar at -20°C.

(b) A liquid sample of 100X enriched colloidal fraction, stored in a 250 mL bottle at 5°C.

(c) A liquid sample of ultrafiltrate, acidified to pH <2 and stored in a 250 mL glass bottle at 5°C.

(d) An SPE extraction disc, stored in a 30-ml glass ampule at -20°C.

(4) Transportation of large volumes of water back to the laboratory was thus eliminated.

(5) Preparation for analysis was largely accomplished in the field, thus saving time in the laboratory on shore and reducing the time between sampling and analysis.

Sample collection and processing on the ship went flawlessly and all samples were obtained without any losses.

176

Chemical analysis in the laboratory utilized multi-elemental inorganic analysis by Inductively Coupled Plasma/ Mass Spectrometry and multi-component organic analysis using selected ion monitoring gas chromatography/mass spectrometry techniques. The elements measured include: As, Al, Au,Ba,Be, Bi, B, Ca, Cd, Cu, Cr, Co, Ce, Fe,Hg, Ir, K, Li, Mg, Mn, Mo, Na, Ni, Os, P, Pd, Pb, Pt , Ra, Sb, Se, Si, Sn, Sr, Th, Tl,, Ti , U, V, Zn. The organics included: 59 (51 resolved by GC) aromatic hydrocarbons, PCBs in 6 chlorination groups, 19 selected chlorinated pesticides, and 6 selected herbicides.

C. Results of Organics Analyses

1. Cruise I, April 1992

Figure 136 graphically depicts the mean values for all stations where a particular analyte was detected, showing the distribution of analytes between the four phases examined. Particulate phases concentration in this graphic were divided by 20 liters to correct for the volume of water that was filtered to obtain the sample. Figure 136 shows that most pollutant concentrations were similar between the particulates phase and the bedded surficial sediments. Exceptions were the herbicides (limited to cyanazine and metolachlor), which were only detected one time each in the particulates phase. PCBs were only detected in the sediments. It should be noted that the detection limit of the particulates phase was approximately three times higher than that for the sediments and was the highest detection limit of all matrices analyzed; therefore, transport of low amounts (parts-per-trillion) of pollutants in this phase could go undetected. Alkylated, or petrogenic PAH were predominant in the particulate and sediment phases, as expected, but were detectable in both dissolved and colloidal phases as well. Naphthalenes were the predominant alkylated PAH in all phases, but especially in the dissolved phase. Dibenzothiophenes were not detected in the colloidal phase. Parent PAH compounds were divided into low molecular weight (LMW) and high molecular weight (HMW) groups with MWs from 128 to 178 (phenanthrene, anthracene) in the former and MW 202-278 in the latter. Figure 136 shows that LMW PAH were predominant in the dissolved phase, while HMW PAH tended to be greater in the other phases. (Refer to the discussion of Cruise II for further discussion of the distribution of individual PAH between the three water phases.)

Following is a discussion of each of the four phases examined as part of Cruise I, including geographical and depth distributions. A comparison of data from the two cruises will be made later in this discussion.

Sediments. Sediment samples were obtained from selected stations within Cruise I, taken as a box pattern adjacent to the Atchafalaya Bay, and in a cruciform pattern of along- and across-plume transects in front of the Calcasieu, Sabine, and Galveston estuaries. Concentrations of parent PAH were uniform between most stations, with the exception of station P921100, just nearshore of the crossing of the two transects at this location. Station P921100 showed concentrations that were an order of magnitude higher than that found at all other stations for all parent PAH except naphthalene and acenaphthene. Alkylated PAH were also in highest concentration at this station, although the magnitude was not as great. The next highest concentrations for these same analytes (both parent and alkylated PAH) occurred in the Atchafalaya box, at stations P921022 and P921023, along the diagonal between S2 and S3, and at the point nearest to shore of S3. A plot of concentration by latitude and longitude is shown in Figure 137 for the C2 (dimethyl) phenanthrenes. It can be seen that concentration gradients for this class of analytes exist at every estuary, with concentrations being highest near shore.

DDT metabolites were detected in the sediments. DDE (p,p') was detected at low concentrations (<2 ppb) at most stations, while o,p'-DDD was found primarily in the Atchafalaya box and at the Calcasieu crossing. Dieldrin was detected twice (3 ppb), both within the Atchafalaya box, and hexachlorobenzene was detected three times within the Atchafalaya box

177

Figure 136. Mean distribution of organic pollutants between three phases of water and bedded sediment samples collected during Cruise I.
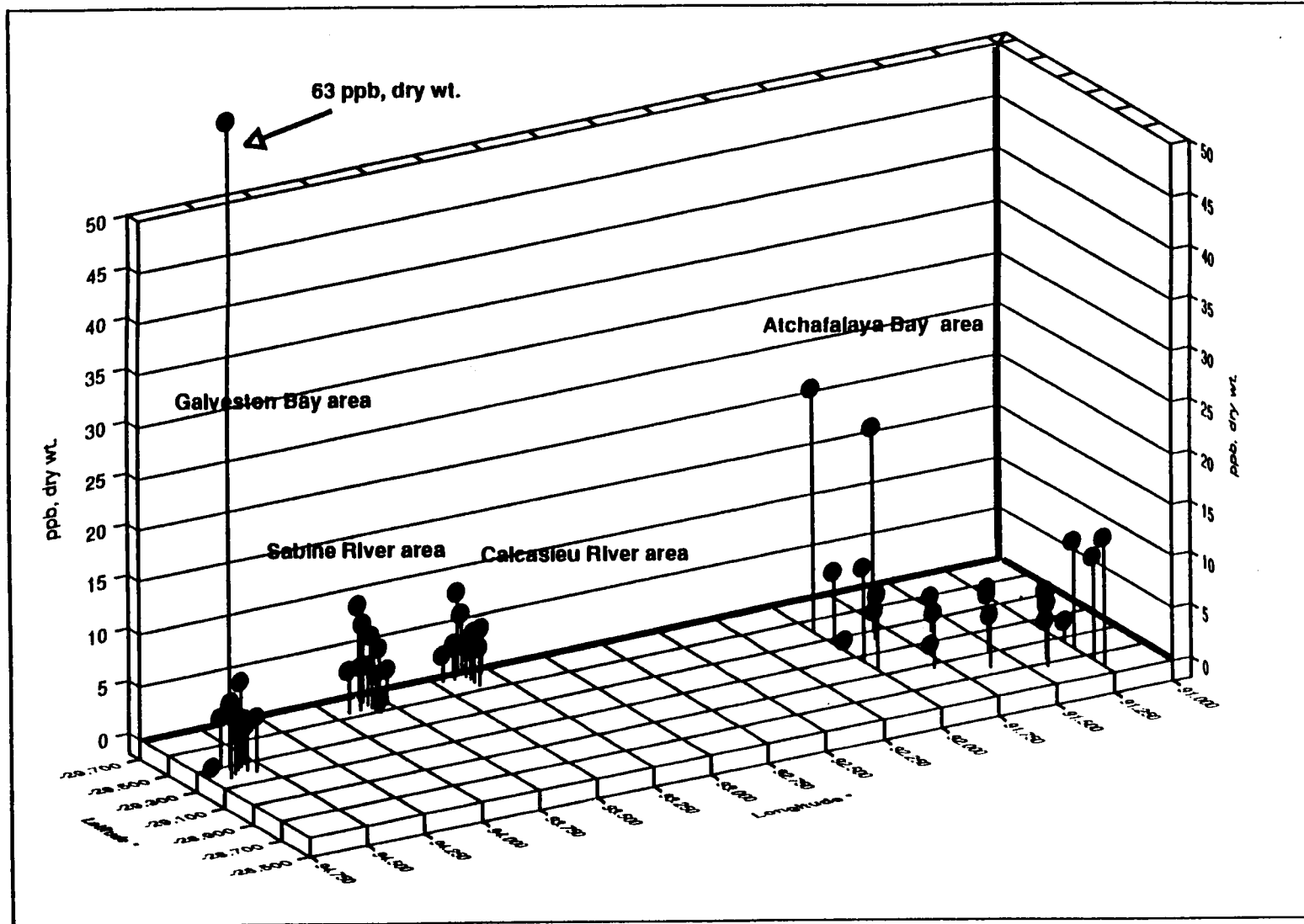
Figure 137. C2-phenanthrenes concentrations (ppb) in bedded sediments collected during Cruise I.

and once at Calcasieu, all at less than 0.5 ppb. PCBs were found in the Atchafalaya box, along the outer edge and the inside diagonal (CL2-CL6), at Calcasieu (CL5 and CL6), and once at Sabine (CL5-CL7), showing the highest concentrations observed (7 ppb CL5), at station 80, closest to shore.

Particulate Phase. Naphthalenes were seen in very high concentrations (2000 ng/g) in the early samples taken on Cruise 1. As this chemical is the most water soluble of the PAHs, and high concentrations were not seen in the other phases, it is presumed that this is an artifact of sample processing on ship. Fluorine and acenaphthene were detected in this phase at most stations and at uniform levels (mean 7.7 and 9.7 ng/g, respectively); other parent PAHs were detected sporadically over all stations, but fairly consistently at station P921001, with the bottom sample generally showing higher concentrations than the surface sample.

Alkylated PAHs were detected more frequently in the particulate phase than were parent PAHs. The alkylated naphthalenes were detected at nearly all stations, and showed highest concentrations nearshore in the transects S6, S7, and X4. No alkylated dibenzothiophenes were detected. C2-phenanthrenes were only detected at three stations, with a significant concentration only at station P921001, in the bottom sample. C3-phenanthrenes were detected more frequently than the C2s, and showed significant concentrations nearshore in transects S4 (one observation) and S6 (three stations, surface and bottom). Chlorinated pesticides, herbicides, and PCBs were observed only at trace levels. Metolachlor and cyanazine were frequently detected at trace levels at eastern stations (P921001 to P921028), representing the Timbalier Bay transect and the Atchafalaya box.

Colloidal Phase. Currently, data for the colloidal phase are reported as "pg/ml," reflecting the concentration of the sample *containing* the colloidal phase. The colloidal phase is actually suspended in an aliquot of the dissolved phase, and when data is available to correct for the actual mass of colloids (along with subtraction of the dissolved phase contribution), the true pollutant concentrations will likely increase dramatically. For example, the current factors for determining final concentration of analytes contain the value 240 (ml volume of sample) in the divisor. This value will be replaced by a much smaller number, the mass of colloids in g, which will most likely be <1 g/l, and is expected to vary between samples and with salinity.

LMW parent PAHs detected in the colloidal phase consisted of predominantly naphthalene, fluorine, phenanthrene and anthracene. Both were detected at one station on S8 and two stations each on S5 and S6. For HMW PAHs, fluoranthene and pyrene were detected at a majority of stations (frequency 46 and 47, respectively, out of 68 samples), followed by benz(a)anthracene and chrysene (frequencies of 21 and 31). A concentration gradient for these analytes was observed on S1 in both surface and bottom water samples. Other HMW PAHs, such as benzo(b)fluoranthene, benzo(a)pyrene, and benzo(g,h,i)perylene, were also detected in samples from S1. Additionally, benzo(e)perylene, which was not on the target analyte list, was detected on S1.

No patterns were observed for the alkylated PAHs in this phase, with detection occurring sporadically. No chlorinated pesticides were detected. Atrazine was the most abundant analyte in the colloidal phase, occurring at 67% of sample stations. The highest concentration of atrazine in surface and bottom water samples occurred on S3. Concentrations for other transects were similar, with the highest concentration observed in X2, Aransas Pass. Metolachlor was the only other herbicide detected in the colloidal phase, detected in four samples from S3, twice on S6, and once each on S1 and S8.

Dissolved Phase. Like the colloidal phase, herbicides were an important constituent of the dissolved phase. Trifluralin was the only herbicide not detected in quantifiable amounts. Atrazine averaged 200 pg/ml over all stations, followed by cyanazine at 100 pg/ml, metolachlor

180

at 36 pg/ml, and simazine at 31 pg/ml. The highest concentrations for atrazine were recorded for both the surface and bottom samples in S6 (averaging 2500 pg/ml) and in one surface sample in transect X2. Plots of transects S1 through S4 for all the herbicides shows that concentrations decrease with distance from shore. Metolachlor showed a geographic distribution similar to atrazine, with the same two high points, but the concentrations were lower and fairly uniform among stations. Simazine was absent from S1, and occurred mainly in the Atchafalaya box and S4, however, the highest value (130 pg/ml) was again recorded at station P921125, X2, in the surface sample. Cyanazine was only detected in transects S1 through S4, and was highest in transect S1, where a clear concentration gradient was shown. A three-dimensional plot of this region showing the geographic distribution suggests that it is possible that cyanazine might be useful as a marker of Mississippi River inputs. Alachlor also was detected only in this region, although less frequently.

Several of the parent and alkylated PAHs showed highest concentrations at the same stations (P921076 and P921125) as for the herbicides. Alkylated PAHs were detected more frequently in this phase compared to the colloidal phase; this is most likely due to the lower detection limits afforded by concentration of 2 liters of dissolved phase sample, while the colloidal fraction is much smaller (240 ml).

2. Cruise II, October 1992

Figure 138 shows the summary data obtained for three phases of water samples collected on Cruise II. Compared to the summary data for Cruise I (Figure 136), the particulate fraction concentrations are significantly lower for Cruise II, while the concentrations of the dissolved and colloidal phases was of the same order between cruises, with Cruise II values slightly higher than for Cruise I. This can be explained for the LMW PAH category in terms of the high naphthalene values observed in Cruise I particulates from early stations. The sample dry weights for the particulate fractions were also lower in the fall cruise compared to the spring, with mean values of 0.78g, and ranging from 0.43 to 4.1 g for the fall cruise compared to a mean of 1.1g, ranging from 0.17 to 16.0g, for Cruise I. High flow volumes occur in the spring and carry a greater proportion of particulates. This is also related to salinity, which reflects freshwater dilution, and was higher in the fall cruise. Salinity is also an important factor in the 3-phase distribution of hydrophobic pollutants.

Figures 139-141 show the distribution of individual PAHs along S1 for each of the three water phases. Within each phase, it can be seen that the relative distribution of PAHs was similar between stations regardless of concentration. Between phases, the distribution of PAH follows MW—e.g., lower MW PAHs predominate in the dissolved phase, and the HWM PAHs were seen primarily in the particulate phase. Naphthalene was generally the most abundant PAH in each phase and is not shown in the figures.

River-source Samples. Prior to Cruise II, samples of source-rivers were collected and subjected to the 3-phase analysis. Figure 142 shows the herbicide concentrations detected in the various river samples. Three samples were taken from the Mississippi River, one at Belle Chase (BC), and two at Baton Rouge (BR. A and BR. B). Note that concentrations were significantly higher in the BC sample, indicating that input downstream of Baton Rouge is an important source of herbicides to the Gulf. Atrazine was a ubiquitous contaminant, with highest concentrations in Mississippi river sources, which includes the Atchafalaya River. The ratio between dissolved and colloidal fractions is fairly constant in these samples as compared to the distribution in samples taken from the Gulf, where salinity was increasing. Simazine and alachlor were seen only in Mississippi River sources. The Sabine River sample showed low concentrations of all analytes, including the herbicides. Concentrations of herbicides were greatest in the dissolved phase; however, all herbicides were detected in the colloidal phase, and alachlor and metolachlor were detected in the particulate phase. Hexachlorobenzene was
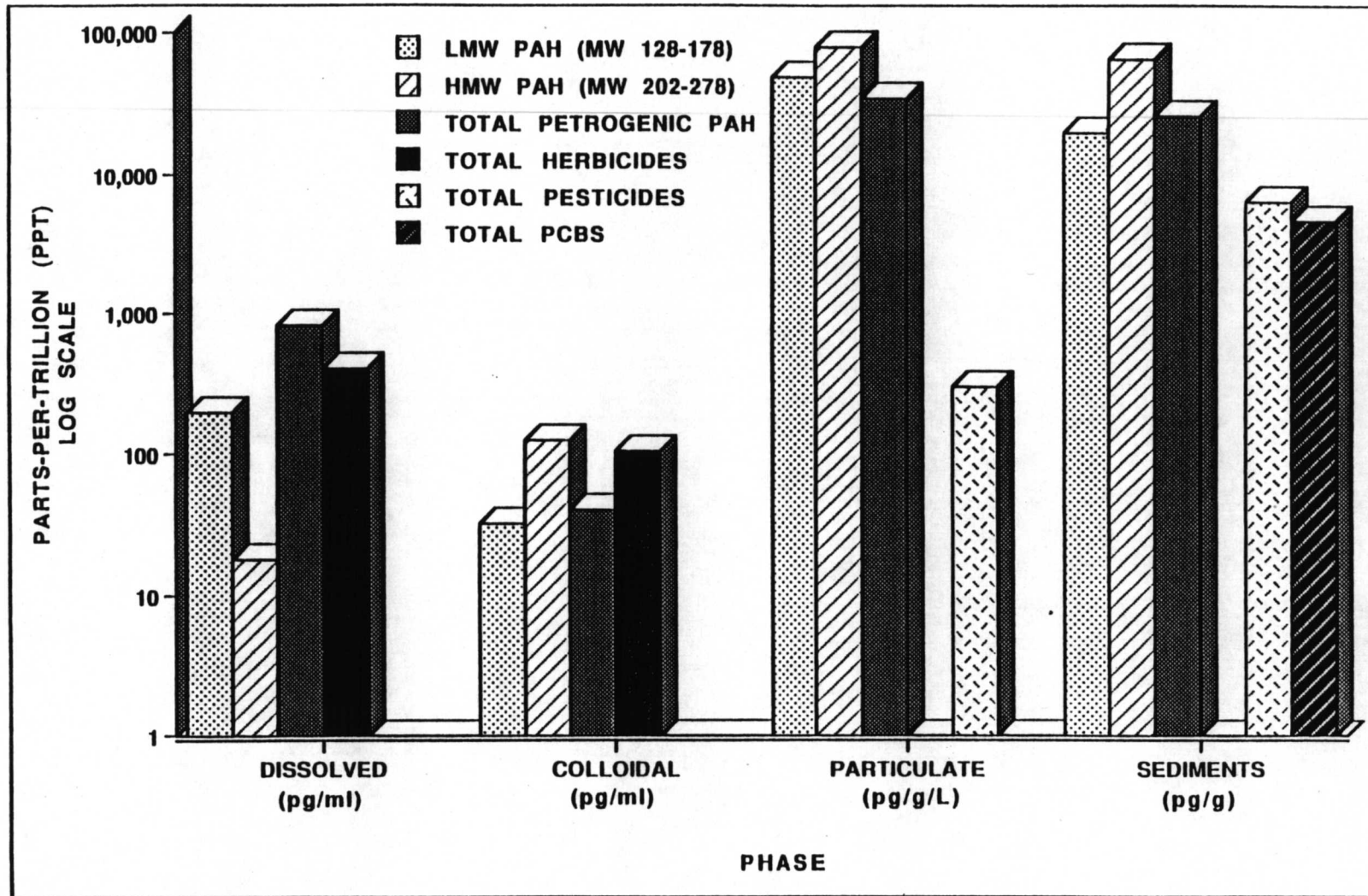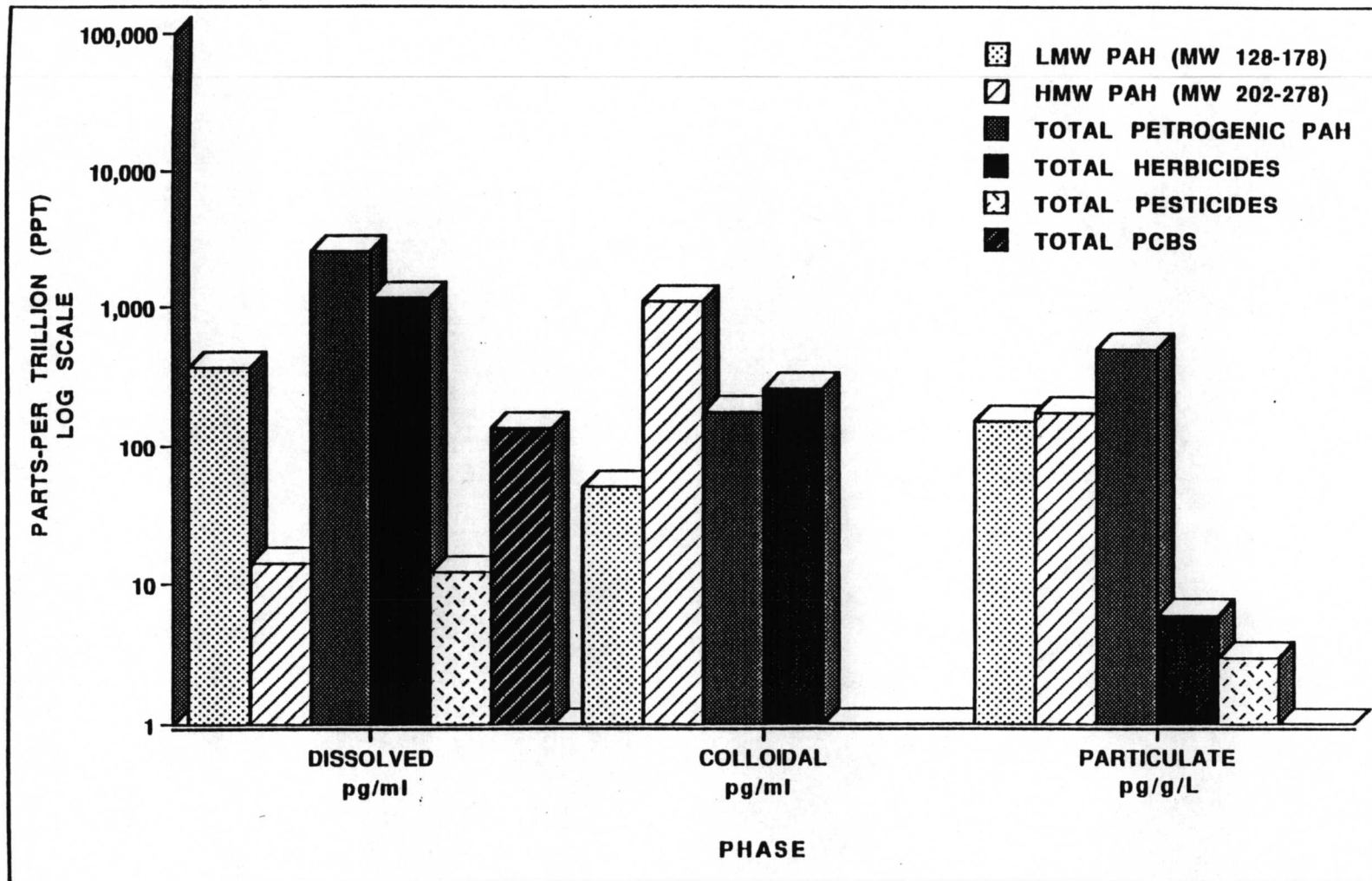
Figure 138. Mean distribution of pollutants between three phases of water in samples collected during Cruise II. (LMW=low molecular weight; HMW=high molecular weight).
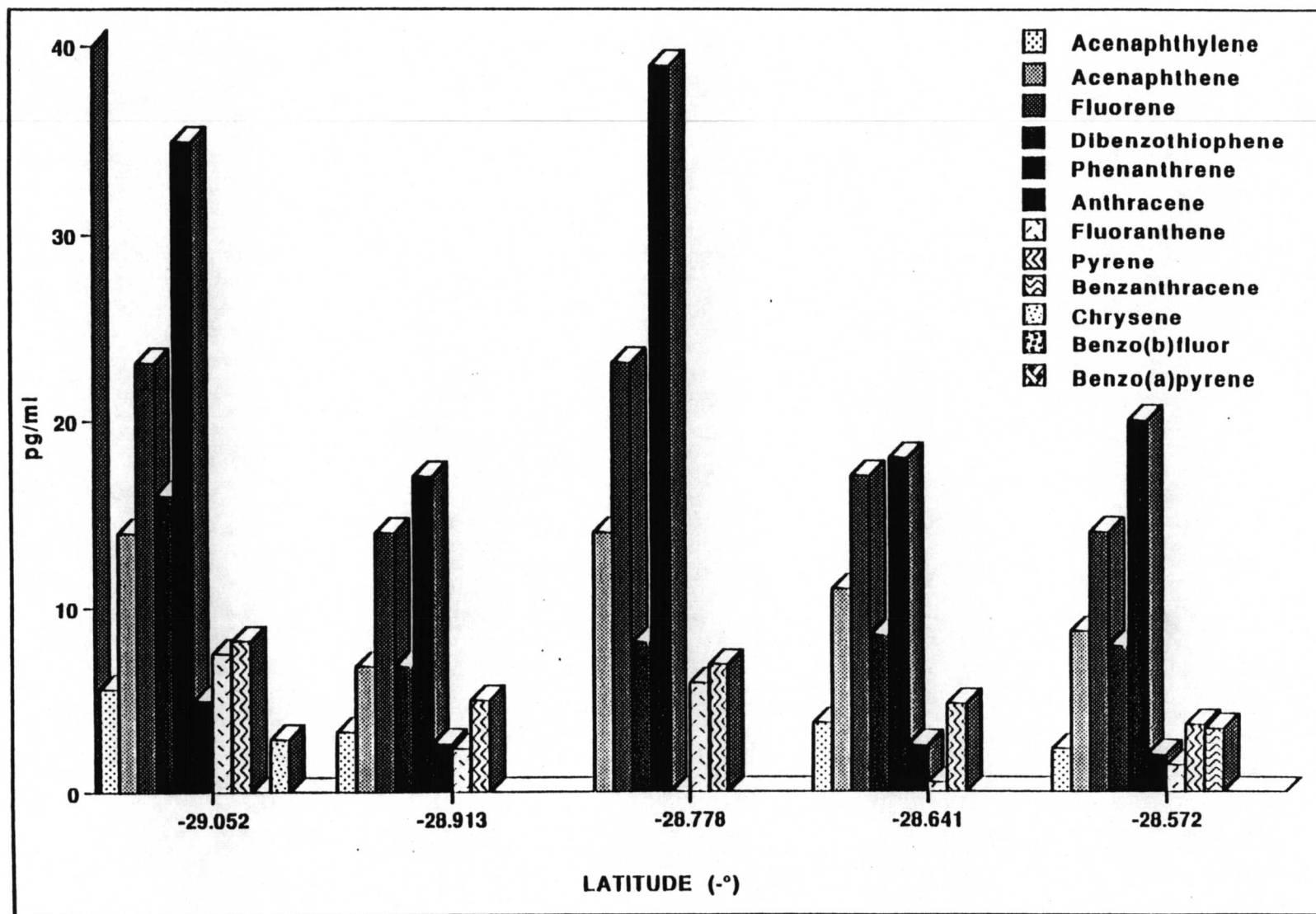
Figure 139. Dissolved phase PAH concentrations off Timbalier Bay, transect S1, Cruise II.

183
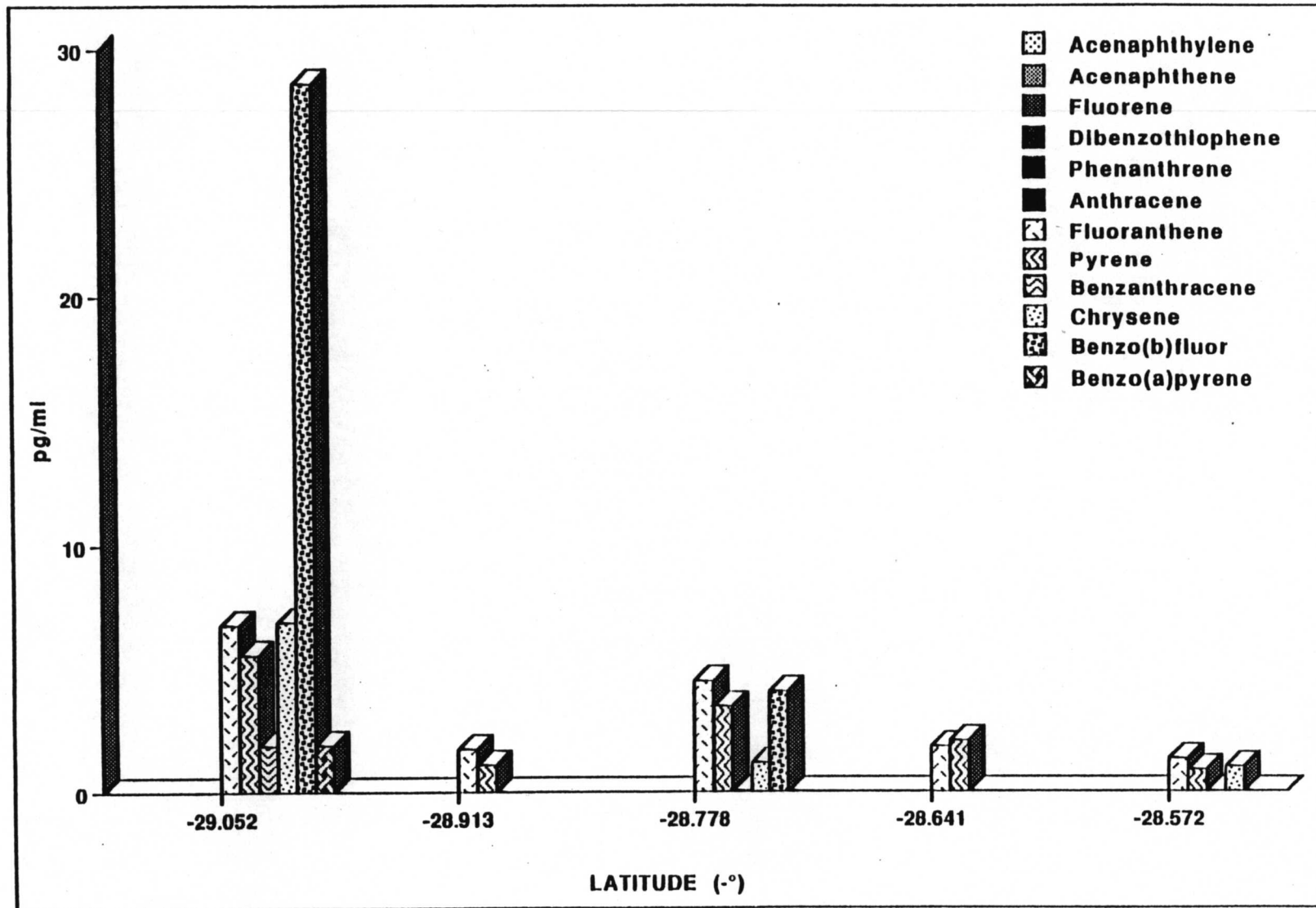
Figure 140. Colloidal phase PAH concentrations off Timbalier Bay, transect S1, Cruise II.
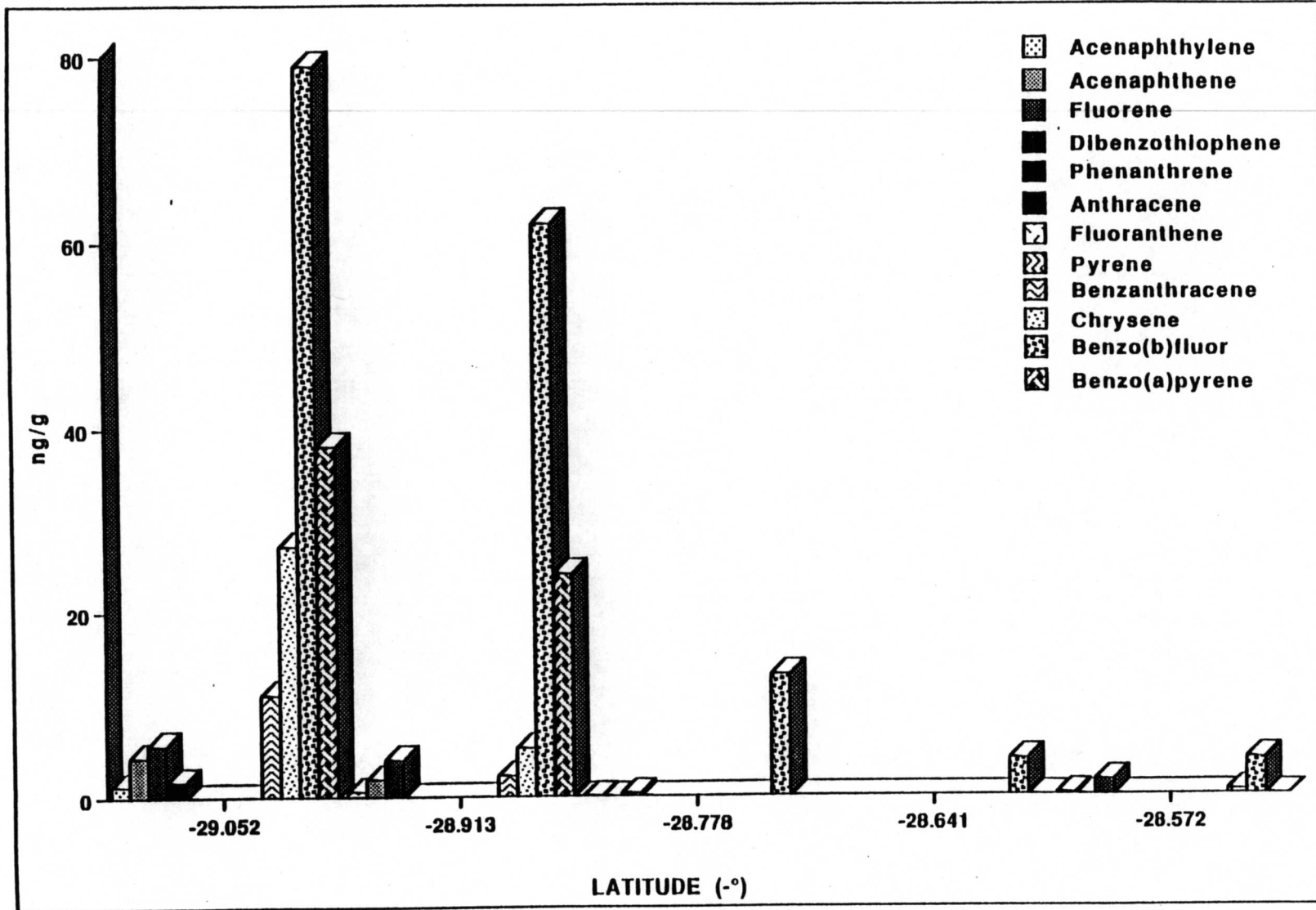
Figure 141. Particulate phase PAH concentrations off Timbalier Bay, transect S1, Cruise II.
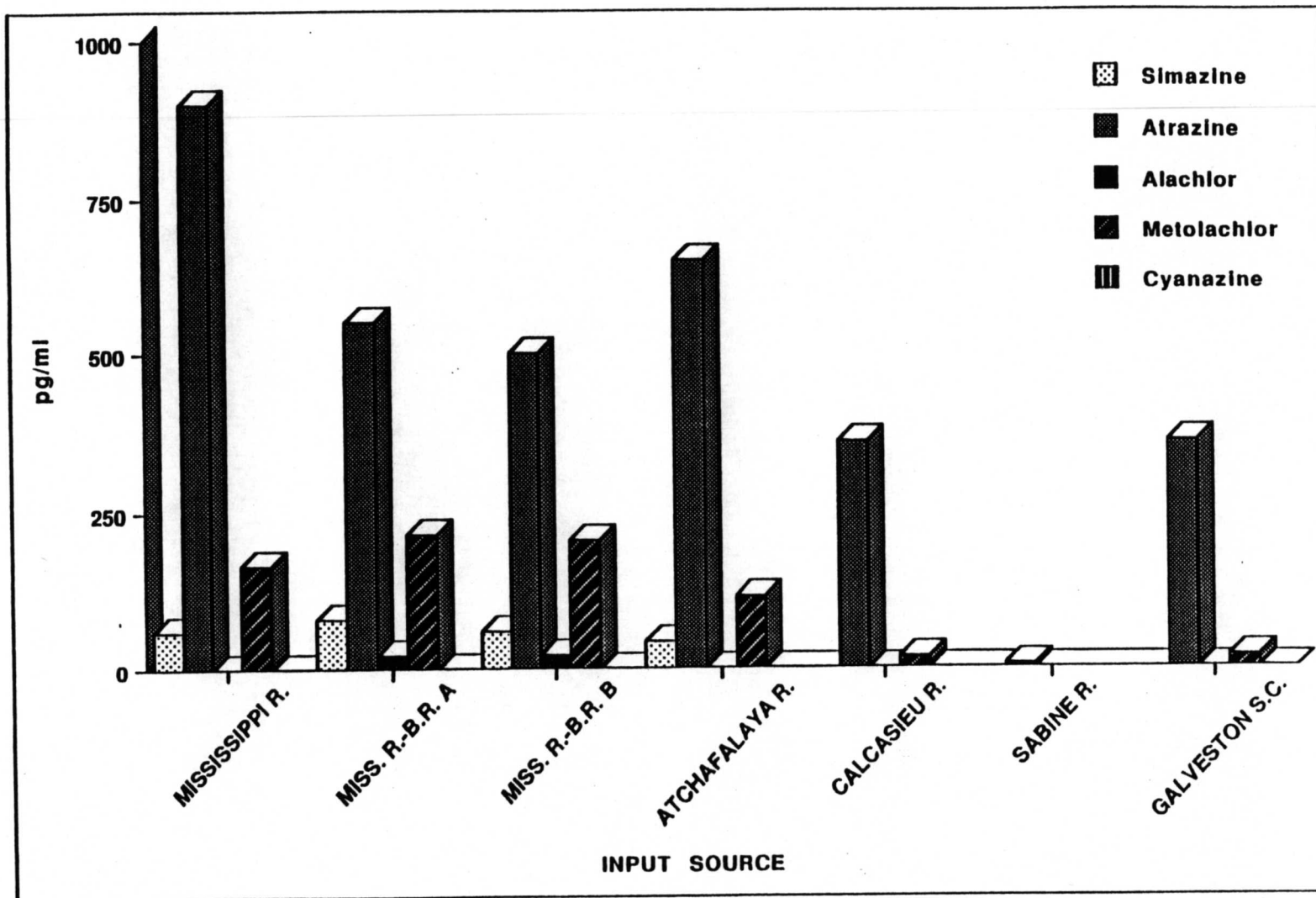
Figure 142. Herbicides detected in the dissolved phase of samples from river sources.

detected in one sample, particulate phase, at Baton Rouge. The BR samples also showed high concentrations of alkylated-naphthalenes in the dissolved phase, at ~100 times greater than observed in other samples, including the BC sample.

Particulate Phase. Particulates have already been discussed in the summary section as being comparatively low on the Cruise II compared to Cruise I. In addition, the herbicide metolachlor was also detected in four samples representing transects S7 and S8, south of Galveston Bay, compared to only one detection each of metolachlor and cyanazine in the particulate phase for Cruise I. Naphthalene, fluorine, benzo(b)fluoranthene, and alkylated naphthalenes showed elevated concentrations at the same stations as metolachlor. Hexachlorobutadiene also was detected only in transect S8. Benzo(b)fluoranthene showed a pronounced concentration gradient with distance from shore in transect S1.

The alkylated naphthalenes tended to show concentration gradients with distance from shore in transects S1 and S3, the C2-phenanthrenes showed a slight pattern of decreasing concentration with distance from shore in transect S1.

Colloidal Phase. The mean concentrations of atrazine and simazine for Cruise II was higher, and concentration gradients were more apparent in each transect, than for Cruise I. Colloidal phase concentrations of atrazine in transect S3 were approximately three times higher in Cruise II compared to Cruise I. The mean concentration of metolachlor was slightly higher in the first cruise compared to the second; however, MQL-uncorrected data showed that metolachlor was ubiquitous in Cruise II samples. Simazine concentrations were highest in transect S3 for cruise II and showed a slight concentrations gradient. Cyanazine was not detected in the first cruise but also showed widespread occurrence in Cruise II samples, appearing in all transects.

LMW PAHs in Cruise II samples were similar in composition to data for Cruise I, with the addition of the detection of acenaphthene. Geographic distribution appeared to be random, with most observations in S2 and S3. HMW PAHs, such as fluoranthenes, were detected frequently, but at concentrations below MQL values. High concentrations of fluoranthene and pyrene were detected in the surface sample from station 195, in transect S6. Alkylated PAH showed no patterns in these samples.

Dissolved Phase. Consistent with data from the other phases for Cruise II, atrazine concentrations were higher in the fall cruise for both surface and bottom samples. Note, however, that the surface concentrations were higher in the spring, while bottom samples showed highest concentrations in the fall. Compared to data from Cruise I, it is clear that there were seasonal differences in the pollutants carried in the coastal current layer. The highest concentration of atrazine occurred in transect S4, compared to S6 for Cruise I. For simazine, the highest concentrations (380 pg/ml in the bottom sample from station P922159) were in transect S4, Cruise II, compared to X2 for Cruise I. Metolachlor was also highest in S4, compared to high values in transects S6 and X2 for Cruise I. Cyanazine was distributed more westerly in Cruise II, with highest concentrations observed in transects S4 and S7, whereas Cruise I showed detectable concentrations only in transects east of longitude 93.0, the Mississippi/Atchafalaya region. Alachlor was not detected in any samples from Cruise II.

Fluorine concentrations showed more variability in Cruise II samples. One of the highest concentrations occurred in transect S6, similar to Cruise I; however, in Cruise II, high concentrations were also seen in transects S3, S4, and S7. This pattern was also found for the parent PAH dibenzothiophene and phenanthrene, and the alkylated PAH. The highest concentrations in S3 were in the central stations: P922141, the bottom sample, and P922143, the surface sample. In transects S4 the highest concentrations occurred in the second sample away

187

from the shore, P922159 (surface and bottom). In transect S6 the highest concentration was found in the bottom sample at station P922194, nearest to shore.

The most interesting aspect of the dissolved phase data was the detection of trichloro- and tetrachlorobiphenyls (PCBs) in transects S1, S2, and S3. Figure 143 shows a plot of concentrations for both chlorination levels in transect S1, where the concentrations were highest and showed a clear trend of decreasing concentrations with distance from shore. Chlordane was also detected twice in transect S1.
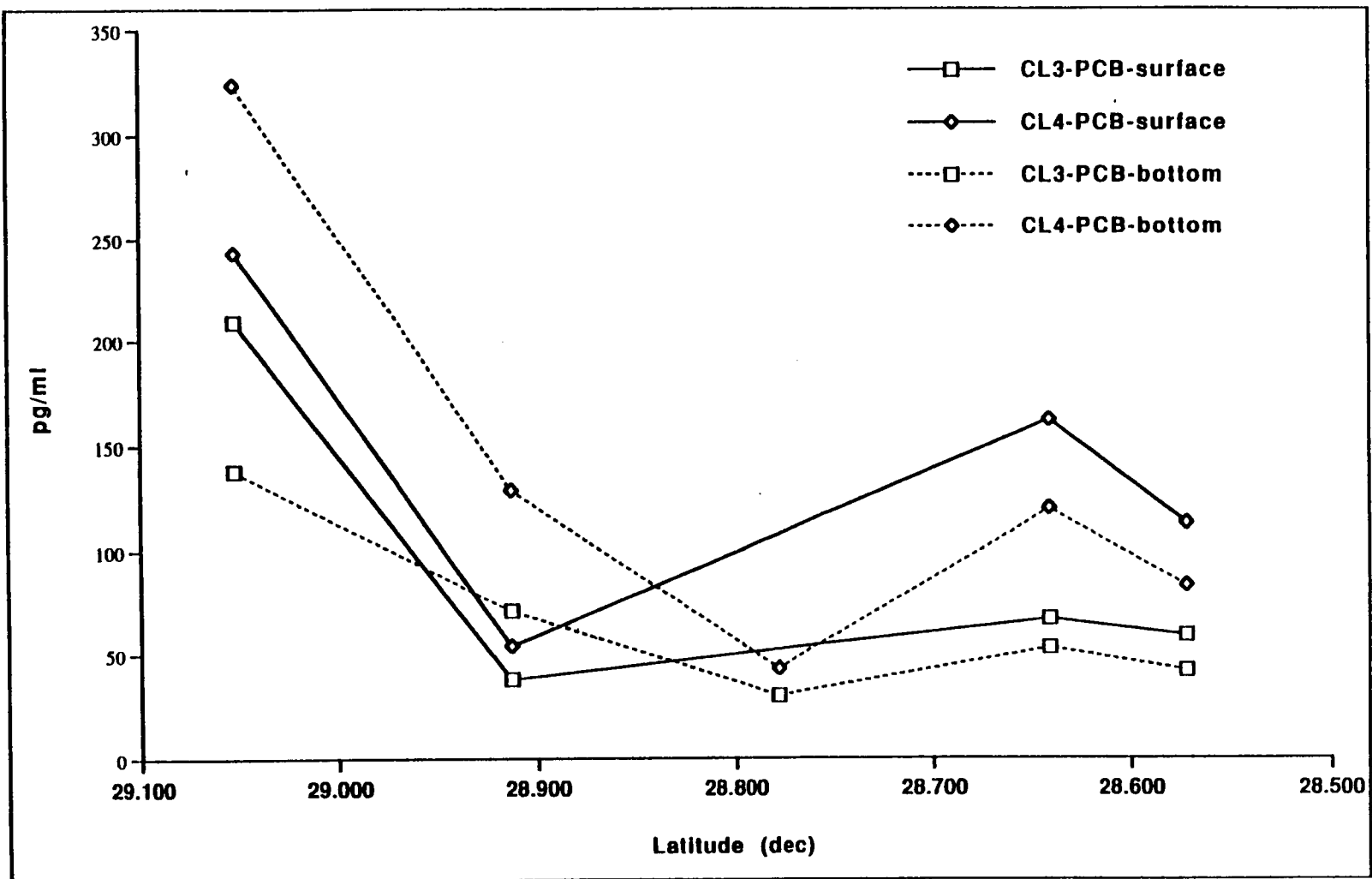
Figure 143. Dissolved phase PCB concentrations in surface samples from transect S1, Cruise II.

VII. Remote Sensing and Imaging
(Nan D. Walker, Lawrence J. Rouse, Jr. and Oscar K. Huh)

A. Methodology and Image Analysis Synthesis

NOAA Advanced Very High Resolution Radiometer (AVHRR) satellite data coverage of the Gulf of Mexico is acquired several times each day at the Earth Scan Lab, Coastal Studies Institute, Louisiana State University. These data are captured and archived using a SUN Sparc II computer running Terascan™ software from Seaspace, San Diego, California. After capture, the thermal and visible channels are calibrated from count values to science units. The thermal infrared channels are converted to brightness temperatures in Celsius, and the visible channels are calibrated to percent albedo (Kidwell, 1991). The Gulf of Mexico portion of the image is automatically cut out of the raw data and placed on the Earth Scan Lab's newest computer, the S.G.I. Crimson server with 85 mips and 144 mb RAM. All further processing and analysis of the satellite data is performed on this computer, accessed by Tektronix X-11 terminals. The data is screened for cloud cover and general image quality. A determination is made at this time whether further processing is to be performed. If an image is sufficiently free of cloud-cover over an area of interest, the dataset is run through additional processing procedures, which include calculation of sea surface temperature (SST), calculation of reflectance (to reveal surface suspended sediment), and navigation/registration of the image to a standard rectangular map projection. Sea surface temperatures are computed using the multi-channel algorithms of McClain et al. (1985). Reflectance is obtained from the bias correction technique of Stumpf (1988, 1992). Estimates of suspended sediment concentrations are sometimes made using a calibration equation developed specifically for Mississippi River plume waters (Walker and Rouse, 1993). The satellite data processing procedures are summarized in Figure 144. Frontal analyses are routinely performed on the satellite image data with the assistance of the sobel filtering method and digitizing software, available within the Terascan image processing package. Information on coastal and river plume fronts, shelf fronts, squirts and jets, Loop eddies, and the Loop Current were digitized from the satellite image data.

Further processing of the frontal information for provision to the other LATEX tasks via GULF.MEX was performed on a PC using the OPCPLOT software package (Dr. Murray Brown, pers. comm.). GIF images were routinely provided (corresponding to the GULF.MEX frontal analyses) covering either the LATEX area or the entire Gulf of Mexico. They are made available via anonymous ftp on "nevado.srcc.lsu.edu." In support of the LATEX cruises or overflights, more detailed information was provided in either GIF image format, as line drawings (faxable) or as color prints. In 1992, 45 frontal analyses were posted to GULF.MEX (Table 9) and approximately 23 GIF images were provided to LATEX researchers in near real-time (Table 10). In addition, support was provided to four LATEX B cruises: April 1992, July 1992 (postponed), August 1992 (postponed) and October 1992.

```
┌─────────────────────────────────────────────────────────────┐
│                                                               │
│        Calibration of  Visible and Thermal Infrared          │
│        Channel Data                                           │
│          from count values to science units                  │
│                                                               │
│                           ↓                                   │
│                                                               │
│        Initial Screening of the Data for Cloud Cover         │
│                                                               │
│                           ↓                                   │
│                                                               │
│              Calculation of Reflectance                      │
│                                                               │
│                           ↓                                   │
│                                                               │
│          Calculation of Sea Surface Temperatures             │
│                                                               │
│                           ↓                                   │
│                                                               │
│      Navigation/Registration of  Images to Map Projection    │
│                                                               │
│                           ↓                                   │
│                                                               │
│                    Frontal Analyses                          │
│                                                               │
│                           ↓                                   │
│                                                               │
│                Production of GIF images                      │
│                                                               │
│                           ↓                                   │
│                                                               │
│                  Archival of products                        │
│         (4mm tape,  35 mm slide film, and color prints)      │
│                                                               │
└─────────────────────────────────────────────────────────────┘
```

Figure 144. Image processing procedure summary for NOAA AVHRR data.

An additional component of the satellite data analysis is to analyze a representative sample of the historical NOAA AVHRR data sets within the Earth Scan Lab archive, which begins in July 1988. During 1992, approximately 2 images/day were uploaded from the archive tapes between July 1988 and January 1992, totaling 3000 images. The images were screened for image quality and the best images were processed for further analysis by the investigators. In this report, analyses of satellite data obtained in 1992 and early 1993 are presented. Selected analyses of historical data are also incorporated in this report. A more extensive analysis of the historical satellite data set will be presented in the next annual report.

Table 9. Frontal analysis posted to GULF.MEX in 1992.

7 Feb 92			1 Sep 92	0927Z	
12 Feb 92	09Z		2 Sep 92	2032Z	
12 Feb 92			9 Sep 92	0931Z	
29 Feb 92	20Z		18 Sep 92	0918Z	
7 Mar 92	2105Z		20 Sep 92	0900Z	
15 Mar 92	21Z		30 Sep 92	2100Z	
24 Mar 92	0940Z		4 Oct 92	20Z	
22 Apr 92	2018Z		5 Oct 92	0900Z	
28 Apr 92	2047Z		12 Oct 92	0939Z	
6 May 92	0934Z		19 Oct 92	0953Z	
13 May 92	1348Z		26 Oct 92	1009Z	
24 May 92	0914Z		28 Oct 92	09Z	
18 Jun 92	0922Z		14 Nov 92	0100Z	
2 Jul 92	21Z	(Squirt Alert)	21 Nov 92	0952Z	
8 Jul 92	01Z		29 Nov 92	2119Z	
12 Jul 92	0151Z		2 Dec 92	2100Z	
18 Jul 92	1000Z		4 Dec 92	1400Z	
22 Jul 92	1401Z		10 Dec 92	0900Z	
28 Jul 92	2103Z		11 Dec 92	0109Z	
2 Aug 92	21Z		17 Dec 92	2100Z	
3 Aug 92	21Z		20 Dec 92	0100Z	(Squirt Alert)
6 Aug 92	0923Z		24 Dec 92	0100Z	
8 Aug 92	1439Z				
9 Aug 92	1439Z				

Table 10. GIF images provided to LATEX researchers in 1992.

2 July	29 November
9 July	2 December
28 July	4 December
30 July	7 December
2 May	10 December
1 September	11 December
5 October	17 December
12 October	20 December
19 October	1 January
26 October	9 January
2 November	16 January
14 November	26 January
21 November	31 January

B. Climatology of the Mississippi and Atchafalaya River Plumes

The Mississippi River is the major source of sediments, pollutants, and nutrients for the Gulf of Mexico. Draining 41% of the continental U.S., it discharges freshwater into the northern Gulf of Mexico through the Balize Delta and the Atchafalaya Delta at a rate of 580 km³ yr-1. This amounts to 10% of the volume of the entire Louisiana-Texas shelf out to the 90 meter isobath (Dinnel and Wiseman, 1986). In addition, approximately 210 million tons of sediment are discharged into the Gulf of Mexico each year (Milliman and Meade, 1983). The Atchafalaya averages about 50% of the water discharge and over 60% of the suspended load of the

Mississippi (Mossa and Roberts, 1990). The fresh water influence from these rivers has been observed as far as Port Aransas, Texas, a distance of 800 km from the Balize delta (Smith, 1980).

The Atchafalaya and Mississippi River sediment plumes are easily detected along the Louisiana coastline using reflectance information obtained by the Advanced Very High Resolution Radiometer (AVHRR) of the NOAA satellites. The river water can also be detected using thermal infrared satellite data when river water temperatures contrast with those of the continental shelf. A knowledge of the spatial distribution and circulation characteristics of plume waters is of importance to the understanding of hypoxia and the distribution of pollutants. This section reports on results of preliminary analyses of the river plume variability using the historic archive of NOAA AVHRR satellite data.

River discharges of the Mississippi and Atchafalaya Rivers from January 1988 through September 1993 are illustrated in Figure 145. Discharge into the northern Gulf of Mexico exhibits a distinct annual cycle with peak discharges occurring between January and June and lowest flow occurring from August through October. During the past six years, considerable interannual variability in discharge has occurred, with 1988 and 1992 exhibiting discharge rates below normal and 1989, 1990, 1991, and 1993 exhibiting above normal discharge rates. Inspection of Figure 146 also reveals a substantial amount of variability on shorter time-scales, such as months and weeks.

In an attempt to better understand circulation of river water on the continental shelf, an investigation of suspended sediment distribution in the northern Gulf of Mexico was performed using clear-sky satellite imagery during contrasting conditions of river discharge. The low discharge spring of 1992 and the high discharge spring of 1993 were chosen for this analysis. Average discharge during March through May of 1993 was double that of 1992. The satellite data were atmospherically corrected and calibrated to surface suspended sediment concentrations, using an algorithm developed for the Mississippi River plume (Walker and Rouse, 1993). For this analysis, 16 clear-sky images were available for the 1993 spring (March-May), and 8 images were available for the 1992 spring (March-May). The technique of compositing was used to reveal mean distributions of suspended sediments during these two spring periods. The results of this analysis are presented in Figure 152 where the sediment plume is defined by the position of the 5 mg/liter suspended sediment contour. It is easily seen that the mean composite sediment plumes during the high discharge spring of 1993 covered much more of the continental shelf than those of 1992.

During the 1992 low discharge spring, the Atchafalaya and Mississippi sediment plumes appeared separate, whereas in 1993, a continuous zone of suspended sediments was observed close to the coast. The mean Atchafalaya plume in 1993 covered 7167 km², whereas that in 1992 covered 3890 km², approximately 50% of the 1993 area (Table 11). Similarly, the Mississippi plume covered 6354 km² in 1993 and 3229 km² in 1992.

Table 11. Tabulated areas for the composite sediment plumes.

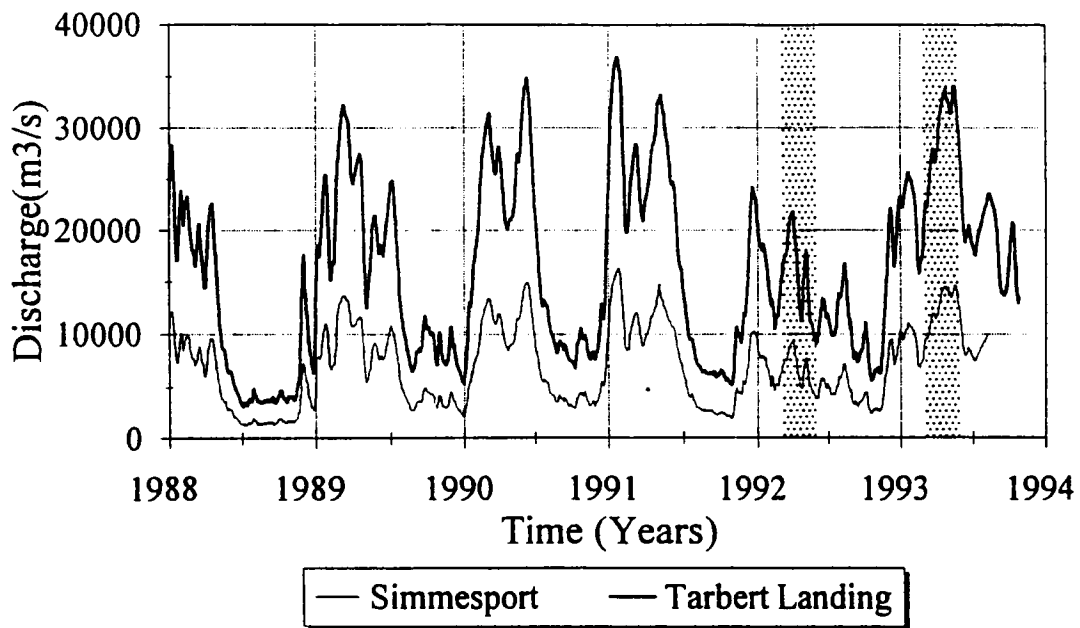| Time Period	Atchafalaya Plume (km²)	Mississippi Plume (km²)
March-May 1992 Mean	3890	3229
March-May 1993 Mean	7167	6354
January-May 1992 Mean	6557	3944
January-May 1992 Minimum	1097	716
January 20, 1992	14516	6023
February 7, 1992	15893	3900

194

Figure 145. River discharge of the Mississippi (Tarbert Landing) and the Atchafalaya (Simmesport) from January 1988 through October 1993.
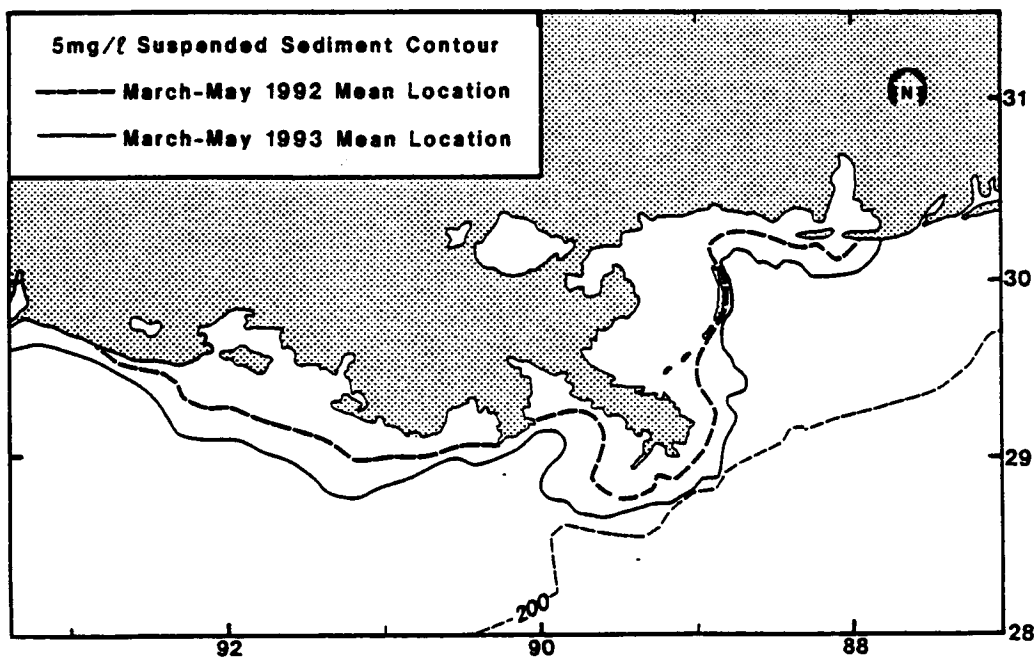

Figure 146. Mean position of the 5 mg/l suspended sediment contour for the March-May 1992 and March-May 1993 composited satellite data.

This analysis suggests that the plumes undergo considerable variability on the interannual time scale, which is related to changes in river discharge. Both of the mean composite sediment plumes were observed to increase substantially in area with increasing river discharge, which doubled from the 1992 to the 1993 spring. It is interesting to note that the mean Atchafalaya plume and the mean Mississippi plume were similar in size.

A more detailed analysis of suspended sediment distributions was made during the winter and spring of 1992. In Figure 147a, the minimum and mean composite sediment plumes are shown for the January through May 1992 time period. A large difference was observed between the spatial extent of the minimum and mean plumes. The minimum Atchafalaya plume covered 1097 km² during January through May 1992, whereas the mean area was 6557 km². The minimum Mississippi plume was 716 km², in contrast to the mean of 3944 km². Both plumes underwent a 5- to 6-fold increase in area between their minimum and mean states. It is interesting to note that the mean plumes derived from the January through May 1992 images were larger than those of the March through May 1992 time period. This was particularly true for the Atchafalaya plume. Close inspection of the January and February satellite images that were used in the compositing analysis revealed the occurrence of enormous sediment plumes, particularly seaward of the Atchafalaya River delta. On January 20, 1992, the Atchafalaya sediment plume covered 14,516 km² and extended offshore 100 km from Atchafalaya Bay. The Mississippi sediment plume was approximately 1/2 the size of the Atchafalaya plume, measuring 6023 km². Together the plumes covered approximately 43% of the Louisiana shelf to the 100 meter contour. In Figure 147b, the January 20 sediment plumes are compared with the mean composite plumes of January through May 1992. An analysis of Louisiana coastal wind data revealed that a cold front, accompanied by very strong north-northeasterly winds, had moved over the Gulf early on January 19. Wind speeds averaged 10-15 m/s along the coast for the 36 hours prior to image acquisition. A similar meteorological event occurred in early February and the sediment plumes of February 7, 1992 also covered large areas of the continental shelf (not shown). The area covered by the February 7, 1992 plumes was similar to that covered by the January 20 plumes (Table 11). These analyses suggest that northerly winds associated with winter cold-front passages maximize plume areas and cross-shelf exchange of river water, sediments, nutrients, and pollutants. Wind effects were particularly noticeable in the Atchafalaya plume case, where a vast reserve of fine-grained sediments resides on the shallow shelf seaward of Atchafalaya Bay. These sediments are easily resuspended by wind-waves and subsequently transported by the prevailing winds and shelf currents. In contrast, much of the Mississippi plume is discharged into relatively deep water; thus, resuspension of sediments is not as prevalent. This analysis supports that of Walker et al. (1992) which revealed that wind exerts a more important control on the Atchafalaya sediment plume than does river discharge.

An analysis of individual satellite images in the Earth Scan Laboratory data archive has revealed that plume orientation responds rapidly to changes in wind direction. Under the influence of the prevailing easterly winds (southeasterly from March through September and northeasterly from October through February (Rhodes et al., 1985)), Atchafalaya and Mississippi River waters (South Pass and Southwest Pass) usually move westward along the coast. Much of the Mississippi River water curves anticyclonically towards the coast. The Atchafalaya River water also curves anticyclonically upon exiting the bay and flows westward along the inner shelf towards Texas. Disruption of this westward flow has only been observed under the influence of major wind reversals, from easterly to westerly wind forcing. Wind reversals occur every 3 to 9 days during autumn, winter, and spring because of eastward-moving cold fronts.

There is some evidence from thermal infrared satellite imagery, however, that the short-lived westerly winds may not always reverse the coastal current downstream from Atchafalaya Bay. For example, satellite imagery obtained on March 10, 1988 (Figure 148a) and March 4, 1990 (Figure 148b) reveal Atchafalaya River water moving southeastward out of the bay and

196

A

5mg/ℓ Suspended Sediment Contour

— — — January-May 1992 Minimum

——————January-May 1992 Mean

B

5mg/ℓ Suspended Sediment Contour

——————January-May 1992 Mean Location

— — — —January 20, 1992 Location
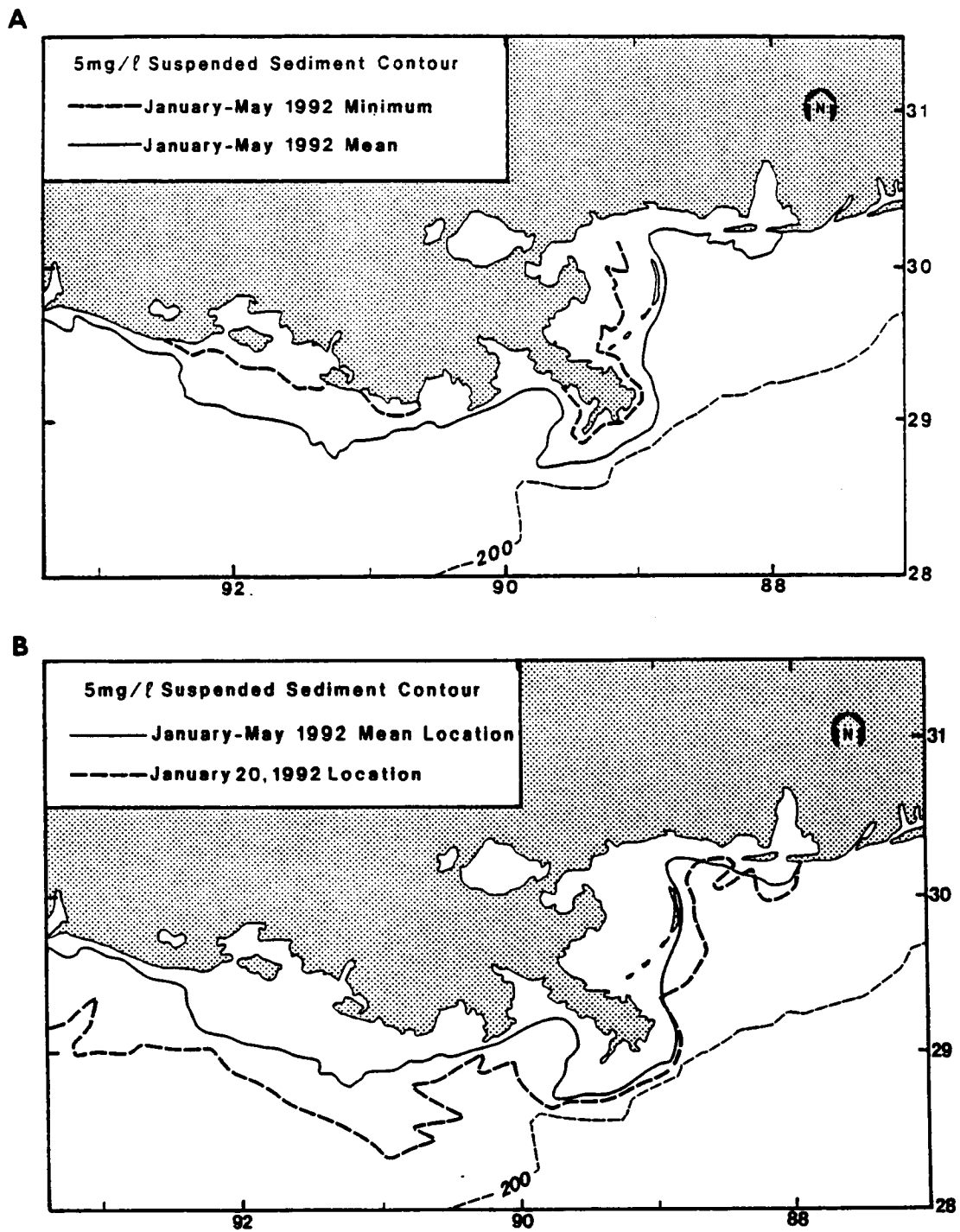
Figure 147. (a) Minimum and mean position of the 5 mg/l suspended sediment contour for the January-May 1992 composited satellite data. (b) Mean position of the 5 mg/l suspended sediment contour for the January-May 1992 composited satellite data compared with the plume position on January 20, 1992.

197

A


```
10 March 1988 1350 Z
NOAA-10 AVHRR Thermal Fronts
Coastal Studies Institute, LSU
```

Coastal Current

Atchafalaya
Plume

Mississippi
Plume

-200

-200   -200

B


```
4 March 1990 0800 Z
NOAA-11 AVHRR Thermal Fronts
Coastal Studies Institute, LSU
```

Coastal
Current

CLOUDS

Atchafalaya
Plume

Mississippi
Plume   -200

-200   -200
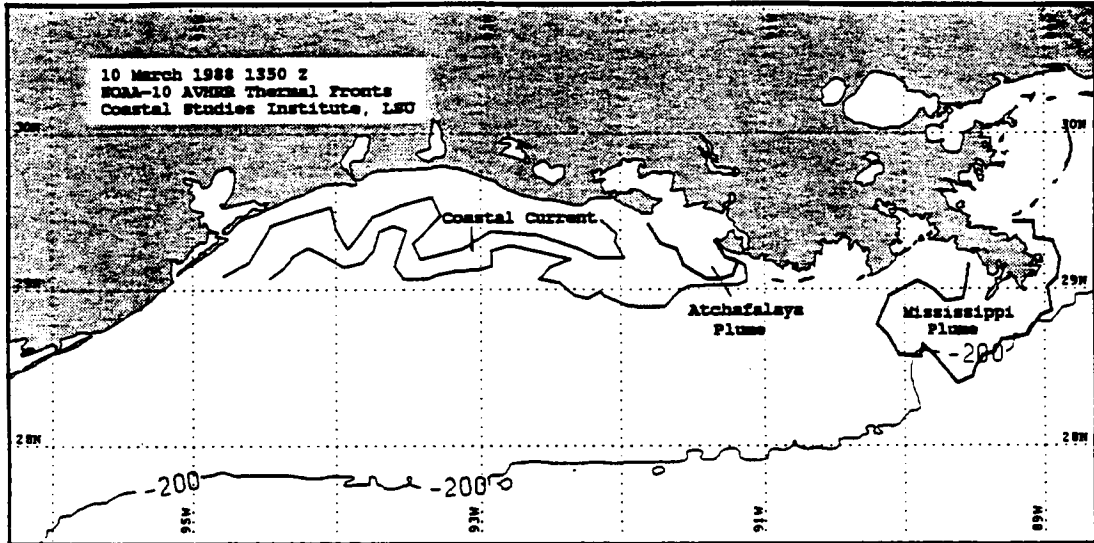
Figure 148. Schematic of the Mississippi and Atchafalaya sediment plumes and the coastal current on (a) March 10, 1988 and (b) March 4, 1990.

onto the inner shelf as a result of northwesterly wind forcing. However, in both cases, at approximately 35 km from the coast, the cool river water executed an abrupt turn to the west, suggesting that it encountered a westward flowing coastal current inshore of the 20 meter contour. These satellite imagery (and others) suggest that the westward-flowing coastal current is not always disrupted by westerly winds accompanying the passage of cold fronts. It is interesting to note that the coastal current appeared much wider in the March 1990 image. This probably resulted from the fact that river discharge in 1990 was about double that of 1988. The Mississippi plume covered more of the shelf in 1990 as it extended further west and further south. In both months, the southern margin of the main Mississippi plume front was observed in close proximity to the 200 m isobath. However, in 1990, a secondary front was observed south of the 200 m isobath. This secondary front appeared to separate Loop Current water from an intermediate zone where mixing of water masses had occurred.

C. Coastal and Shelf Sea Surface Temperature Analysis

Since the beginning of this project, we have been inspecting and analyzing the AVHRR data sets for sea surface temperature (SST) fronts in the northwestern Gulf of Mexico. We routinely place frontal analyses on the GULF.MEX kiosk (bulletin board) of OMNET as required by the contract. In addition to the frontal analysis on appropriately clear images, we also extract profiles of SST along five transects on the shelf of the northwestern Gulf of Mexico. These five transects coincide with the five major current meter mooring lined maintained by the LATEX A program and extend from the coast to the shelf edge (Table 12).

Table 12. The five major current meter mooring locations maintained by LATEX A.

	Inshore	Offshore
Line A	27°14.75 N, 97°13.40 W	27°08.21 N, 96°23.06 W
Line B	28°41.40 N, 95°31.88 W	27°52.05 N, 95°05.45 W
Line C	29°37.60 N, 94°00.00 W	28°20.99 N, 94°00.00 W
Line D	29°29.47 N, 92°00.00 W	27°56.54 N, 94°00.00 W
Line E	29°04.77 N, 90°30.00 W	27°55.80 N, 90°30.00 W

Analysis of profiles from the early months of 1992 provides insight into the evolution of the strength of coastal fronts. During the first four months of t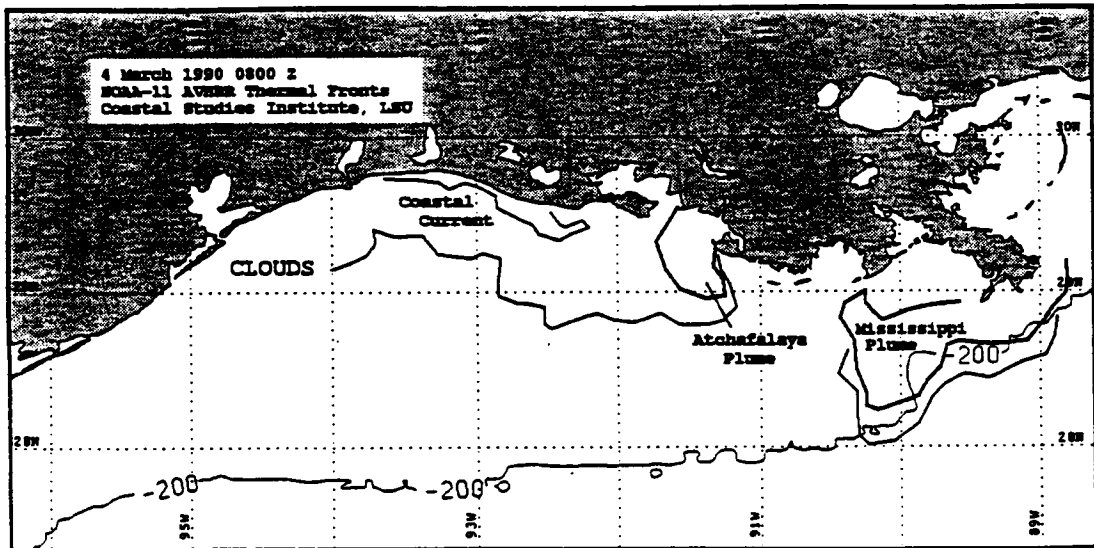he year, surface temperatures near the coast rose from lows below 10°C on Lines C and D in January, to above 22°C on Line D in April. Offshore the temperatures had much less variation. At approximately 100 km from the coast, the January temperature was about 15°C and rose to just above 20°C by April. On Line E, the temperature range offshore was less, on the order of 1°C.

A little more than one day before the January 20 image was acquired, a cold front passed across the LATEX shelf. The high pressure system behind front brought the coldest air of that season. Coastal winds were brisk (10 to 15 m/s) and from the northeast. Along Line D (Figure 149), coastal SST was a little more than 7°C. Temperatures slowly rose toward a relatively sharp front approximately 60 km offshore where the cold Atchafalaya River discharge encountered warmer shelf waters (Figure 150). The temperature at this front rose 4° over a distance of less than 10 km. Along Line C, a similar front is observed, but it is much closer to shore (less than 20 km offshore). To the east, no sharp fronts are present, as the main Mississippi River plume lay to the east of Line E. The plume generally followed the 200 m isobath, displaying anticyclonic curvature (discussed in the previous section) on the west side. The January 20 image depicts the maximum end of the spatial extent of the river plumes.

By the end of February, the winter season had begun to wane and inshore temperatures were rising (Figure 149). Offshore temperatures showed less of a rise, except along Line E
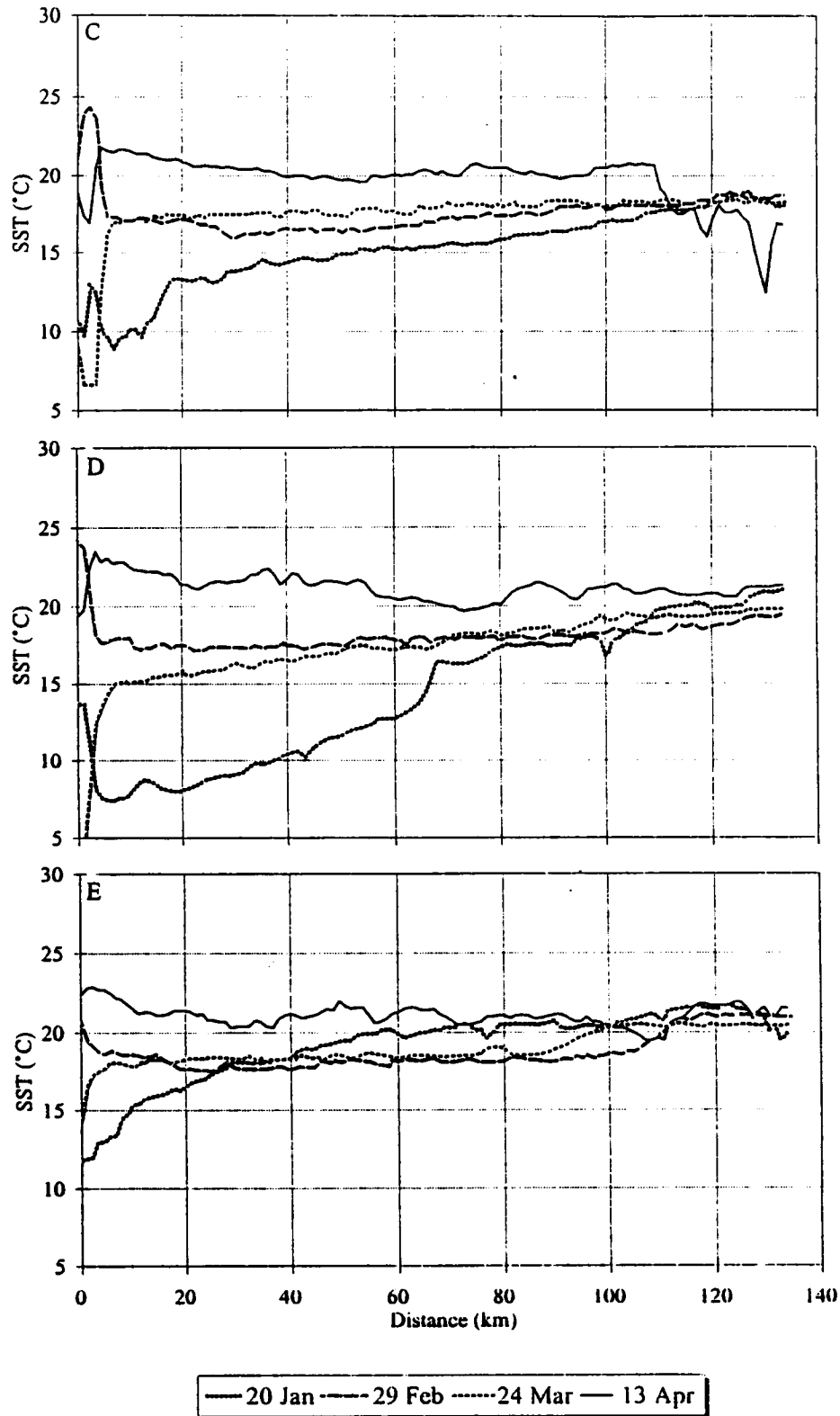
199

Figure 149. Sea surface temperature profiles from AVHRR image data, January-April, 1992. Profile locations are given in Table 12 and Figure 150.
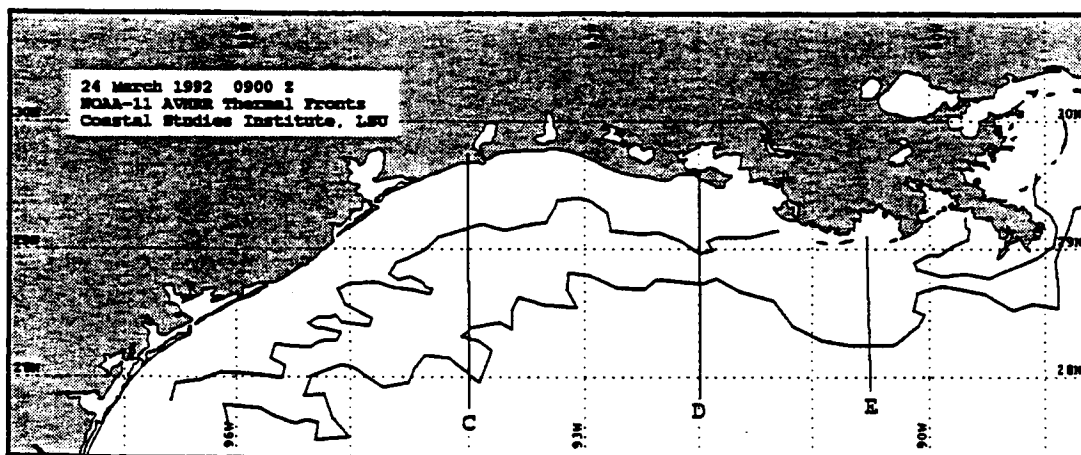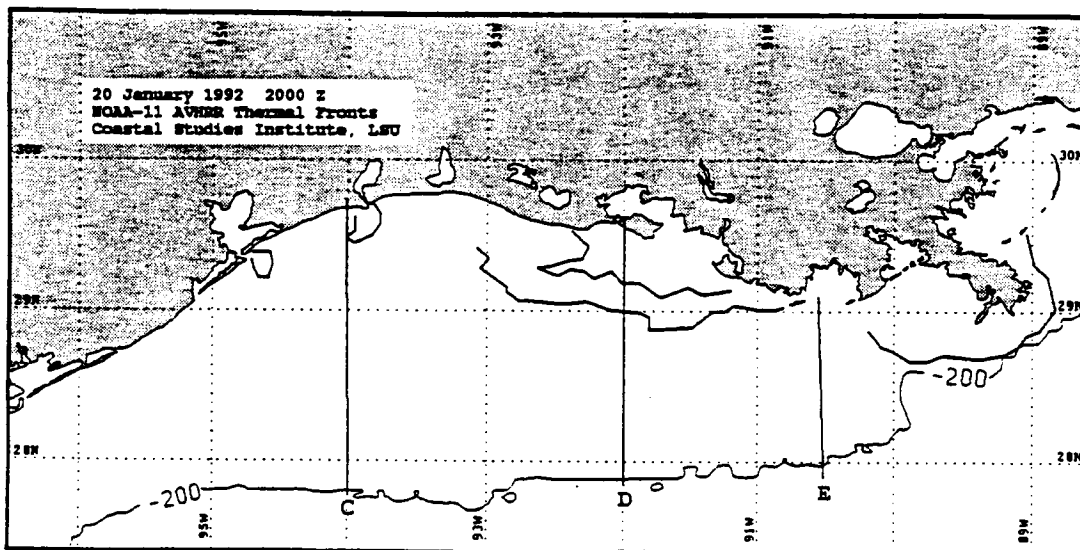
Figure 150. Frontal analyses for the Louisiana shelf on January 20 and March 24, 1992. Lines C, D, and E are the locations along which the SST profiles in Figures 149 and 151 were taken.

where the February temperatures were lower than in January. A minor front along Line E is observed about 80 km offshore where the temperature rises about 2° in 5 km. There is still a front along Line D, but has moved further offshore (75 to 80 km) and is not as sharp.

Compared to the 20 January situation, fronts in the 24 Marsh image (Figure 150) were weak but were more continuous within the region and had a wavy structure west of Atchafalaya Bay. Finger-like extensions of cool inner shelf water, 30-40 km long and 10-20 km wide, were situated between the 20 and 30 m isobaths to the west of Line C. A second weak, wavy front was also observed further offshore. near the Mississippi River delta, the scale of the waves (100 km wide) was much greater than to the west. These wave-like features may be indicative of areas of onshore-offshore exchange. As seen in the profiles (Figure 149), the fronts on Line D are not very sharp. AT about 66 km, corresponding to the outer front, the temperature rises about 1° in 5 km. Along the other lines, the existence of frontal features is not as obvious.

The end of the winter season is evident in the April 13 image. Sea surface temperatures have increased across the shelf. The spring heating has created a situation where the inner shelf waters are as warm as or warmer than the offshore surface waters.

The changes in the surface temperature field that occurred at the beginning of the winter of 1992-93 can be seen in the profiles of Figure 151. The October 12 profiles illustrate the relatively warm surface waters that results from summer heating. Even at this early stage, however, the development of shelf thermal fronts is evident. Between 30 and 40 km offshore on Line C, a relative sharp 1°-5°C front developed. At about the same offshore distance, a front of similar form is evident in the December 10 profile, through 9° colder.

Along Line D in October, a very broad temperature rise of about 2°C was found beginning at about the same distance offshore as the front on Line C. In the December image the water temperatures decreased by 9° to 10°C and the frontal structure between 30 and 60 km offshore becomes complicated with several sharp fronts (Figure 152) and indications of mixing of inner and outer shelf waters.

In October, along Line E, the surface waters were relatively uniform in temperature. By the end of November, inshore temperatures had decreased by more than 5°C and a plume of cooler water bounded by sharp fronts of 2 to 2.5°C existed between 30 and 40 km offshore. The December 10 profile shows the development of a relatively sharp 2°C front slightly inshore of 40 km. It is interesting to note that a front of this same magnitude and at around the same temperatures, but near 80 km offshore, was observed in the February 28, 1992 data.

Based on the analysis of this one year of data, preliminary observations are that sharp fronts can develop early in the winter (October) even in relatively warm waters. The sharpest fronts tend to develop about 40 km offshore during the first half of the winter season. Later on in the winter, the fronts migrate offshore (60 to 80 km) in January and February) as a result of consecutive outbreaks of polar air. By early to mid-April, the fronts have disappeared and the inner shelf waters have become as warm or warmer than the outer shelf waters.

D. Squirts And Jets during 1992

1. July 1992

A large and persistent squirt was observed in early July 1992 off the southern Texas coast. Three frontal analyses and a squirt alert were provided via GULF.MEX to the LATEX participants. These frontal analyses are illustrated in Figure 153. The squirt was first detected on July 2, 1992 (Figure 153a) as cool shelf water extending northeastward to beyond the 500 meter isobath. On July 2, it was approximately 200 km long and its width varied from 50 km
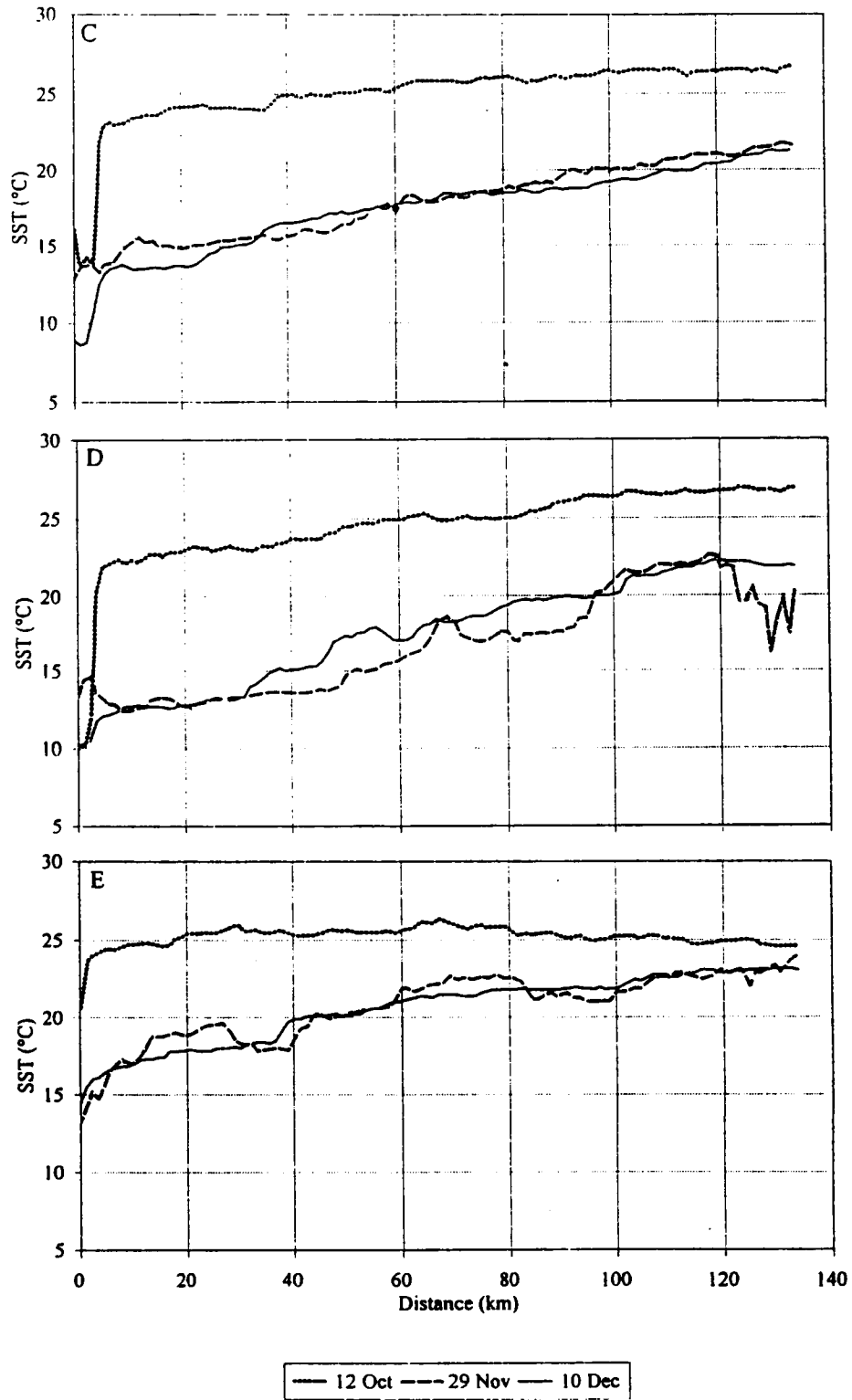
Figure 151. Sea surface temperature profiles from AVHRR image data, October-December, 1992. Profile locations are given in Table 12 and Figure 152.
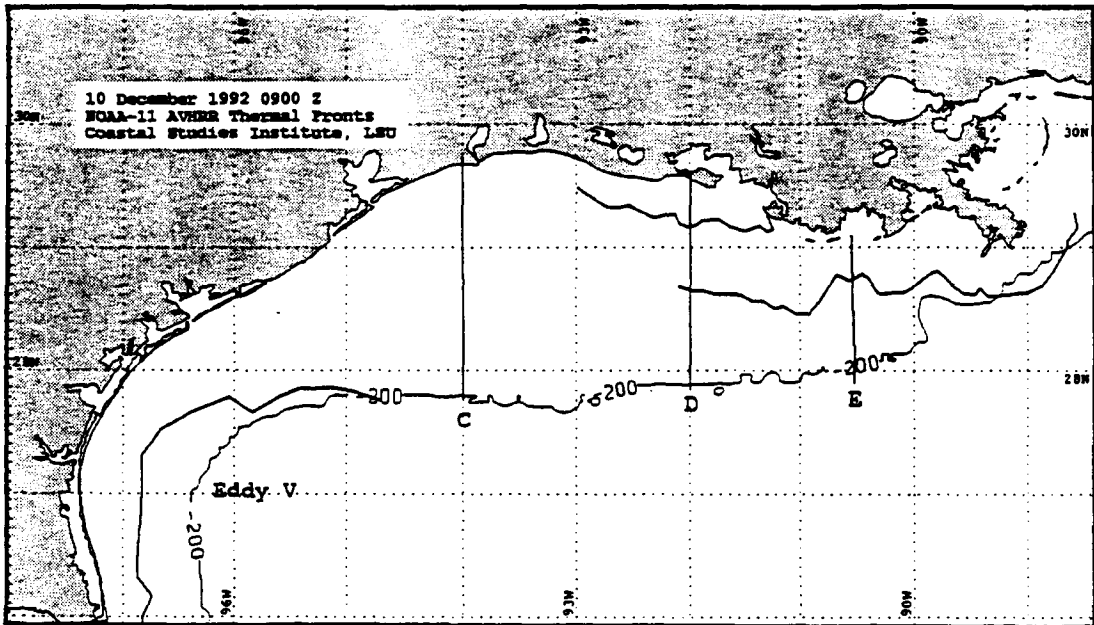
Figure 152. Frontal analyses for the Louisiana shelf on December 10, 1992. Lines C, D, and E are the locations along which the SST profiles in Figures 151 were taken.
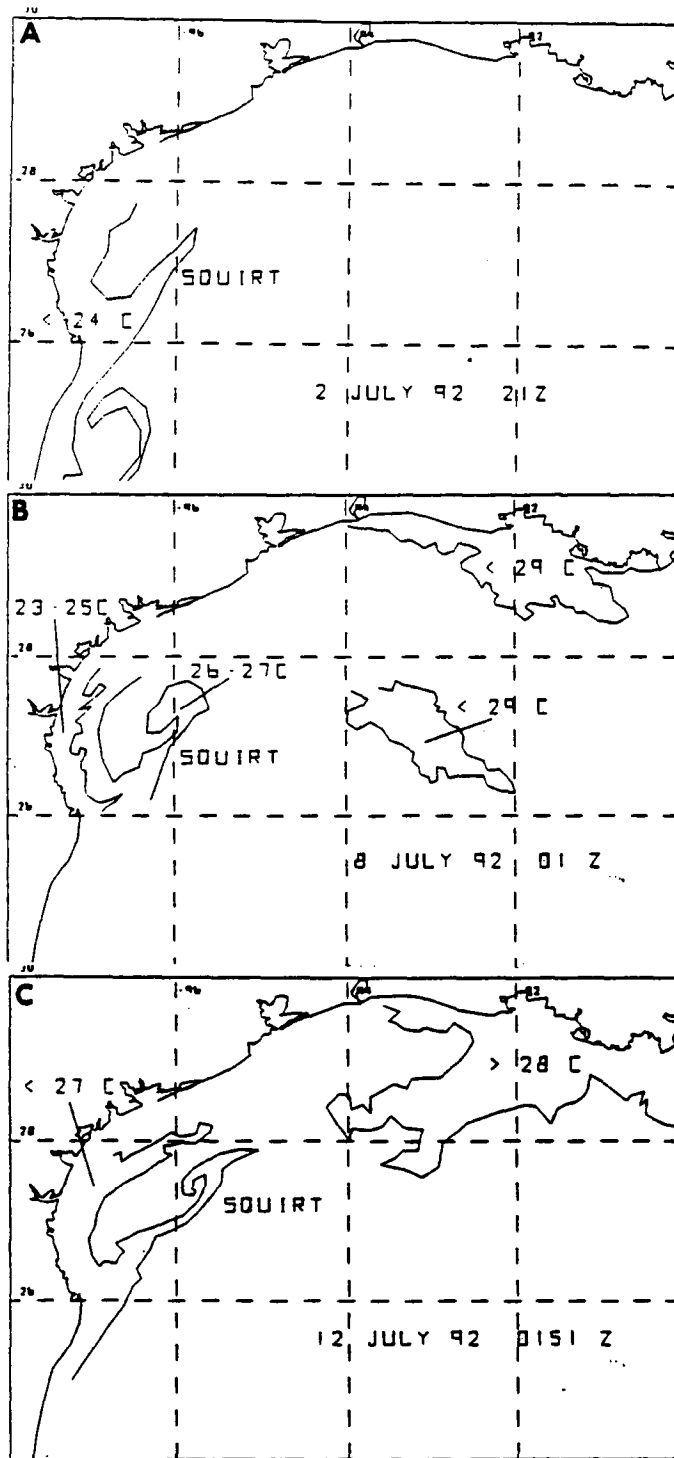
Figure 153. Evolution of the July 1992 squirt along the Texas shelf and slope as observed in NOAA AVHRR thermal infrared satellite imagery on (a) July 2; (b) July 8; and, (c) July 12, 1992.

205

(measured along the 50 m isobath) to 10 km (at its outer reaches). By July 8, the squirt had lengthened 30 km and a distinct cyclonic circulation was observed on the shelf side of the seaward end of the feature (Figure 153b). The imagery suggests that the squirt formed between Eddy Triton and a cyclonic feature over the upper slope. The squirt was again observed on July 12 (Figure 153c). Between July 8 and July 12 the seaward edge and cyclonic feature appeared to have moved seaward approximately 50 km. Based on squirts observed in 1993, this was a relatively large and persistent feature.

2. October 1992

In October 1992, a high velocity wind-driven jet of cool water was detected southwest of the Mississippi delta region. Frontal analyses on October 4, 12, and 19 were produced and posted to GULF.MEX in support of the LATEX program. A brief description of the evolution and circulation associated with this extensive plume is given here. Additional information on its temperature and salinity structure, as well as on currents associated with it, are presented in the cruise section of this report. On October 4, the jet-like plume feature was 140 km long and 10 km wide. The satellite imagery revealed its source areas to be the Mississippi River and coastal waters east and west of the delta. Currents within the high-velocity jet, estimated at 150-200 cm/s, caused the suspension of drilling operations at Ensearch Corporation's semi-submersible rig anchored in the Mississippi Canyon.

The available evidence suggest that the feature was wind-driven. A tropical low pressure system moved north from the Yucatan bringing sustained northeasterly winds of 12-14 m/s from October 1 to 3, which provided the forcing for this jet-like flow. The cool plume continued to flow towards the southwest over the next two weeks, during which time several clear sky images were obtained, enabling a study of its circulation. A schematic of the evolution of the plume is shown in Figure 154. After October 4, the cool plume continued to move southwestward, even though the northeasterly wind forcing had weakened substantially. On October 11, another cold front passed over the region increasing wind speed from the north and bringing clear sky conditions to the northern Gulf of Mexico. By October 11, a narrow plume of cool water extended south-southwestward from the delta across the deeper portions of the Mississippi Canyon. Further west, plume was observed to extend over the continental slope between the 200 and 1000 m isobath, with a maximum westward extent of 91° 25' W (Figure 154b). By October 13, a portion of the cool plume feature had been advected along the 1000 m contour by slope currents towards the east (Figure 154, 'A') and a large mushroom-shaped feature (probably an eddy dipole) had formed along the northwest margin of the cool plume (Figure 154c,'B').

Animation of clear-sky imagery enabled visualization of circulation at the leading edge of the plume. A convergence of water masses occurred on the west side of the cool plume due to anticyclonic circulation associated with Eddy Vasquez, which was centered southwest of the plume near 26°30' N, 93°30' W (Figure 155). Eastward flow along its northern margin obviously influenced shelf circulation as far north as the 50 m isobath. The convergence of water masses inhibited the westward flow of portions of the cool plume and resulted in a northwestward flow of plume waters, towards the coast (Figure 154c, 'B'). Almost a week later on October 19, a large portion of the plume had separated from the expansive zone of cool water around the Mississippi delta. It moved southwestward towards the saddle point between the two Eddies (Vasquez and Unchained) (Figure 155). Subsequent imagery revealed that the cool water mass continued to be advected towards the gap, however, mixing with surrounding waters soon removed its thermal signature. At its largest, on October 13, the cool river/coastal water mass extended 200 km from the Mississippi delta and covered 16,100 km², an area equivalent to about 35% of the continental shelf.
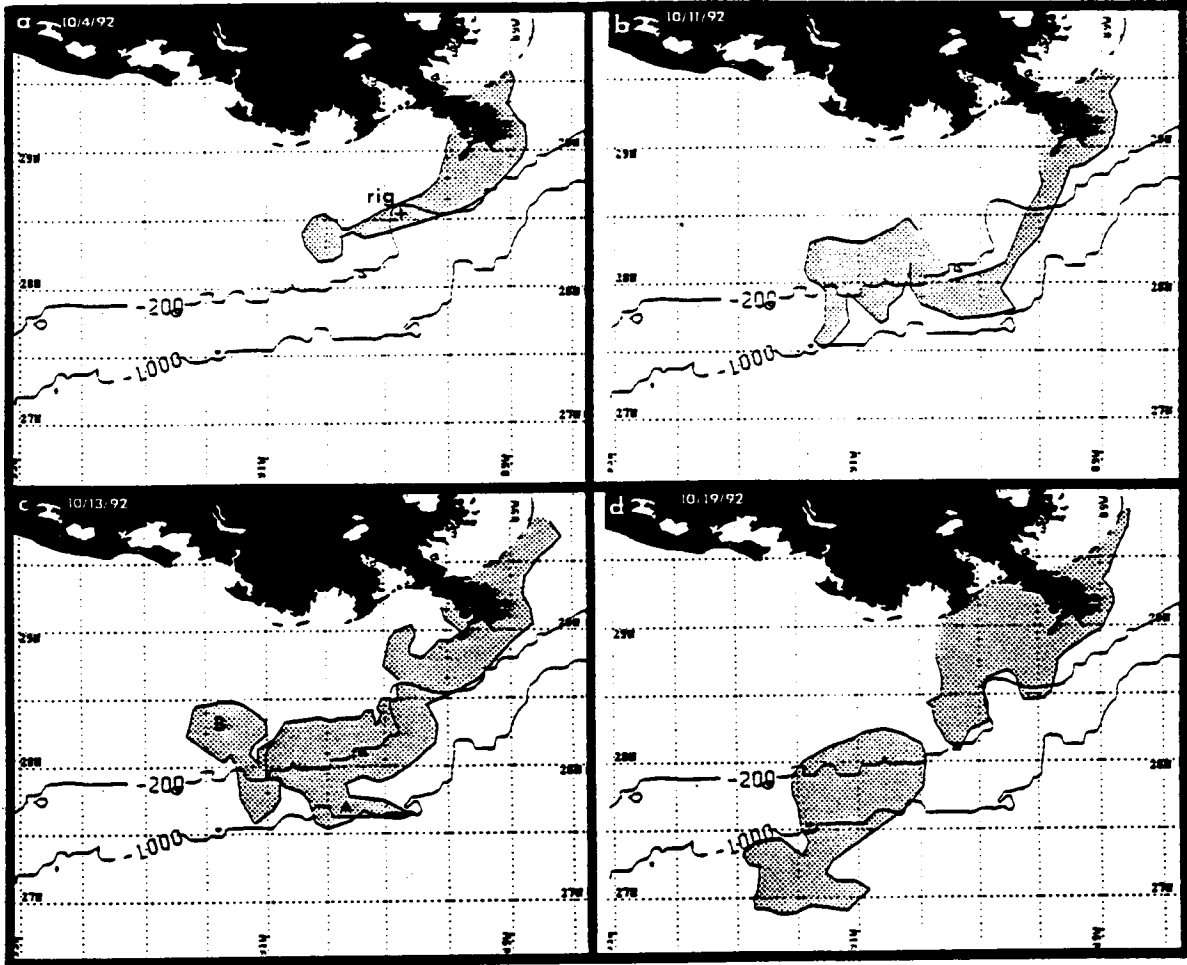
Figure 154. Schematic representation of the October 1992 Mississippi jet as observed in
NOAA AVHRR thermal infrared satellite imagery on (a) October 4; (b)
October 11; (c) October 13; and, (d) October 19.
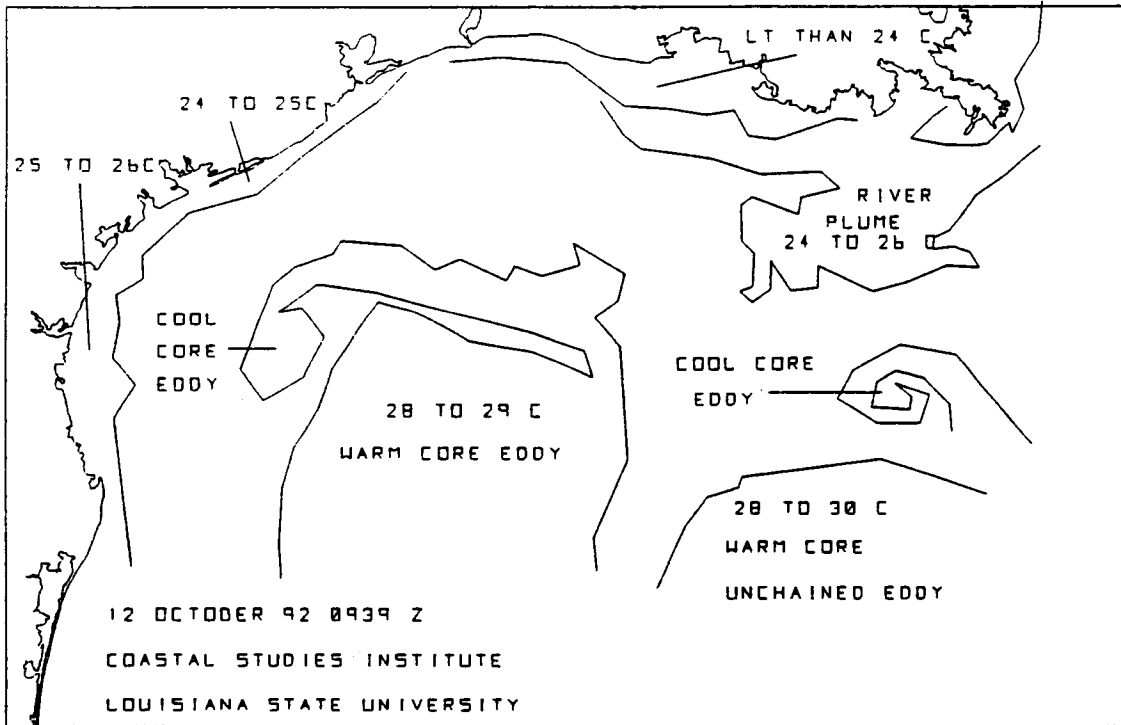
Figure 155. Frontal analysis of October 12, 1992, depicting the extensive cool plume southwest of the Mississippi delta and two large warm core Loop Eddies, Vasquez and Unchained.

208

3. December 1992

A large squirt was observed on December 20, 1992 along the Mexican shelf near 24° N. A frontal analysis and squirt alert were posted to GULF.MEX although the squirt was not within the LATEX region. This squirt was again observed on December 24 and January 9 and this information was provided to the other LATEX tasks in the form of frontal analyses and GIF images.

VIII. *MIDAS* SURVEY OF THE CALCASIEU RIVER PLUME
(Jeff Cox and Curtis Ebbesmeyer)

A. Objective

Plumes exiting the bays, estuaries, and rivers along the coast contribute significant quantities of sediments, organic material, and chemicals to the coastal plume of the Louisiana-Texas shelf. To investigate these plumes, surveys of the position and characteristics of several plumes were planned as part of the LATEX B program. The Calcasieu plume was the first of these to be surveyed, with sampling occurring on October 10 and 14 1992. It should be noted that the October 14 survey was conducted shortly after the passage of a front with associated northerly winds.

B. Parameters Measured

The object of the survey was to characterize the plume by sampling the plume's water structure, sediments, biology, and circulation. This section reports on the plume's physical parameters (see Section VI, Pollutant Chemistry.

Five north-south and five east-west transects were conducted off the mouth of Calcasieu Lake to map the plume on October 10, while a single north-south transect off the mouth of Calcasieu Lake was sampled on October 14 (Figure 156). This latter transect overlapped the north-south transect (P5) conducted directly off the mouth of Calcasieu Bay on October 10th, as well as the basic survey transect S5.

While underway on both survey dates, surface water temperature, conductivity, light transmission, and chlorofluorescence were sampled with LUMCON's Multi-Interface Data Acquisition System (MIDAS), while currents were measured with the ADCP. Salinity and density (sigma-t) were calculated from the temperature and conductivity data. No CTD profiles were attempted on October 10 because of instrument malfunction. A backup CTD was also obtained shortly thereafter, and the main CTD was also repaired; therefore five CTD profiles (stations P922410-P922414) were obtained on October 14 along with biological and chemical samples at three of the five locations (stations P922410, P922412, P922414). The CTD was outfitted to obtain profiles of temperature, conductivity, optical backscatter, dissolved oxygen, light transmission, and chlorofluorescence.

C. Results of the October 10 Survey

Water Properties. The near-surface characteristics of the Calcasieu plume may be distinguished using five parameters: temperature; salinity; density; light transmission; and chlorofluorescence. Plan view contours of the MIDAS data are presented in Figure 157a,b; profiles of these data from each north-south transect versus latitude are also displayed (bottom). Water temperatures off the mouth of Calcasieu Lake range from 22.9°C within the central portion of the plume to 24.5°C at the offshore edge of transect P9 (Figure 157a). Review of the regional temperature distributions from the basic survey indicate water temperatures upstream to the east generally exceeded 23.6°C; temperatures less than approximately 23.4°C appear to be attributed to effluent from Lake Calcasieu. The influence of the plume may also extend at least to temperatures of 23.8°C. As Calcasieu Lake discharges at approximately 93.37°W longitude, the measured temperatures indicate the plume moves westward upon discharge from the channel and extends to at least 93.58°W (~24 km westward). Over this interval the plume extends approximately 9 km offshore before reaching 23.4°C.

The salinity measurements do not provide as clear a resolution of the plume's location. Salinities along transects P3-P9 indicate slight salinity increases from the channel along the

211
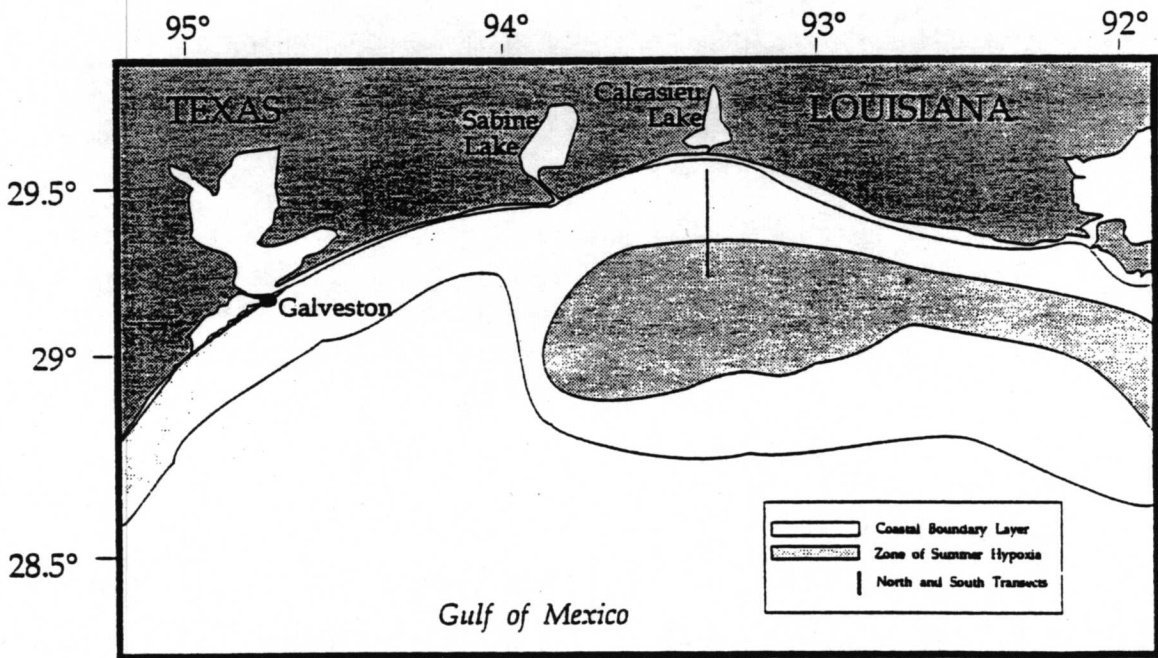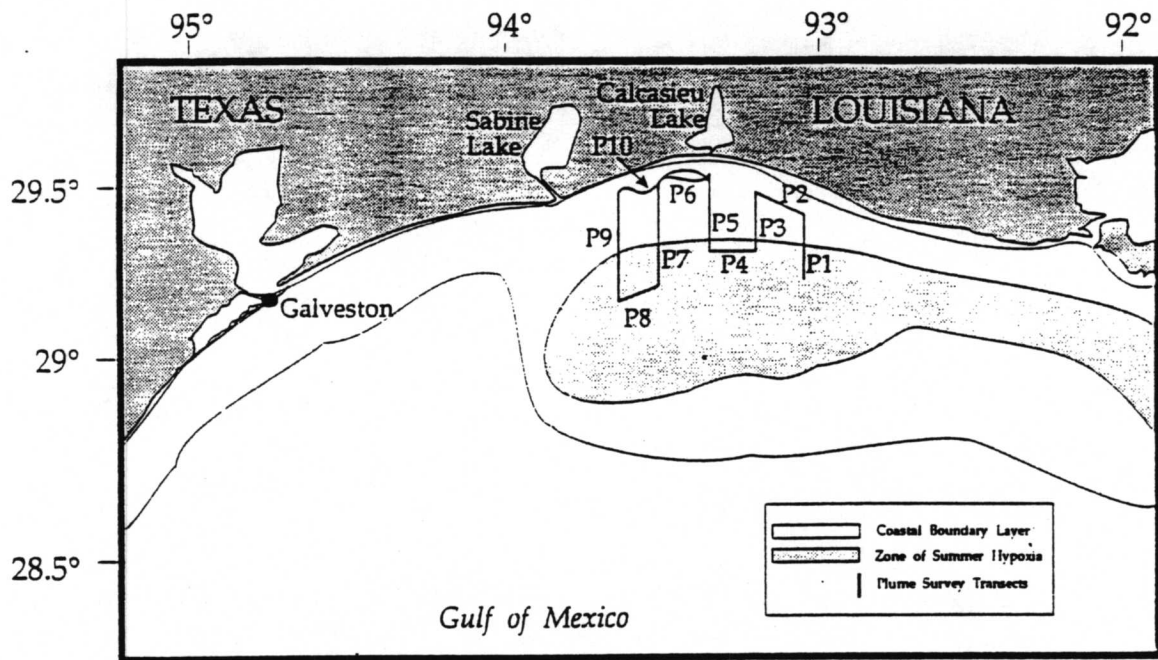
Figure 156. Transects used to survey the Calcasieu Plume on October 10 (upper) and October 14 (lower), 1992.

Figure 157. Measurements from MIDAS, October 10, 1992. (a) temperatures in the Calcasieu plume, plan view (upper) and along selected transects (lower). (b) Light transmission in the Calcasieu plume, plan view (upper) and along selected transects (lower).
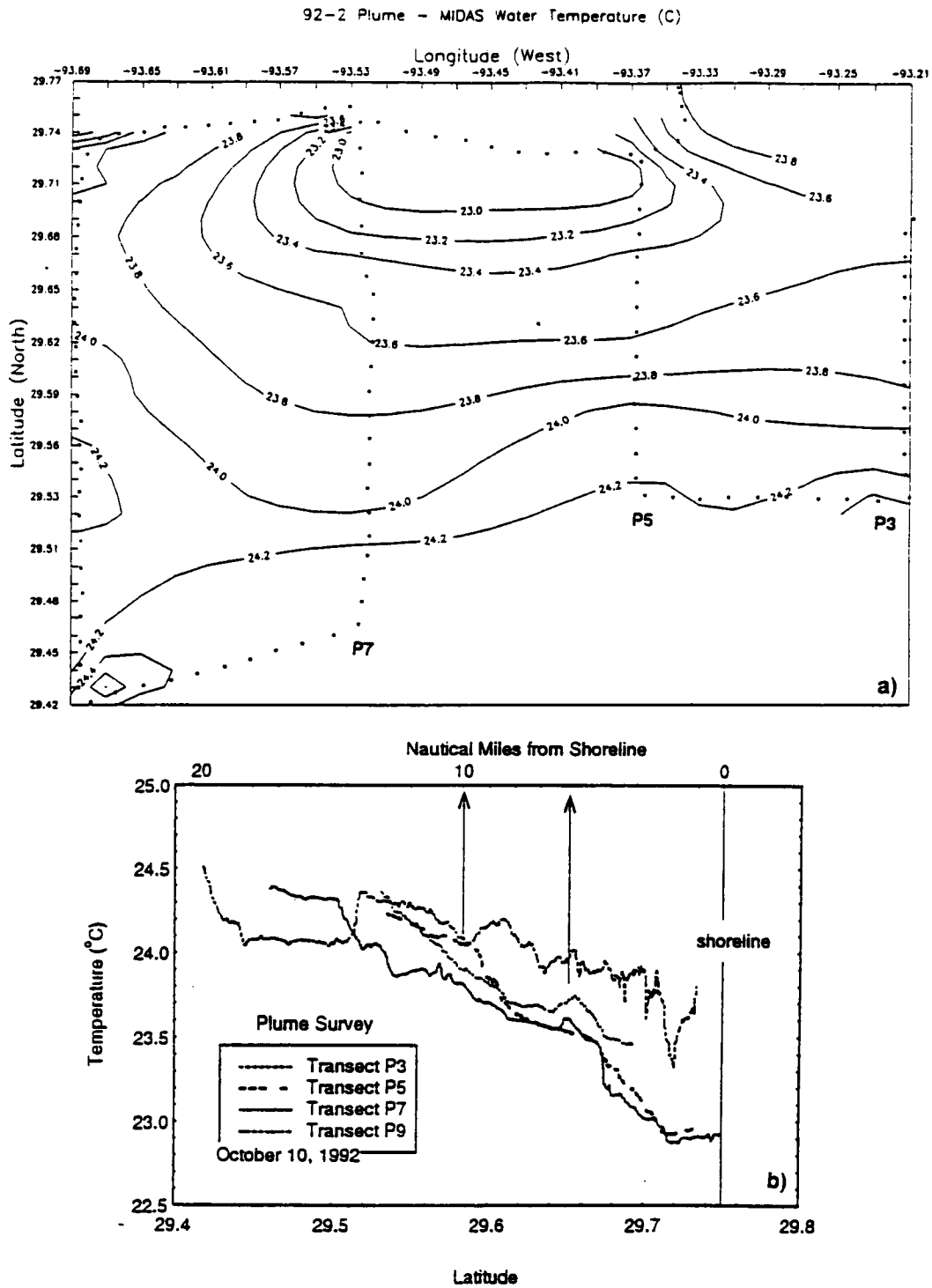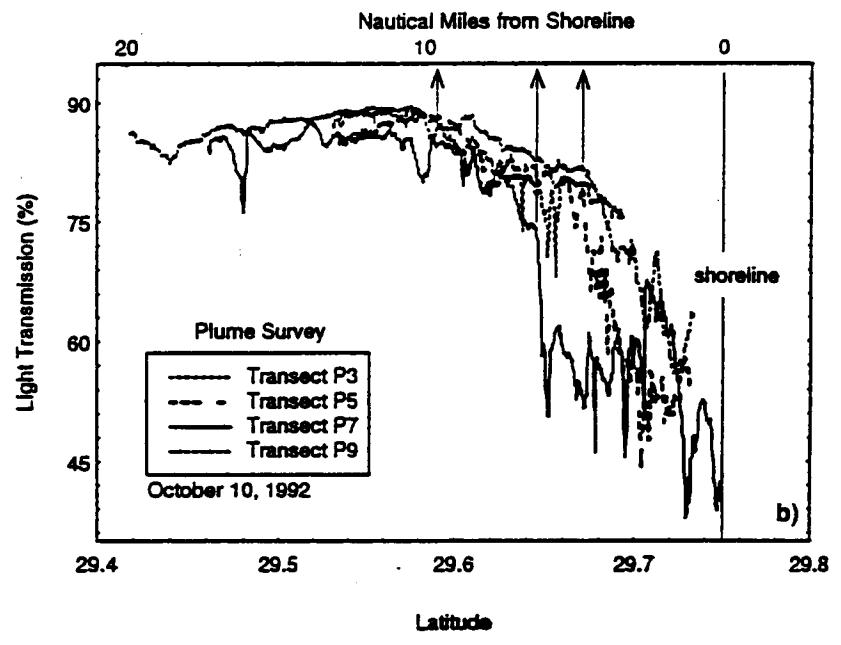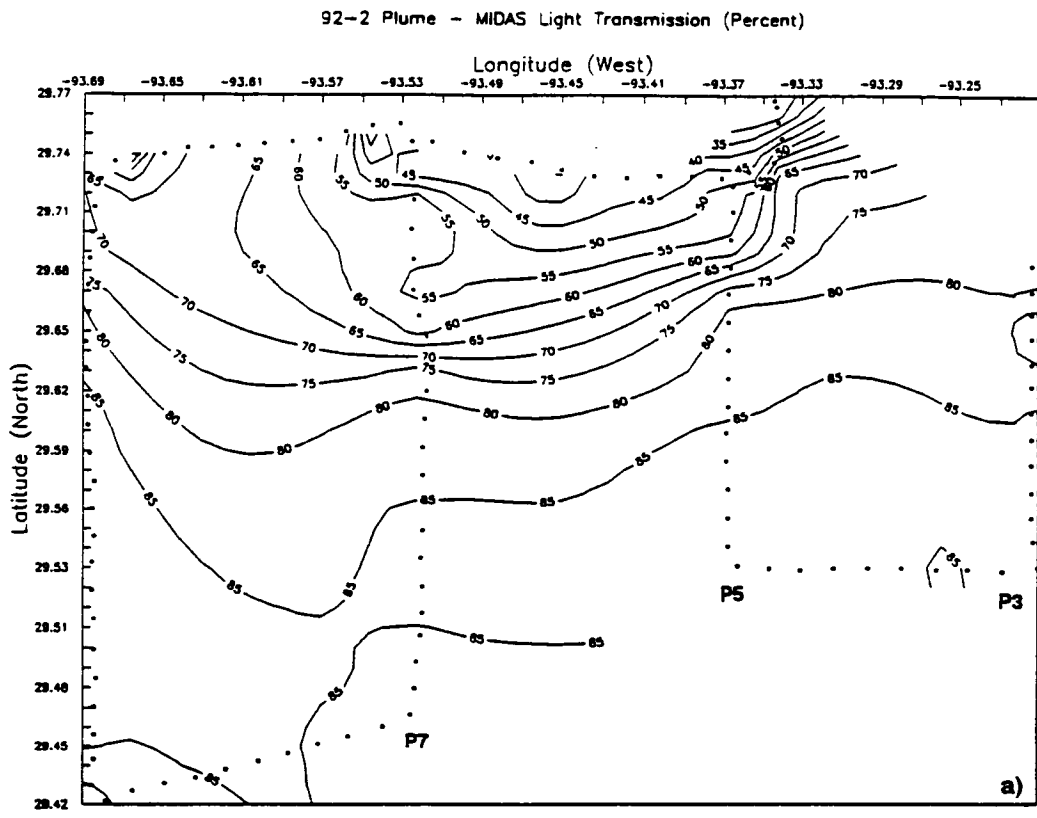
213

Figure 157 cont'd. Measurements from MIDAS, October 10, 1992. (a) temperatures in the
Calcasieu plume, plan view (upper) and along selected transects (lower).
(b) Light transmission in the Calcasieu plume, plan view (upper) and
along selected transects (lower).

shoreline either east or west. In the offshore (southward) direction, the salinity increases at differing rates along the transects, with transects P5 and P7 perhaps providing the indications of the plume. Salinities along both transects increase uniformly from the coast to approximately 10-12 km, then increase less rapidly southward to 16 (P5) or 24 (P7) km, after which salinities increase rapidly over the next 10 km along each transect. Salinity gradients within the three regions are approximately 0.65psu/km in the plume, 0-0.07psu/km in the intermediate region, and approximately 0.94psu/km farther southward. The calculated densities present patterns similar to those of salinity.

Light transmission percentages (Figure 157b) define the plume's area comparable to temperature. The 75% light transmission circumscribes the plume, the downstream edge of the plume lies approximately 61 km west of the channel, and the offshore extent is approximately 9-11 km south of the coast (Figure 157b). Background percentages were not reached until approximately 20 km southward.

Most of the plume's areal extent is characterized by depressed light transmission. Moving northward along each transect, the light transmission percentage begins decreasing at approximately 29.6°N, or approximately 20 km from shore. At this distance from shore the decrease is quite rapid along transect P7, decreasing from approximately 80% to 45% light transmission between 29.64°N and the shoreline (27.5°N). At 7 km offshore this rapid decrease occurs along transect P5. Differences in light transmission percentage between the 4 transects at a given latitude varies up to 30% within 11 km of shore, whereas farther offshore the variation does not exceed approximately 10%.

Contours of chlorofluorescence differs substantially from those of other MIDAS parameters. Profiles of chlorofluorescence along the north-south transects indicate values exceeding 0.20 generally within 6 km of shore, except along transect P9 where they reach 13 km offshore.

Circulation. Currents associated with the plume generally flow westward as shown by ADCP current vectors at 4 m depth (Figure 60).

ADCP currents along the plume transect T-5 are shown in Figure 158, where upper panels show current vectors at half meter depth intervals, and two lower panels contours of the U (east positive) and V (north positive) current components.

D. Results of October 14 Hydrographic Survey

Water Properties. As only a single north-south transect was executed, the plume's east-west extent could not be re-evaluated on October 14. The northward leg was conducted from 0305-0600 GMT, while the southward leg occurred from 0600-0953 GMT. The north-south extent of the plume may be assessed from the five MIDAS parameters shown versus latitude along the transect for both the northward and southward transits of the vessel. Figure 159a, b, c shows the temperature, salinity and light transmission along this transect. As shown by temperature and salinity gradients at this transect, the outer edge of the plume was located 4-6 km further offshore than on October 10.

Current Structure. Velocity components along Transect P5 measured during both the north and south bound transits indicated a banded structure (Figure 159). This structure may be seen most clearly in the U-component. Situated at the center of the strong north-south density gradient (29.55°N) lies a core of westward current. Speeds in this core reach 20 cm/sec. North and south of the core there are eastward speeds in the range of 5-10 cm/sec.
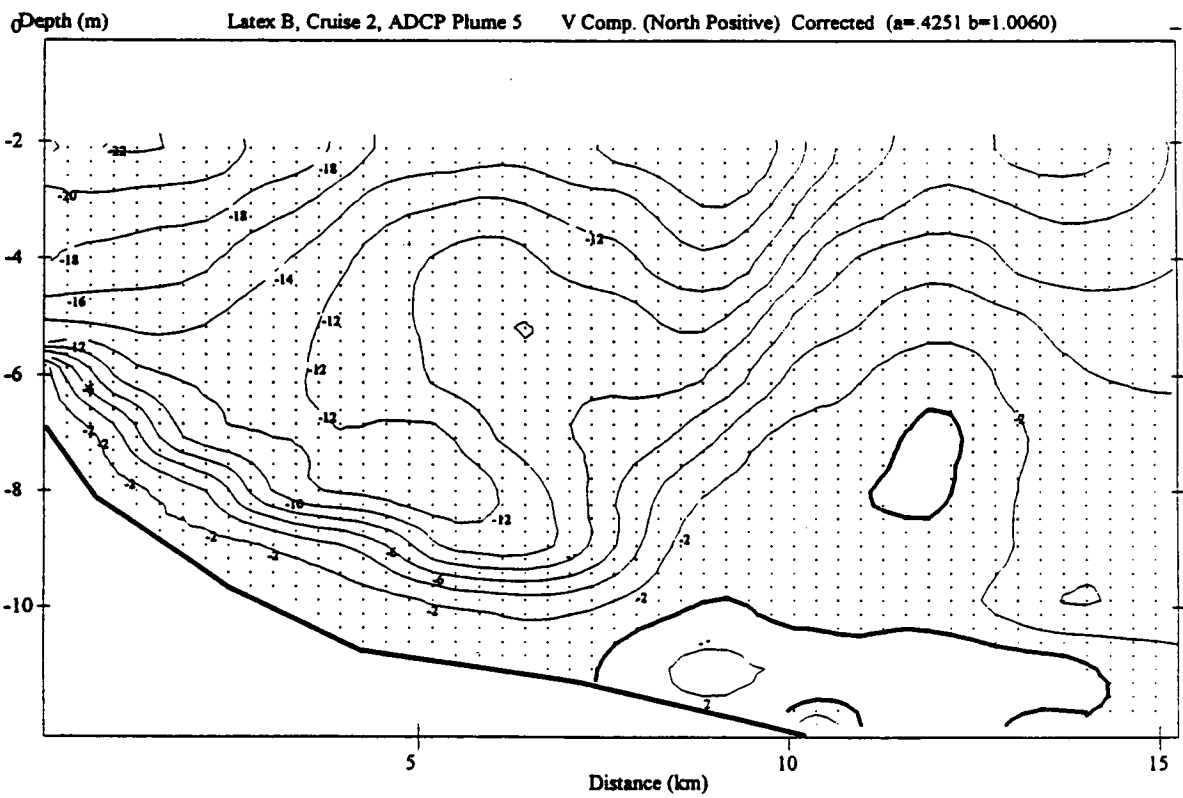
Distance (km)

Distance (km)
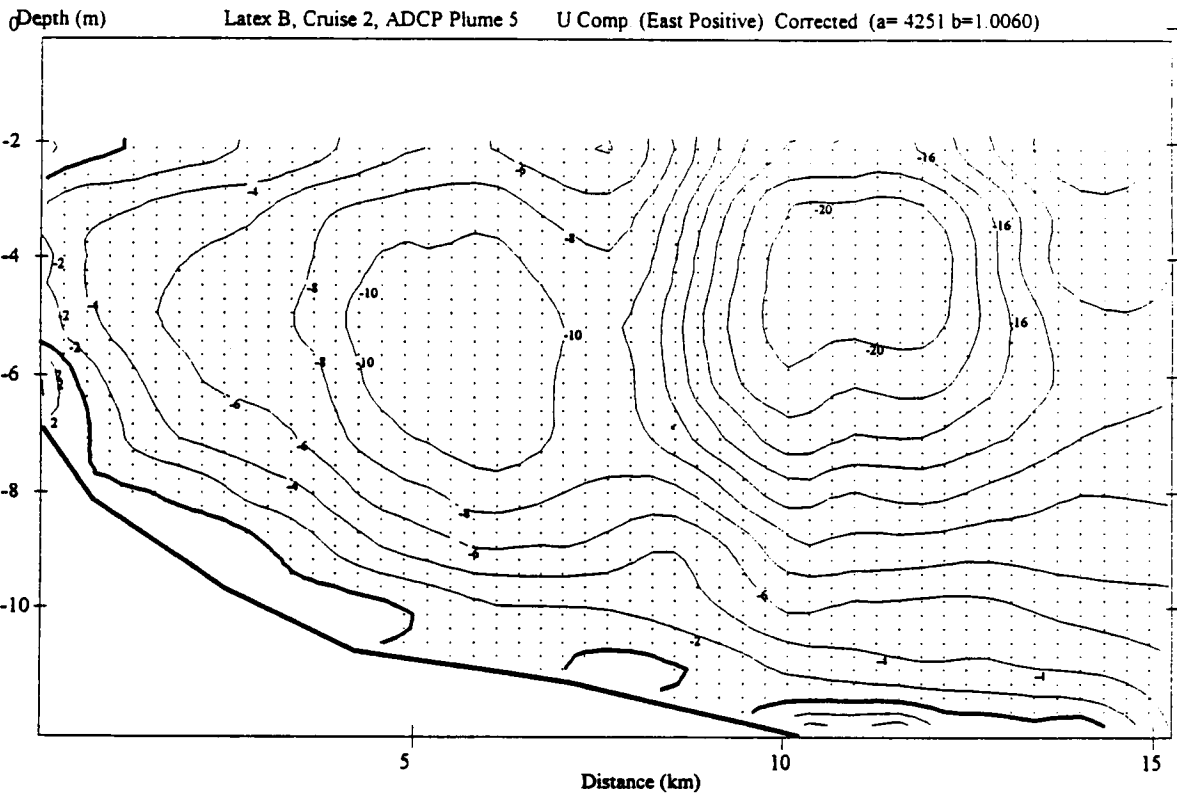
Figure 158. ADCP currents in the vicinity of the Calcasieu plume, October 10, 1992, along T-5 (a) U component; (b) V component.
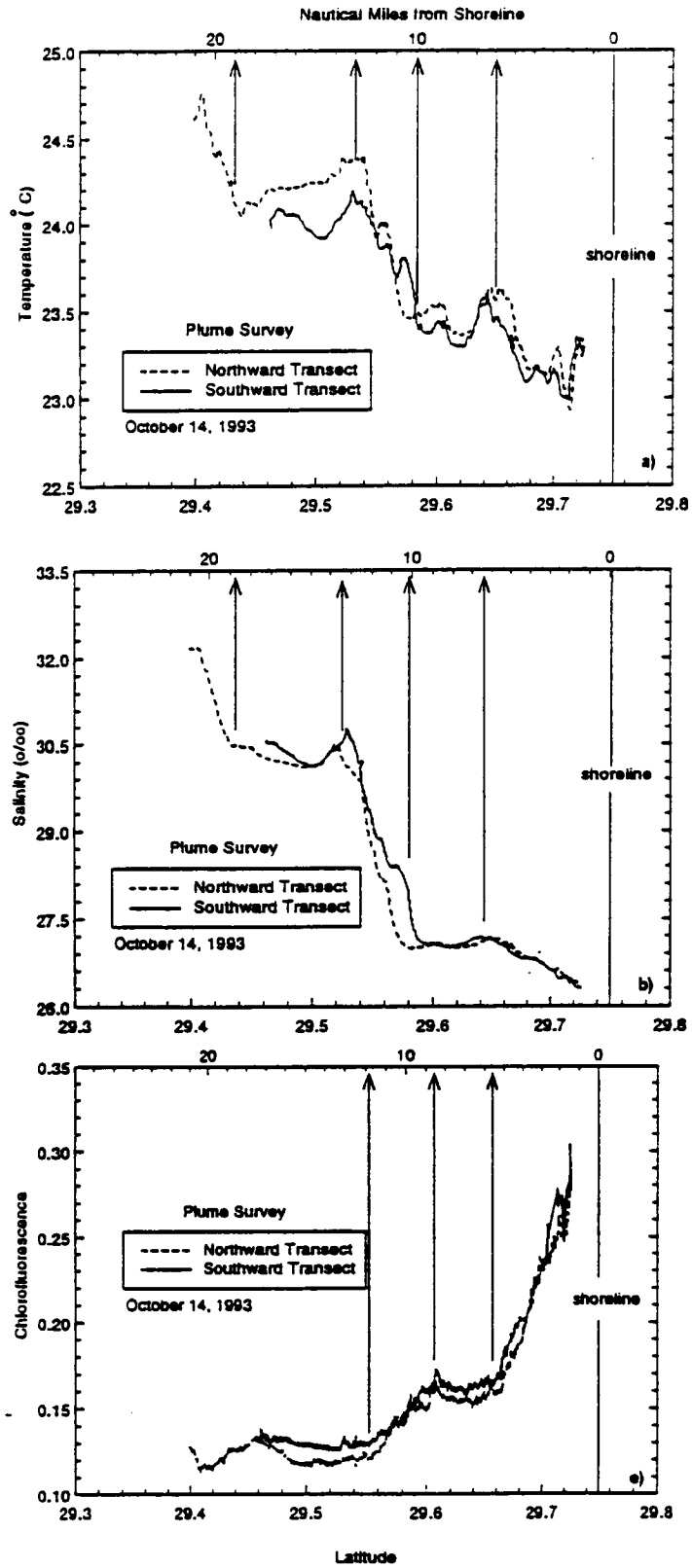
Figure 159. MIDAS measurements on October 14, 1992, along north (dashed) and south (solid) transits of transect P5: (a) temperature; (b) salinity; and, (c) light transmission.

217

E. Calcasieu Plume Biological Survey (Nancy Rabalais, Richard F. Shaw)

Stations P922410 through P922414 were reoccupied along the S4 line (P922175-P922179) to document the biological characteristics of the Calcasieu plume. Salinity distributions were similar for the two collection periods. Chlorophyll *a* was higher at station P922410 than the previous sample (P922175), but similar values for P922412 and P922414 and their respective stations, P922177 and P922179, were found. Continuously recorded salinity and *in vivo* fluorescence from the MIDAS system are shown in Figure 160. In all data sets, as the salinity in the surface waters increased with distance from the freshwater source, the chlorophyll *a* or *in vivo* fluorescence declined. The decrease in chlorophyll was much more precipitous than the gradual increase in salinity with distance from Calcasieu Pass. Changes in chlorophyll were more pronounced in the second transect than the first transect.

The highest zooplankton biomass during the cruise occurred along the plume and the three density variables were highest at the inshore station. At the two stations, biomass was 0.010 and 0.074 g/m^3 for the 153-μm fraction and 0.002 and 0.008 g/m^3 for the 335-μm fraction. Larval density was 5.0 and 20.8 larvae/100 m^3.

Figure 160. MIDAS percent light transmission, salinity, and scaled *in vivo* fluorometer voltage data (approximately 2-min. intervals) for Calcasieu Plume (stations P92410-P92414), Cruise II, October 1992.

IX. FRONTAL SURVEY
(Jeff Cox and Curtis Ebbesmeyer)

A. Objective

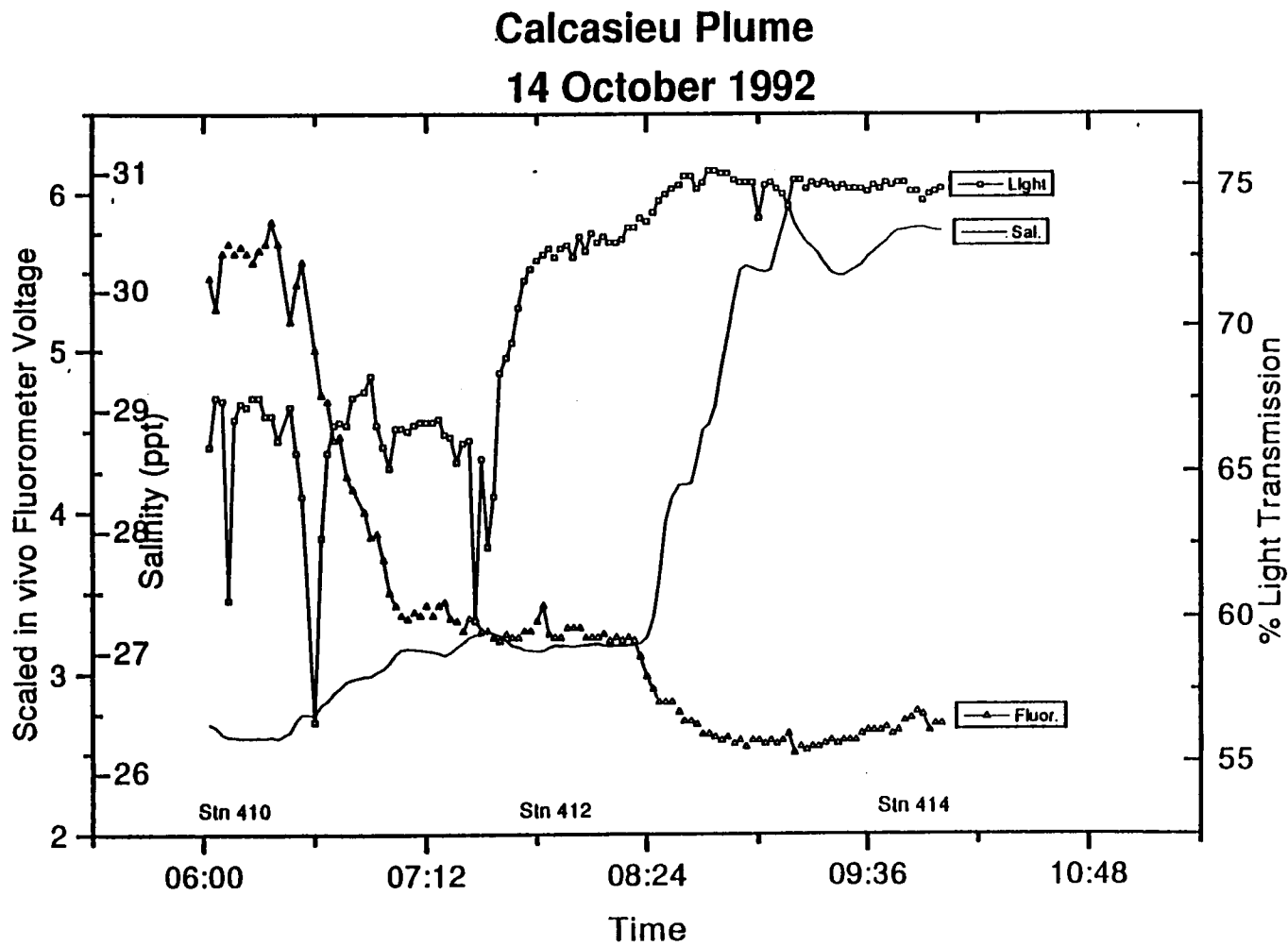The coastal plume and contiguous shelf water contains inputs from a number of freshwater sources leading to a variety of fronts on the shelf. Fronts between major water masses farther offshore in the Gulf of Mexico evident in satellite sea surface temperature maps have been located by the National Ocean Service on frontal analysis charts and are also mapped by the LATEX B satellite imaging team. However, the dynamics occurring within fronts, and associated distribution of plankton, nutrients, and chemicals is not well understood. Therefore, a secondary objective of the LATEX B program is to document the rapid change in water properties and circulation occurring within a few selected fronts associated with the coastal plume. This chapter presents physical measurements in the vicinity of a small front off Louisiana.

B. Parameters Measured

On October 13, 1992 a small intense front was located using MIDAS while transiting northward, searching for a larger front seen in a satellite image received aboard the R/V *Pelican* from LSU's image processing team. On the northbound leg this front showed as a sharp decrease in salinity. After passing through this front, the course was turned south and five CTD profiles spaced across the front were made.

The front was located off the Louisiana coast at approximately 29°18'N; the transect intersected through the front at 92°30'W. Surface water properties, including temperature, conductivity (salinity), light transmittance, and chlorofluoresence were measured while underway using MIDAS, and currents were recorded using the ADCP. Five CTD stations (P922301-P922305) were performed along the transect at intervals over a total distance of 5.6 km; water temperature, conductivity, and dissolved oxygen profiles were measured from which salinity and density (sigma-t) were calculated.

C. Results

Water Properties. Contours of water temperature, salinity, (Figure 161a, b) density, and dissolved oxygen were prepared from a combination of near-surface measurements from MIDAS and five CTD profiles during the southward pass through the front. The front is shown clearly by salinity, to a limited degree by temperature, and not clearly by oxygen. From north to south salinity increases by 5 psu, density increases by 4 sigma-t units, and temperature increases 0.6°C over a distance of approximately 1700 m (29.306° -29.291°N). At their steepest, the gradients are 2.3 psu/km and 1.5 sigma-t/km. The waters north of the front are less saline, colder and less dense than south of the front. The front extends to a depth of approximately 10 meters and bends northward under the lighter waters closer to shore.

Surface water properties were also examined by overlaying data from the northward and southward transits obtained with MIDAS. In both transits the front is centered between 29.293° and 29.300°N. The northern portions of the transits, northward from station P922301, are similar. From station P922302 through the front, and extending southward, the values measured during the two transects differ significantly. South of station P922304, temperature was lower, salinity higher, light transmission higher, and chlorofluoresence lower at the beginning of the northward transect than at the end of the southward transect. During the northward transect the front appears stretched over a greater distance (2.7 km), with a more gradual change in the measured parameters. During the southward transect, the front may have intensified by contracting to total distance of approximately 2.0 km and larger gradients of the parameters
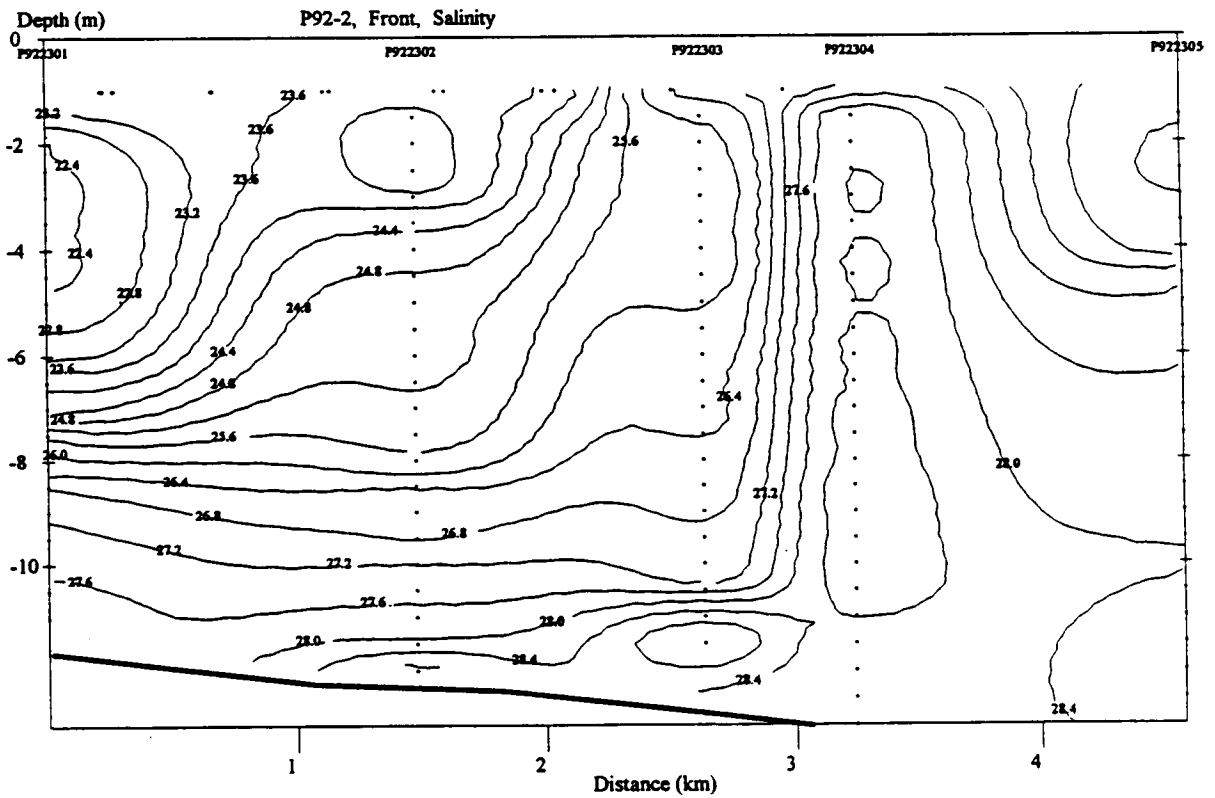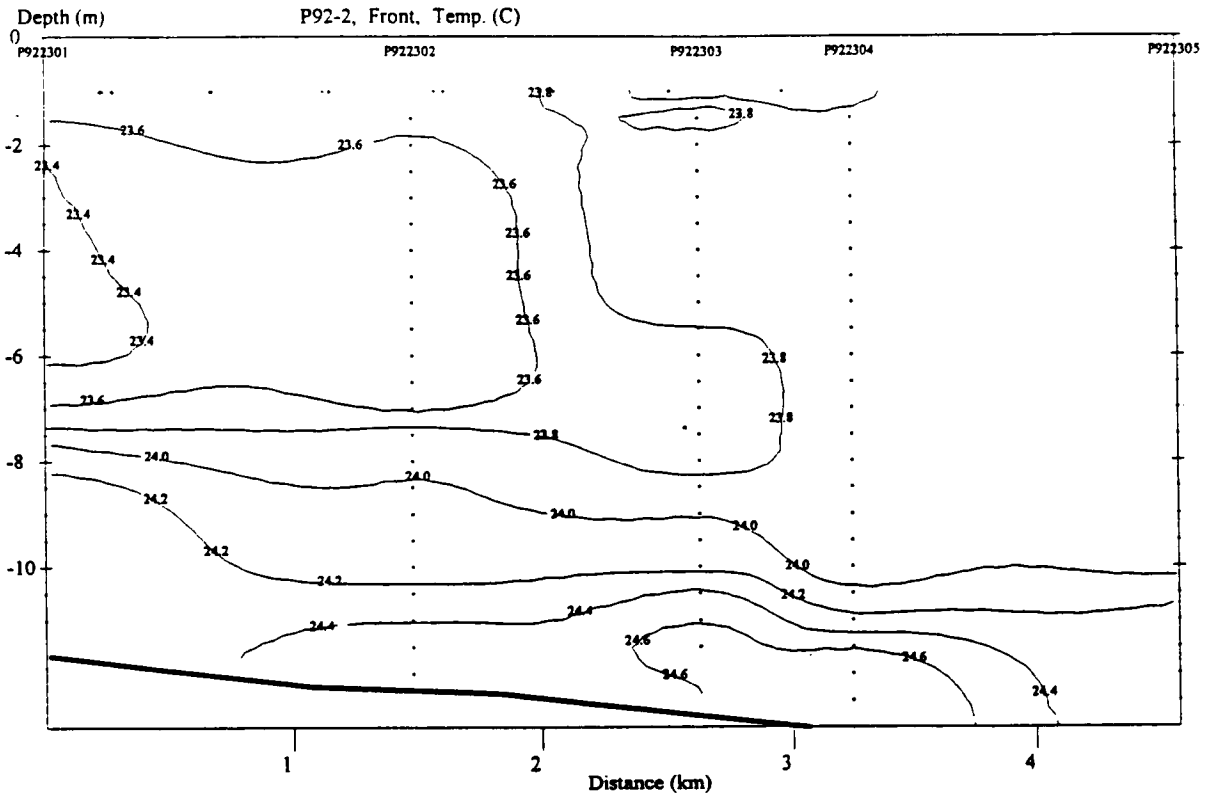
Figure 161. Contours across the front on October 13, 1992: (a) temperature; (b) salinity.
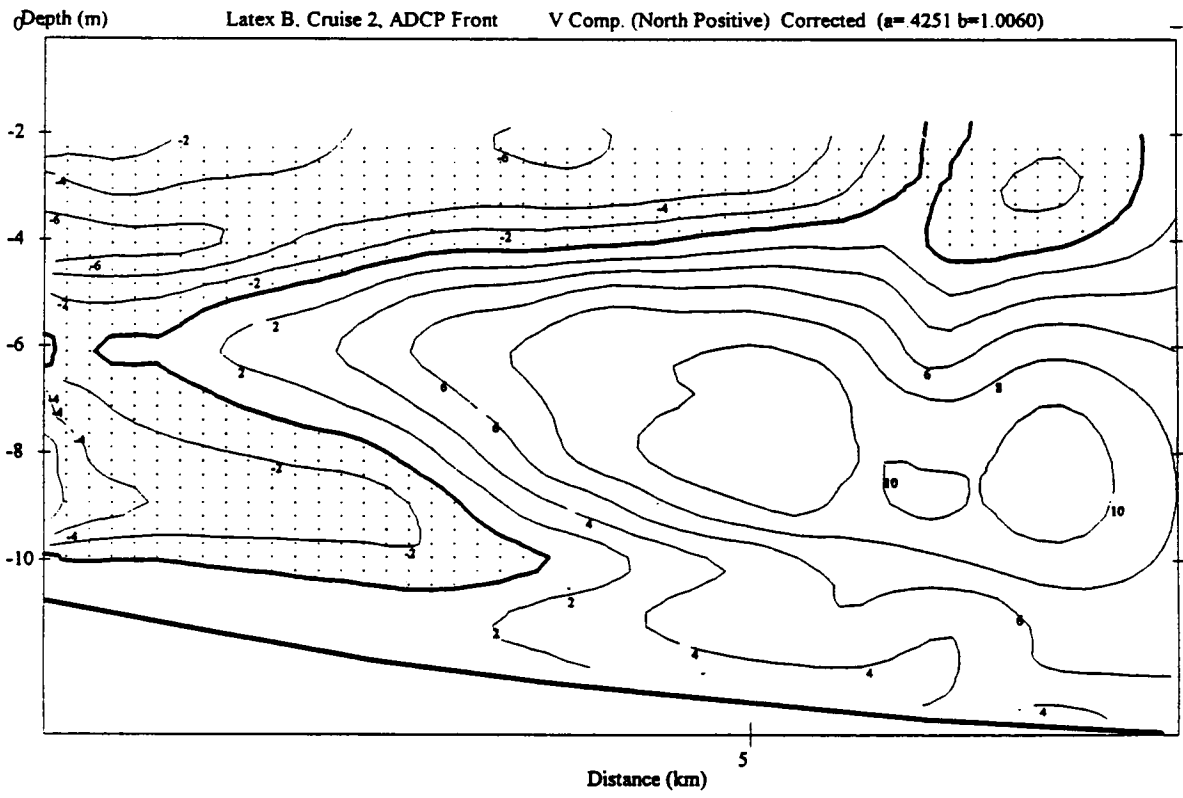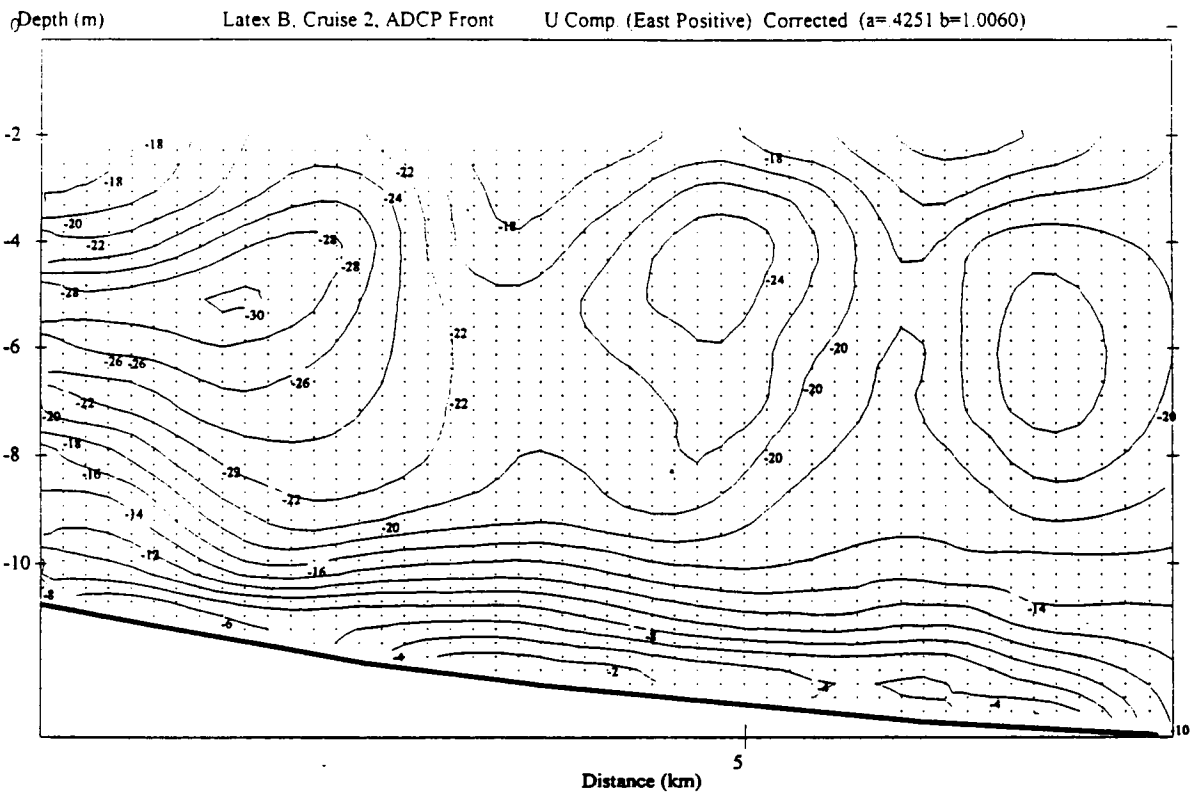
Figure 162. ADCP currents through the front on October 13, 1992: (a) U component; (b) V component.

occur, especially at approximately 29.295°N. Note particularly the 4% decrease of light transmission between transects south of station P922304.

Circulation. As the transects across the front were conducted, currents were measured with the ADCP. Contours of the velocity components are shown in Figure 162. Waters in the colder, fresher water mass north of the front appear to flow at a higher speed to the northwest, compared with warmer, saltier water deeper and to the south.

D. Significant Hydrographic Findings

A front between colder, fresher and warmer saltier water masses was observed in two transects. The front was particularly dramatic, with a salinity change of 5 psu in 1.7 km; a modest temperature change of approximately 0.6°C was noted. A current shear was also noted with the ADCP.

E. Atchafalaya Front Biological Survey (Nancy Rabalais, Richard F. Shaw)

Salinities were lower than the Calcasieu Plume transects (23.5 ppt to 27.5 ppt vs..26 to 31 ppt). Chlorophyll a concentrations were similar to the Calcasieu Plume values. Continuously recorded salinity and *in vivo* fluorescence from the MIDAS system for the Atchafalaya front transect are shown in Figure 163. The MIDAS salinity values were similar to the surface water samples taken with the chlorophyll a samples and showed stepwise increases across the front, with a slight decrease on the seaward end. The *in vivo* fluorescence rather than declining with increasing salinity, was initially high, decreased, increased, then decreased precipitously.

Cursory examination of the MIDAS data for the Calcasieu S4 Line, the Calcasieu Plume and the Atchafalaya Front (Figure 163) indicated there was a negative relationship between % light transmission and scaled *in vivo* fluorescence from the MIDAS system. Plots of these same data in regression against each other (Figure 164) indicated that there was a strong negative relationship between % light transmission and *in vivo* fluorescence only for the Calcasieu S4 Line (Stations P922175-P922179). While the relationship for the Calcasieu Plume (Stations P922410-P92414) was negative, it was not strong. There was no relationship between % light transmission and MIDAS *in vivo* fluorescence for the Atchafalaya Front (Stations P92301-P92305).

Biomass estimates for the 153-μm samples ranged 0.005-0.009 g/m³. The 335-μm biomass and larval density tended to increase as the distance from shore increased. Dry weight for the 335-μm samples increased from 0.001-0.005 g/m³, while larval density incrased from 0=14.2 larvae/100m³.

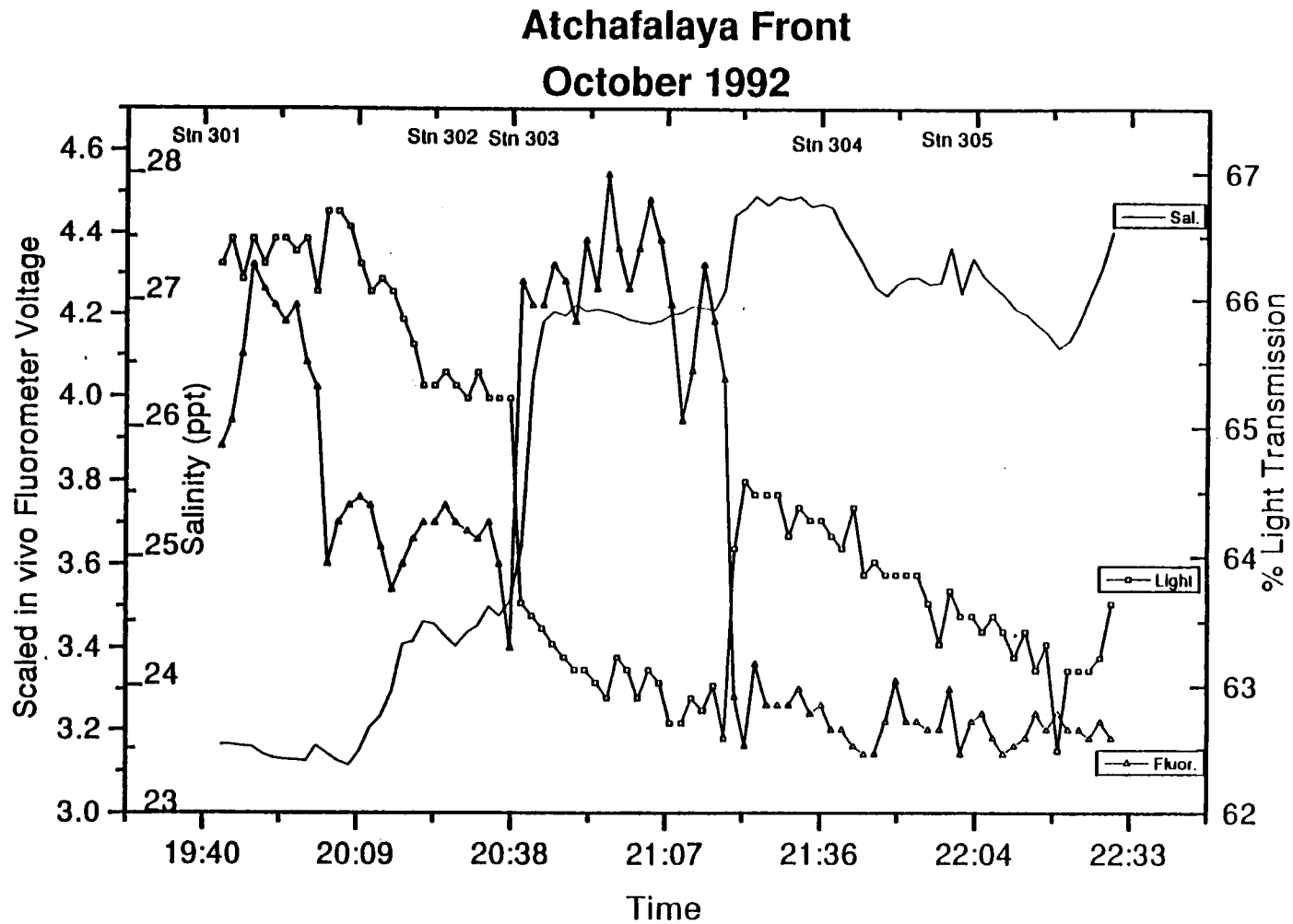Figure 163. MIDAS percent light transmission, salinity, and scaled in vivo fluorometer voltage data (approximately 2-minute intervals) for Atchafalaya Front (stations P92301-P92305), Cruise II, October 1992.
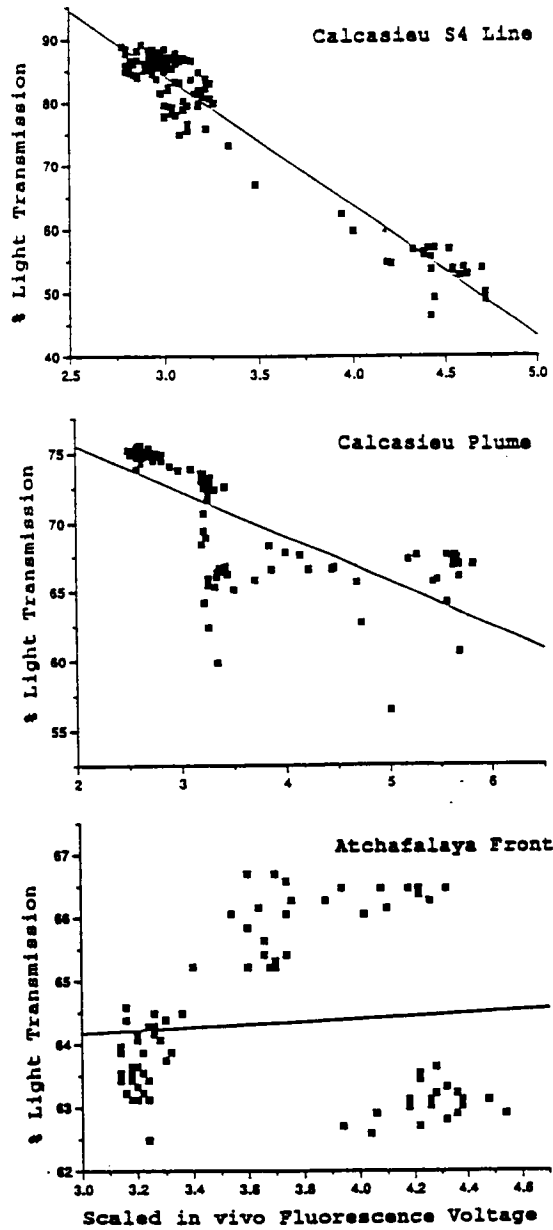
Figure 164. Comparison of MIDAS percent light transmission data with scaled in vivo
fluorometer voltage data for the Calcasieu S4 line (upper); Calcasieu Plume
(middle); and, Atchafalaya Front (lower).

226

X. Literature Cited

Baker, E.T., H.B. Milburn, and D.A. Tennant. 1988. Field assessment of sediment trap efficiency under varying flow conditions. J. Mar. Res. 46:573-592.

Butler, J.L. 1992. Collection and preservation of material for otolith analysis. Pp. 13-17. In: Stevenson, D.K. and S.E. Campana (eds.). Otolith Microstructure Examination and Analysis. Can. Spec. Publ. Fish. Aquat. Sci. 117.

Carpenter, E. J., J. Chang, and L. P. Shapiro. 1991. Green and blue fluorescing dinoflagellates in Bahamian waters. Marine Biology 108:145-150.

Dickey, R.W., G.A. Fryxell, H.R. Granade, D. Roelke. 1992. Detection of the marine toxins okadaic acid and momoic acid in shellfish and phytoplankton in the Gulf of Mexico. Toxicon 30:355-359.

DiMego, G. J., L. F. Bosart, and G. W. Enderson. 1976. An examination of the frequency and mean conditions surrounding frontal incursions into the Gulf of Mexico and Caribbean Sea. Mon. Wea. Rev. 104(6):7010-718.

Dinnel, S.P. and W.J. Wiseman, Jr. 1986. Freshwater on the Louisiana and Texas shelf. Continental Shelf Res. 6(6):765-784.

Gardner, W.D. and M.J. Richardson, 1992. Particle export and resuspension fluxes in the western North Atlantic. In: Rowe, G. T. and V. Pariente (eds.). Deep-sea food chains and the global carbon cycle. Netherlands: Kluwer Academic Publishers. Pp. 339-364.

Hallegraeff, G.M. 1993. A review of harmful algal blooms and their apparent global increase. Phycologia 32:79-99.

Harper, D.E.J., and G. Guillen. 1989. Occurrence of a dinoflagellate bloom associated with an influx of low salinity water at Galveston, Tx and coincident mortalities of demersal fish and benthic invertebrates. Contr. Mar. Sci. 31:147-161.

Huh, O.K., L.J. Rouse, Jr. and N.D. Walker. 1984. Cold air outbreaks over the northwest Florida continental shelf: heat flux processes and hydrographic changes. J. of Geophysical Res. 89(C1):717-726.

Kidwell, K.B. 1991. NOAA Polar Orbiter Data Users Guide, Satellite Data Service Division, U.S. Dept. of Commerce.

Laurence, G.C. 1976. Caloric value of some north Atlantic calanoid copepods. Fish. Bull. 74:218-220.

Lovegrove, T. 1966. The determination of the dry weight of plankton and the effect of various factors on the values obtained. pp. 429-467. In: Barnes, H. (ed.). Some Contemporary Studies in Marine Science. George Allen and Unwin Ltd., London.

Martin, J., K. Haya, and L.E. Burridge. 1990. *Nitzschia psuedodelicatissima*—a source of domoic acid in the Bay of Fundy, eastern Canada. Mar. Ecol. Prog. Ser. 67:177-182.

McClain, E.P., W.G. Pichel, and C.C. Richardson. 1985. Comparative performance of AVHRR-based multichannel sea surface temperatures. J. Geophys. Res. 90:11,587-11,601.

McEwen, G.F., M.W. Johnson, and Th.R. Folsom. 1954. A statistical analysis of the performance of the Folsom plankton sample splitter, based upon test observations. Arch. Met. Geophys. Bioklim, Series A. 7:502-527.

Meade, R.H. and R.S. Parker. 1985. Sediment in rivers of the United States. National Water Supply-Summary 1984. U.S. Geological Surver Water-Supply Paper No. 2275, U.S. Dept. Interior, Geological Survey, Washington, D.C.

Means, J.C., S.G. Wood, J.J. Hassett, and W.L. Banwart. 1980. Sorption properties of polynuclear aromatic hydrocarbons by sediments and soils. Envir. Sci. Tech. 14:1524-1528.

Methot, Jr., R.D., and D. Kramer. 1979. Growth of northern anchovy, *Engraulis mordax*, larvae in the sea. Fish. Bull. 77(2):413-423.

Milliman, J.D. and R.H. Meade. 1983. World-wide delivery of river sediment to the ocean. J. of Geology. 91(1):1-21.

Mossa, J. and H.H. Roberts. 1990. Synergism of riverine and winter storm-related sediment transport processes in Louisiana's coastal wetlands. Transactions, Gulf Coast Assoc. of Geological Societies. XL:635-642.

Murphy, L.S., and E.M. Haugen. 1985. The distribution and abundance of phototrophic ultraplankton in the North Atlantic. Limnol. Oceanogr. 30:47-58.

Olson, R.J., S.W. Chisholm, E.R. Zettler, and E.V. Armbrust. 1988. Analysis of Synechococcus pigment types in the sea using single and dual beam flow cytometry. Deep-Sea Res. 35:425-440.

Parsons, M.L., Q. Dortch, N.N. Rabalais, D. Milsted, and S. Pool. 1992. Potential for toxic algal blooms in Louisiana coastal waters, Gulf Estuarine Research Society Meeting, April 3-4, 1992, Port Aranas, TX.

Parsons, T.R., Y. Maita, and C.M. Lalli. 1984. A manual of chemical and biological methods for seawater analysis. Pergamon Press, New York. 173 pp.

Pick, F.R. 1991. The abundance and composition of freshwater picocyanobacteria in relation to light penetration. Limnol. Oceanogr. 36:14570-1462.

Rabalais, N.N., R.E. Turner and W.J. Wiseman, Jr. 1991. A brief summary of hypoxia on the northern Gulf of Mexico continental shelf: 1985-1988. In: Tyson, R.V. and T. H. Pearson (eds.). Modern and Ancient Continental Shelf Anoxia, Geological Society Special Publication No. 58. The Geological Society, London. Pp. 35-47.

Rabalais, N.N., R.E. Turner and W.J. Wiseman, Jr. 1992. Distribution and characteristics of hypoxia on the Louisiana shelf in 1990 and 1991. In: Proceedings, NECOP Synthesis Meeting. Publ. No. TAMU-SG-92-109, Texas Sea Grant College Program, College Station, Texas. Pp. 62-67.

Renaud, M.L. 1986. Hypoxia in Louisiana coastal waters during 1983: implications for fisheries. Fish. Bull. 84(1):19-26.

Rhodes, R.C., A.J. Wallcraft, and J.D. Thompson. 1985. Navy-corrected geostrophic wind set for the Gulf of Mexico. NORDA Technical Note 310. 103 pp.

SAS Institute Inc. 1985. SAS user's guide: basics, version 5 edition. Cary, NC. 1290 pp.

Shapiro, L.P. and E.M. Haugen. 1988. Seasonal distribution and temperature tolerance of Synechococcus in Boothbay Harbor, ME. Est. Coast. Shelf Sci. 26:517-526.

Shapiro, L.P., E.M. Haugen, and E.J. Carpenter. 1989. Occurance and abundance of green fluorescing dinoflagellates in surface waters of the Northwest Atlantic and Northeast Pacific Oceans. J. Phycol. 25:189-191.

Shumway, S.E. 1990. A review of the effects of algal blooms on shellfish and aquaculture. J. World Aquaculture Society 21:65-104.

Sigleo, A.C. and J.C. Means. 1990. Organic and inorganic components of estuarine colloids: implications for transport of pollutants. Rev. Envir. Toxicol. Contam. 112:123-147.

Smayda, T.J. 1989. Primary production and the global epidemic of phytoplankton blooms in the sea: A linkage? In: Cosper, E.M., V.M. Bricelj, and E.J. Carpenter (eds.). Novel Phytoplankton Blooms. Coastal and Estuarine Studies 35, Springer-Verlag, NY. Pp. 449-483.

Smayda, T. J. 1990. Novel and nuisance phytoplankton blooms in the sea: Evidence for a global epidemic. In: Graneli, E., B. Sundstrom, R. Edler, and D.M. Anderson (eds.). Toxic Marine Phytoplankton. Elsevier Science Publishing Co., N.Y. Pp. 29-40.

Smith, N.P. 1980. On the hydrography of shelf waters off the central Texas gulf coast. J. Physical Oceanogr. 10:806-813.

Smith, R.A., R.B. Alexander and M.G. Wolman. 1987. Water-quality trends in the nation's rivers. Science 235:1607-1615.

Stumpf, R.P. 1988. Remote sensing of suspended sediments in estuaries using atmospheric and compsitional corrections to AVHRR data. Proceedings of the 21st Intl. Symp. on Remote Sensing of Environment. Ann Arbor, Michigan. Pg. 205-222.

Stumpf, R.P. 1992. Remote sensing of water clarity and suspended in coastal waters. In: Proceedings of the First Thermatic Conference on Remote Sensing for Marine and Coastal Environments. 13 pp.

Taylor, F.J.R. 1976. Appendix: treatment of micro- and nanoplankton samples. Pp. 32-33. In: Steedman, H.F. (ed.). Zooplankton Fixation and Preservation. Unesco Press, Paris.

Taylor, F.J.R. (ed.). 1987. The biology of dinoflagellates. Botanical Monographs, Vol. 21, Blackwell Scientific Publications, Oxford.

Tennant, D.A. and E.T. Baker. 1992. A fast, high-precision splitter for particle suspensions. Mar. Geol. 107:247-252.

Tranter, D.J. and P.E. Smith. 1968. Filtration performance. In: Tranter, D.J. (ed.). Zooplankton Sampling. Unesco Press, Paris. Pp. 27-56.

Turner, R.E., R. Kaswadji, N.N. Rabalais, and D.F. Boesch. 1987. Long-term changes in the Mississippi River water quality and its relationship to hypoxic continental shelf waters. pp 261-266. In: Estuarine and Coastal Management—Tools of the Trade. Proceedings, Tenth National Conference, the Coastal Society, October 12-15, 1986, New Orleans, Louisiana.

Vaulot, D. and X. Ning. 1988. Abundance and cellular characteristics of marine Synechococcus spp. in the dilution zone of the Changjiang (Yangtze) River, China. Cont. Shelf Res. 8:1171-1186.

Walker, N.D., L.J. Rouse, Jr., O.K. Huh, D.E. Wilensky, and V Ransibrahmanatal. 1992. Assessing the spatial characteristics and temporal variabilities of the Mississippi and Atchafalaya River plumes. Proceedings of the First Thematic Conference on Remote Sensing for Marine and Coastal Environments. New Orleans, Louisiana. SPIE 1930:719-728.

Walker, N.D. and L.J. Rouse, Jr. 1993. Satellite assessment of Mississippi River discharge plume variability. OCS Study MMS 93-0044. U.S. Department of the Interior, Minerals Management Service, Gulf of Mexico OCS Regional Office, New Orleans, Louisiana. 50 pp.

Waterbury, J.B.S., S.W. Watson, F.W. Valois, and D.G. Franks. 1986. Biological and ecological characterization of the marine unicellular cyanobacterium Synechococcus. In: Platt, T. and W.K.W. Li (eds.). Photosynthetic Picoplankton. Can. Bull. Fish. Aquat. Sci. 214:71-120.

Wells, J.T. and G.P. Kemp. 1981. Atchafalaya mid stream and recent mudflat progradation: Louisiana Chenier plain, Transactions, Gulf Coast Association of Geological Societies, Vol. XXXI, pp. 409-416.

Wood, A. M., P.K. Horan, K.Muirhead, D.A. Phinney, C.M. Yentsch, and J.B. Waterbury. 1985. Discrimination between types of pigments in marine Synechococcus spp. by scanning spectroscropy, epifluorescence microscopy, and flow cytometry. Limnol Oceanogr. 30:1303-1316.

Yentsch, C.S. and J.F. Hebard. 1957. A gauge for determining plankton volume by the mercury immersion method. J. Conseil. 22(2):184-190.

The Department of the Interior Mission

As the Nation's principal conservation agency, the Department of the Interior has responsibility for most of our nationally owned public lands and natural resources. This includes fostering sound use of our land and water resources; protecting our fish, wildlife, and biological diversity; preserving the environmental and cultural values of our national parks and historical places; and providing for the enjoyment of life through outdoor recreation. The Department assesses our energy and mineral resources and works to ensure that their development is in the best interests of all our people by encouraging stewardship and citizen participation in their care. The Department also has a major responsibility for American Indian reservation communities and for people who live in island territories under U.S. administration.

The Minerals Management Service Mission

As a bureau of the Department of the Interior, the Minerals Management Service's (MMS) primary responsibilities are to manage the mineral resources located on the Nation's Outer Continental Shelf (OCS), collect revenue from the Federal OCS and onshore Federal and Indian lands, and distribute those revenues.

Moreover, in working to meet its responsibilities, the **Offshore Minerals Management Program** administers the OCS competitive leasing program and oversees the safe and environmentally sound exploration and production of our Nation's offshore natural gas, oil and other mineral resources. The MMS **Minerals Revenue Management** meets its responsibilities by ensuring the efficient, timely and accurate collection and disbursement of revenue from mineral leasing and production due to Indian tribes and allottees, States and the U.S. Treasury.

The MMS strives to fulfill its responsibilities through the general guiding principles of: (1) being responsive to the public's concerns and interests by maintaining a dialogue with all potentially affected parties and (2) carrying out its programs with an emphasis on working to enhance the quality of life for all Americans by lending MMS assistance and expertise to economic development and environmental protection.